A structural and geochronological investigation of the Keno Hill area, central Yukon, Canada

by

Anastasia Kulchycki

BSc, Queen's University, 2022

MASTER OF SCIENCE

in

THE COLLEGE OF GRADUATE STUDIES

(Earth and Environmental Sciences)

THE UNIVERSITY OF BRITISH COLUMBIA

(Okanagan)

September 2024

©Anastasia Kulchycki, 2024

The following individuals certify that they have read, and recommend to the College of Graduate Studies for acceptance, a thesis entitled:

A structural and geochronological investigation of the Keno Hill area, central Yukon, Canada

submitted by Anastasia Kulchycki in partial fulfillment of the requirements of

the degree of Master of Science .

Dr. Kyle Larson, Irving K. Barber Faculty of Science – Department of Earth, Environmental and Geographic Sciences

Supervisor

Dr. Diane Skipton, Geological Survey of Newfoundland & Labrador

Supervisory Committee Member

Dr. Dawn Kellett, Geological Survey of Canada

Supervisory Committee Member

Dr. Conor Pranckevicius, Irving K. Barber Faculty of Science – Department of Chemistry

University Examiner

ABSTRACT

The western margin of North America was shaped by the Cordilleran orogen. In the mid-Cretaceous, northeast-directed convergence resulted in compression-related structures that span the Cordillera, including the Selwyn thrust and fold belt in central Yukon. Bordering the Keno Hill area are two northwest-southeast extending thrust faults of the Selwyn thrust and fold belt. These faults are the Robert Service Thrust (RST), to the south, and the underlying Tombstone Thrust (TT), to the north. Previous detailed studies of the Keno Hill area have focussed on the late, brittle structures that host vein mineralization, leaving the structural evolution of the early, ductile structures largely unresolved. To investigate the geological evolution of the early structures, this study incorporates 1:25000 scale structural field mapping, microstructural analysis, and geochronology, including: *c*-axis crystallographic preferred orientation investigations, grain size piezometry, crystallographic vorticity axis investigations, *in situ* $^{87}Rb/^{87}Sr$ and $^{40}Ar/^{39}Ar$ geochronology, and Raman spectroscopy-based thermometry of carbonaceous materials. The *in situ* geochronology and thermometry investigations on weakly metamorphosed, clastic metasedimentary rocks from the hanging wall and footwall of the RST show a break across the approximate fault trace, with higher temperatures (>480 °C) and older dates in the hanging wall (130-102 Ma), with both the temporal and thermometry data showing a general decrease in the footwall, moving towards the approximate trace of the TT. This coincides with microstructural investigations which showed less grain boundary area reduction farther north. While the strain investigations did not show any obvious spatial or structural relationships, the area was dominated by predominantly non-coaxial constrictional strain. Contrary to other studies that have tried to date movement along the regionally extending thrust faults, the data could support that movement along the TT potentially continued until ca. 88 Ma as opposed to cessation ca. 100-104 Ma.

LAY SUMMARY

Keno City in central Yukon Territory is known for its silver, lead, and zinc deposits. Bordering the town are two thrust faults: the overlying Robert Service Thrust (RST) to the south and underlying Tombstone Thrust (TT) to the north. Previous studies have characterized the vein mineralization and have hypothesized the tectonic and kinematic evolution of the area prior to the mineralization, but many questions remain unanswered. This study focused on understanding the timing, temperature, and extent of deformation prior to mineralization. The results of this study show deformation occurred between around 130 to 102 Ma, potentially continuing until about 88 Ma. This deformation possibly occurred at, or shortly after regional metamorphism, with peak deformation temperatures around 400-550 °C. While there was no obvious variation in the deformation geometry, the results show a break in temperature and timing across the RST.

PREFACE

Fieldwork for this project was conducted in the summer of 2022 and was facilitated through the Yukon Geological Survey. All of the data processing and writing of this thesis took place between September 2022 and August 2024. My supervisor, Dr. Kyle Larson, provided guidance and feedback throughout all stages of the project. Dr. Diane Skipton and Dr. Dawn Kellett also provided insight at various points throughout the project and provided feedback during the editing phase. Samples 22AK-001-1-1 through 22AK-082-1-2 were collected during fieldwork, and sample 18-709 was provided by Hecla Mining Company (formerly known as Alexco Resource Corp).

Figures 1.1, 1.2, 2.1, 2.2, 2.4, and 5.3 contain material adapted from copyrighted sources and are printed with permissions. There was no use of generative AI at any point during this project.

TABLE OF CONTENTS

Abstract ... **iii**

Lay Summary ... **iv**

Preface ... **v**

Table of Contents ... **vi**

List of Tables ... **ix**

List of Figures ... **x**

List of Equations ... **xv**

List of Abbreviations ... **xvi**

Acknowledgements ... **xviii**

1 Introduction ... **1**

1.1 The Keno Hill area: competing structural models and unknowns ... 1

1.2 Project Area ... 3

1.3 Problem Statement ... 3

1.4 Objectives ... 5

1.5 Significance ... 6

2 Geologic Background ... **7**

2.1 Evolution of the Canadian Cordillera ... 7

2.1.1 Selwyn Basin ... 11

2.2 Geology of the Keno Hill District ... 11

2.2.1 Stratigraphy ... 11

2.2.2 Structural History ... 12

2.2.3 Previous Geochronology ... 15

3 Methods ... **17**

3.1 Fieldwork ... 17

3.2 Microtectonics ... 17

3.2.1 Petrography and Microstructures ... 17

3.2.2 Quartz CPO ... 17

3.2.3 Quartz CVA and Grain Size Piezometry 20
3.3 Geochronology 22
3.3.1 $^{87}Rb/^{87}Sr$ Dating 22
3.3.2 $^{40}Ar/^{39}Ar$ Dating 24
3.4 Thermometry 25
4 Results 26
4.1 Fieldwork 26
4.2 Microtectonics 33
4.2.1 Petrography and Microstructures 33
4.2.2 Quartz CPO 38
4.2.3 Grain Size Piezometry 41
4.2.4 Quartz Crystallographic Vorticity Axes 44
4.3 Geochronology 51
4.3.1 $^{87}Rb/^{87}Sr$ Dating 51
4.3.2 $^{40}Ar/^{39}Ar$ Dating 53
4.4 Thermometry 58
5 Interpretations 62
5.1 Structural Framework 62
5.2 Microtectonics 64
5.2.1 Microstructures 64
5.2.2 Quartz CPOs 64
5.2.3 Quartz Crystallographic Vorticity Axes 67
5.3 Geochronology 68
5.4 Thermometry 69
6 Discussion 71
6.1 Strain 71
6.2 Structural Framework 71
6.3 Thermal History 72
6.4 Timing 73
6.5 Regional Kinematic Framework 75
7 Conclusions 78

7.1 Recommendations for future work 78
References 80
Appendices 89
Appendix A: Fieldwork Station Descriptions 89
Appendix B: Thin Section Descriptions 108
Appendix C: Sample quartz *c*-axis CPO Descriptions 115
Appendix D: Geochronology 119
Appendix D.1: $^{87}Rb/^{87}Sr$ 119
Appendix D.2: $^{40}Ar/^{39}Ar$ 132
Appendix E: Thermometry Data 136

LIST OF TABLES

Table 3.1: List of thin-section samples and the analyses conducted. 19
Table 3.2: EBSD Parameters. 20
Table 3.3: List of rotations used in the CVA script. 21
Table 3.4: ESL 193 nm laser ablation parameters including TwoVOL3 sample chamber for all 3 sessions. Session 1 had a fluence of 3.6, Session 2 and 3 had a fluence of 3.5. 23
Table 3.5: Reproduced ages of references materials through in situ $^{87}Rb/^{87}Sr$ geochronology, using an inverse isochron from IsoplotR (Vermeesch, 2018) after correction with Mica-1O. Reference materials: Mica Mg (Hogmalm et al., 2017), Mica-Fe (Rösel & Zack, 2022), Mica-1O (Camacho et al., 2020; Larson et al., 2023b)), and Mica-1B (Camacho et al., 2012; Larson et al., 2023b). In addition to the analyses, the dates in this table were calculated using the initial $^{87}Sr/^{86}Sr$ ratios shown in the bottom row. Uncertainty is reported as Two Standard Error (2SE) absolute. 24
Table 4.1: In situ $^{40}Ar/^{39}Ar$ results. 56
Table 4.2: Average G, D1, and D2 position reported with one standard deviation and the corresponding number of spots targeted per thin section as well as the number of D2 peaks observed. 60
Table 4.3: Peak intensity ratio (R1), peak area ratio (R2) and temperature (°C) reported with one standard deviation for each sample. 60

LIST OF FIGURES

Figure 1.1: Terrane Map of Yukon Territory (modified from Yukon Geological Survey, 2020). Field area outlined by the red box. Robert Service Thrust (RST) and Tombstone Thrust (TT) indicated. 2

Figure 1.2: Cross-sections through the Keno Hill area, oriented SW-NE from left to right. A) from Murphy and Roots, 1996; and B) reflected across a vertical axis, from Read et al., 2020. ... 4

Figure 2.1: Map of the terranes and major faults that make up the Canadian Cordillera with an inset in the top right corner illustrating the approximate boundaries of the five morphogeological belts (modified from Nelson et al., 2013). Approximate study area shown by the red square. 8

Figure 2.2: a) illustrates the counterclockwise rotation of Stikinia (ST) terrane in the Early Jurassic. The relative positions of the Alexander (AX), Wrangellia (WR), Yukon-Tanana (YT), and Quesnellia (QN) terranes are marked; b) illustrates the movement of the North American continent and its effect on the strike-slip faults within the continent; c) illustrates the configurations of the oceanic plates along the western margin of the North American continent around i) 53 Ma, ii) 39 Ma, iii) 5 Ma. All figures are modified from Nelson et al. (2013). 10

Figure 2.3: Stratigraphy and geochronology of the Keno Hill area (adapted from McOnie, 2016). 13

Figure 2.4: Regional map illustrating the location of the thrust faults. Modified from Mair et al. (2000) which is modified after Murphy (1997). 14

Figure 2.5: Map illustrating the approximate location of the upper limit of the TSZ and the locations of Ar-Ar samples of Mair et al. (2006). Figure was created by combining information from figures from Mair et al. (2006) and Roots (1997). 16

Figure 3.1: Station map of the Keno Hill area based off field work conducted in 2022. Station 22AK-081 is located on Cobalt Hill, east of the map area. Simplified from Read et al. (2020). . 18

Figure 4.1: Geologic map of the Keno Hill area with samples and structural measurements labelled. Simplified from Read et al. (2020). 27

Figure 4.2: A) foliation parallel isoclinal folds with an inset of stereonet of the measurements of the foliations (Station 22AK-050). B) isoclinal folds with quartz veins and an inset of a stereonet of the fold axis and axial plane measurements (Station 22AK-071)……...27

Figure 4.3: A) Open fold and stereonet inset showing axial planes and fold axis measurements (Station 22AK-004); and B) Crenulations and stereonet inset showing crenulation lineation

measurements (Station 22AK-004). Relationship of isoclinal folds with open folds from stations: C) 22AK-063 (Bermingham open pit); and D) 22AK-064 (Coral WigWam open pit)..... 29

Figure 4.4: Station 22AK-058 (Onek property). A) isoclinal folds truncated by local thrust faults; B) normal-oblique vein fault with greenstone (right) outlining an isoclinal fold. 31

Figure 4.5: Shear sense indicators as observed at stations: A) 22AK-072, B) 22AK-045, C) 22AK-014, and D) 22AK-015. 32

Figure 4.6: Possible staurolite as a result of contact metamorphism at station 22AK-073……..32

Figure 4.7: Petrographic images of chlorite (Chl) in A) PPL, and B) XPL for sample 22AK-061-1-1. Petrographic images of calcite (Ca) in C) PPL, and D) XPL for sample 22AK-072-1-2. Quartz (Qtz) and white mica (Wm) are labelled as well……...33

Figure 4.8: Petrographic images of sample 22AK-073-1-1 in A) PPL, and B) XPL……..…..34

Figure 4.9: Thin section images of quartz textures in XPL: A) small equiant grains bordering larger grains from station 22AK-043; B) mica grains bordering the long edge of quartz grains from station 22AK-061; C) an example of undulose extinction from station 22AK-006; and D) lamellae in large quartz grain (sigma clast) and mica grains bordering long edge of quartz grains from station 22AK-061……..……35

Figure 4.10: All thin section images are shown in XPL. A) and B) show interlobate quartz grains. A) is from station 22AK-037, and B) is from station 22AK-023. Both A) and B) are from the northern portion of the map area. C) and D) show polygonal quartz grains with triple junctions. C) is from station 22AK-011 and D) is from station 22AK-061. Both C) and D) are from the southern portion of the map area…….……..36

Figure 4.11: thin section images in XPL, illustrating shear sense. Samples were taken from stations: A) 22AK-011, B) 22AK-060, C) 22AK-078, D) 22AK-023, E) 22AK-041, F) 22AK-061, G) and H) 22AK-045, I) 22AK-069, J) 22AK-081, and K) 22AK-80. All these stations can be located in Fig. 3.1 or the samples as annotated in the images from Fig. 4.1……37

Figure 4.12: Quartz c-axis CPO lower hemisphere Schmidt plots (contoured (left) and scatter (right)) for 25 samples (labelled below). Red annotation on the lower hemisphere scatter plot represents the interpreted fabric type. Number of grains per CPO plot is presented beside sample number underneath the plots. JPF-index written to the left of the contoured plot (in black), and the opening angles (when applicable) are written to the right of the scatter plot (in red). Black arrows indicate interpreted shear sense. Contour density colour gradient shown bottom centre. z) illustrates location of foliation and lineation, and activated slip systems. All plots made using FabricPlotR (Larson, 2022) script…….……39

Figure 4.13: A) JPF -index from fabric analyser investigations plotted with respect to relative structural position; and B) approximate percent of phyllosilicates in those samples with respect to the JPF-index. Where the asterisks (*) in A) delineate which samples were collected from previously mapped klippes……..….40

Figure 4.14: All samples labelled on the left. A) Grain orientation spread inflexion point. Grain size distribution histogram for: B) all grains with text showing the differential stress for the sample, and C) relict and recrystallized grains with text showing the recrystallized RMS grain size. On the right are thin section maps of 22AK-023-1-1 for: D) grain orientation spread, and E) relict and recrystallized grains. Plots from A-C, and F were made using the Cross et al. (2017) script with the trade-off function. D was made using Aztec Crystal……..…..42

Figure 4.15: A) RMS grain size for recrystallized and relict grains plotted with respect to relative structural position. B) Differential stress calculated from recrystallized and relict RMS grain size plotted against relative structural position. All data from EBSD investigations, calculated using RexRelict.M script (Cross et al., 2017)..... 43

Figure 4.16: Quartz c- and a-axis CPOs, 2-10° misorientation axes IPF, CVAs, and lattice orientation from the observer reference frame for the bulk, recrystallized and relict grains of sample 22AK-061-1-1. Legend shows the kernel densities for CPO plots, multiplies of uniform density for CVA plots. 44

Figure 4.17: Quartz c- and a-axis CPOs, 2-10° misorientation axes IPF, CVAs, and lattice orientation from the observer reference frame for the bulk, recrystallized and relict grains of sample 22AK-060-1-1. Legend shows the kernel densities for CPO plots, multiples of uniform density. 45

Figure 4.18: Quartz c- and a-axis CPOs, 2-10° misorientation axes IPF, CVAs, and lattice orientation from the observer reference frame for the bulk, recrystallized and relict grains of sample 22AK-006-1-2. Legend shows the kernel densities for CPO plots, multiplies of uniform density for CVA plots. 46

Figure 4.19: Quartz c- and a-axis CPOs, 2-10° misorientation axes IPF, CVAs, and lattice orientation from the observer reference frame for the bulk, recrystallized and relict grains of sample 22AK-001-1-1. Legend shows the kernel densities for CPO plots, multiples of uniform density. 47

Figure 4.20: Quartz c- and a-axis CPOs, 2-10° misorientation axes IPF, CVAs, and lattice orientation from the observer reference frame for the bulk, recrystallized and relict grains of sample 22AK-082-1-2. Legend shows the kernel densities for CPO plots, multiplies of uniform density for CVA plots. 48

Figure 4.21: Quartz c- and a-axis CPOs, 2-10° misorientation axes IPF, CVAs, and lattice orientation from the observer reference frame for the bulk, recrystallized and relict grains of

sample 22AK-023-1-1. Legend shows the kernel densities for CPO plots, multiples of uniform density. 49
Figure 4.22: Quartz c- and a-axis CPOs, 2-10° misorientation axes IPF, CVAs, and lattice orientation from the observer reference frame for the bulk, recrystallized and relict grains of sample 22AK-032-2-1. Legend shows the kernel densities for CPO plots, multiplies of uniform density for CVA plots. 50
Figure 4.23: Isochron plots for 6 samples (labelled), with outliers removed. Plots generated with IsoplotR (Vermeesch, 2018)……...…...52
Figure 4.24: Sample 22AK-037-1-1 populations of white mica targeted shown in C) in XPL and their corresponding isochrons shown in A) (1) and B) (2). Isochron plots made using IsolpotR (Vermeesch, 2018)…….…53
Figure 4.25: 40Ar/39Ar weighted mean date plots with outliers removed for: A) i) sample 22AK-061-1-1, with ii) showing an example of targeted mica, B) sample 22AK-060-1-1, C) 22AK-082-1-1, D) 22AK-023-1-1, and E) 22AK-037-1-1. All plots made using IsoplotR (Vermeesch, 2018)…….....55
Figure 4.26: Carbonaceous material spectra in i) of both and A) and B), with an example of carbonaceous material from the respective thin section (PPL) in ii) for both A and B…….58
Figure 4.27: Raman spectroscopy of carbonaceous material (RSCM) temperature plotted alongside latitude of the samples. 61
Figure 5.1: Schematic geologic cross-section of the Keno Hill area along the A-A' transect presented in the geologic map in Figure 4.1. 63
Figure 5.2: Spatial variations of in situ geochronology dates, temperatures, CVAs (Simple Shear = SS; Pure Shear = PS; and Transtension = TT), and microstructres (Subgrain rotation dominant = SG). The * refers to samples collected on Sourdough Hill, with the filled circles depicting where the data as the area is presently mapped (with the klippe on Sourdough Hill), and the hollow squares depict their relative orientation to other samples collected if the klippe on Sourdough Hill does not exist. The location of the Robert Service Thrust (RST) and the potential unmapped fault are depicted with a dashed line. 65
Figure 5.3: A) Quartz slip systems (modified from Fossen (2016)). B) Misorientation axes inverse pole figure slip system key (modified and simplified from Piette-Lauzière et al. (2020). 66

Figure 5.4: CPO opening angle temperature estimates plotted alongside relative structural position in relation to the RST showing A) absolute, and B) relative uncertainties. 67
Figure 6.1: Schematic diagram of the structural evolution of the Keno Hill area. Depicting: A) isoclinal folding event; B) movement along the Robert Service Thrust (RST); C) in-sequence (re)activation of the Tombstone Thrust (TT) and an unmapped structure; D) open folding event and the late veins/normal-oblique faults.……..……74

Figure D.1: Sample 22AK-011-1-1. November 22nd, 2022. 120
Figure D.2: Sample 22AK-037-1-1. Group 1. November 22nd, 2022 121
Figure D.3: Sample 22AK-037-1-1. Group 2. November 22nd, 2022 122
Figure D.4: Sample 22AK-061-1-1. November 22nd, 2022. 123
Figure D.5: Sample 22AK-037-1-1. January 16th, 2023. 124
Figure D.6: Sample 22AK-061-1-1. January 16th, 2023. 125
Figure D.7: Sample 22AK-006-1-2. Part 1. March 3rd, 2023. 126
Figure D.8: Sample 22AK-006-1-2. Part 2. March 3rd, 2023. 127
Figure D.9: Sample 22AK-023-1-1. Part 1. March 3rd, 2023. 128
Figure D.10: Sample 22AK-023-1-1. Part 2. March 3rd, 2023. 129
Figure D. 11: Sample 22AK-082-1-1. Part 1. March 3rd, 2023. 130
Figure D.12: 22AK-081-1-2. Part 2. March 3rd, 2023. 131
Figure D.13: Sample 22AK-023-1-1 in situ $^{39}Ar/^{40}Ar$ spots. 132
Figure D.14: Sample 22AK-037-1-1 in situ $^{40}Ar/^{39}Ar$ spots. 133
Figure D.15: Sample 22AK-082-1-1 in situ $^{40}Ar/^{39}Ar$ spots. 134
Figure D.16: Sample 22AK-082-1-1 in situ $^{40}Ar/^{39}Ar$ spots……...135

LIST OF EQUATIONS

Equation 1: Calculates differential stress using root mean square grain (Cross et al., 2017)……..……21

Equation 2: Calculates uncertainty for differential stress (equation 1)…….…..21

Equation 3: Calculates peak intensity ratio for Raman spectroscopy on carbonaceous materials (RSCM) (Beyssac et al., 2002)…….……..25

Equation 4: Calculates peak area ratio for Raman spectroscopy on carbonaceous materials (RSCM) (Beyssac et al., 2002)……..……..……..25

Equation 5: Calculates RSCM temperatures (Beyssac et al., 2002)…….....……..49

Equation 6: Calculates opening angle temperature estimates (Faleiros et al., 2016)……...……66

LIST OF ABBREVIATIONS

Elemental Abbreviations

Al	Aluminum
Ar	Argon
Ca	Calcium
Fe	Iron
Mg	Magnesium
Mn	Manganese
Pb	Lead
Rb	Rubidium
Sr	Strontium
U	Uranium

Mineral Abbreviations

Ca	Calcite
Chl	Chlorite
Wm	White mica
Qtz	Quartz

Microstructural Abbreviations

CPO	Crystallographic Preferred Orientation
CVA	Crystallographic Vorticity Axis
GBAR	Grain Boundary Area Reduction
PPL	Plane-polarized light
SGR	Subgrain rotation
XPL	Cross-polarized Light

Investigation Abbreviations

EBSD	Electron backscatter diffraction
LA-ICP-MS	laser-ablation inductively coupled plasma mass spectrometry
MSWD	mean squared weighted deviation

OA	opening angle
RMS	root mean square
RSCM	Raman spectroscopy of carbonaceous materials
SEM	Scanning electron microscope
T	Temperature

Directional Abbreviations

N	North
S	South
E	East
W	West
NW	Northwest
NE	Northeast
SE	Southeast
SW	Southwest
NNW	North-Northwest
NNE	North-Northeast
SSW	South-Southwest
SSE	South-Southeast
WNW	West-Northwest
ESE	East-Southeast

Structure Abbreviations

RST	Robert Service Thrust
TSZ	Tombstone Strain Zone
TT	Tombstone Thrust

ACKNOWLEDGEMENTS

I would like to first acknowledge that fieldwork was undertaken on Nacho Nyak Dun Nation Territory and the studies were completed on the unceded Syilx Okanagan Nation Territory.

I would like to thank my supervisor, Dr. Kyle Larson, for all his guidance and support over the past two years. I could not have done this without his feedback and understanding. I would also like to thank Dr. Diane Skipton for her mentorship and advice in the field and over the course of the project as well as her input during the writing and data interpretation stages. I would like to thank Dr. Dawn Kellett for her perspective and feedback over the course of this project. Overall, I would like to thank all three members of my committee for giving me the opportunity to undertake this project and help me on this step in pursuing my career aspirations. I am extremely grateful and appreciative of everything you all have done for me over the past couple years and for your continuous support.

I would like to acknowledge the Yukon Geological Survey for facilitating the fieldwork and for their support. Thank you to Sarah Bowie and Sofia Bond for your assistance during fieldwork. I truly could not have done this without either of you.

I would like to thank Hecla Mining (formerly known as Alexco Resource Corp) for granting access to their roads and for providing sample 18-709. Special thanks to Peter Read for his insight, advice, and interest in this project.

Thank you to Dr. Alfredo Camacho of University of Manitoba for facilitating the *in situ* $^{40}Ar/^{39}Ar$ geochronology in this study. Thank you to Dr. Matthew Steele-MacInnis for allowing me to conduct Raman spectroscopy investigations in the lab at University of Alberta.

Thank you to Dr. Sudip Shreshta and Dr. Mark Button of Fipke Laboratory for Trace Element Research for training me on the SEM and LA-ICP-MS and for answering my questions. I would like to thank Kyle Tollefson and Alix Osinchuk for their detailed explanations and continued advice. Overall, I would like to acknowledge all of my colleagues of the UBCO Tectonics Group for their comradery and insight.

Finally, I would like to thank my friends and family for their support while writing this thesis. To Patrick, Laura, and Maya, for always believing me, and for sharing fun anecdotes as

well as baby animal photos. To Matt, for supporting my decision to better my wellbeing and his dog Mocha for always being excited to see me. To my partner, Katie, for her patience and support these past couple years. Her ability to always put a smile on my face does not go unnoticed. I couldn’t have done this without you.

1 INTRODUCTION

1.1 THE KENO HILL AREA: COMPETING STRUCTURAL MODELS AND UNKNOWNS

The Keno Hill area of central Yukon Territory is known for its Ag-Pb-Zn vein mineralization and has long drawn the attention of geologists and prospectors. The area is located on the northeastern edge of the Selwyn Basin (Gordey & Anderson, 1993), which consists of sedimentary rocks that were deposited in a deep-marine environment on the western margin of Laurentia, between the Precambrian to Devonian (Fig. 1.1; Nelson et al., 2013). In the mid Cretaceous (~120-90 Ma), like much of the Cordillera, the basin underwent convergence-related deformation that, locally, resulted in the formation of the northeast-vergent Selwyn thrust and fold belt (Gordey & Anderson, 1993) with orogen-parallel, northwest-trending structures.

The Keno Hill area is structurally complex with multiple phases of folding and faulting, resulting in varying interpretations of the structural evolution of the area (Murphy & Roots, 1996; Read et al., 2020). Broadly speaking, the dominant structures can be broken into two categories: 1) early ductile structures associated with Jurassic-Cretaceous orogenesis, and 2) late brittle structures that host the vein mineralization. The early deformation is thought to have commenced after the deposition of the youngest deformed strata in the Selwyn Basin (Late Jurassic in age) and to have ceased prior to intrusions of the Mayo and Tombstone igneous suites (mid Cretaceous) (Mair et al., 2006). While many studies have focused on better understanding the timing and development of the late structures and associated mineralization, the details of the early structures remain debated. The two main competing models for the evolution of the early structures include: 1) that the regional scale thrusting is early, and folding is late (Murphy, 1997; Roots, 1997), or 2) that all folding predates regional scale thrusting (Read et al., 2021). The lack of consensus about the structural evolution of the Keno Hill area at least partially reflects a general lack of detailed structural, geochronological, and thermometric studies focused on the early stage of deformation within the region.

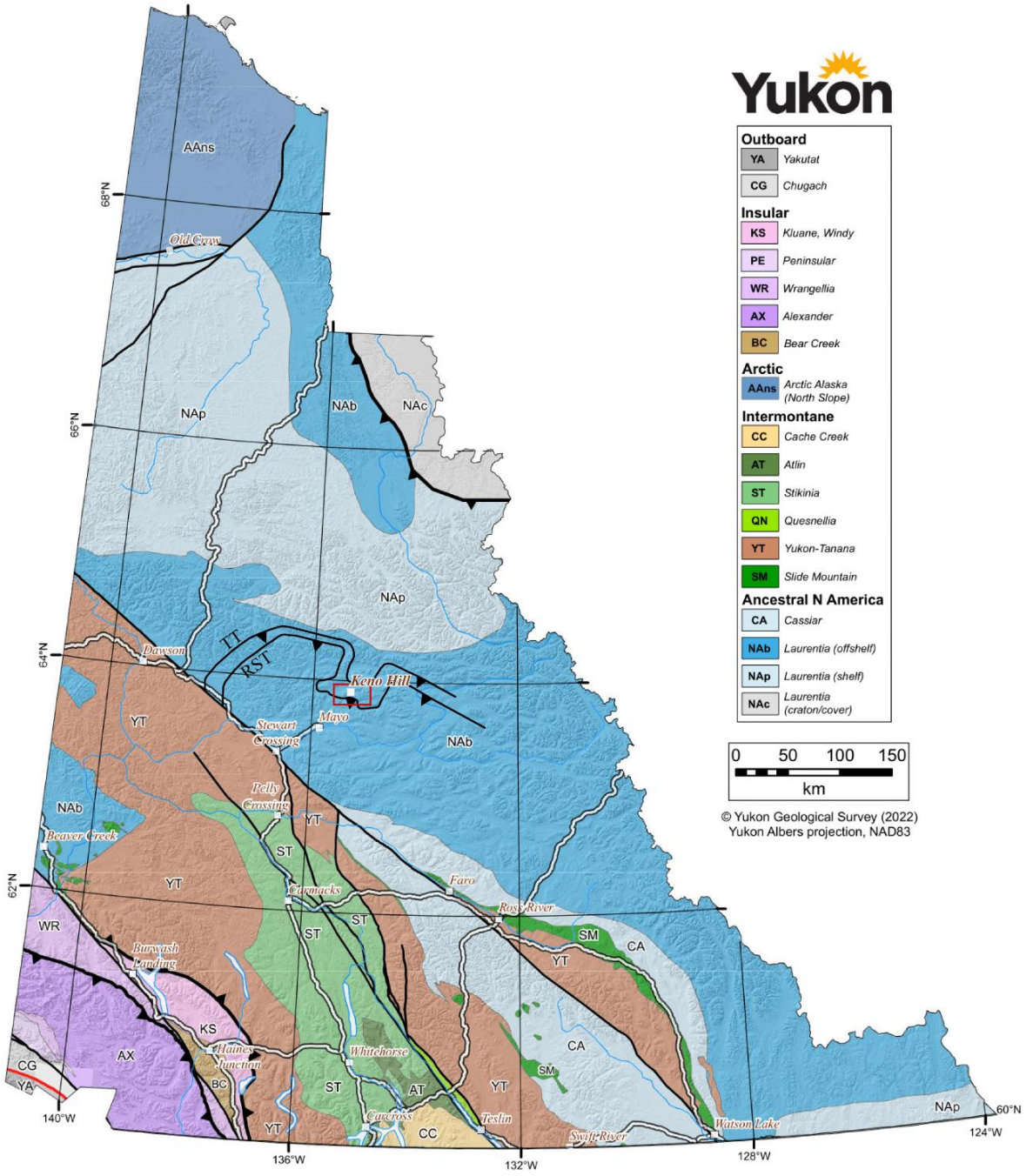


Figure 1.1: Terrane Map of Yukon Territory (modified from Yukon Geological Survey, 2020). Field area outlined by the red box. Robert Service Thrust (RST) and Tombstone Thrust (TT) indicated.

1.2 PROJECT AREA

This thesis project presents the results from 1:25000 scale structural field mapping in the Keno Hill area of central Yukon Territory, which follows similar borders to the NTS sheet 105M/14 (Fig. 1.1; Murphy & Roots, 1996). The area is located approximately 350 km north of Whitehorse and about 45 km northeast of Mayo and is accessible by truck.

The Keno Hill area includes two southeast-striking, regional-scale thrust faults that formed as a result of the Late Jurassic to mid-Cretaceous convergence: the Robert Service Thrust (RST) and Tombstone Thrust (TT) (Fig. 1.1). The activation of the TT is thought to have overprinted the rocks above the TT, including into the hanging wall of the RST (Murphy, 1997). This strain overprint has been termed the Tombstone Strain Zone (TSZ) (Murphy, 1997). The rocks in the Keno Hill area are isoclinally and openly folded, and brittle faults that host Ag-Pb-Zn mineralization crosscut the early structures (e.g. Read et al., 2021).

1.3 PROBLEM STATEMENT

The varying interpretations of the early ductile deformation in the Keno Hill area leaves the structural evolution of the region unclear. D. Murphy and C. Roots mapped across the area, at a 1:50000 scale (Murphy & Roots, 1996), and proposed a deformational history as follows: 1) development of the RST with unknown kinematics, 2) activation of TT overprinting the RST with elongation lineations trending northwest, and west-northwest shear sense indicators (Murphy, 1997), 3) recumbent, isoclinal, northeast-vergent folding as late-stage deformation associated with the TSZ, and 4) the possibility of post-folding faulting (Roots, 1997) (Fig. 1.2A). Murphy (1997) stated that the relationship of the RST to other structural features remains unknown but is inferred to be isoclinally folded within the Keno Hill area as the fault trace was thought to have been crossed multiple times while mapping. Roots (1997) stated that the presence of northeast-trending lineations in the RST indicate that the northeast-vergent isoclinal folds postdate fault-related deformation. Murphy and Roots agree that an open folding event post-dated the TT (Murphy, 1997; Roots, 1997). All fault movement is suggested to have ceased before the Tombstone Suite of intrusions (~95 Ma (Colpron et al., 2016; Craggs, 2022)) (Roots, 1997).

Alexco Resources mapped the Keno Hill District at the 1:5000 scale, incorporating information from ~9000 boreholes and produced a 1:25000 scale map (Read et al., 2020). Alexco geologists proposed three phases of folding denoted as Early Phase, First Phase, and Second Phase (McOnie,

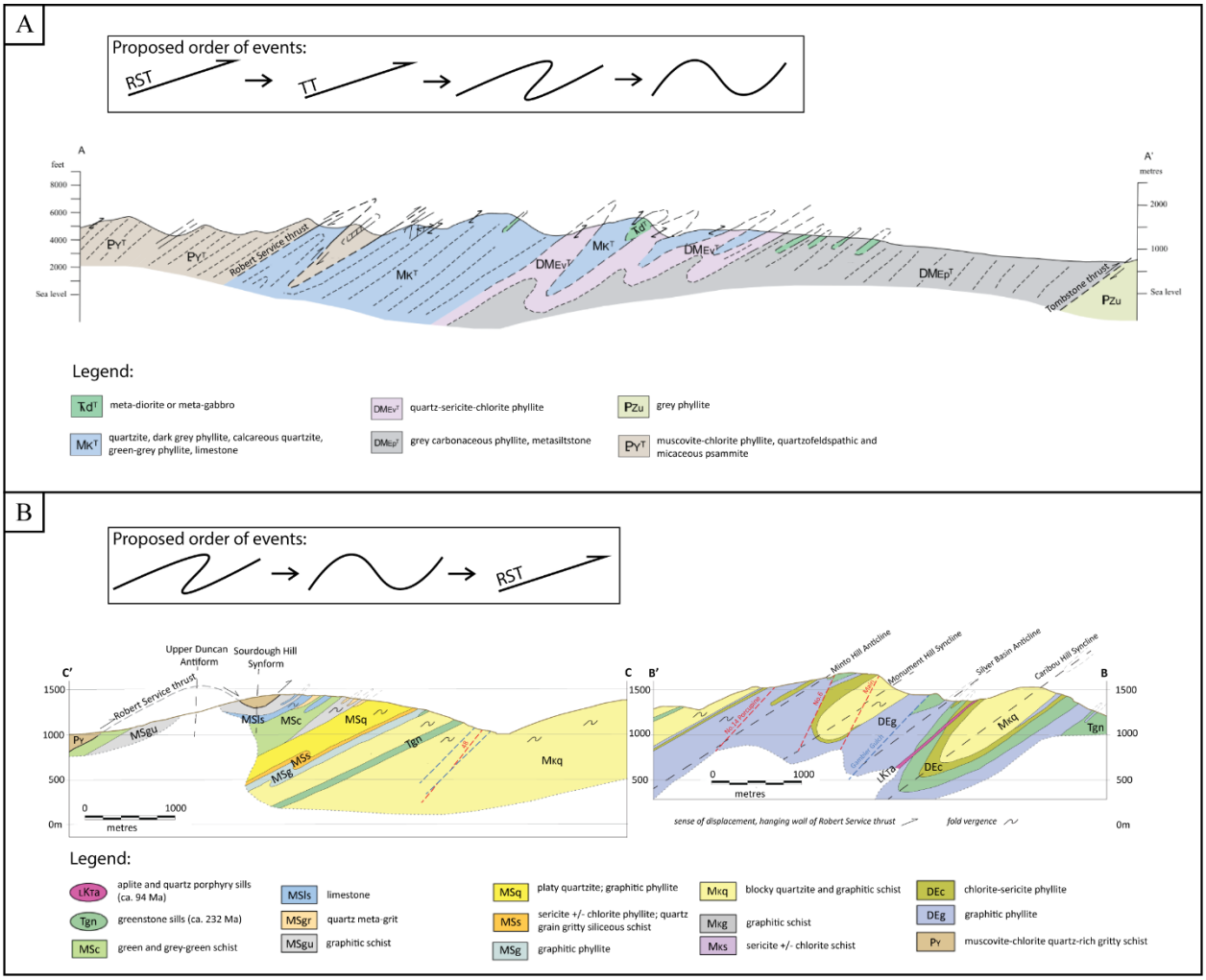


Figure 1.2: Cross-sections through the Keno Hill area, oriented SW-NE from left to right. A) from Murphy and Roots, 1996; and B) reflected across a vertical axis, from Read et al., 2020.

2016). The Early Phase folding event is not well defined, has few occurrences (typically observed in drill core), and has an unknown origin (McOnie, 2016). The First Phase is defined by isoclinal, sub-horizontal, overturned folds that verge to the north, with southerly dipping axial planes and accompanied by low angle syn- to post-folding faulting on the limb shared with anticline-syncline pairs (McOnie, 2016). The Second Phase is defined by subvertical axial planes striking southeast (McOnie, 2016), although its impact on the isoclinal folds remains unstated. Movement along the RST is thought to post-date the second phase of folding; however, a broad warping of the fault plane is thought to have followed the thrust's emplacement (Fig. 1.2B; Read et al., 2021) .

The differences in the previous interpretations of the geology of the region leaves the history of the geological evolution of the Keno Hill area unresolved. As this area is an active mining

district, understanding its structural evolution is critical to ongoing exploration efforts as the early structures could have acted as a secondary conduit for fluid-related mineralization. Moreover, both the RST and TT are regionally significant, extending across central Yukon (Fig. 1.1). This project aims to incorporate geochronology, thermometry, kinematic and tectonic analyses with field observations to investigate the timing, temperature, and strain history across the Keno Hill area. The objectives and significance of this work are outlined in sections 1.4 and 1.5.

1.4 OBJECTIVES

This project is focused on two main objectives:

1. Refine the structural history of the Keno Hill area using structural field mapping and modern structural and geochronological approaches; and use this refined structural history to test against previously proposed models of the structural evolution for the region.
2. Integrate the new data and model with that of the broader region.

The above objectives are achieved through the following methods:

- Field mapping of lithologies, structural fabrics, and their relationships around Keno City, YT in collaboration with the Yukon Geological Survey.
- Tectonic analysis: Creation of a refined structural framework and schematic geologic cross-section based on structural field mapping. Integrate data from this study with data from the broader region to improve the kinematic model of this area.
- Perform geometric and kinematic analyses: along with recorded field observations, petrographic and microstructural analyses, quartz crystallographic preferred orientation (CPO), and quartz crystallographic vorticity axes (CVA) determinations in thin sections, and stereographical analyses of structural measurements will help inform the kinematic development of the area.
- Geochronology: *In situ* $^{87}Rb/^{87}Sr$ and $^{40}Ar/^{39}Ar$ dating of foliation-defining white mica in samples following a SW-NE transect across the main strike and structures within the study area to interpret the timing of movement across those structures based on the thermal history.
- Thermometry: Apply the Raman spectroscopy of carbonaceous material (RSCM) geothermometer to determine peak temperatures across the mapped structures.

1.5 SIGNIFICANCE

This project will contribute to the understanding of the geological evolution of the Keno Hill area and the Selwyn thrust and fold belt. Many of the methodologies used in this project have not been implemented in past studies of the Keno Hill district or in studies of adjacent regions. As such, this project will contribute information that is vital in enhancing our understanding of the kinematic history of the area. For example, *in situ* geochronology may help elucidate:

1. Timing of movement across the RST and/or TT.
2. Thermal perturbations potentially caused by intrusion of the Mayo or Tombstone suites, the vein mineralization event, or possibly later alteration.

Furthermore, peak temperatures obtained through Raman spectroscopy on carbonaceous materials will provide insight into the thermal history of the area, with the possibility of identifying a spatial correlation between temperature and regional structures. Finally, the detailed strain and kinematic analyses will also provide insight on deformation prior to the main mineralization event.

2 GEOLOGIC BACKGROUND

2.1 EVOLUTION OF THE CANADIAN CORDILLERA

The Cordilleran orogen contains a record of geodynamic processes that have shaped the western margin of the North American continent over the past 1.5 Ga (Monger & Price, 1979). The dominant underlying framework of the Canadian Cordillera began to form when the supercontinent Rodinia amalgamated ca. 1000 Myr ago (Monger & Price, 2002) and subsequently broke apart (ca. 750 Ma) leaving a rifted margin along the western edge of Laurentia, ancestral North America (Monger & Price, 2002). The rifted margin developed as a passive margin until at least the Devonian period when portions transitioned into a predominantly convergent, inter-plate margin that has broadly persisted to the modern day (Monger & Price, 2002; Nelson et al., 2013).

The pre-Cordilleran (i.e., largely pre-convergent) western Laurentian margin saw the deposition of Neoproterozoic to early Mesozoic sedimentary rocks that currently make up most of the Foreland belt and part of the Omineca belt of the present-day Canadian Cordillera (Fig. 2.1 inset; Monger & Price, 2002; Monger, 2008). The Selwyn Basin, which dominantly consists of Precambrian to Devonian deep water, off-shelf, primarily clastic sedimentary strata (Gordey & Anderson, 1993) comprises a portion of those rocks. Subduction initiated along the western margin of Laurentia between ca. 390 and 355 Ma, forming arc-related rocks at the edge of the margin (Monger & Price, 2002; Nelson & Colpron, 2007; Nelson et al., 2013). At the beginning of the Carboniferous period the basement of the Stikinia, Yukon-Tanana, and Quesnellia terranes, consisting of Devonian to Permian igneous and sedimentary rocks, was rifted from the western margin of Laurentia through the development of the Slide Mountain back-arc basin (now Slide Mountain terrane; Monger, 2008; Nelson & Colpron, 2007; Nelson et al., 2013). Towards the end of the Permian period, the east-dipping subduction that lined the western margin of the arc-terranes was replaced by west-dipping subduction on their eastern margin (Mair et al., 2006; Nelson et al., 2013) leading to the eventual accretion of the “Intermontane” terranes Stikinia, Yukon-Tanana, Quesnellia, and Slide Mountain to the western margin of Laurentia in the early Mesozoic, along with the Cache Creek accretionary complex (limestone atolls and oceanic plateaus) (Monger, 2008; Nelson & Colpron, 2007; Nelson et al., 2013). This accretion was complicated by oroclinal rotational and/or strike-slip faulting that reoriented the Stikinia terrane and captured the Cache

Creek terrane between Stikinia and Quesnellia (Fig. 2.2a; Monger & Price, 2002; Monger, 2008; Nelson & Colpron, 2007; Nelson et al., 2013).

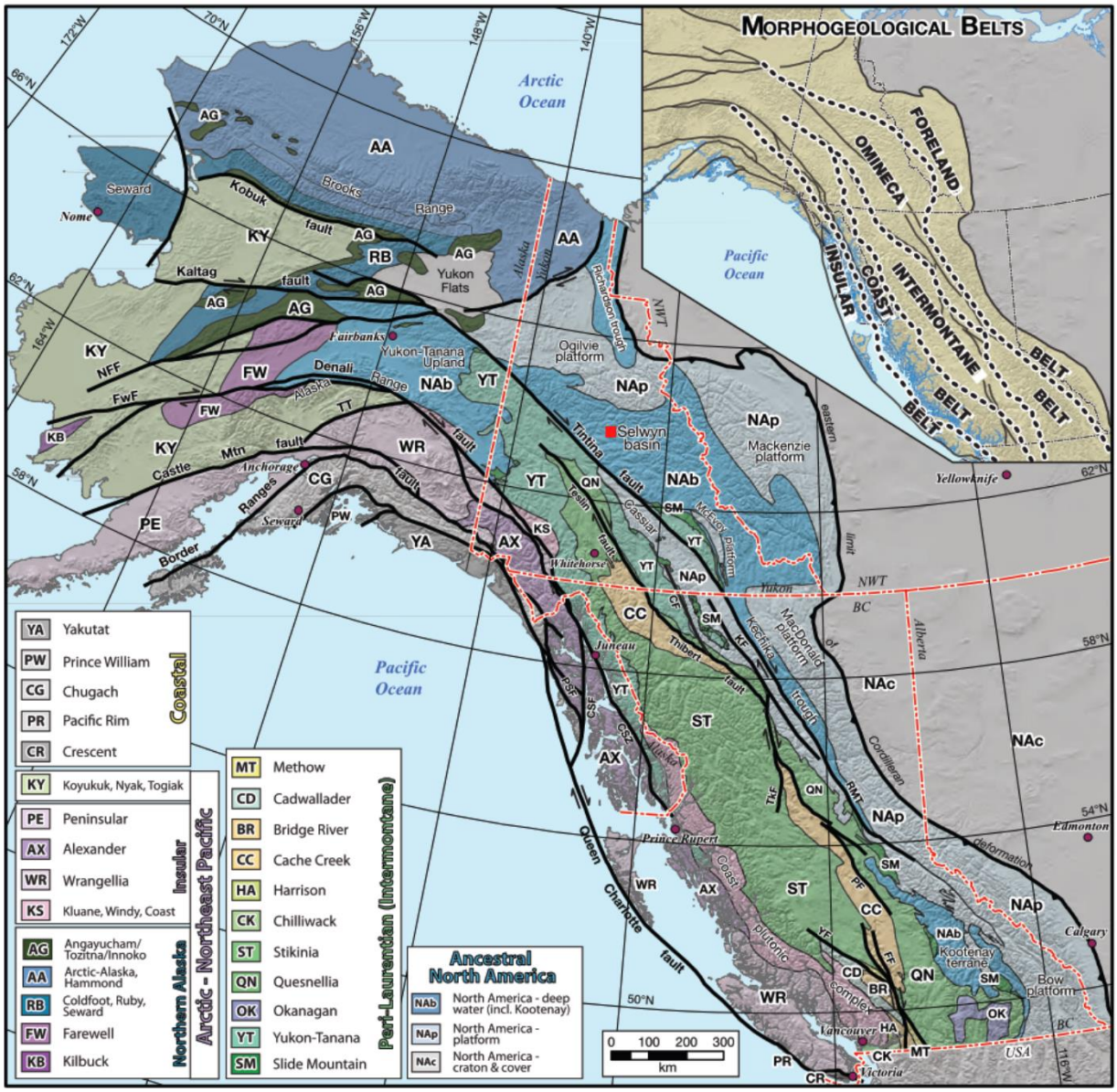


Figure 2.1: Map of the terranes and major faults that make up the Canadian Cordillera with an inset in the top right corner illustrating the approximate boundaries of the five morphogeological belts (modified from Nelson et al., 2013). Approximate study area shown by the red square.

In the Middle Jurassic, renewed east-dipping subduction along the western margin of North America outboard of the Intermontane terranes resulted in the generation of the Coast Plutonic complex (inset Fig. 2.1; Monger, 2008; Nelson & Colpron, 2007; Nelson et al., 2013). Oblique convergence between Laurentia and the subducting plate drove sinistral transpression within the Cordillera, resulting in strike-slip faulting within the continental margin (Fig. 2.2b; Monger, 2008; Nelson & Colpron, 2007; Nelson et al., 2013). By the end of the Middle Jurassic, the Wrangellia and Alexander terranes had accreted along the western margin forming the Insular belt (Fig. 2.1; Monger, 2008; Nelson & Colpron, 2007; Nelson et al., 2013). The Alexander and Wrangellia terranes are composed of pericratonic and arc-rocks, respectively (Nelson et al., 2013). Later in the Middle Jurassic, accretionary complexes including the Pacific Rim, Chugach, and Yakutat terranes (from south to north, respectively) that comprise seamounts and sediments eroded from the evolving Cordillera, began accreting as part of the northern Insular belt (Fig. 2.1; Monger, 2008; Nelson et al., 2013). The final accretion of the Insular and Intermontane terranes is marked by asymmetrical collapse of the Jurassic-Cretaceous basins and the onset of dextral transpression starting in the south and propagating northward (Vice et al., 2020) ca. 70-55 Ma (McKenzie et al., 2024).

At ca. 55 Ma the Cordillera transitioned into a largely transtensional regime marked by extension in the southern Canadian Cordillera and the continuation of dextral displacement across faults and shear zones within the interior of the continent (Fig. 2.2c, i; Monger, 2008; Nelson & Colpron, 2007; Nelson et al., 2013). These structures, which include the Tintina and Denali faults, accommodated hundreds of kilometers of displacement (Fig. 2.2c; Nelson et al., 2013). By ca. 45 Ma, subduction along much of the western margin of North America was replaced by the dextral strike-slip Queen Charlotte fault (Fig. 2.2c, ii; Nelson et al., 2013) essentially ending magmatism along much of the margin by ca. 40 Ma (Nelson et al., 2013).

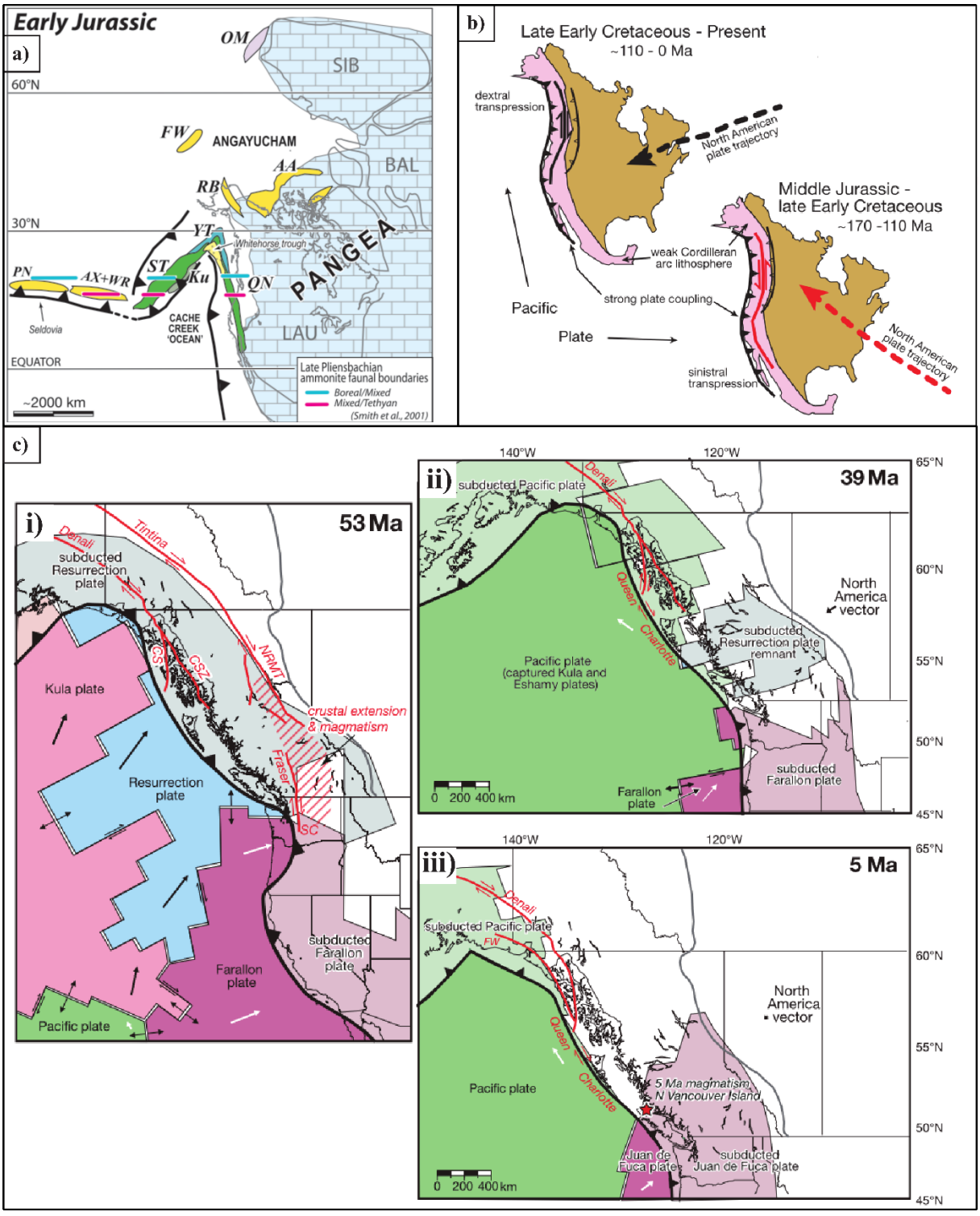


Figure 2.2: a) illustrates the counterclockwise rotation of Stikinia (ST) terrane in the Early Jurassic. The relative positions of the Alexander (AX), Wrangellia (WR), Yukon-Tanana (YT), and Quesnellia (QN) terranes are marked; b) illustrates the movement of the North American continent and its effect on the strike-slip faults within the continent; c) illustrates the configurations of the oceanic plates along the western margin of the North American continent around i) 53 Ma, ii) 39 Ma, iii) 5 Ma. All figures are modified from Nelson et al. (2013).

2.1.1 Selwyn Basin

Within the Jurassic-Cretaceous timeframe, northeast-directed convergence led to the development of compression-related, northeast-vergent thrusting and folding across central Yukon, including the Selwyn Basin (Gordey & Anderson, 1993; Mair et al., 2006). Within the basin, the Robert Service Thrust (RST), Tombstone Thrust (TT), and Dawson Thrust (from the highest structural position in the south to the lowest, respectively) comprise a thrust and fold belt (Mair et al., 2006). The fold axes within the belt trend roughly northwest, with varying styles and scales (Gordey & Anderson, 1993).

2.2 GEOLOGY OF THE KENO HILL DISTRICT

2.2.1 Stratigraphy

The Keno Hill area is underlain by greenschist-facies metasedimentary rocks of the Hyland Group, Earn Group, and Tsichu Group, as well as mafic meta-igneous rocks of the Triassic Galena Suite (Fig. 2.3). These are cross-cut by local intrusions of the Tombstone Suite, consisting of lamprophyre sills, and aplite and quartz porphyry sills/dikes (Fig. 2.3).

The Hyland Group rocks in the area comprise Precambrian quartz grit schists of the Yusezyu Formation, which contain abundant white mica and chlorite. The rocks appear shiny, creamy-white on fresh surfaces to a dull grey with rusty white layers on weathered surfaces. The unit is structurally > 500 m thick in the field area (McOnie, 2016).

Exposures of the Mississippian to Permian age Tsichu Group in the Keno Hill area are dominated by the Keno Hill Quartzite Formation (Read et al., 2020), which can exceed 2 km in structural thickness (McOnie, 2016). The Keno Hill Quartzite includes the Basal Quartzite Member (blocky quartzite, graphitic schist, and sericite chlorite schist) and the overlying Sourdough Hill Member (graphitic schist, limestone, chlorite-sericite schist, quartz grit schist, sericite schist, and platy quartzite) (Read et al., 2020; McOnie, 2016). The Basal Quartzite Member is locally intruded by Galena Suite greenstone sills (Read et al., 2020).

The Middle Devonian to Early Mississippian Earn Group consists of a lower graphitic schist (phyllite) unit and an upper chlorite-sericite schist (phyllite) unit (Read et al., 2020). In keeping with the terminology previously used for this field area (Read et al., 2020; Craggs, 2022), both of these units within the Earn Group will be referred to as schist but are actually phyllite. The

graphitic schist appears dark grey in outcrop, while the chlorite-sericite schist appears pale green to white.

In the Keno Hill area, the Basal Quartzite Member is intruded by the Galena Suite greenstone sills (Read et al., 2020). The sills are very fine-grained, Late Triassic in age, and range up to 100 m thick (Read et al., 2021). The weathered surfaces of these greenstone sills are similar to those of the Keno Hill Quartzite (i.e. dark grey), but on fresh surfaces appear more of a dark greenish grey. U-Pb geochronology on zircon and baddeleyite from these sills yielded a date of 232.2 +1.5/-1.2 Ma (McOnie, 2016).

2.2.2 Structural History

East and west of the Keno Hill district, foliation in the Hyland Group is shallowly to steeply north-northeast dipping and folded into south-southwest-vergent isoclinal folds (Gordey, 1990; Murphy, 1997; Murphy et al., 1996; Murphy & Heon, 1996; Roots, 1997). The strata at Keno Hill, however, have been isoclinally folded and overturned to the north/northeast, with fold hinges plunging to the southeast, and the foliation is parallel to the orientation of the axial planes dipping to the south/southwest (Green, 1971; McOnie, 2016; McTaggart, 1960; Murphy, 1997; Murphy & Roots, 1996; Roots, 1997). The difference in vergence in the Keno Hill area relative to the broader region has been suggested to be partially attributable to either different structural levels, the craton-ward vergence during orogenesis shifting between northeast and northwest, and/or a lateral ramp within the TSZ (Murphy, 1997).

The Robert Service Thrust (RST) extends eastward from the southern Ogilvie Mountains to east of the Keno Hill area and north of the Mayo map area, and places the Hyland Group in its hanging wall over Paleozoic to Mesozoic strata (Fig. 2.4; Murphy, 1997; and references therein). While the majority of this regional-scale thrust fault has been mapped with a near-planar surface, the RST within the greater Keno Hill area is mapped as folded, interpreted to reflect deformation resulting from movement on the structurally lower Tombstone Thrust (TT) (Murphy, 1997). Within the Keno Hill area, some exposures of quartz grit schist on Sourdough Hill have been interpreted as belonging to the Hyland Group, defining a klippe of the RST as depicted by Fig. 1.2; Read et al., 2020; Murphy & Roots, 1996).

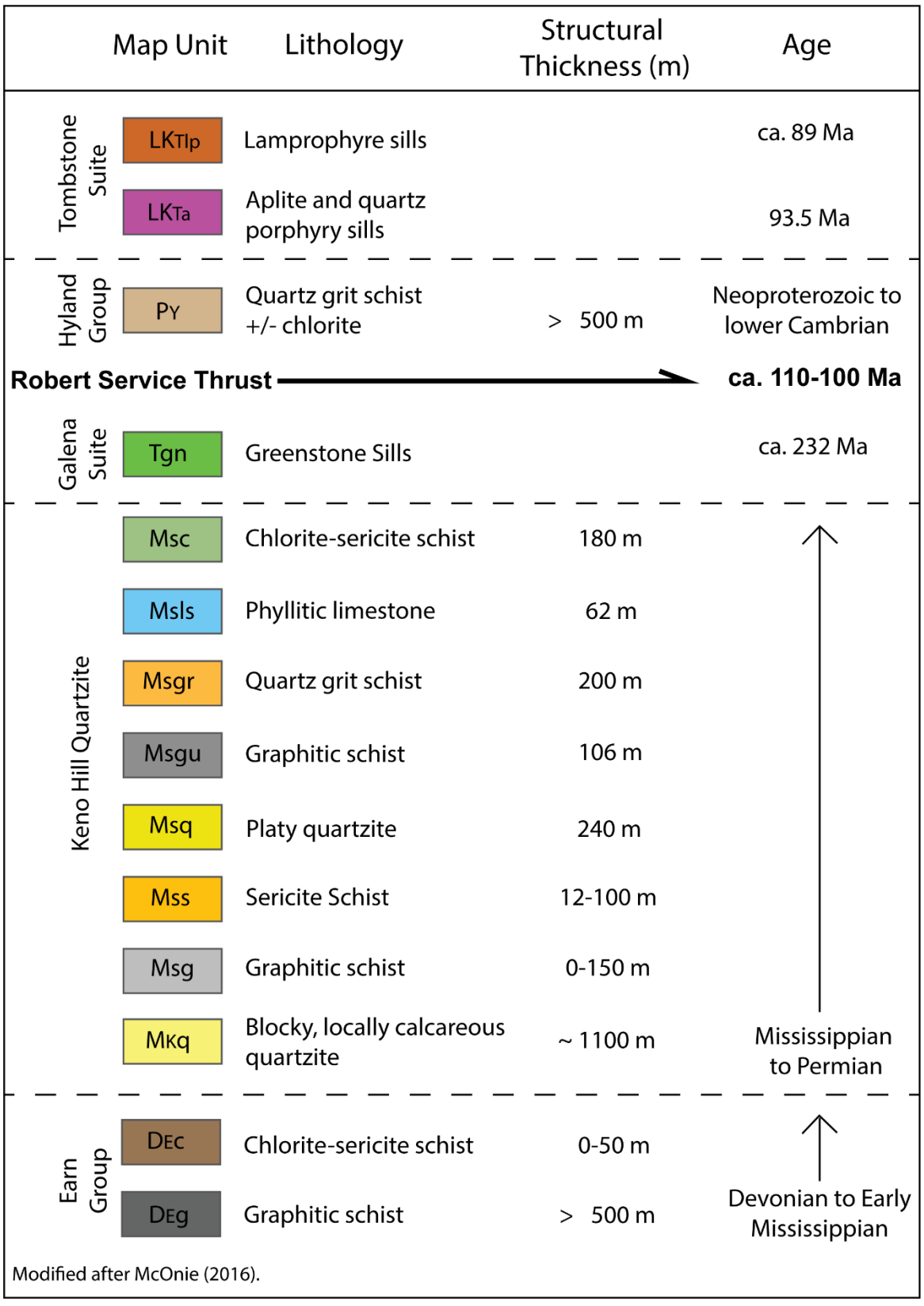


Figure 2.3: Stratigraphy and geochronology of the Keno Hill area (adapted from McOnie, 2016).

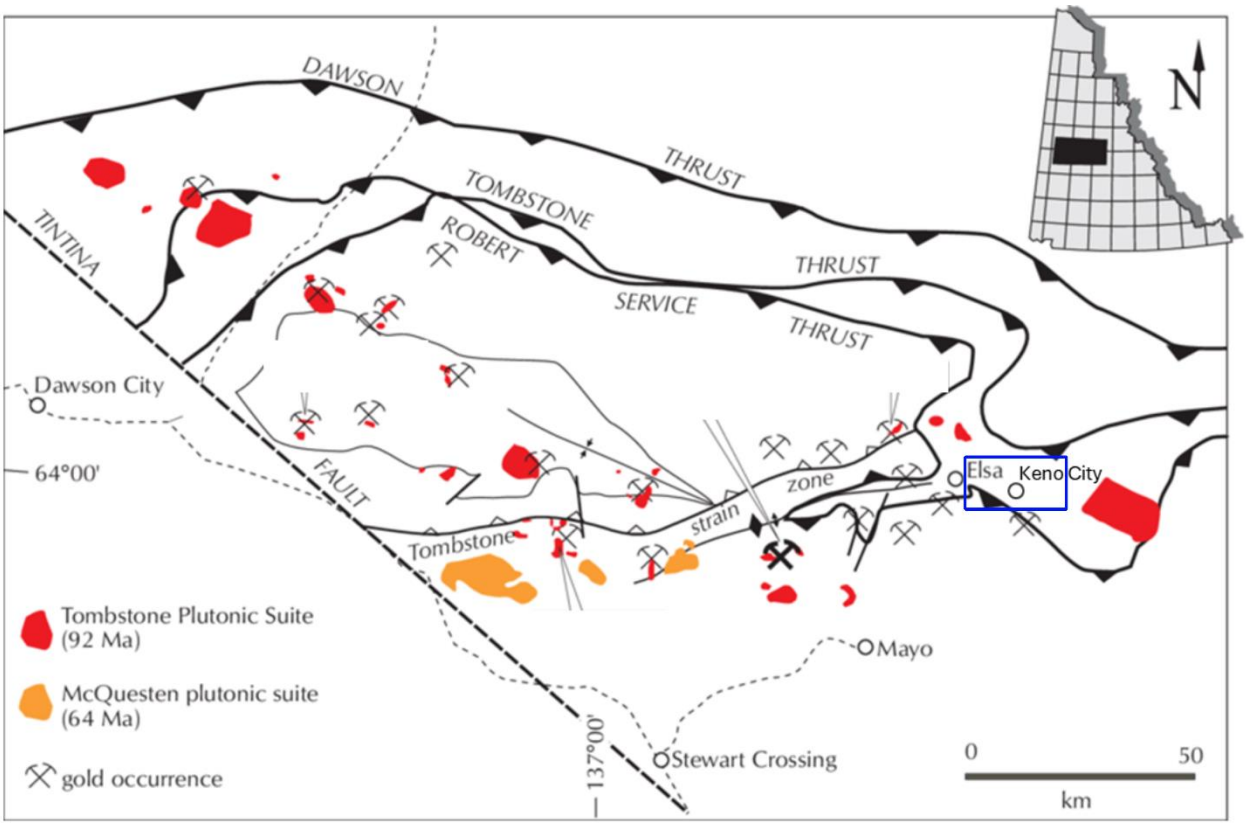


Figure 2.4: Regional map illustrating the location of the thrust faults. Modified from Mair et al. (2000) which is modified after Murphy (1997).

The TT extends generally east (varies in strike) for about 200 km across central Yukon, from the Ogilvie Mountains to northeast of the Keno Hill area (Fig. 2.4; Murphy, 1997; and references therein). The thrust places Devonian to Jurassic strata atop pre-Triassic to Late Jurassic strata (locally variable). Murphy (1997) suggested that there is an imposed high strain zone (referred to as the Tombstone Strain Zone; TSZ), related to TT movement extending from the discrete fault plane of the TT into the lower part of the RST hanging wall (Fig. 2.5). Timing of movement along both the RST and TT has been bracketed by Late Jurassic (Oxfordian) rocks in the immediate footwall of the RST (Murphy, 1997) collected east of Dawson City (Poulton & Templeman-Kluit, 1982) and the stitching/undeformed (Roots, 1997) Roop Lakes Pluton of the Mayo suite (Fig. 2.5; dated at 94.20 +/- 0.02 Ma (Geochronology: 18MC044 in Yukon Geological Survey, 2024). Recent studies (e.g. Read et al., 2021), however, have questioned if the Roop Lakes pluton actually stitches the RST.

Within the Keno Hill area, both isoclinal and open folds have been documented through previous geologic mapping (e.g., Murphy, 1997; Read et al., 2021). Although the timing of the

isoclinal folding event (Fig. 1.2) relative to thrusting remains debated, its formation predates the deformation discussed below.

A widespread open folding event affects rocks from the hanging wall of the RST into the footwall of the TT in the region (Green, 1971; McOnie, 2016; Murphy, 1997; Roots, 1997). This event appears related to a pervasive southeast-trending crenulation lineation that runs parallel to the orientation of the fold axes of the open folds within the Keno Hill area (Green, 1971; McOnie, 2016; Roots, 1997). The timing of the open fold development is contentious (e.g. Green, 1971; Craggs, 2022), with reports of multiple phases and/or scales (e.g. Read et al., 2021). Regardless of when this folding event occurred in relation to thrusting or intrusions of the Tombstone and Mayo Suites, later, brittle faults postdate the granitic intrusions (Craggs, 2022; Green, 1971; McOnie, 2016). The late, brittle faults include syn-mineralization northeast-trending sinistral oblique normal faults, and post-mineralization northwest-trending dextral oblique normal faults (Craggs, 2022; Green, 1971; McOnie, 2016).

2.2.3 Previous Geochronology

A combination of *in situ* and *step-heating* $^{40}Ar/^{39}Ar$ geochronology on muscovite from two samples in the hanging wall of the RST, south-southwest of the Keno Hill area, yielded dates between 104 and 100 Ma (Fig. 2.5; Mair et al., 2006). As the samples were taken from rocks that were interpreted as being overprinted by the TSZ, the dates were thought to record the last stage of ductile deformation related to the movement of the TT (Mair et al., 2006). The Roop Lakes pluton has been interpreted to plug the RST (Fig. 2.5; Roots, 1997) at ca. 94 Ma (U-Pb chemical abrasion – thermal ionization mass spectrometry on zircon; Yukon Geological Survey, 2024). U-Pb dating of zircon grains from a rhyolite sill (ca. 93 Ma), and $^{40}Ar/^{39}Ar$ on biotite from an unaltered lamprophyre sill (ca. 89 Ma), show temporal correlation with Tombstone Suite plutonic rocks (Tupper & Bennett, 2010; McOnie, 2016).

Craggs (2022) carried out U-Pb (zircon) and $^{40}Ar/^{39}Ar$ (mica from mineralized veins and sericite-altered rocks from host rock of the Onek property vein fault) geochronology on a suite of samples collected in the Keno Hill area and suggested three main events: 1) intrusion of Tombstone Suite rocks (~95-90 Ma), 2) mineralization (~82-77 Ma), and 3) hydrothermal alteration (~71-68 Ma). Read et al. (2020) also presented $^{40}Ar/^{39}Ar$ dates of ca. 89-61 Ma from muscovite sampled in mineralized veins, and sericite associated with Ag-Pb-Zn veins has been dated via K-Ar at 87 +/-

3 Ma (Sinclair et al., 1980). Despite the fairly comprehensive application of geochronology to the igneous intrusions and mineralized vein faults, the timing of the early, ductile structures remains unconstrained.

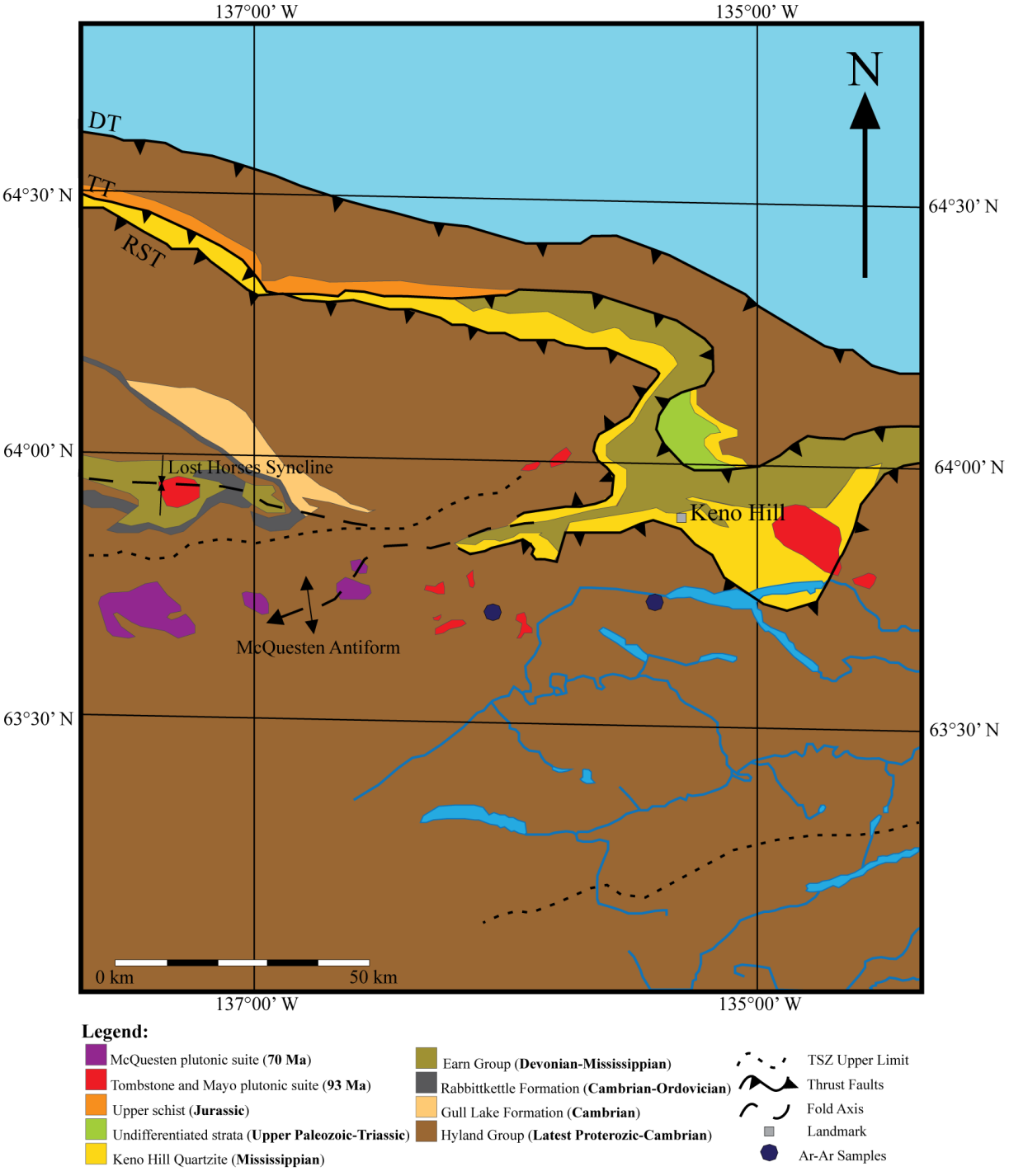


Figure 2.5: Map illustrating the approximate location of the upper limit of the TSZ and the locations of Ar-Ar samples of Mair et al. (2006). Figure was created by combining information from figures from Mair et al. (2006) and Roots (1997).

3 METHODS

3.1 FIELDWORK

Fieldwork was conducted between July 14th and August 9th, 2022, in the ~ 20 x 30 km Keno Hill district. Located ~350 km north of Whitehorse and ~45 km northeast of Mayo, the field camp was situated in the Keno City campground from which daily traverses were conducted. Although most traverses were accessible by truck, there were two helicopter-access sites. Mapping of lithologies, structures, and their relationships was conducted at the 1:25 000 scale independently with a field assistant, and all observations were recorded. A station map is shown in Figure 3.1. Additionally, ~400 photos, ~380 structural measurements, and 107 samples (98 oriented, 9 unoriented) were taken. Samples from drill core were provided by Alexco Resource Corp (i.e., 18-709, from the southwest end of Keno Hill). Of the collected samples, 30 were prepared as polished thin sections, ensuring representation across a southwest northeast transect. Station descriptions can be found in Appendix A.

3.2 MICROTECTONICS

3.2.1 Petrography and Microstructures

The 30 selected samples (27 oriented, 3 unoriented) were cut perpendicular to foliation and parallel to the stretching lineation and made into polished thin sections by Vancouver Petrographics Ltd. in Langley, BC. Detailed examinations of the thin sections to identify mineral phases, microstructures and textures were obtained using a polarizing microscope. A list of the thin sections, and the investigations performed on each, is shown in Table 3.1. Thin section descriptions can be found in Appendix B.

3.2.2 Quartz CPO

Each of the 30 thin sections were scanned at a 5.08 μm resolution using the G60+ Automated Crystal Fabric Analyzer (Russell-Head Instruments) located at University of British Columbia Okanagan to collect quartz crystallographic preferred orientation (CPO) data. Quartz *c*-axis CPO distributions in 25 of the thin sections (Table 1) were built by manually selecting 1000 grains per specimen in the Investigator (v.5.12) software package. Lower hemisphere, equal area projections plotting the pole of the *c*-axis were made using the FabricPlotR script (v.13) (Larson, 2022). Quartz *c*-axis CPO descriptions can be found in Appendix C.

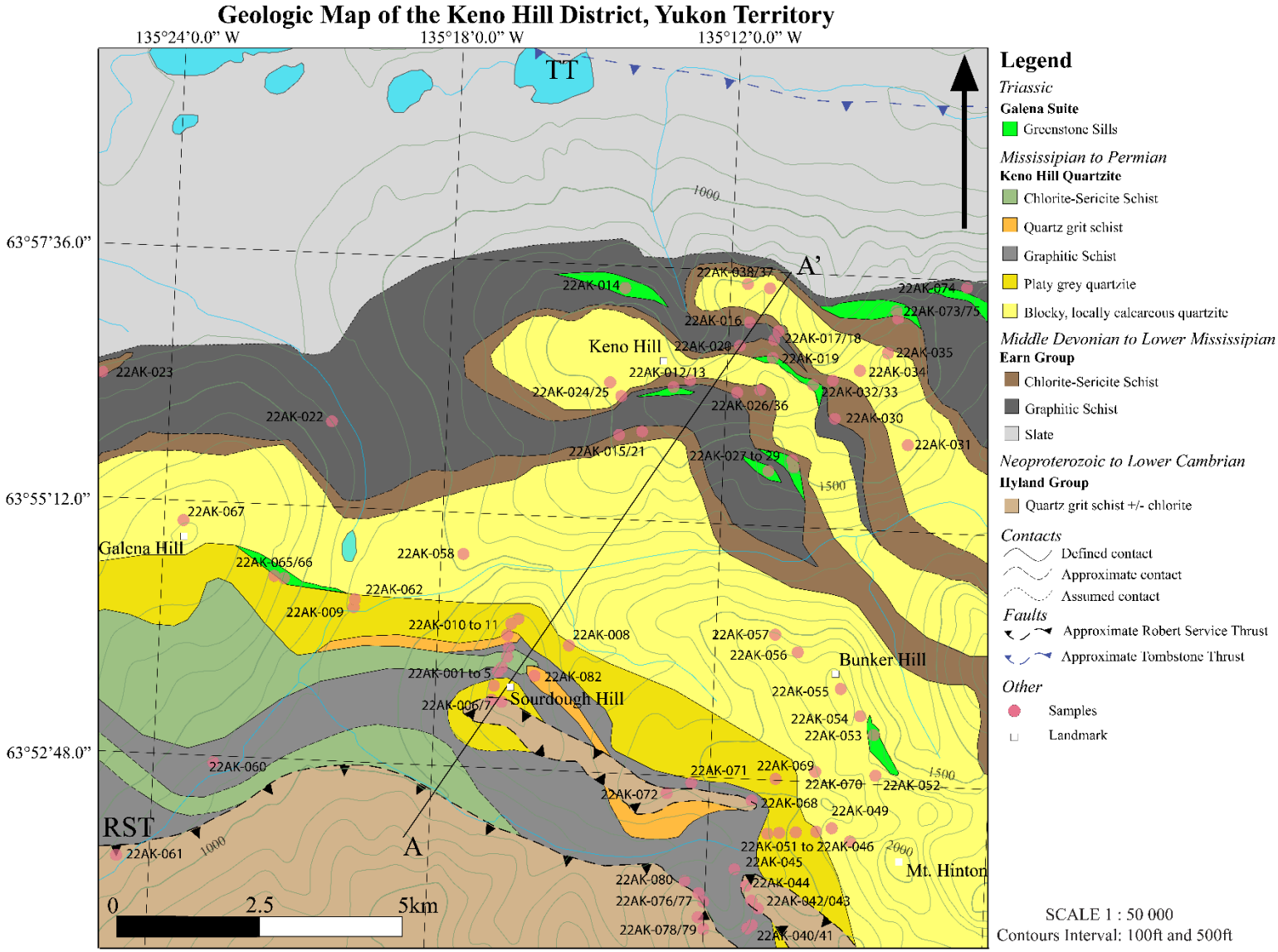


Figure 3.1: Station map of the Keno Hill area based off field work conducted in 2022. Station 22AK-081 is located on Cobalt Hill, east of the map area. Simplified from Read et al. (2020). Robert Service Thrust (RST); Tombstone Thrust (TT).

Table 3.1: List of thin-section samples and the analyses conducted.

Sample	*CPO*	*$^{87}Rb/^{87}Sr$*	*$^{40}Ar/^{39}Ar$*	*EBSD*	*Raman*
22AK-001-1-1	*Y*			*Y*	*Y*
22AK-006-1-1					
22AK-006-1-2	*Y*	*Y*	*Y*	*Y*	*Y*
22AK-011-1-1	*Y*	*Y*			
22AK-023-1-1	*Y*	*Y*	*Y*	*Y*	
22AK-029-1-1	*Y*			*Y*	*Y*
22AK-032-2-1	*Y*			*Y*	
22AK-037-1-1	*Y*	*Y*	*Y*		*Y*
22AK-041-1-1	*Y*				
22AK-043-1-1	*Y*				
22AK-045-2-1	*Y*				*Y*
22AK-045-3-1					
22AK-049-1-1	*Y*				*Y*
22AK-052-1-1	*Y*				*Y*
22AK-053-1-1					
22AK-054-1-1	*Y*				
22AK-055-2-1	*Y*				*Y*
22AK-060-1-1	*Y*		*Y*	*Y*	*Y*
22AK-061-1-1	*Y*	*Y*	*Y*	*Y*	*Y*
22AK-067-1-1	*Y*				
22AK-069-2-1	*Y*				
22AK-072-1-1	*Y*				
22AK-072-1-2	*Y*				*Y*
22AK-073-1-1					*Y*
22AK-078-1-1	*Y*				
22AK-079-1-1	*Y*				*Y*
22AK-080-1-1	*Y*				*Y*
22AK-081-1-2	*Y*				*Y*
22AK-082-1-1	*Y*	*Y*	*Y*	*Y*	*Y*
18-709					

Distribution strength was calculated using the FabricPlotR script (v.13) (Larson, 2022) in the form of the J_{PF}-index. The J_{PF}-index uses the calculated Euclidean norm of the density of pole orientations within a spherical distribution (Larson et al., 2023a; Mainprice et al., 2015). It is a function of Euclidean distance in that the closer the poles cluster together, the higher the J_{PF}-index, and in contrast, if there is an even distribution of the pole orientations then the J_{PF}-index will approach one (Larson et al., 2023a). A larger $J_{(PF)}$-index corresponds to increased organization of the CPO distribution.

3.2.3 Quartz CVA and Grain Size Piezometry

Electron back scattered diffraction (EBSD) analyses were conducted on seven samples at the Fipke Laboratory of Trace Element Research (FiLTER) of University British Columbia Okanagan with a Tescan Mira 3 XMU SEM, and the Oxford Instruments Nordlys EBSD detector (for most samples) and the Oxford Instruments Symmetry S3 EBSD camera (for samples 22AK-023-1-1 and 22AK-029-1-1). When the electron beam hits the sample, diffracted electrons hit the EBSD detector and form a pattern known as Kikuchi bands. These Kikuchi bands are directly related to the mineral lattice and can be used to uniquely determine the mineral phase, the orientation of the crystal, and intragranular distortion. The thin sections selected for the analyses were polished using a 0.06 micron colloidal silica solution with a Saphir Vibro polisher for 60 minutes at 81.7 Hz and then coated with ~10 nm of carbon. Quartz was the only phase selected to be indexed using Oxford Instruments' Aztec software. The list of parameters used for each sample is shown in Table 3.2. The EBSD data were plotted using Aztec Crystal and processed using mtex-5.9.0 through CVA (Graziani, 2022; Michels et al., 2015) and grain size piezometry (Cross et al., 2017) scripts. Using Aztec Crystal, EBSD grain orientation spread (GOS) maps were exported.

Table 3.2: EBSD Parameters.

Sample	Mode	Beam Intensity	Frame Average	Frame Time (s)	Gain	Step Size (µm)
22AK-001-1-1	2x2	20	1	45.7	5	5
22AK-006-1-2	2x2	20.06	1	36.4	5	5
22AK-023-1-1	Speed1	20.6	1	3.41	1	5
22AK-029-1-1	Speed1	20.6	1	3.34	1	5
22AK-032-1-1	2x2	20.6	1	18.7	5	5
22AK-060-1-1	2x2	20.6	1	22.8	5	5
22AK-061-1-1	2x2	20.6	1	37.7	5	5
22AK-082-1-1 (1)	2x2	20.6	1	20.9	5	5
22AK-082-1-1 (2)	2x2	20.6	1	22.8	5	5

When importing EBSD data using MTEX software, samples 22AK-023-1-1 and 22AK-029-1-1 were imported with z into plane, as the EBSD data were acquired on the new EBSD detector (Oxford Instruments Symmetry S3), whereas the rest of the samples were imported with z out of plane as they were acquired on the old EBSD detector (Oxford Instruments Nordlys). The orientation of x-y axes for the samples differs solely if the EBSD data were acquired on the upper or lower half of the thin section. All data were imported with

convertEuler2SpatialReferenceFrame. The rotations applied to the CPO EBSD data when using the CVA script are reported in Table 3.3.

Therefore, relict and recrystallized grains were separated based on their grain orientation spread (GOS) using the trade-off function and the RexRelict.m Matlab script (Cross et al., 2017). Grains with more GOS will have higher dislocation densities, corresponding with relict grains, where the inverse is true for recrystallized grains (Cross et al., 2017). The GOS method allows the recrystallized and relict grains to have overlapping grain size as long as the dislocation densities for the two groups are of different magnitudes (Cross et al., 2017). Differential stress (σ_d) was calculated for each sample based on their root mean square (RMS) grain size (D), using the equation:

$$\sigma_d = \left(\frac{D}{10^{3.91}}\right)^{\frac{1}{-1.41}} \quad (1)$$

from the Cross et al. (2017) RexRelict.m script. The uncertainty of the differential stress (σ_{σ_d}) was calculated by the equation:

$$\sigma_{\sigma_d} = \sigma_d \times \sqrt{\left(\left(\frac{0.41}{3.91}\right)^2\right) + \left(\left(\frac{\sigma_D}{D}\right)^2\right)} \quad (2)$$

where σ_D represents the error (1 standard deviation) of the RMS grain size.

Using the scripts mentioned above, relict and recrystallized maps, grain size histograms, GOS threshold plots, and lower hemisphere equal area plots for relict and recrystallized CVA and CPOs (*a*- and *c*- axes) were made. Previous studies have noted that different flow environments (e.g. monoclinic transpression, transtension) have geometric relationships between the vorticity axis and the stretching lineation (e.g. Jiang & Williams, 1998; Xypolias, 2010). However, in a triclinic flow environment, this relationship is not consistent (Jiang & Williams, 1998; Piette-Lauzière et al., 2020).

Table 3.3: List of rotations used in the CVA script.

Sample	σ1	σ2	σ3
22AK-001-1-1	0	0	0
22AK-006-1-2	0	0	0
22AK-023-1-1	0	0	0
22AK-032-1-1	0	0	0
22AK-060-1-1	-35	-65	35
22AK-061-1-1	45	60	-45
22AK-082-1-1	0	0	0

3.3 GEOCHRONOLOGY

Samples were selected for *in situ* $^{87}Rb/^{87}Sr$ and $^{40}Ar/^{39}Ar$ based on the presence of targetable mica in thin section and location along a southwest to northeast transect crossing major structures in the field area. The specimens for *in situ* $^{40}Ar/^{39}Ar$ geochronology were selected after the analyses for $^{87}Rb/^{87}Sr$ had been conducted and as such some samples were reconsidered based on the $^{87}Rb/^{87}Sr$ results and the requirements of the *in situ* $^{40}Ar/^{39}Ar$ method (Table 3.1).

3.3.1 $^{87}Rb/^{87}Sr$ Dating

In situ $^{87}Rb/^{87}Sr$ geochronology utilizes the decay of parent ^{87}Rb into daughter ^{87}Sr (Zack & Hogmalm, 2016). The modern *in situ* approach followed herein utilizes tandem mass spectrometry (MS) to overcome the mass/charge interference associated with measuring ^{87}Rb and ^{87}Sr. Essentially, the first MS allows for filtering of only the mass of interest (i.e. 87) after which the ^{87}Sr and ^{87}Rb pass into a collision cell charged with a reactive gas that only ^{87}Sr reacts with, changing its mass and allowing it to be measured distinctly from ^{87}Rb via the second MS (Zack & Hogmalm, 2016).

In situ $^{87}Rb/^{87}Sr$ dating was conducted on white mica in six polished thin sections (Table 1) via laser ablation inductively coupled plasma mass spectrometry (LA-ICP-MS) at the FiLTER facility of University British Columbia, Okanagan. The laser ablation system comprises an ESL193 Excimer with a TwoVOL 3 sample chamber paired with an Agilent 8900 triple quadrupole ICP-MS. Mica grains were targeted over three sessions using a circular 50 μm laser spot. Each session used a bracketing approach in which ~10 spot analyses from the unknown samples were bracketed by analyses of reference materials to facilitate isotope ratio normalization, instrument drift corrections, and to verify the analytic setup. The laser parameters used for the analyses are shown in Table 3.1. The targeted mineral phases for each sample included white mica, +/- plagioclase and/or calcite. Spot locations were selected to encompass the largest possible area of dateable material and in sample 22AK-037-1-1, an attempt was made to date two potentially different generations of white mica. Spot locations for each run can be found in Appendix D.1.

The raw signal from the LA-ICP-MS data generated was processed using Iolite 4 (Paton et al., 2011) and isotopic ratios were calculated using the FiLTER Rb-Sr data reduction scheme (DRS). Although a variety of reference materials were included in each session, the same primary and secondary materials were used to maintain consistency. The reference glass NIST 610

(Woodhead & Hergt, 2001) was used as the primary reference material to correct for instrument drift and primary ratio calibration. The natural mica Mica-1O (Camacho et al., 2020; Larson et al., 2023b) was used for matrix correction for natural mica grains. Both the standards and the unknowns were detector corrected. The data were processed using the Larson (2024) *Process Iolite Rb Sr Data v4* script.

Table 3.4: ESL 193 nm laser ablation parameters including TwoVOL3 sample chamber for all 3 sessions. Session 1 had a fluence of 3.6, Session 2 and 3 had a fluence of 3.5.

Parameter	Value	Unit
Rep Rate	8	Hz
Fluence	3.5/3.6	J/cm2
Ablation Time	25	s
Washout Time	15	s
Pre-ablation Shots	2	
Laser Gas	ArF	
Carrier Gas	UHP He	
Beam Train Purge Gas	UHP N2	

The reproduced ages of the secondary reference materials are reported in Table 3.5. It is worth noting that the standards that are nano-powders (Mica Mg and Mica-Fe) have runs with ages outside the 3% accepted accuracy window (Redaa et al., 2021). However, a downhole fractionation correction was not applied. As nano-powders have different ablation rates, downhole fractionation, and crater shapes than those of the natural micas targeted in the unknowns, these standards should be recognized with lesser weight than those that exhibit similar ablation behaviours to those of the unknowns (such as Mica-1O, Mica-1B, and MA2). In particular, MA2 is a natural white mica, which should exhibit the same ablation patterns to those of the unknowns and as such a higher weight should be applied to the accuracy and reproducibility of that reference material.

Table 3.5: Reproduced ages of references materials through in situ *$^{87}Rb/^{87}Sr$ geochronology, using an inverse isochron from IsoplotR (Vermeesch, 2018) after correction with Mica-1O. Reference materials: Mica Mg (Hogmalm et al., 2017), Mica-Fe (Rösel & Zack, 2022), Mica-1O* (Camacho et al., 2020; Larson et al., 2023b)*, and Mica-1B* (Camacho et al., 2012; Larson et al., 2023b)*. In addition to the analyses, the dates in this table were calculated using the initial $^{87}Sr/^{86}Sr$ ratios shown in the bottom row. Uncertainty is reported as Two Standard Error (2SE) absolute.*

	Mica Mg	**Mica-Fe**	**Mica-1O**	**Mica-1B**	**MA2**
Run 1: 22 November 2022	470.2 +/- 2.0 Ma (MSWD = 11, n = 25/25)	275.88 +/- 0.87 Ma (MSWD = 14, n = 25/25)	980.8 +/- 4.3 Ma (MSWD = 5, n = 25/25)	980.8 +/- 3.9 Ma (MSWD = 6.3, n = 25/25)	N/A
	486.2 +/- 3.4 Ma (MSWD = 3.9, n = 10/25)	283.5 +/- 1.3 Ma (MSWD = 3.1, n = 10/25)	986.1 +/- 4.5 Ma (MSWD = 2.1, n = 24/25)	986.0 +/- 4.0 Ma (MSWD = 2.1, n = 23/25)	
Run 2: 16 January 2023	533 +/- 4 Ma (MSWD = 27, n = 10/10)	320.6 +/- 1.7 Ma (MSWD = 2.2, n = 10/10)	984.5 +/- 7.4 Ma (MSWD = 1.5, n = 10/10)	N/A	N/A
	519.3 +/- 4.5 Ma (MSWD = 15, n = 7/10)				
Run 3: 3 March 2023	500.7 +/- 2.4 Ma (MSWD = 6.2, n = 20/20)	305.8 +/- 1.3 Ma (MSWD = 6.8, 20/20)	985.7 +/- 5.2 Ma (MSWD = 1.1, n = 20/20)	977.2 +/- 5.4 Ma (MSWD = 15, n= 20/20)	364.5 +/- 2.2 Ma (MSWD = 2, n = 20/20)
	502.9 +/- 2.8 Ma (MSWD = 2.4, n= 15/20)	306.3 +/- 1.4 Ma (MSWD = 3.7, n= 17/20)		990.5 +/- 6.1 Ma (MSWD = 3.5, n= 16/20)	364.6 +/- 2.2 Ma (MSWD = 1.2, n = 19/20)
Expected Age	519.4 +/- 6.5 Ma	305.4 +/- 2 Ma	986 +/- 5 Ma	990 +/- 5	350-360 Ma
Initial $^{87}Sr/^{86}Sr$ ratio	0.726	0.71	0.703	0.7035	0.75

3.3.2 $^{40}Ar/^{39}Ar$ Dating

$^{40}Ar/^{39}Ar$ geochronology is derived from the K/Ar decay system but allows a single phase (gas) to be targeted by use of a single instrument (McDougall & Harrison, 1999). The ^{40}Ar is the daughter product of the K/Ar decay system, and the ^{39}Ar is a proxy for ^{40}K but is converted from ^{39}K through nuclear irradiation (McDougall & Harrison, 1999). The *in situ* method uses an ultraviolet laser to ablate the sample, and a multi-collector mass spectrometer to measure the different isotopes of Ar (McDougall & Harrison, 1999; Schaen et al., 2021). Within the spectrometer, a gas is introduced to remove ions that interfere with Ar, and the other isotopes of Ar (e.g. ^{36}Ar) allow for corrections of extraneous Ar (e.g. atmospheric) (McDougall & Harrison, 1999; Schaen et al., 2021).

Five samples along a southwest-northeast transect across the field area were selected for $^{40}Ar/^{39}Ar$ geochronology and prepared as 200 µm thick sections. The sections were mounted with cyanoacrylate glue and polished only on the top surface. The procedures followed are outlined in Barnes et al. (2023). The ~1 cm^2 areas of interest on each thick section were photographed using

a reflected light microscope and then sent to the University of Manitoba to be prepared for irradiation alongside reference materials of known age. The samples were then irradiated for 20 h at Oregon State University using the TRIGA reactor facility. *In situ* analyses of the unknowns alongside standards were conducted at the University of Manitoba using a Thermo Fisher Scientific ARGUS VI mass spectrometer equipped with a 193 nm laser. Spot locations are presented in Appendix D.2. The unknowns were targeted using 50 µm by 150 µm length ablation lines on foliation-defining white mica.

3.4 THERMOMETRY

Raman spectroscopy-based thermometry utilizes the irreversible graphitization of carbonaceous material. As metamorphic temperatures increase, the carbonaceous material becomes progressively more ordered/crystalline recording the peak conditions to which it was exposed (Beyssac et al., 2002). Raman spectroscopy uses an infrared laser to target the sample to determine the difference in the vibrational fingerprint that is backscattered from the targeted material and the laser (Beyssac et al., 2002). This difference is known as the Raman shift (measured in cm^{-1}; Beyssac et al., 2002). The ratio of the peak areas of the unique first-order bands that are associated with carbonaceous material have a negative, linear relationship with temperature (Beyssac et al., 2002).

Raman spectroscopy of carbonaceous material (RSCM) was conducted at University of Alberta in Edmonton using the Horiba LabRam HR Evolution Raman microscope following a similar procedure to Li et al. (2023). Data were collected with a grating of 1800 grooves/mm, a 532 nm laser focussed with 100x objective lens, a laser power of 75 mW, and 3 exposures of 20 s. We targeted 2 spots per grain totalling approximately 10 carbon spectra per thin section. The amount of targetable carbonaceous material grains limited the number of spots targeted. The analyses focussed on the first-order bands (D1, G, and D2; Beyssac et al., 2002) within the range of 1200 cm^{-1} to 1700 cm^{-1}. For each spot analyzed within each sample, the peak position, peak amplitude, and peak area were recorded for each of the first-order bands. The peak intensity ratio (R1) was calculated as follows:

$$R1 = D1/G \quad (3).$$

The peak area ratio (R2) was calculated using the peak areas for the respective bands as:

$$R2 = D1/(D1 + G + D2) \quad (4).$$

4 RESULTS

4.1 FIELDWORK

Structural mapping at the 1:25 000 scale of the Keno Hill area revealed a consistent, shallow-to-moderate southwest dipping foliation, affected by at least two phases of folding and cut by late brittle faults. Discrete fault planes associated with the Robert Service Thrust (RST) or Tombstone Thrust (TT) were not identified. The lithologies observed generally match the 1:20 000 map of Read et al. (2020). A new 1:50 000 scale geologic map based on the observations from this study and the detailed lithological mapping of Read et al. (2020) is presented in Figure 4.2. It is worth noting that the two quartz grit schists (one from the klippe of the RST, and the other from the footwall) identified on Sourdough Hill are nearly indistinguishable, and as such may belong to the same formation, in the absence of geochronological data proving otherwise.

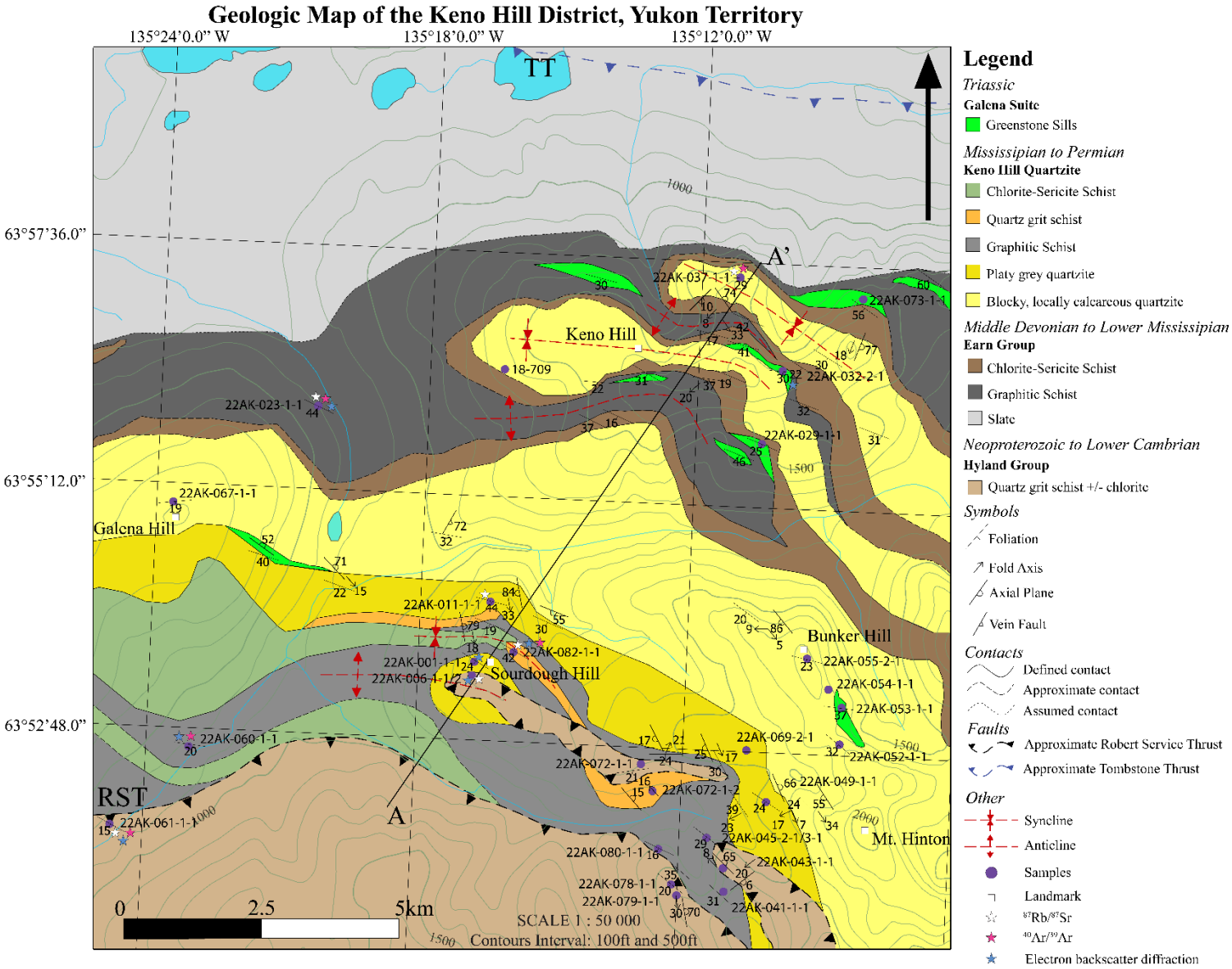


Figure 4.1: Geologic map of the Keno Hill area with samples and structural measurements labelled. Robert Service Thrust = RST; Tombstone Thrust = TT. Simplified from Read et al. (2020).

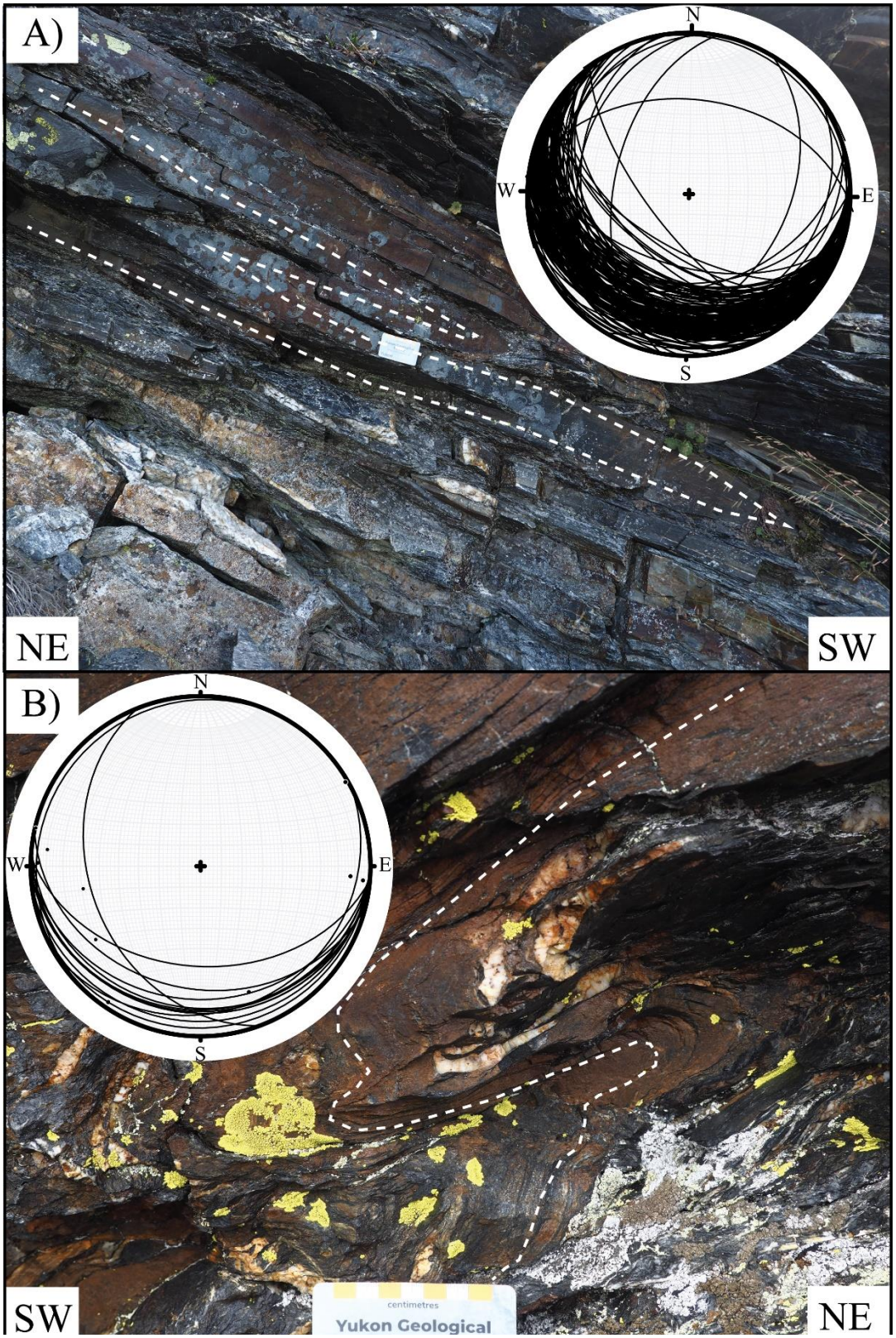


Figure 4.2: A) foliation parallel isoclinal folds with an inset of stereonet of the measurements of the foliations (Station 22AK-050). B) isoclinal folds with quartz veins and an inset of a stereonet of the fold axis and axial plane measurements (Station 22AK-071).

The axial planes of the isoclinal folds (F_1) follow a similar orientation to the southwest-dipping foliation (Fig. 4.2) and indicate that this folding event is north-vergent. These folds occur at the centimeter to meter scale in outcrop, while the mirrored occurrence of the blocky quartzite on Keno Hill (Fig. 4.1) indicates that these folds occur at the map scale as well. Quartz veins that parallel the dominant foliation are also folded into F_1 structures (Fig. 4.2B).

Metre-scale open (F_2) folds with subvertical axial planes that strike southeast-northwest postdate the isoclinal (F_1) folds (Fig. 4.3). A pervasive crenulation lineation, common in schistose layers, parallels the F_2 fold axes (Fig. 4.3B).

Isoclinal (F_1) folds are truncated by locally curviplanar thrust faults at the south end of Keno Hill, within the Onek property (Station 22AK-058; Fig. 4.4A). Late, brittle normal-oblique faults that strike northeast host Ag-Pb-Zn vein mineralization in the field area (as shown in Fig. 4.4B). The vein-filled fault crosscuts F_1, but its relationship with F_2 was not observed. Previous

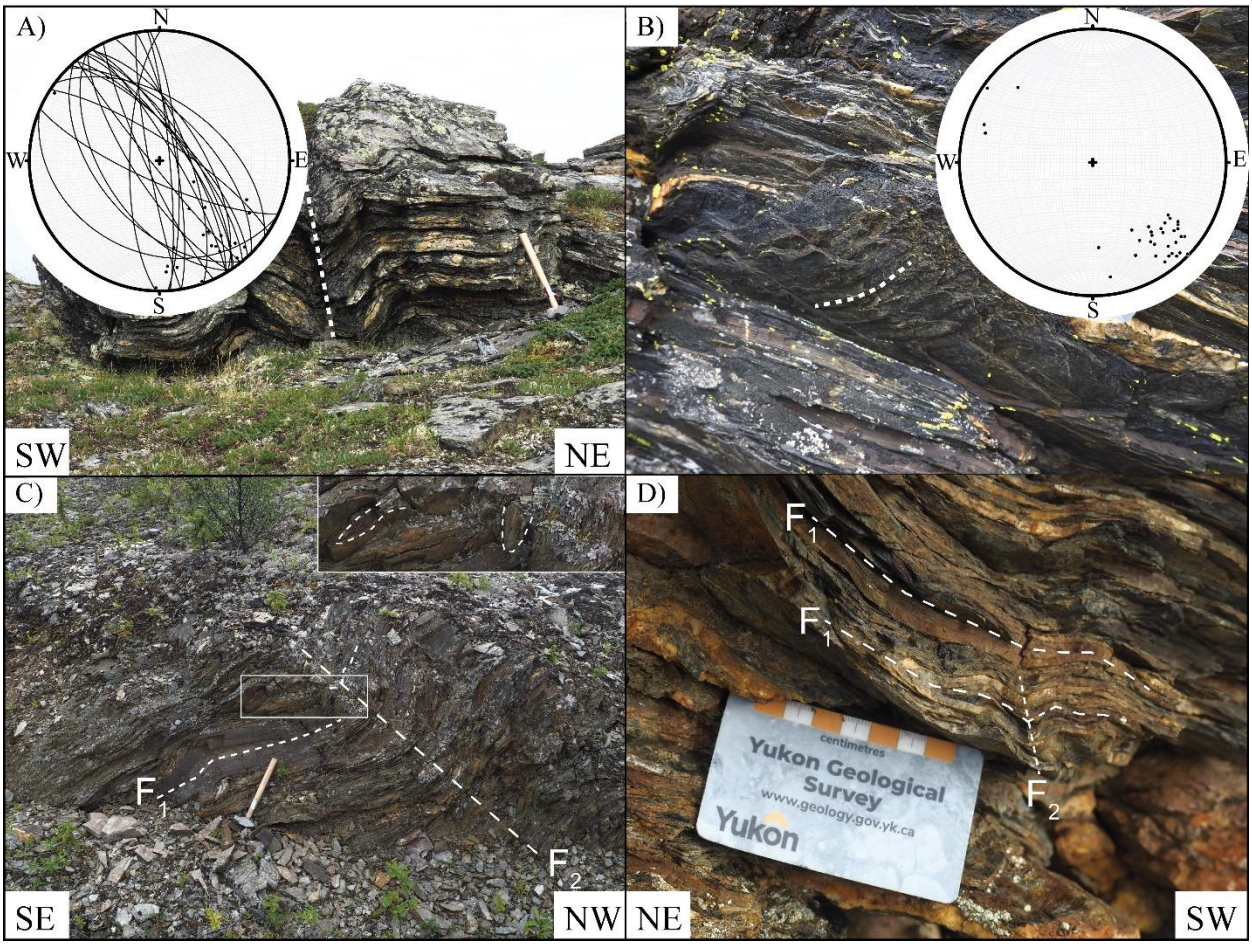


Figure 4.3: A) Open fold and stereonet inset showing axial planes and fold axis measurements (Station 22AK-004); and B) Crenulations and stereonet inset showing crenulation lineation measurements (Station 22AK-004). Relationship of isoclinal folds with open folds from stations: C) 22AK-063 (Bermingham open pit); and D) 22AK-064 (Coral WigWam open pit).

geologic work in the area notes the presence of NW-striking normal-oblique brittle faults that crosscut the NE-striking brittle faults, although these NW-striking faults were not observed in this study.

The sense of shear observed in outcrop across the field area is predominantly top-to-the northwest defined by C-S fabrics and asymmetric boudins (Fig. 4.5A-B). On Keno Hill, however, shear sense is more variable (Fig. 4.5C), with some localities exhibiting top-to-the southeast shear (Fig. 4.5D). Shear strain increases in proximity to the approximate RST. Shearing appears to be coeval- with or postdate F_1 as shear sense indicators are common along fold limbs and shear sense indicators do not reverse around the isoclines.

Previous geologic work noted the occurrence of aplite sills, quartz porphyry sills, and lamprophyre sills/dikes in the region (Murphy & Roots, 1996; Read et al., 2020). An aplite sill was observed at station 22AK-073 (Fig. 3.1) with post-kinematic porphyroblasts (Fig. 4.6) on foliation planes in the country rock. In the field, the porphyroblasts were provisionally mapped as staurolite, perhaps reflecting contact metamorphism related to either the sill or the Roop Lakes Pluton farther east. Limited exposure of the dike in outcrop precluded assessment of its cross-cutting relationship with country rock and deformation events recorded therein.

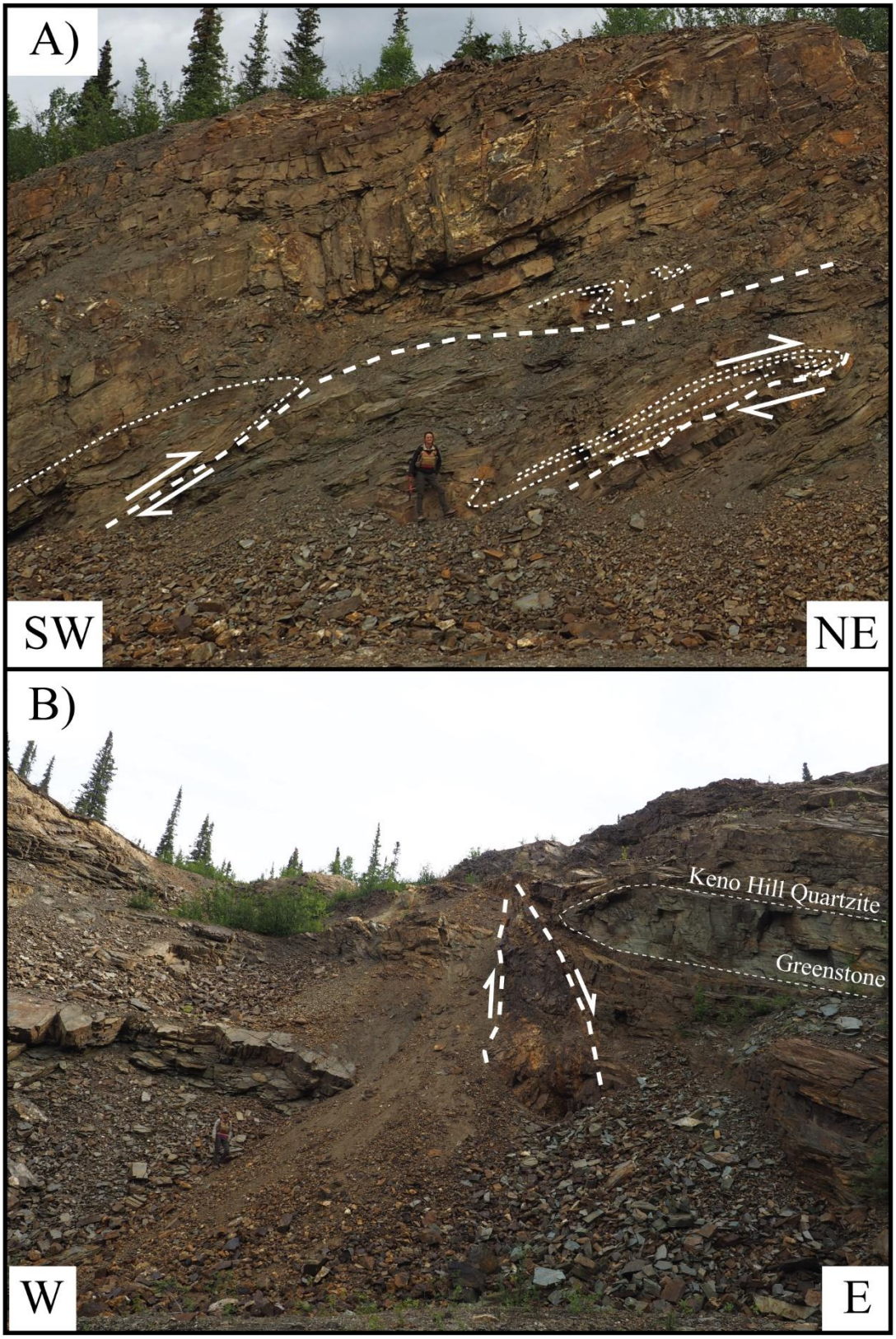


Figure 4.4: Station 22AK-058 (Onek property). A) isoclinal folds truncated by local thrust faults; B) normal-oblique vein fault with greenstone (right) outlining an isoclinal fold.

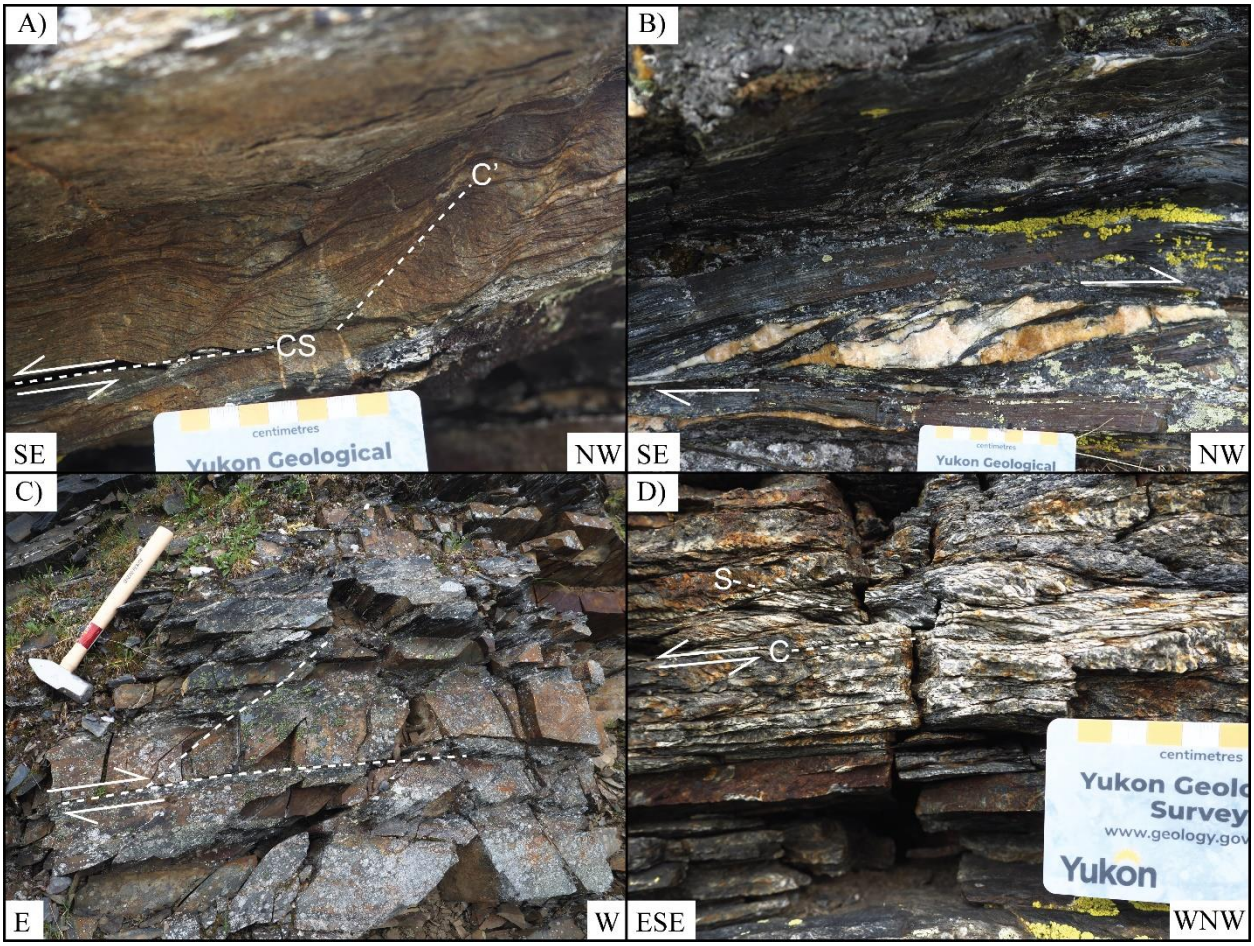


Figure 4.5: Shear sense indicators as observed at stations: A) 22AK-072, B) 22AK-045, C) 22AK-014, and D) 22AK-015.



Figure 4.6: Possible staurolite as a result of contact metamorphism at station 22AK-073.

4.2 MICROTECTONICS

4.2.1 Petrography and Microstructures

Petrographic Observations

Almost all of the samples collected and examined are dominated by quartz and white mica, with some samples also containing significant amounts of chlorite, calcite, and feldspar. Foliation in the samples is defined by aligned mats of white mica and elongate quartz grains. Chlorite, where present, typically forms laths that occur at an angle to the foliation, with lesser amounts following the predominant foliation associated with white mica. In some samples, however, chlorite forms large, irregularly-shaped grains (Fig. 4.7 A-B). Calcite, where present, typically forms irregular lobate shapes (Fig. 4.7 C-D).

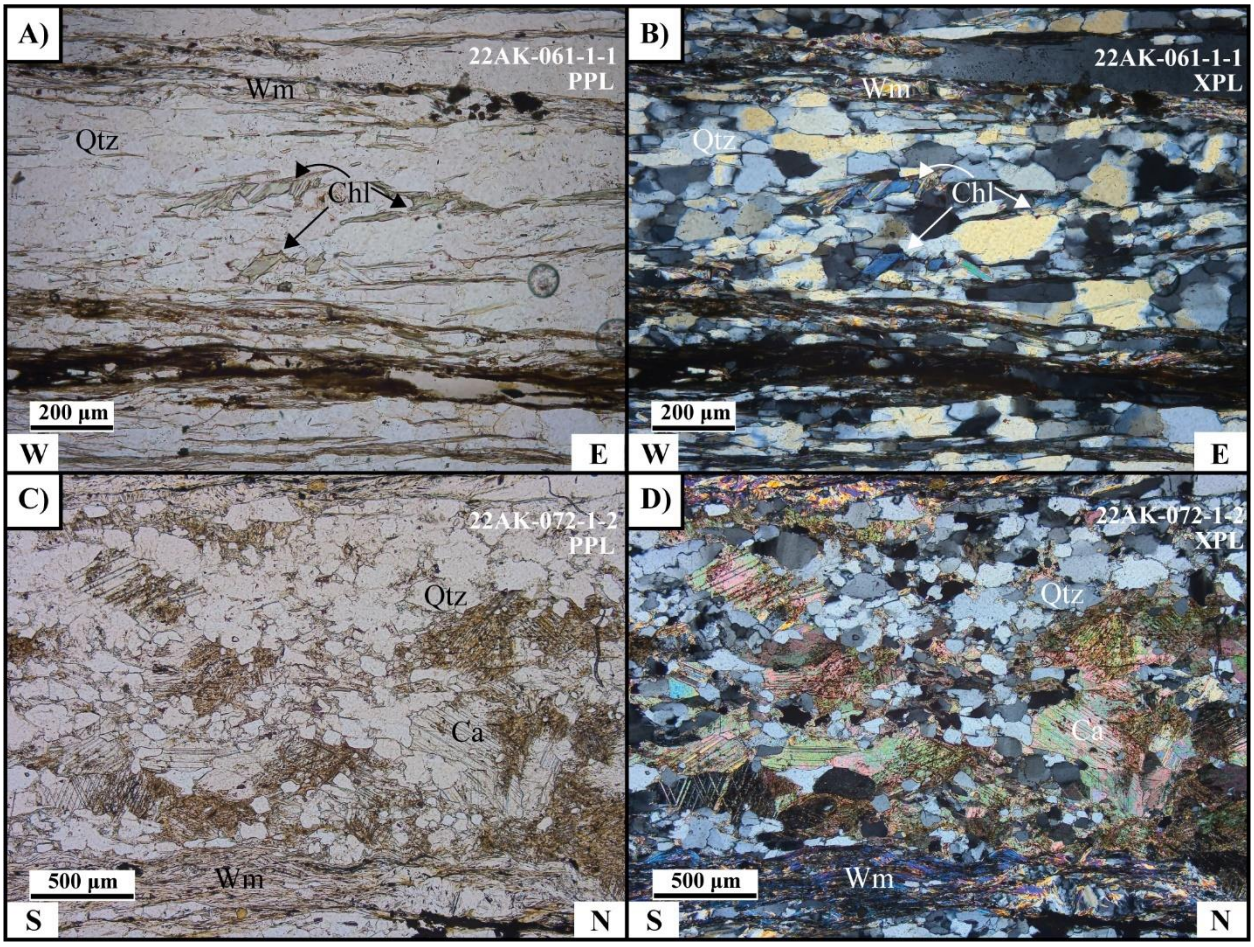


Figure 4.7: Petrographic images of chlorite (Chl) in A) PPL, and B) XPL for sample 22AK-061-1-1. Petrographic images of calcite (Ca) in C) PPL, and D) XPL for sample 22AK-072-1-2. Quartz (Qtz) and white mica (Wm) are labelled as well.

Euhedral, post-kinematic porphyroblasts noted in association with an aplite dike at station 22AK-073 (Fig. 4.1) have been completely replaced (Fig. 4.8). Replacement appears to have been facilitated by fluid movement along the dominant foliation planes. Point and map investigations via scanning electron microscopy and micro-X-Ray fluorescence indicate that the porphyroblast replacement is deficient in Al, but has high Ca and Mn. While the original mineral phase remains unknown, the porphyroblast shape (i.e. cross) is consistent with expected staurolite morphologies.

Quartz grit schists (22AK-006-1-1, 22AK-006-1-2, 22AK-061-1-1, 22AK-072-1-1, 22AK-072-1-2, and 22AK-082-1-1; Fig 4.1) occur in both the hanging wall and the footwall of the RST, with nearly identical mineralogy. Samples 22AK-006-1-1/2, 22AK-061-1-1, and 22AK-072-1-1 (from the previously mapped RST hanging wall/klippe; Fig. 4.1), have elongate quartz grains that parallel foliation, while samples 22AK-072-1-2 and 22AK-082-1-1 (from the footwall) have equant quartz grains.

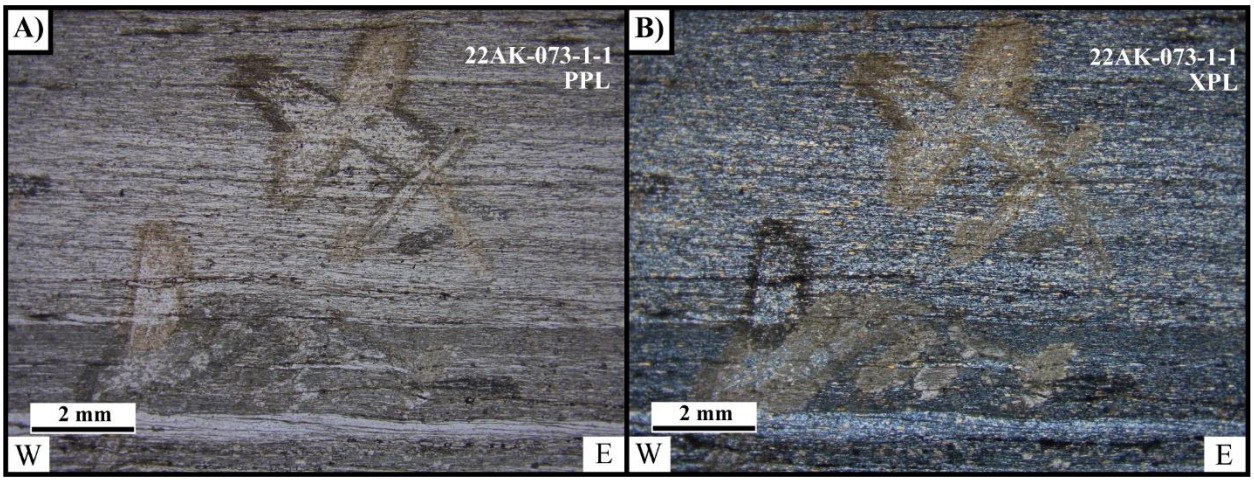


Figure 4.8: Petrographic images of sample 22AK-073-1-1 in A) PPL, and B) XPL.

Quartz Textures

Samples from across the entire field area exhibit small, equant grains moating larger, more elongate grains (Fig. 4.9A) with undulose extinction (Fig. 4.9C) and local lamellae (Fig. 4.9D). Typically, mica grains directly mantle the long edge of elongate quartz grains (as delineated by Fig. 4.9 B). Quartz in samples collected from the southern portion of the field area (both from the RST hanging wall and immediate footwall) is characterized by polygonal grain shapes, forming triple junctions and a wide range of grain sizes (~20 µm – 2 mm; Fig. 4.10 C-D). In contrast, samples collected on Keno Hill and in northern parts of the field area, have generally smaller quartz grains (~10 – 500 µm) with more interlobate shapes (Fig. 4.10 A-B).

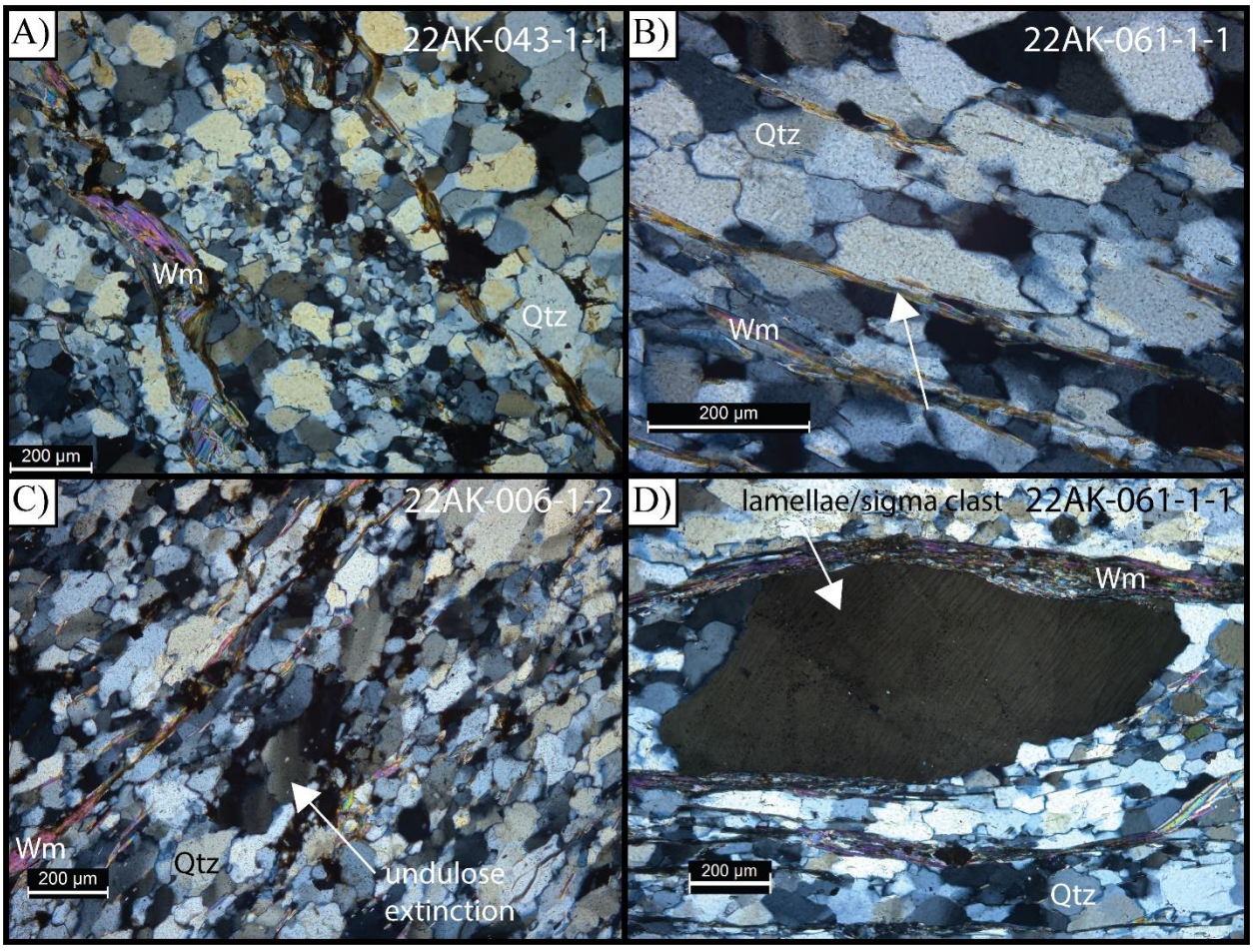


Figure 4.9: Thin section images of quartz textures in XPL: A) small equiant grains bordering larger grains from station 22AK-043; B) mica grains bordering the long edge of quartz grains from station 22AK-061; C) an example of undulose extinction from station 22AK-006; and D) lamellae in large quartz grain (sigma clast) and mica grains bordering long edge of quartz grains from station 22AK-061.

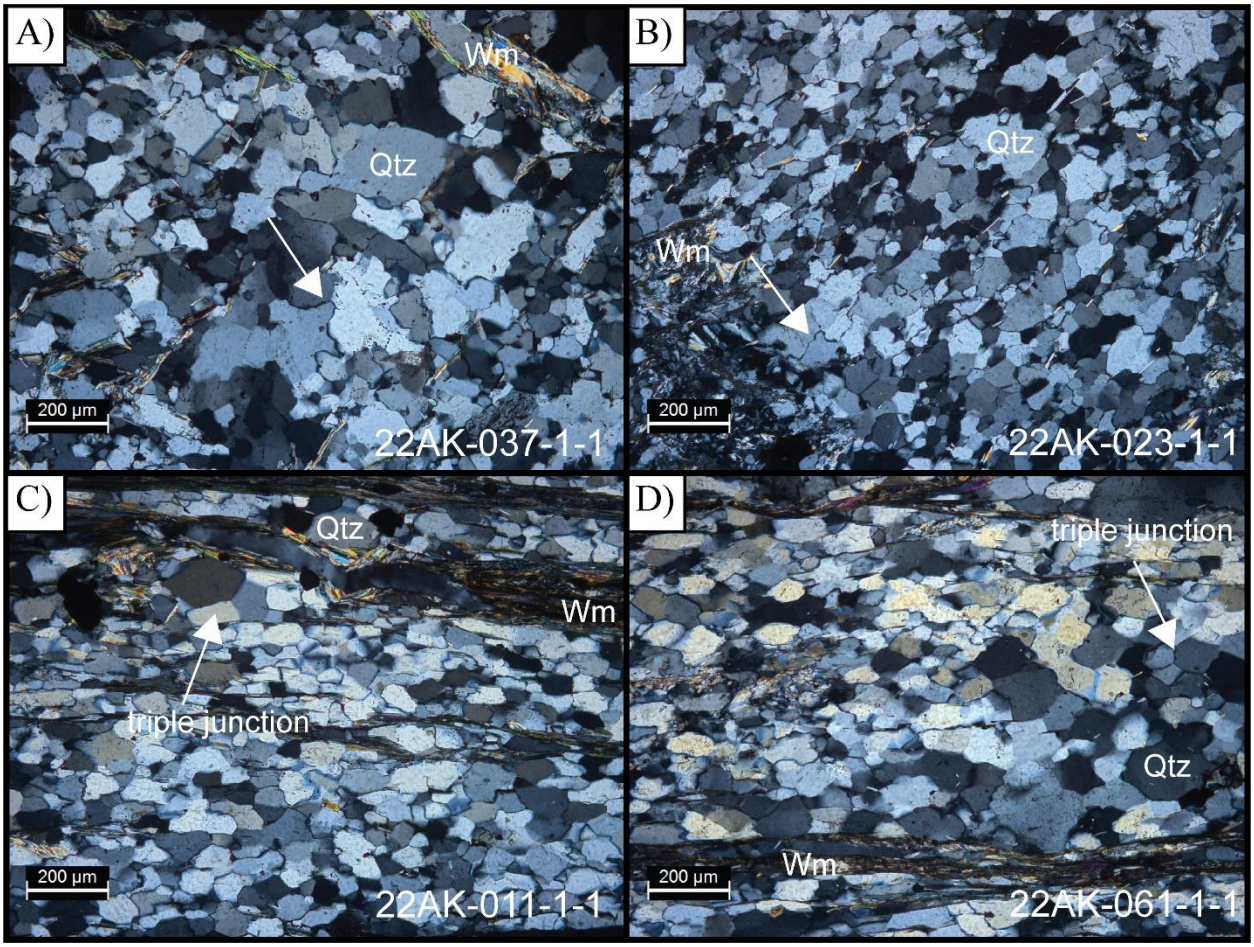


Figure 4.10: All thin section images are shown in XPL. A) and B) show interlobate quartz grains. A) is from station 22AK-037, and B) is from station 22AK-023. Both A) and B) are from the northern portion of the map area. C) and D) show polygonal quartz grains with triple junctions. C) is from station 22AK-011 and D) is from station 22AK-061. Both C) and D) are from the southern portion of the map area.

Shear Sense

Shear sense as observed in thin section is variable and commonly inconclusive. Where they occur, shear sense indicators are dominated by S-C-C' fabrics (Fig. 4.11), although a few samples have sigma clasts (e.g., Fig. 4.9D). Most shear sense indicators are either top-to-the southeast or top-to-the west/northwest, though samples also variably record top-to the east, and northeast (Fig. 4.11). There are no obvious spatial or structural trends with shear sense.

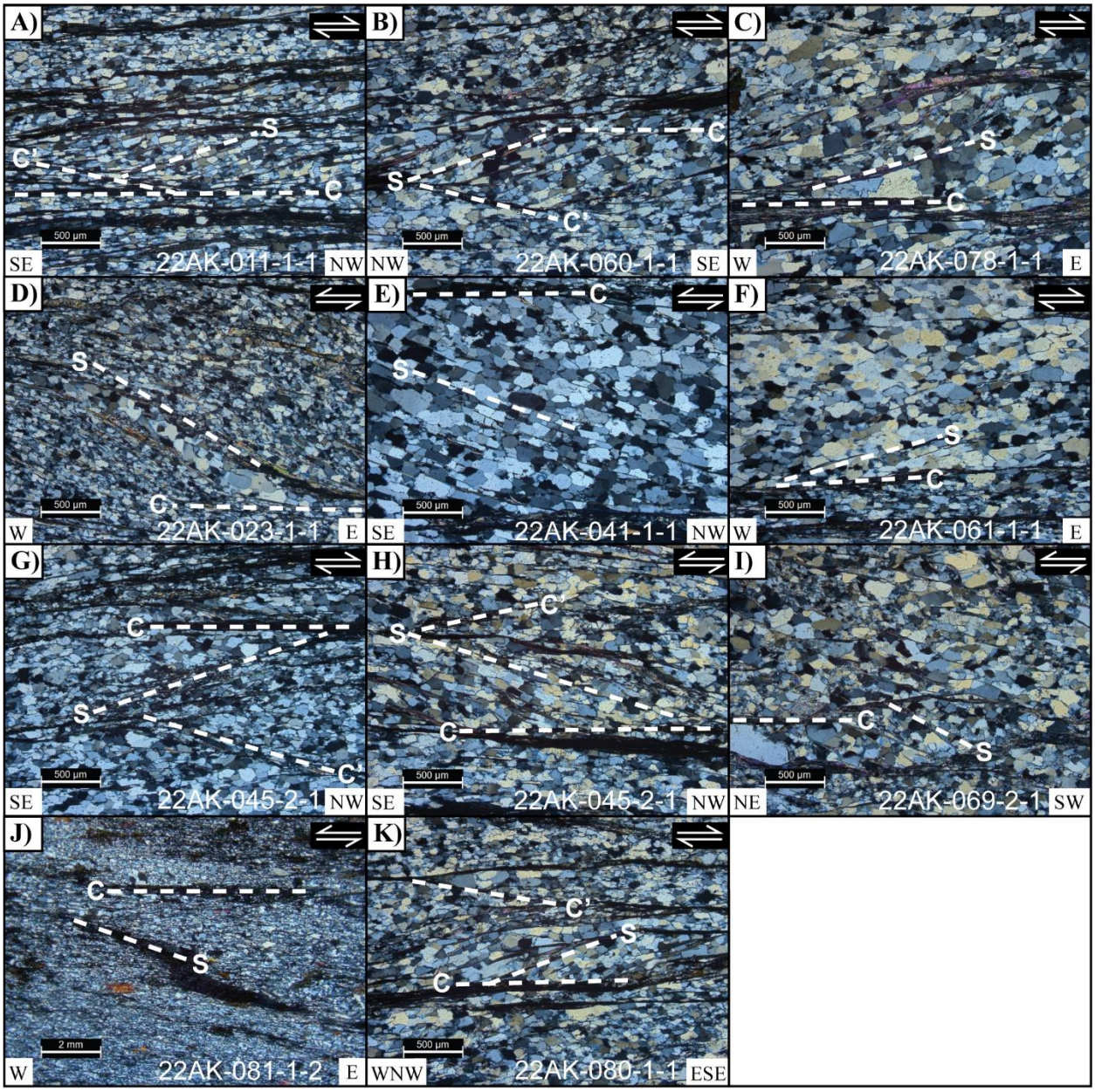


Figure 4.11: thin section images in XPL, illustrating shear sense. Samples were taken from stations: A) 22AK-011, B) 22AK-060, C) 22AK-078, D) 22AK-023, E) 22AK-041, F) 22AK-061, G) and H) 22AK-045, I) 22AK-069, J) 22AK-081, and K) 22AK-80. All these stations can be located in Fig. 3.1 or the samples as annotated in the images from Fig. 4.1.

4.2.2 Quartz CPO

Quartz *c*-axis crystallographic preferred orientation (CPO) investigations were conducted on 25 samples using the Fabric Analyzer. The quartz *c*-axis plots shown in Fig. 4.12 are lower hemisphere, equal area Schmidt contour and scatter plots made using the FabricPlotR (Larson, 2022) script. The foliation plots as a horizontal line representing a vertical east-west plane (in the reference frame of the plot; Fig. 4.12G), as the thin sections were cut parallel to lineation and perpendicular to foliation. The lineation in this reference frame plots as a point at each end of the foliation red line (Fig. 4.12G).

Variable geometries in the CPO plots are observed in the 25 investigated samples. The single girdle (e.g. 22AK-049-1-1; Schmid & Casey, 1986) is the most common distribution type, however, both Type I (e.g. 22AK-054-1-1; Lister, 1977) and Type II (e.g. 22AK-061-1-1; Schmid & Casey, 1986) crossed girdle fabrics are also observed. The distribution opening angles for crossed girdle specimens range from 54-65°. Some samples also show patterns that reflect a transition between crossed girdle and single girdle distributions (e.g. 22AK-032-1-1; Hunter et al., 2018), as well as some with an irregular and/or inconclusive geometry (e.g. 22AK-037-1-1). There is no obvious spatial or structural relationship with CPO type. The asymmetries of the CPOs broadly align with top-to-the-north shear.

CPO strength was calculated in terms of the J_{PF}-index using the FabricPlotR (Larson, 2022) script. There is no apparent correlation between the J_{PF}- index with respect to sample location (Fig. 4.13), even when taking into account the potential effect of phyllosilicates on the distribution strength (Bouchez & Pecher, 1981; Hippertt, 1994; Larson, 2018; Larson et al., 2014).

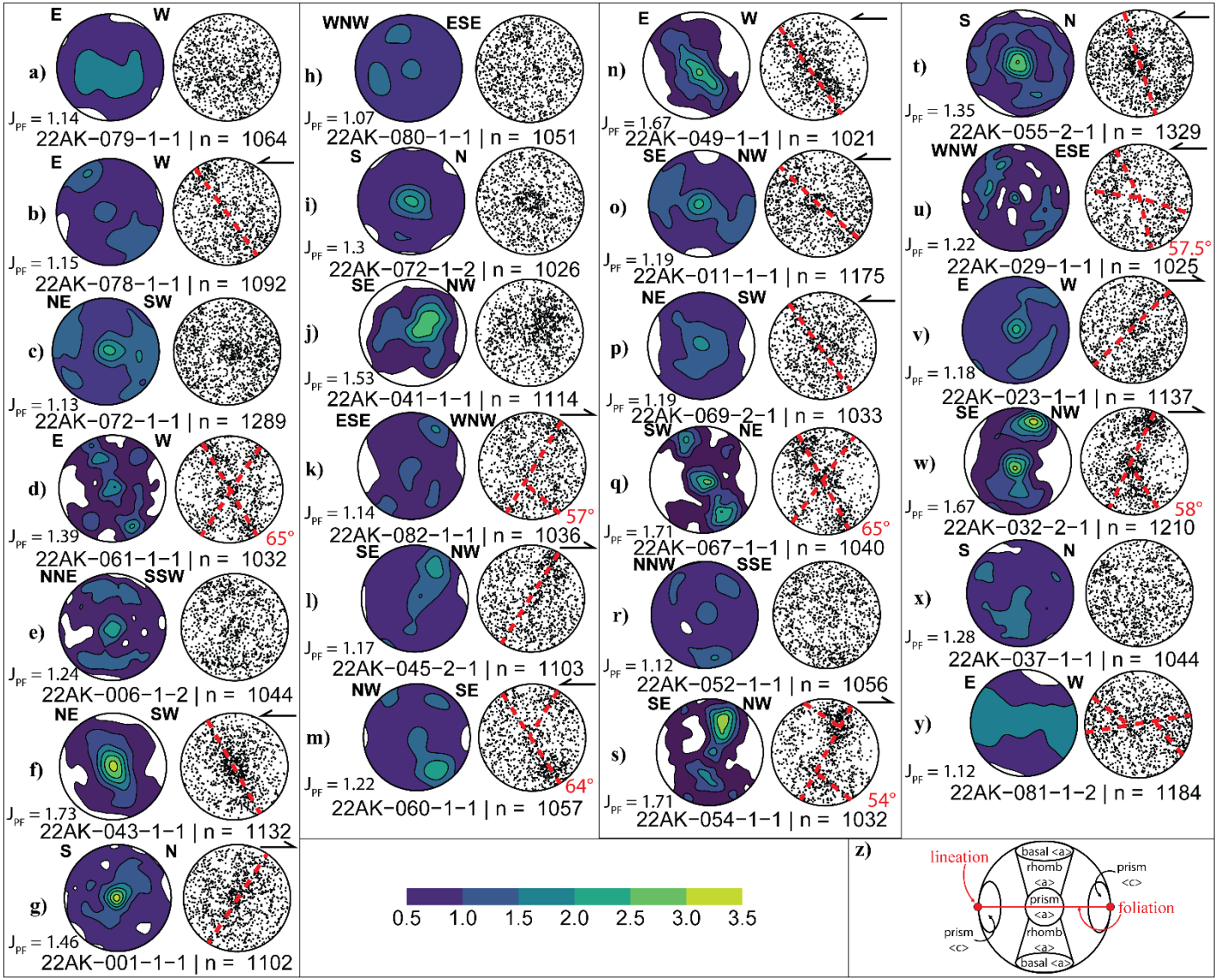


Figure 4.12: Quartz c-axis CPO lower hemisphere Schmidt plots (contoured (left) and scatter (right)) for 25 samples (labelled below). Red annotation on the lower hemisphere scatter plot represents the interpreted fabric type. Number of grains per CPO plot is presented beside sample number underneath the plots. JPF-index written to the left of the contoured plot (in black), and the opening angles (when applicable) are written to the right of the scatter plot (in red). Black arrows indicate interpreted shear sense. Contour density colour gradient shown bottom centre. z) illustrates location of foliation and lineation, and activated slip systems. All plots made using FabricPlotR (Larson, 2022) script.

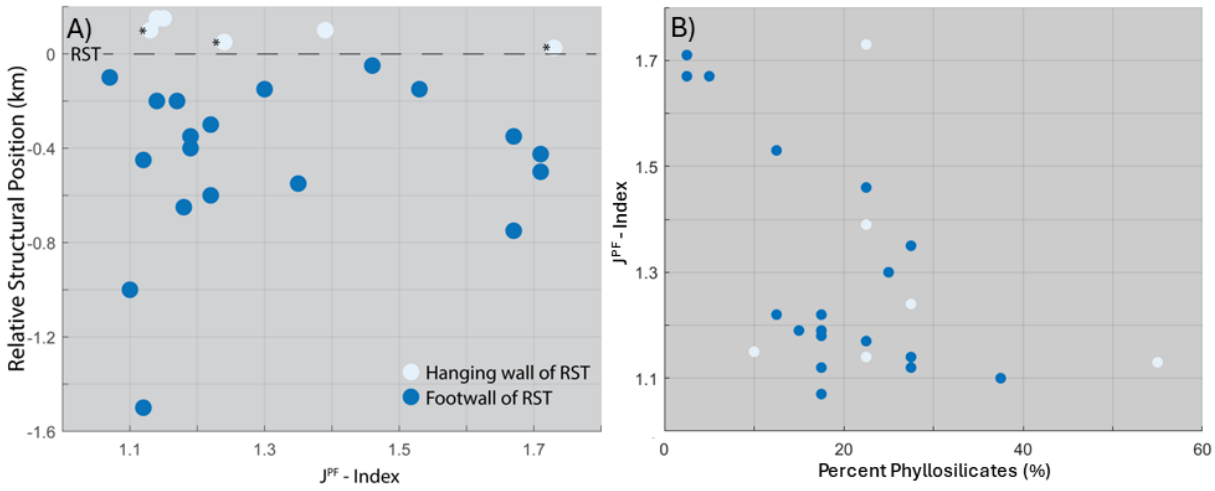


Figure 4.13: A) J_{PF} -index from fabric analyser investigations plotted with respect to relative structural position; and B) approximate percent of phyllosilicates in those samples with respect to the J_{PF}-index. Where the asterisks (*) in A) delineate which samples were collected from previously mapped klippes.

4.2.3 Grain Size Piezometry

EBSD analysis was conducted on quartz in 7 samples for grain size piezometry investigations. The Cross et al. (2017) grain size piezometer, used for this investigation, is based on a 1 μm step size, following the recommendation to use a step size of at most 1/5 of the size of the smallest recrystallized grain (Cross et al., 2017). As the EBSD investigations were conducted with a 5 μm step size, this could inhibit the interpretations as the grain size distribution is not viable for grains smaller than 10 μm.

The grain orientation spread (GOS; Cross et al., 2017) inflection point separating the relict and recrystallized grains (e.g. Fig. 4.14D-E) was between 2-4° for all investigated samples (Fig. 4.14A). The root mean square (RMS; Cross et al., 2017) recrystallized grain size ranges from ~20-80 μm (Fig. 4.14C) whereas that for the relict grains ranges from ~30-120 μm. Those grain sizes correspond to differential stresses of between 15 and 70 MPa for recrystallized grains (Fig. 4.14B) and 15 to 55 MPa for relict grains. There are no obvious relationships with RMS grain size (recrystallized or relict) nor differential stress with the samples' spatial or structural location, as all samples have overlapping uncertainties. The recrystallized grains have larger grain sizes and higher differential stress overall than the relict grains (Fig. 4.15).

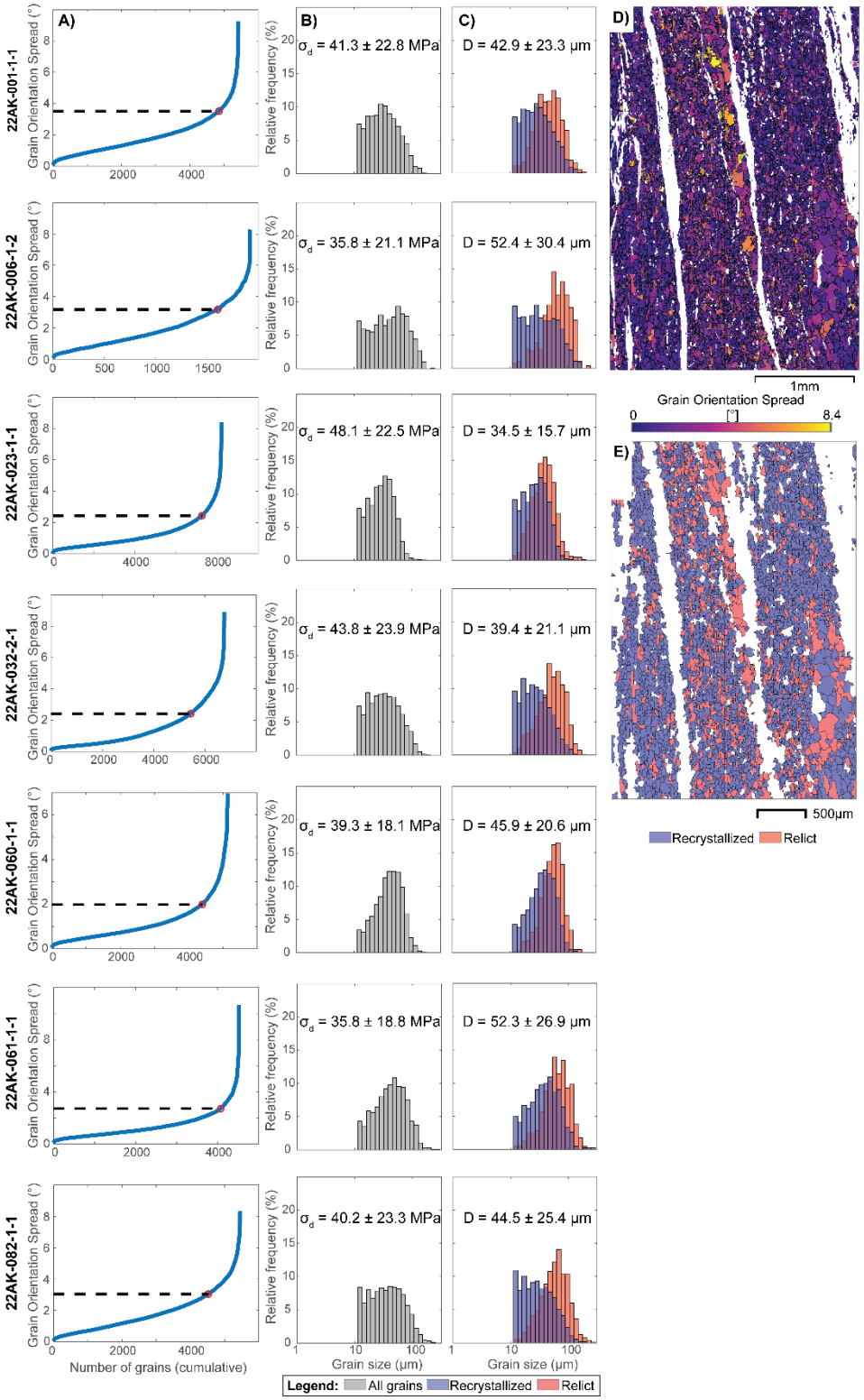


Figure 4.14: All samples labelled on the left. A) Grain orientation spread inflexion point. Grain size distribution histogram for: B) all grains with text showing the differential stress for the sample, and C) relict and recrystallized grains with text showing the recrystallized RMS grain size. On the right are thin section maps of 22AK-023-1-1 for: D) grain orientation spread, and E) relict and recrystallized grains. Plots from A-C, and F were made using the Cross et al. (2017) script with the trade-off function. D was made using Aztec Crystal.

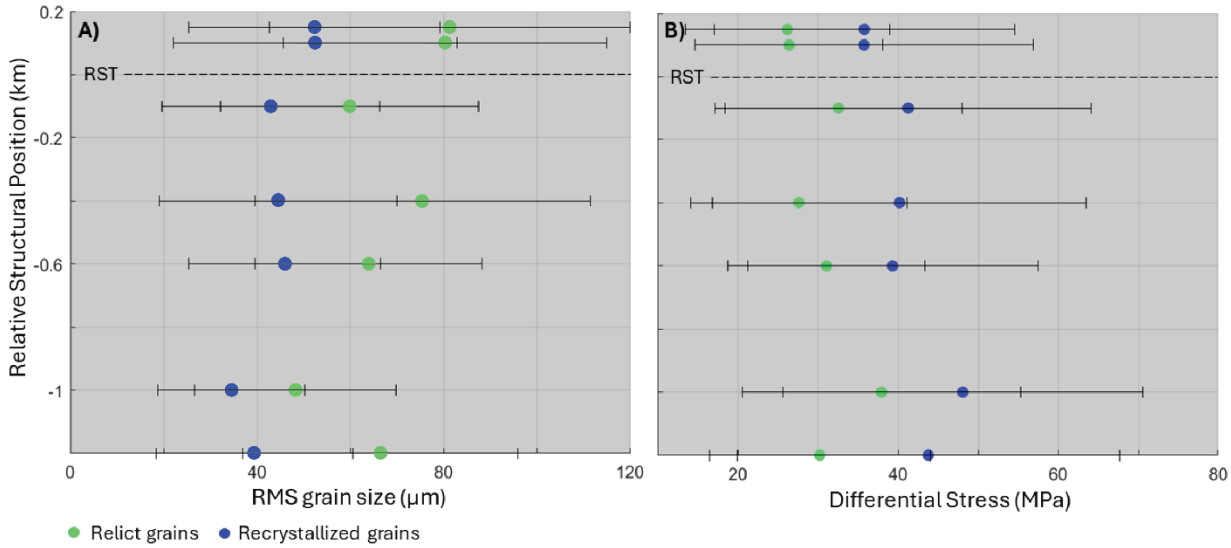


Figure 4.15: A) RMS grain size for recrystallized and relict grains plotted with respect to relative structural position. B) Differential stress calculated from recrystallized and relict RMS grain size plotted against relative structural position. All data from EBSD investigations, calculated using RexRelict.M script (Cross et al., 2017).

4.2.4 Quartz Crystallographic Vorticity Axes

Quartz crystallographic vorticity axes (CVA; Michels et al., 2015) for the samples analysed via EBSD are plotted in lower hemisphere stereographic projections in the CPO reference frame as defined by the EBSD data (Fig. 4.16-22; the bulk quartz *c*-axis CPOs from EBSD data resemble those from the Fabric Analyzer). This means that the quartz *c*-axis plots were rotated (if applicable) to bring the maximum density of the *c*-axis poles to the center of the stereographic projection, to simultaneously orient the *a*-axes along the periphery of the plot. In the CPO reference frame, the foliation is roughly oriented within the same E-W reference frame as the specimen. Rotations were necessary as not all samples had obvious lineations and, as such cutting thin sections parallel to the elongation direction was difficult.

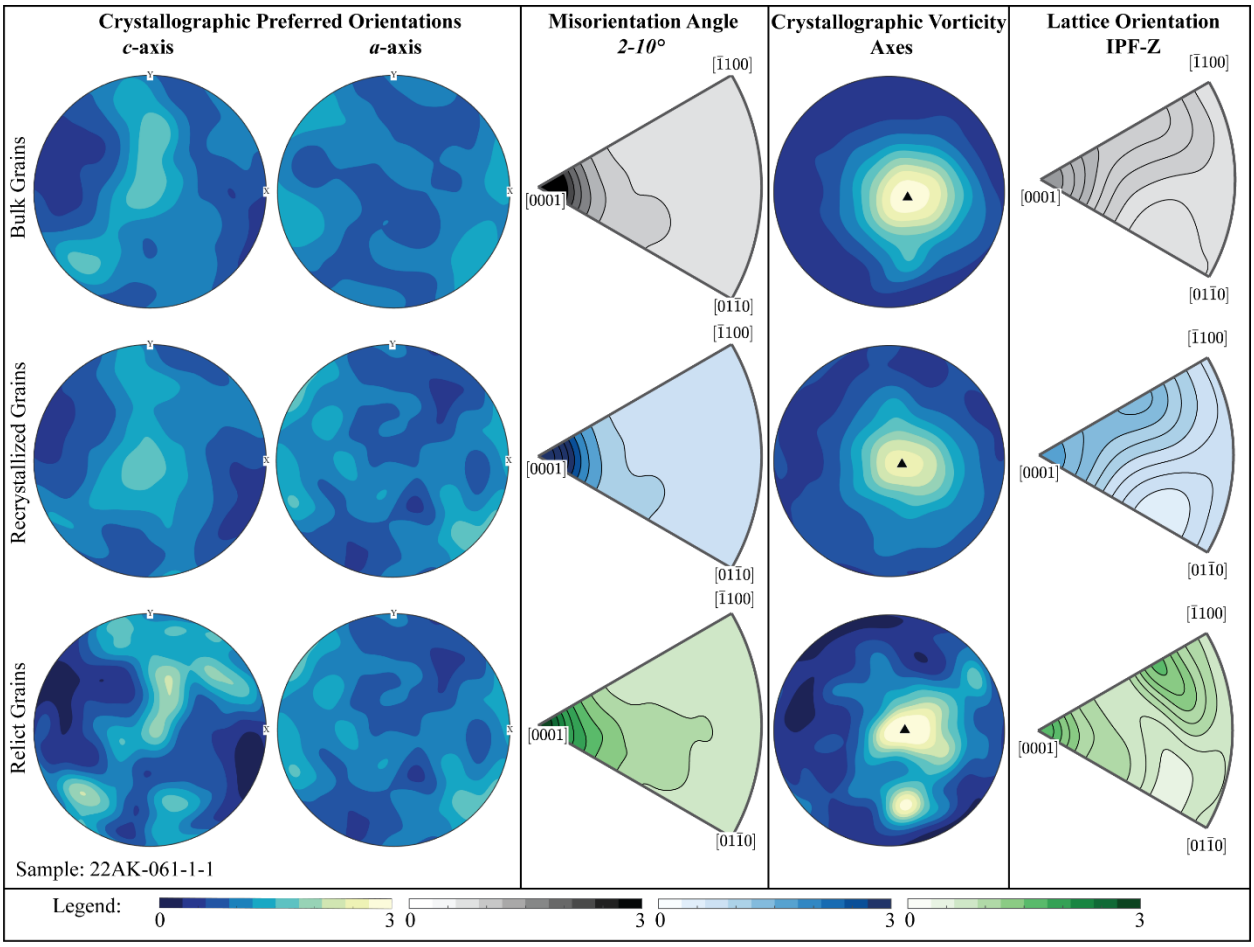


Figure 4.16: Quartz c- and a-axis CPOs, 2-10° misorientation axes IPF, CVAs, and lattice orientation from the observer reference frame for the bulk, recrystallized and relict grains of sample 22AK-061-1-1. Legend shows the kernel densities for CPO plots, multiplies of uniform density for CVA plots.

The location of the CVA maxima can help interpret whether deformation was dominated by monoclinic transpression, triclinic transpression, or transtension (e.g. Brown, 2022; Michels et al., 2015). The CVA maxima locations measured in the samples have a range of orientations, most notably within the centre (i.e. Fig. 4.16, Fig. 4.20), along the east-west poles (i.e. Fig. 4.19), and the north-south poles (i.e. Fig. 4.17, Fig. 4.18, Fig. 4.22), though some do not have significant maxima (22AK-023-1-1; Fig. 4.21). Overall, there appears to be a decrease in maximum density of the poles of the CVAs the farther the samples are from the RST. However, there is no spatial or structural relationship of the orientations of the CVA maxima within the samples.

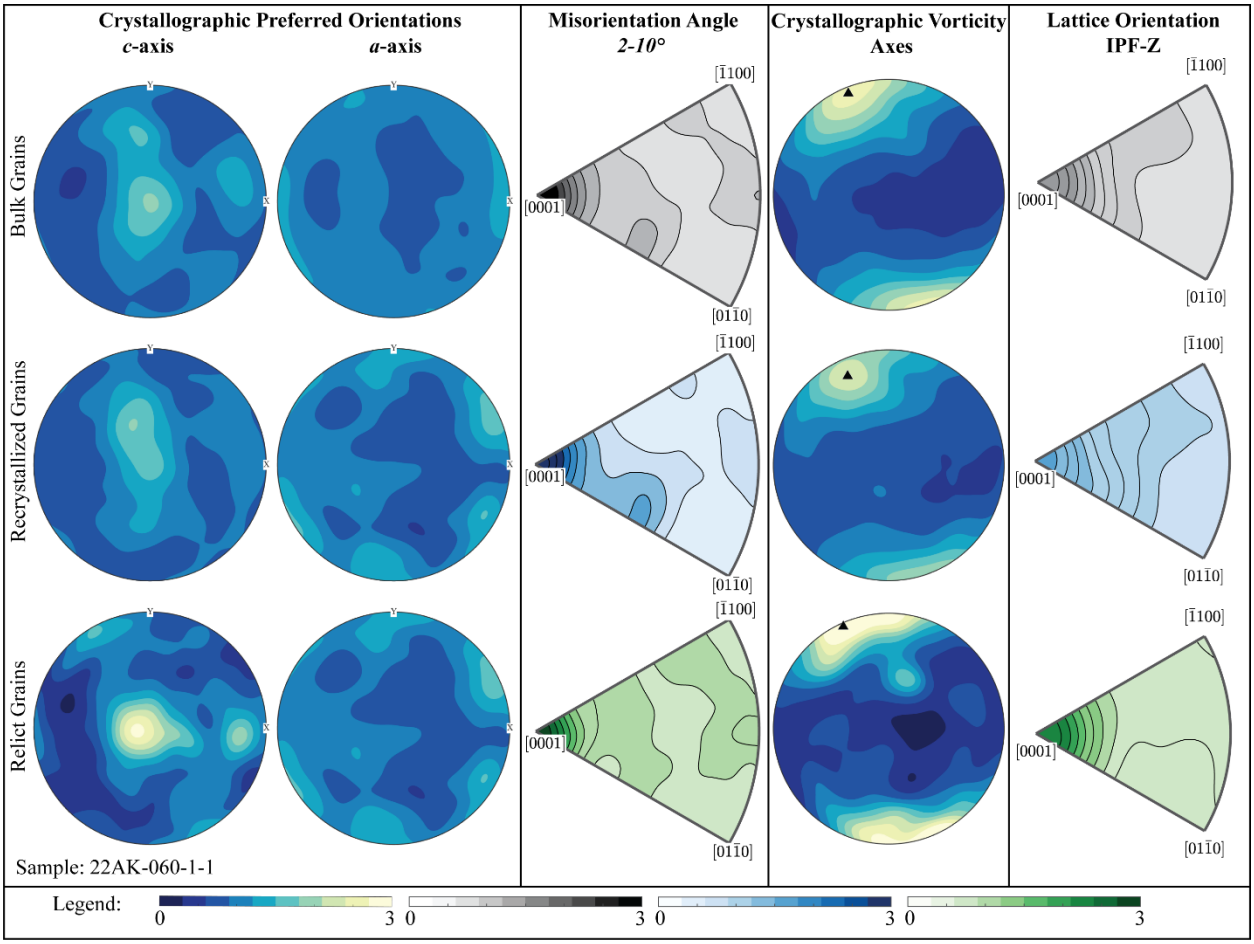


Figure 4.17: Quartz c- and a-axis CPOs, 2-10° misorientation axes IPF, CVAs, and lattice orientation from the observer reference frame for the bulk, recrystallized and relict grains of sample 22AK-060-1-1. Legend shows the kernel densities for CPO plots, multiples of uniform density.

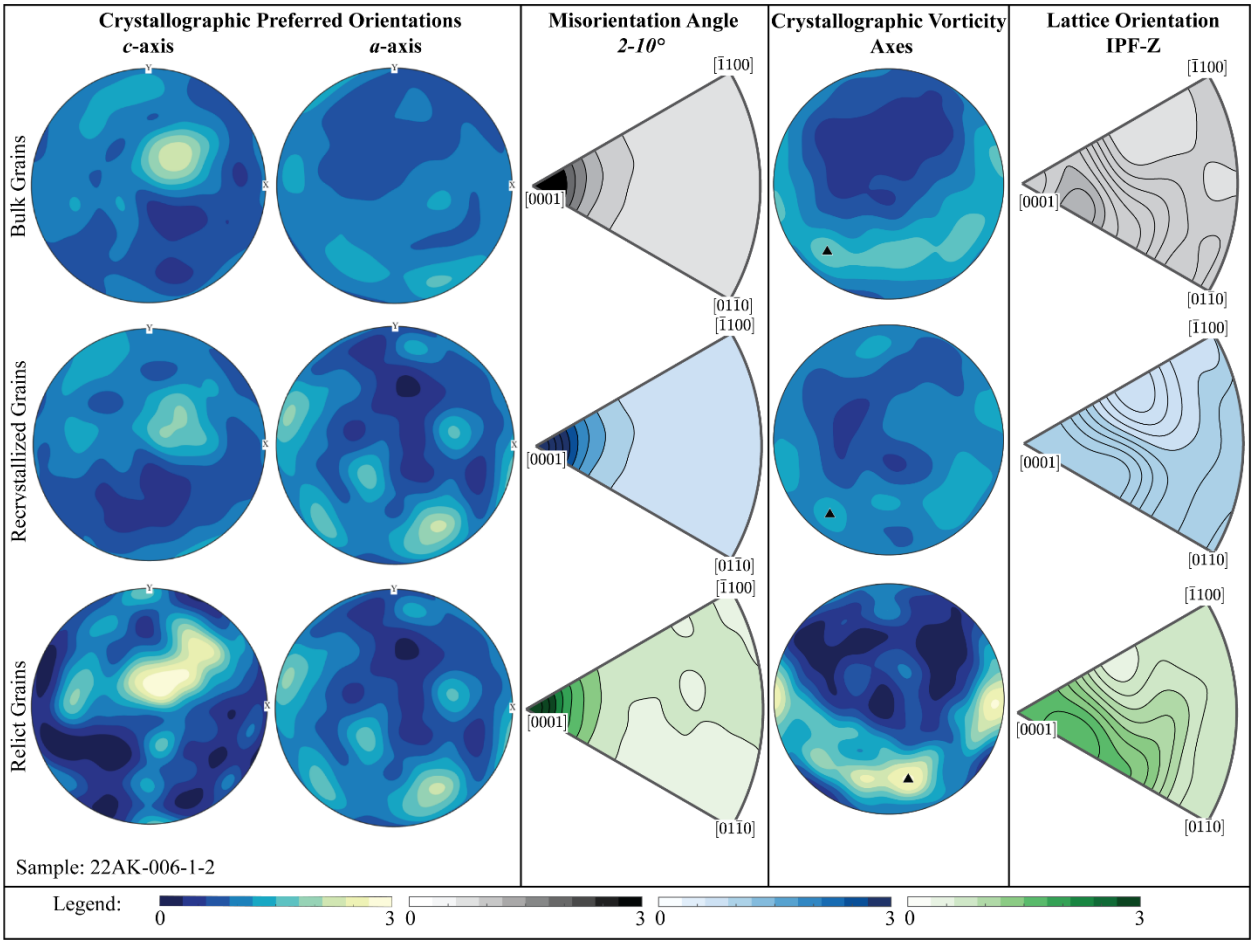


Figure 4.18: Quartz c- and a-axis CPOs, 2-10° misorientation axes IPF, CVAs, and lattice orientation from the observer reference frame for the bulk, recrystallized and relict grains of sample 22AK-006-1-2. Legend shows the kernel densities for CPO plots, multiples of uniform density.

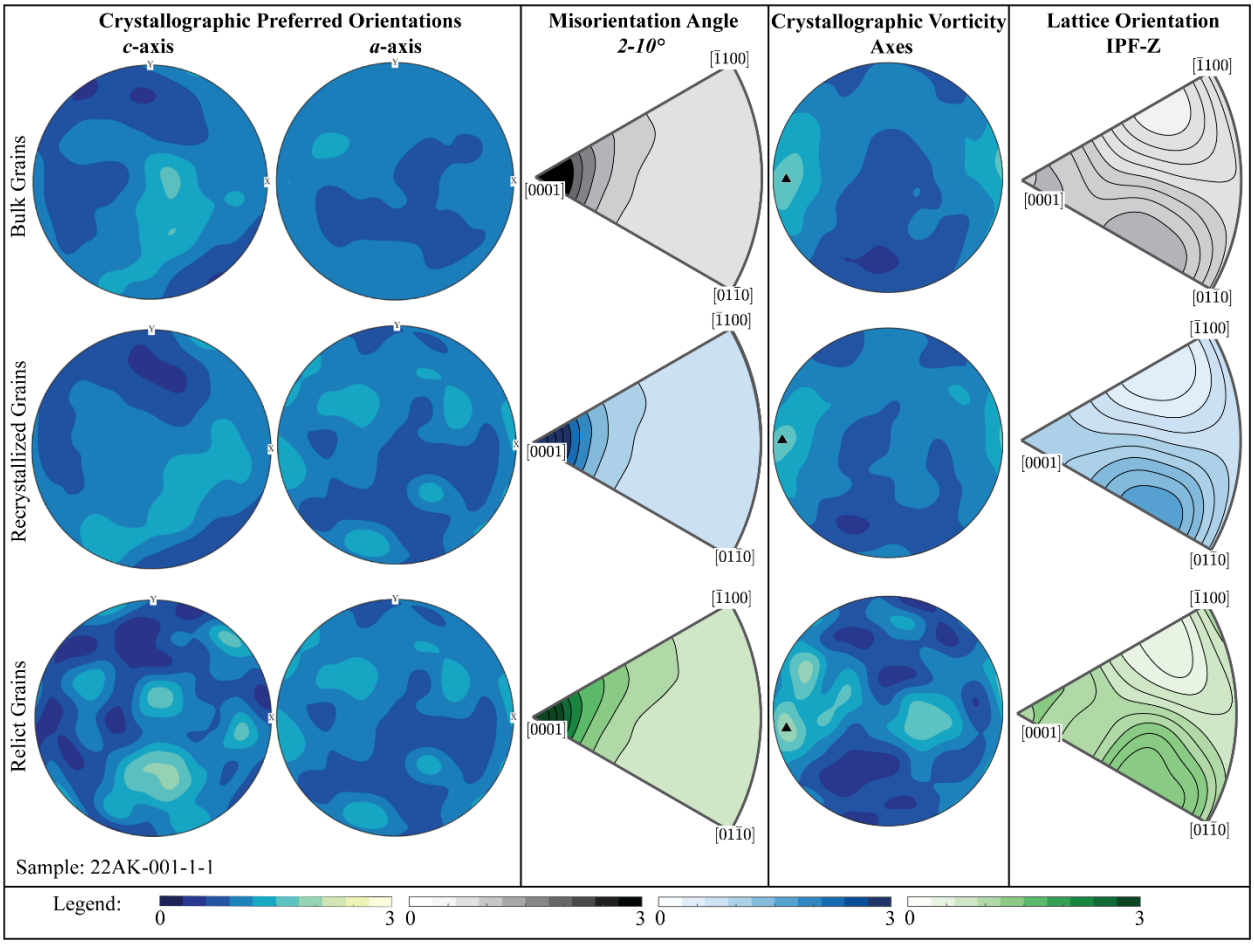


Figure 4.19: Quartz c- and a-axis CPOs, 2-10° misorientation axes IPF, CVAs, and lattice orientation from the observer reference frame for the bulk, recrystallized and relict grains of sample 22AK-001-1-1. Legend shows the kernel densities for CPO plots, multiples of uniform density.

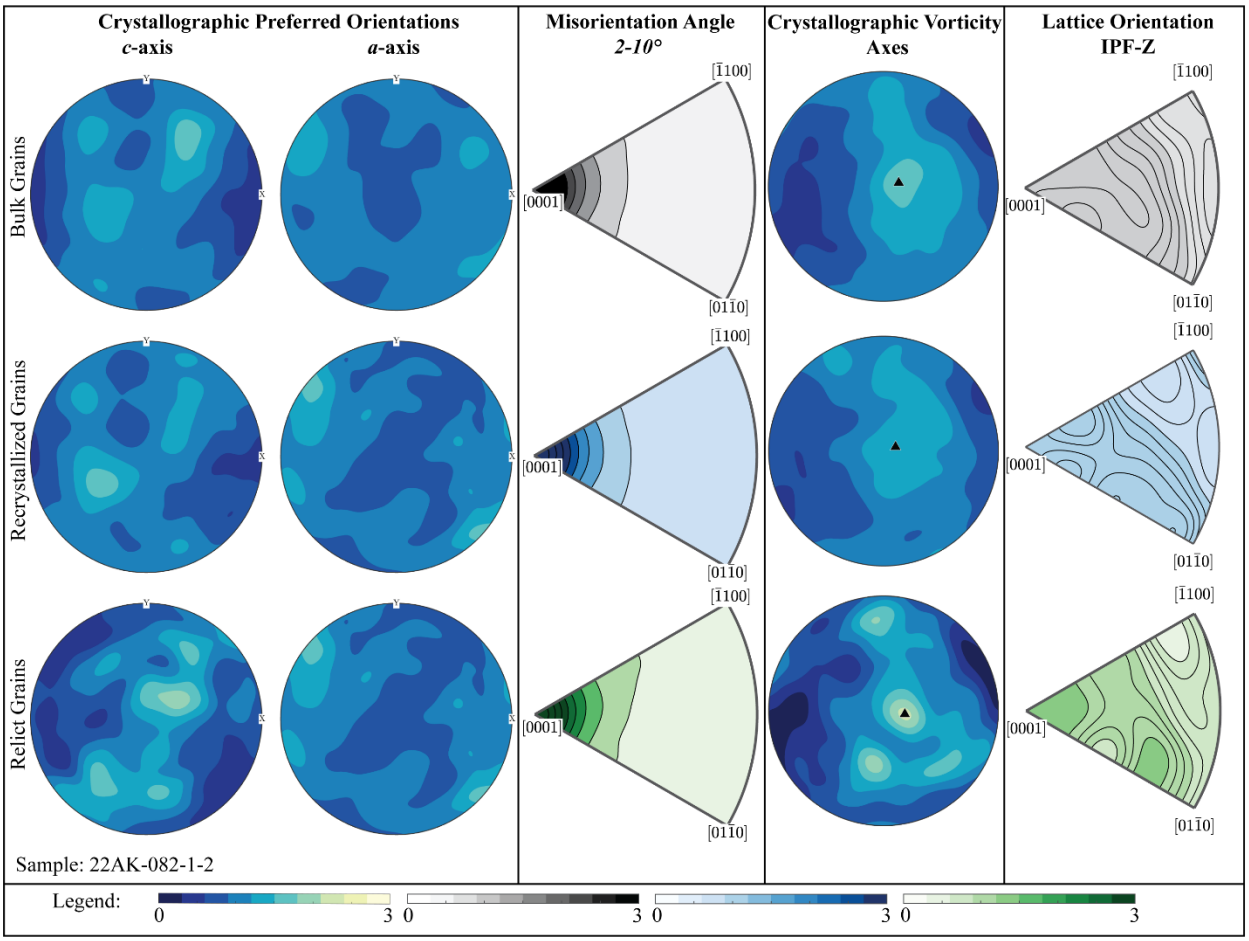


Figure 4.20: Quartz c- and a-axis CPOs, 2-10° misorientation axes IPF, CVAs, and lattice orientation from the observer reference frame for the bulk, recrystallized and relict grains of sample 22AK-082-1-2. Legend shows the kernel densities for CPO plots, multiples of uniform density.

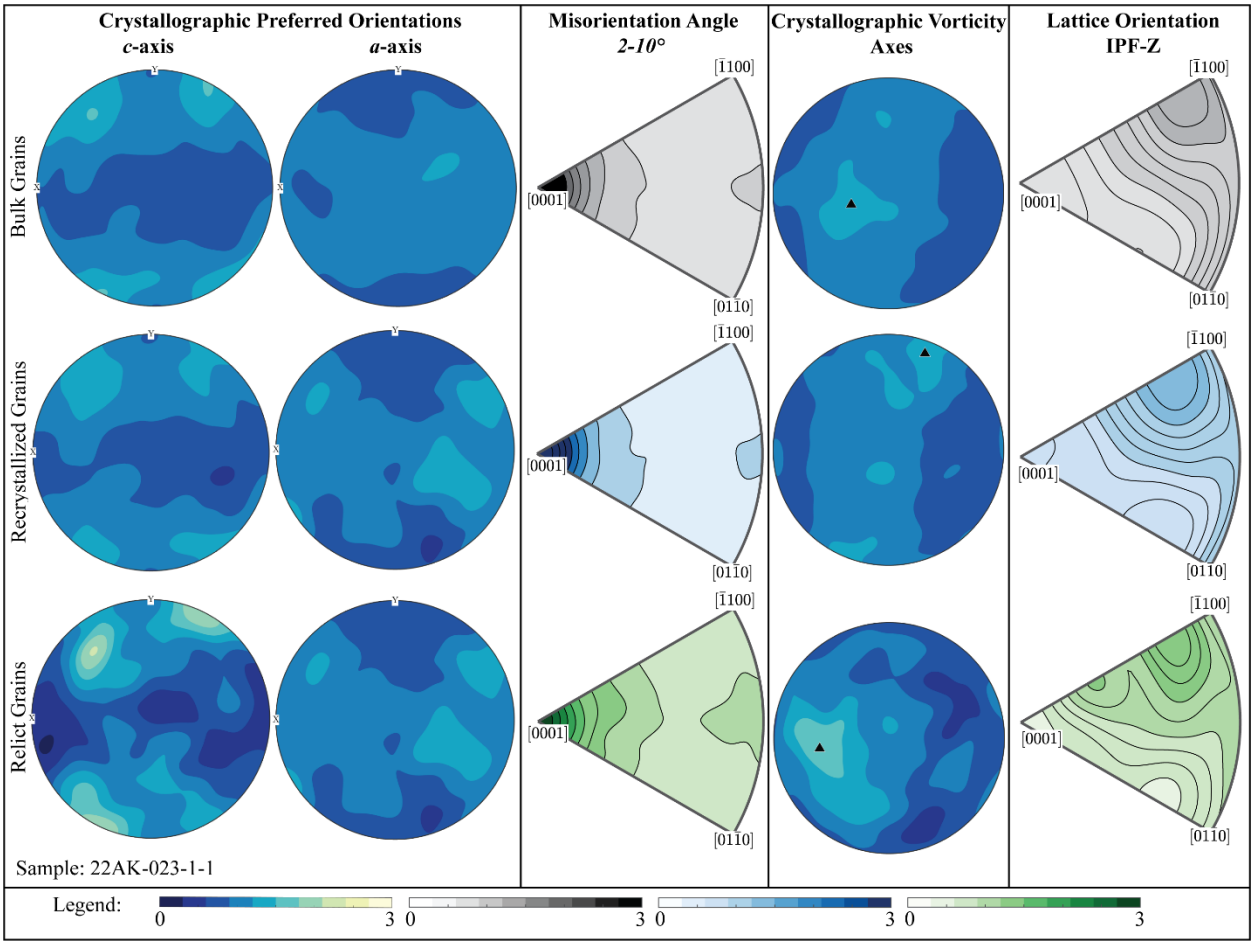


Figure 4.21: Quartz c- and a-axis CPOs, 2-10° misorientation axes IPF, CVAs, and lattice orientation from the observer reference frame for the bulk, recrystallized and relict grains of sample 22AK-023-1-1. Legend shows the kernel densities for CPO plots, multiples of uniform density.

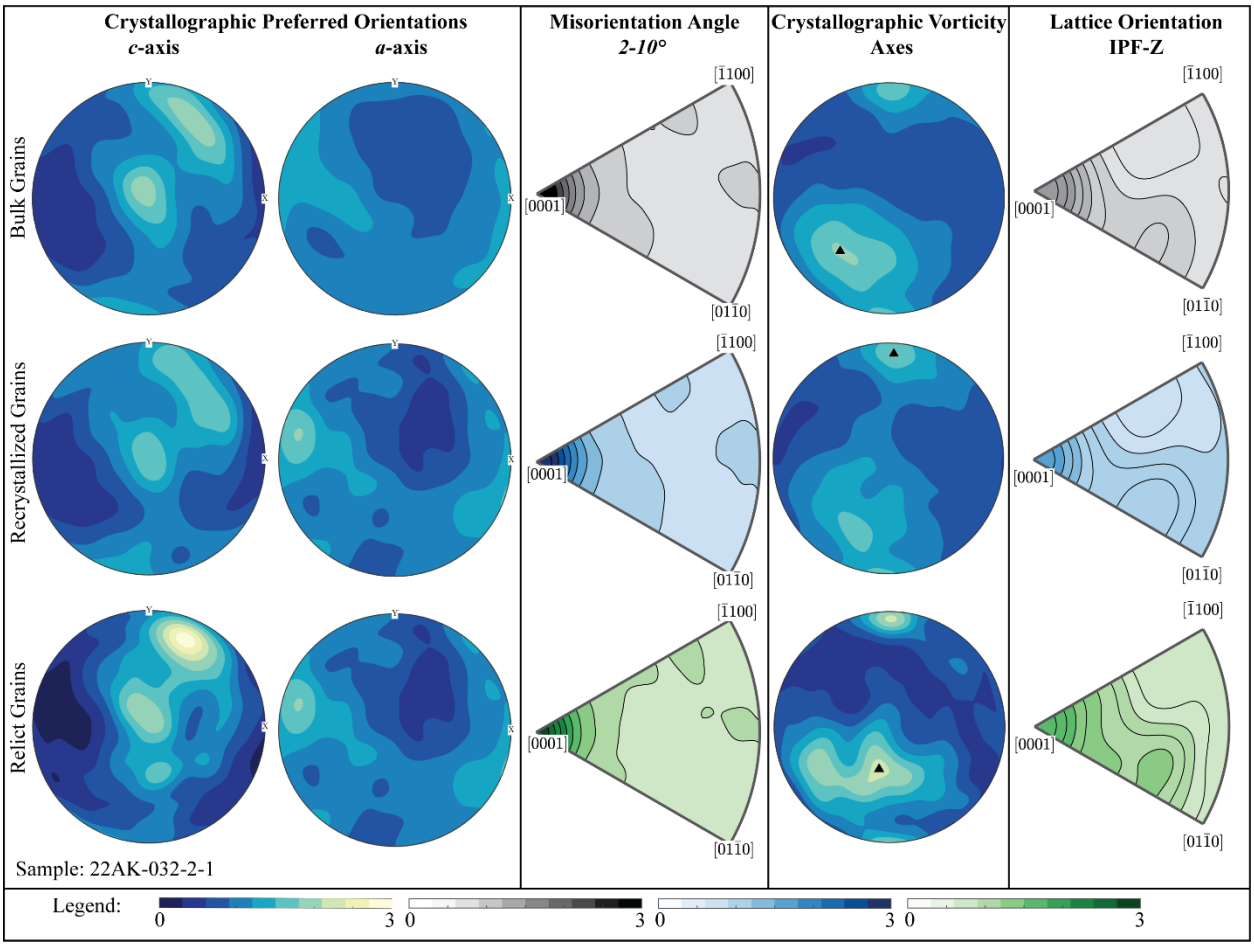


Figure 4.22: Quartz c- and a-axis CPOs, 2-10° misorientation axes IPF, CVAs, and lattice orientation from the observer reference frame for the bulk, recrystallized and relict grains of sample 22AK-032-2-1. Legend shows the kernel densities for CPO plots, multiples of uniform density.

4.3 GEOCHRONOLOGY

4.3.1 $^{87}Rb/^{87}Sr$ Dating

The results of $^{87}Rb/^{87}Sr$ geochronology are discussed below from southwest to northeast across the field area. All sample dates are reported with outliers removed with uncertainties cited at two standard errors of the mean (absolute). Outliers were defined by the error ellipse not crossing the isochron as there is a possibility the targeted material incorporated an additional phase that was not at equilibrium with the other targeted material or insufficient material was ablated. Specimen 22AK-061-1-1 is a quartz grit mica schist sampled from the hanging wall of the RST, around 100 m from the approximate trace (Fig. 4.1). Data for this sample were collected over two runs. The first run targeted foliation-defining white mica, while the second run predominantly targeted feldspars. A regression through the data defines a single population isochron at 116 +/- 14 Ma (mean square weighted deviation (MSWD) = 1, n = 60) (Fig. 4.23A). Specimen 22AK-006-1-2 is also a quartz grit schist, but from the hanging wall of a previously mapped, possible klippe of the RST sheet on Sourdough Hill (Fig. 4.1), around 50 m from the inferred thrust trace. Foliation-parallel white mica defines a single regression at 85.5 +/- 6.2 Ma (MSWD = 0.7, n = 64) (Fig. 4.23B).

The rest of the samples dated using $^{87}Rb/^{87}Sr$ *in situ* geochronology are from the footwall of the RST. Samples 22AK-082-1-1, and 22AK-011-1-1 are both from Sourdough Hill (Fig. 4.1). Analyses of foliation-defining white mica in sample 22AK-082-1-1 (quartz grit schist) outline a low precision isochron date of 137 +/- 121 Ma (MSWD = 0.97, n = 57) (Fig. 4.23C). Sample 22AK-011-1-1 is sericite schist collected about 1.25 km away from 22AK-082-1-1. The foliation-defining white mica analysed therein also yielded a low precision isochron date of 128 +/- 33 Ma (MSWD = 0.83, n = 51) (Fig. 4.23D).

Sample 22AK-023-1-1 is a chlorite sericite schist collected about 10 km northwest of sample 22AK-011-1-1 (Fig 4.1). The foliation-defining white mica outline an $^{87}Rb/^{87}Sr$ isochron date of 75 +/- 33 Ma (MSWD = 0.72, n = 56) (Fig. 4.22E). The farthest north sample analysed was collected from Keno Hill, approximately 10 km east-northeast of sample 22AK-023-1-1. Sample 22AK-037-1-1 is chlorite-sericite schist with isoclinally folded fabric in which two textural populations of white mica (foliation-parallel and perpendicular to foliation) were targeted (Fig. 4.24). Feldspars were targeted in a separate run to collect initial $^{87}Sr/^{86}Sr$ ratio data to fit a higher

precision regression through the data. The two textural populations of mica overlapped in isochron space; the combined dataset yields a single population isochron date of 92.9 +/- 4.9 (MSWD = 0.86, n = 138) (Fig. 4.23F).

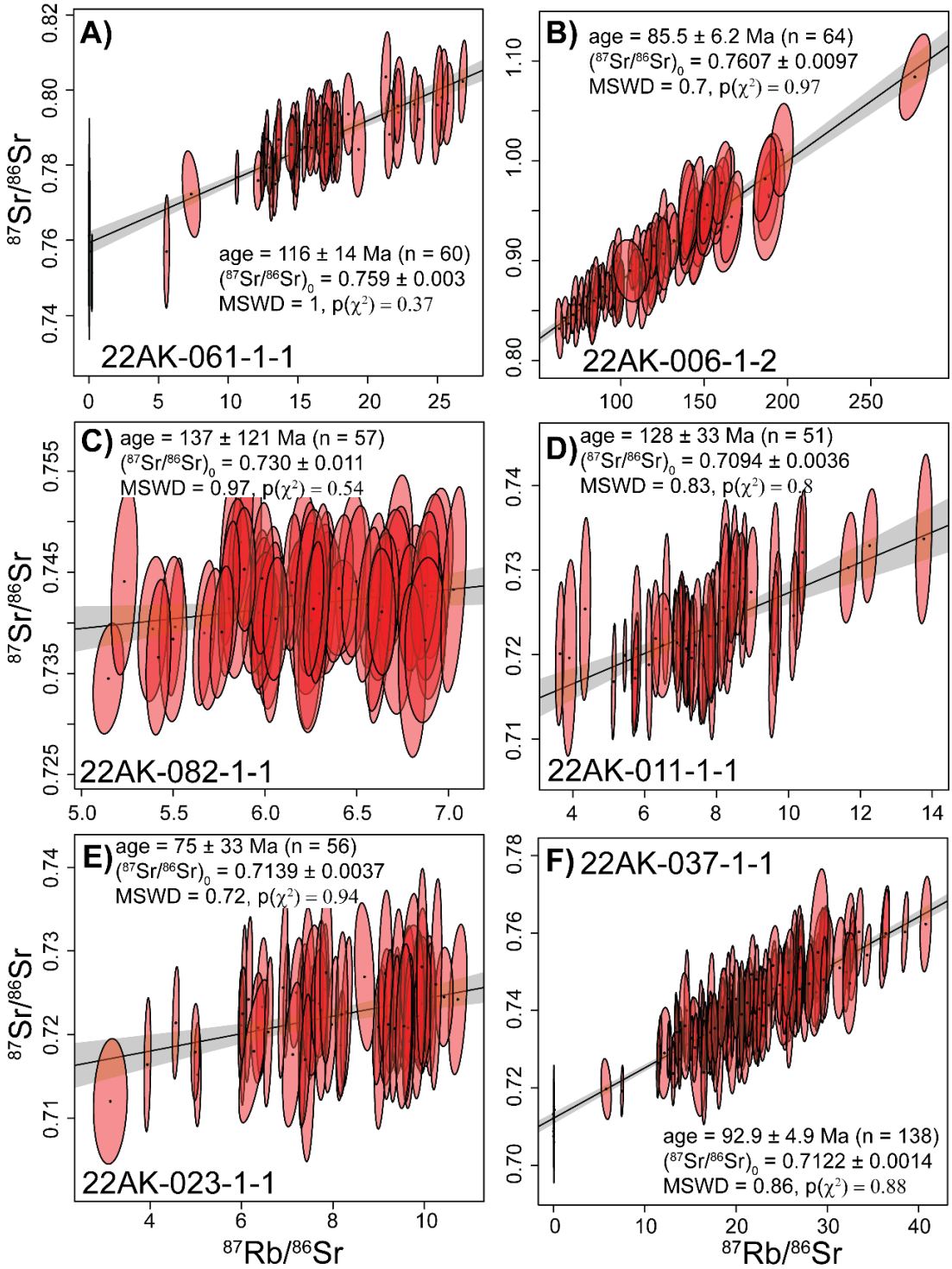


Figure 4.23: Isochron plots for 6 samples (labelled), with outliers removed. Plots generated with IsoplotR (Vermeesch, 2018).

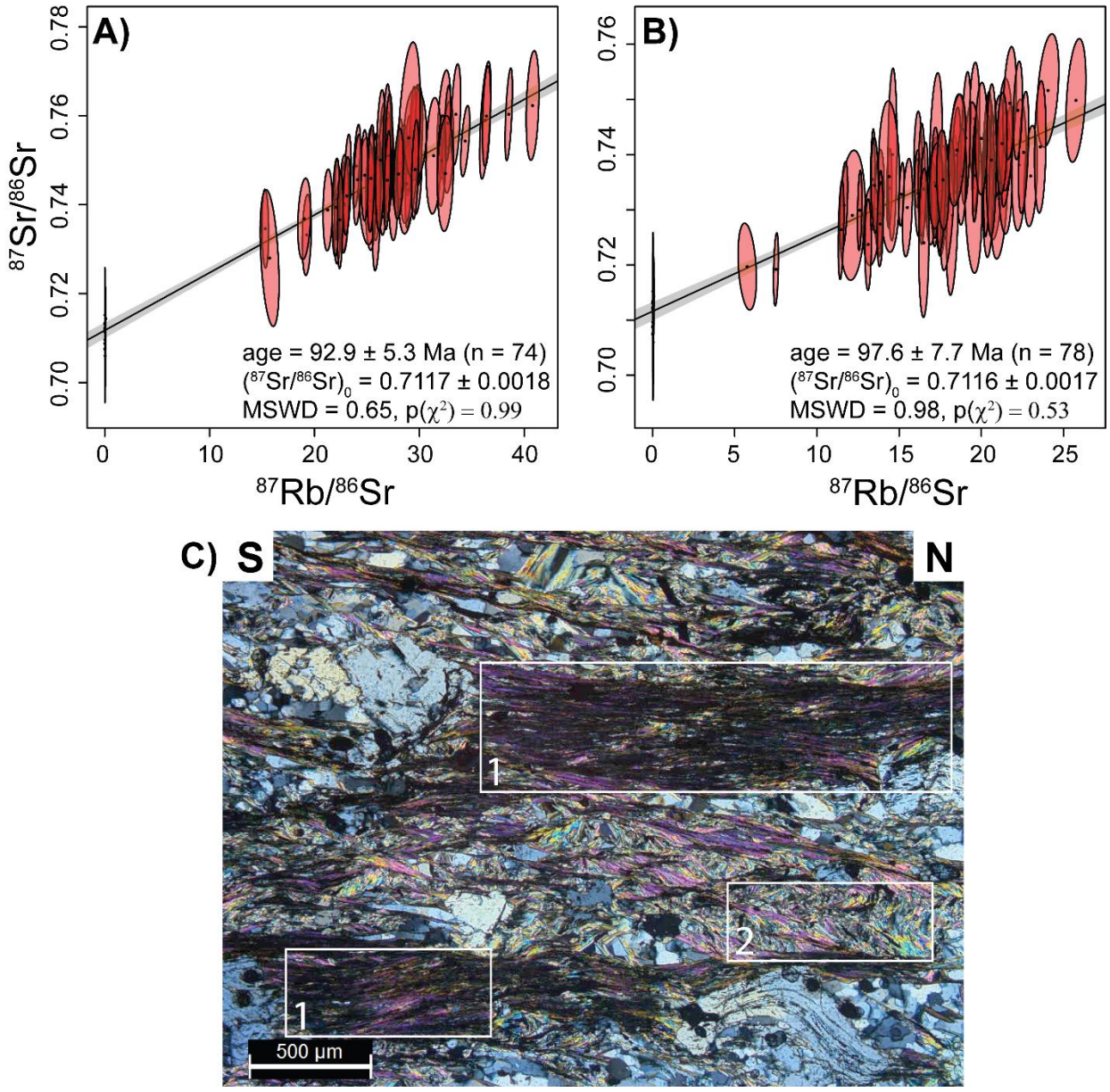


Figure 4.24: Sample 22AK-037-1-1 populations of white mica targeted shown in C) in XPL and their corresponding isochrons shown in A) (1) and B) (2). Isochron plots made using IsolpotR (Vermeesch, 2018).

4.3.2 $^{40}Ar/^{39}Ar$ Dating

In situ $^{40}Ar/^{39}Ar$ geochronologic data were collected on foliation-defining white mica in five samples to provide additional geochronological information. The $^{40}Ar/^{39}Ar$ reported dates in Figure 4.25 are derived using the weighted mean function in IsoplotR (Vermeesch, 2018) of the individual spot dates of the sample after removing outliers (Table 4.1). Outliers were determined by factoring in geologically implausible dates (e.g., 1027 Ma), insufficient volume of ablated

materials resulting in ^{40}Ar and ^{39}Ar contents of a different magnitude and considering a cutoff of 53% radiogenic ^{40}Ar. Uncertainties are reported at two standard errors of the mean (absolute). The weighted mean dates are presented for statistical purposes only, as geological significance is attributed to the maximum and minimum spot dates for each sample. As above, the results are discussed from south to north across the field area.

White mica in sample 22AK-061-1-1, a quartz grit schist from the hanging wall of the RST (Fig. 4.1), yielded a weighted mean spot date of 105.97 +/- 0.88 Ma (MSWD = 25, n = 10) (Fig. 4.25A). The maximum and minimum spot dates are 119.3 +/- 1.4 Ma and 97.2 +/- 1.6 Ma, respectively. Farther north, and structurally lower, 6 analyses of white mica in sample 22AK-060-1-1, a graphitic schist collected from the footwall of the RST (Fig. 4.1), define a weighted mean date of 103.9 +/- 1.6 Ma (MSWD = 4.9) (Fig. 4.25B). The maximum spot date is 110.9 +/- 2.1 Ma and the minimum is 99.3 +/- 2.4 Ma. Sample 22AK-082-1-1 is a quartz grit schist from the footwall of the RST, collected about 7 km away from sample 22AK-060-1-1 on Sourdough Hill (Fig. 4.1). The weighted mean of 20 *in situ* spot analyses corresponds to a date of 99.26 +/- 0.71 Ma (MSWD = 22, n = 20) (Fig. 4.25C). The sample has a maximum spot date of 118.1 +/- 4.5 Ma and a minimum spot date of 88.3 +/- 2.0 Ma. The dates from these three samples, taken together, broadly form two populations with an older grouping between ca. 120 to 100 Ma and a younger grouping between 100 to 95 Ma. Farther north, sample 22AK-023-1-1 (a chlorite-sericite schist) yields a weighted mean $^{40}Ar/^{39}Ar$ spot date of 94.5 +/- 0.62 Ma (MSWD = 4.9, n = 8) (Fig. 4.25D). The maximum and minimum spot dates are 96.5 +/- 1.7 Ma and 89.0 +/- 1.2, respectively. Finally, from the northern end of Keno Hill, *in situ* white mica $^{40}Ar/^{39}Ar$ analyses in sample 22AK-037-1-1, a chlorite sericite schist from the foot wall of the RST about 10 km away from sample 22AK-023-1-1 (Fig. 4.1), define a date of 92.75 +/- 0.66 Ma (MSWD = 9.9, n = 10) (Fig. 4.25E). The maximum spot date is 96.8 +/- 0.8 Ma and the minimum spot date is 88.1 +/- 0.7 Ma. Overall, the $^{40}Ar/^{39}Ar$ dates show a general decrease toward the northeast with the 3 samples farther south and structurally higher, showing two date populations as opposed to one.

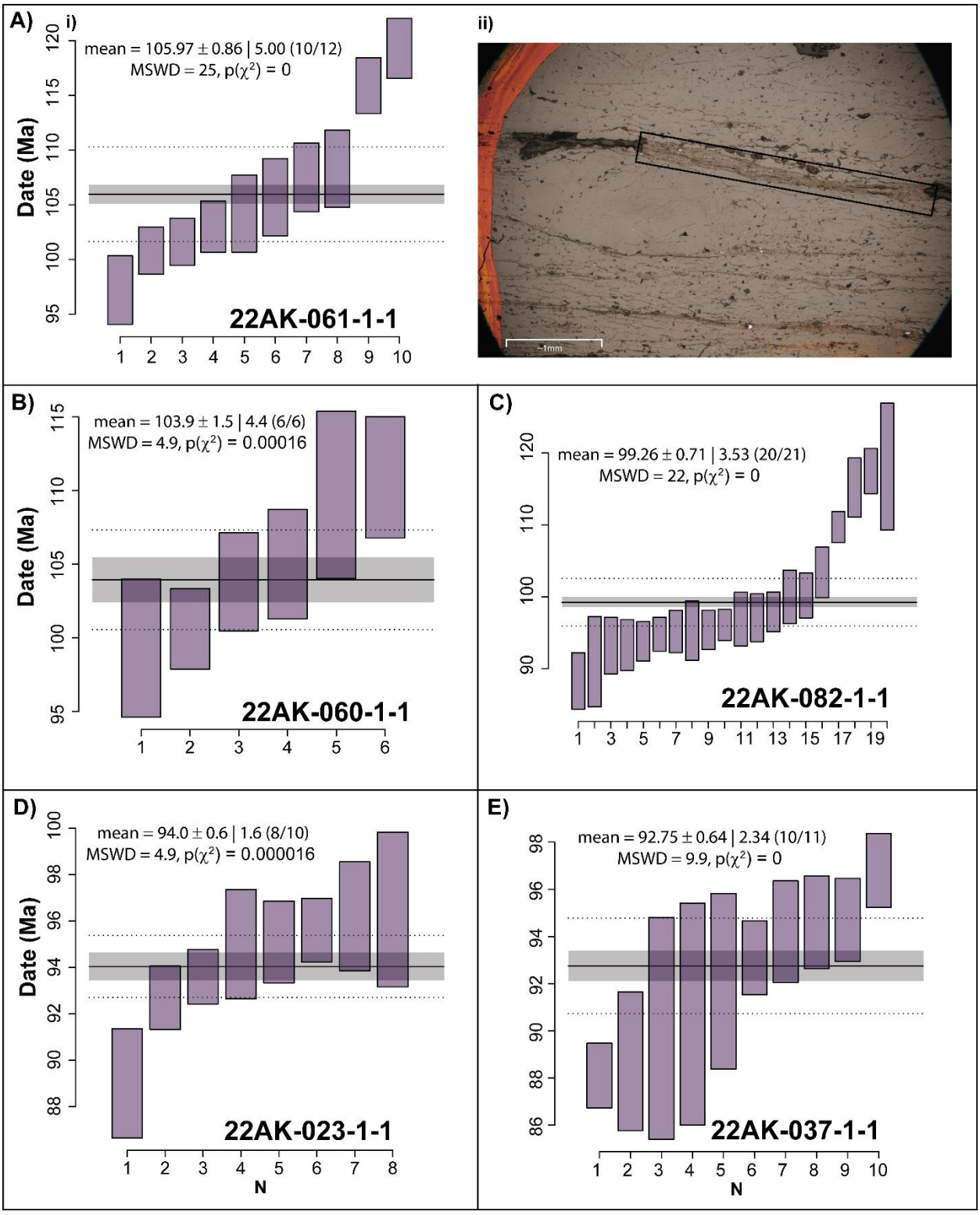


Figure 4.25: $^{40}Ar/^{39}Ar$ weighted mean date plots with outliers removed for: A) i) sample 22AK-061-1-1, with ii) showing an example of targeted mica, B) sample 22AK-060-1-1, C) 22AK-082-1-1, D) 22AK-023-1-1, and E) 22AK-037-1-1. All plots made using IsoplotR (Vermeesch, 2018).

Table 4.1: In situ $^{40}Ar/^{39}Ar$ *results from ultraviolet laser ablation. The rows highlighted in grey outline outliers determined by the criteria outlined above.*

Spot	^{40}Ar	±1σ	^{39}Ar	±1σ	^{38}Ar	±1σ	^{37}Ar	±1σ	^{36}Ar	±1σ	$^{40}Ar^*/^{39}Ar_K$	±1σ	Age	±1σ
22AK-061-1-1														
1	12.6	0.03	3.1	0.01	0.04	0.02	0.008	0.014	0.000	0.000	4.07	0.05	119.3	1.4
2	9.1	0.03	2.4	0.01	0.03	0.01	-0.006	0.012	0.002	0.000	3.59	0.06	105.7	1.8
3	15.2	0.03	3.4	0.01	0.03	0.01	-0.008	0.013	0.006	0.000	3.95	0.04	115.9	1.3
4	12.2	0.03	3.2	0.01	0.01	0.02	-0.020	0.013	0.003	0.000	3.50	0.04	103.0	1.2
5	9.4	0.03	2.5	0.01	0.01	0.01	0.001	0.013	0.001	0.000	3.65	0.06	107.5	1.6
6	8.9	0.03	2.2	0.01	0.03	0.01	-0.030	0.013	0.002	0.000	3.68	0.06	108.3	1.8
7	13.0	0.03	2.9	0.01	0.02	0.01	-0.016	0.013	0.011	0.001	3.30	0.06	97.2	1.6
8	13.4	0.03	3.7	0.01	0.05	0.01	0.032	0.013	0.002	0.000	3.45	0.04	101.6	1.1
9	16.2	0.03	2.6	0.01	0.06	0.01	-0.015	0.013	0.026	0.001	3.28	0.07	96.8	2.0
10	4.6	0.03	0.8	0.01	0.03	0.01	0.031	0.012	0.008	0.000	2.95	0.18	87.4	5.2
11	12.6	0.03	3.6	0.01	0.05	0.02	0.020	0.013	0.001	0.000	3.42	0.04	100.8	1.1
12	9.0	0.03	2.1	0.01	0.00	0.02	0.020	0.013	0.005	0.000	3.55	0.06	104.2	1.8
22AK-060-1-1														
1	6.4	0.03	1.5	0.01	0.01	0.02	0.013	0.012	0.002	0.000	3.74	0.10	109.7	2.9
2	7.3	0.03	1.8	0.01	0.04	0.01	0.037	0.013	0.003	0.000	3.78	0.08	110.9	2.1
3	8.6	0.03	2.3	0.01	0.02	0.02	-0.021	0.013	0.001	0.000	3.54	0.06	103.8	1.7
4	9.6	0.03	2.7	0.01	0.01	0.01	0.005	0.012	0.002	0.000	3.42	0.05	100.6	1.4
5	7.2	0.03	1.9	0.01	0.01	0.01	-0.008	0.013	0.002	0.000	3.58	0.07	105.0	1.9
6	6.6	0.03	1.6	0.01	0.00	0.01	-0.017	0.012	0.004	0.000	3.38	0.08	99.3	2.4
22AK-082-1-1														
1	17.5	0.03	3.1	0.01	0.02	0.02	0.011	0.013	0.026	0.001	3.16	0.06	93.3	1.8
2	22.7	0.03	3.3	0.01	0.08	0.01	-0.004	0.013	0.032	0.001	4.01	0.06	117.5	1.6
3	7.9	0.04	1.1	0.01	0.02	0.01	-0.009	0.012	0.012	0.001	4.03	0.16	118.1	4.5
4	8.7	0.03	2.3	0.01	0.03	0.02	-0.013	0.013	0.003	0.000	3.39	0.07	100.0	1.9
5	8.3	0.03	2.2	0.01	0.02	0.02	0.036	0.013	0.005	0.001	3.23	0.07	95.3	2.1
6	9.2	0.03	2.1	0.01	0.03	0.02	0.007	0.013	0.010	0.000	2.98	0.07	88.3	2.0
7	8.9	0.03	2.4	0.01	0.04	0.01	0.029	0.011	0.004	0.000	3.28	0.07	96.9	1.9
8	6.2	0.03	1.5	0.01	0.04	0.02	0.027	0.013	0.006	0.001	3.08	0.11	91.0	3.2
9	174.5	0.04	3.7	0.01	0.03	0.01	-0.020	0.012	0.013	0.001	45.70	0.17	1027.8	2.8
10	9.7	0.03	2.7	0.01	0.03	0.01	0.004	0.013	0.003	0.000	3.29	0.06	97.1	1.7
11	11.0	0.03	3.2	0.01	0.06	0.01	0.012	0.013	0.003	0.000	3.23	0.05	95.4	1.4
12	16.0	0.03	4.4	0.01	0.04	0.01	-0.021	0.013	0.005	0.001	3.25	0.04	96.1	1.1
13	9.1	0.03	2.4	0.01	0.03	0.02	0.019	0.013	0.002	0.000	3.51	0.06	103.4	1.8
14	15.6	0.03	3.2	0.01	0.06	0.02	0.026	0.013	0.016	0.001	3.40	0.05	100.2	1.6
15	22.3	0.03	4.7	0.01	0.05	0.01	0.010	0.013	0.016	0.001	3.73	0.04	109.7	1.1
16	15.1	0.03	3.4	0.01	0.04	0.01	-0.004	0.013	0.014	0.001	3.17	0.05	93.8	1.4
17	17.3	0.03	4.2	0.01	0.05	0.01	-0.012	0.012	0.013	0.001	3.21	0.04	94.8	1.2
18	9.7	0.03	2.4	0.01	0.05	0.01	-0.034	0.013	0.007	0.001	3.16	0.07	93.2	2.0
19	13.7	0.03	3.1	0.01	0.03	0.01	0.005	0.013	0.012	0.001	3.22	0.05	95.2	1.5
20	16.6	0.04	3.7	0.01	0.08	0.01	-0.010	0.013	0.015	0.001	3.32	0.05	97.9	1.4

Spot	^{40}Ar	±1σ	^{39}Ar	±1σ	^{38}Ar	±1σ	^{37}Ar	±1σ	^{36}Ar	±1σ	$^{40}Ar^*/^{39}Ar_K$	±1σ	Age	±1σ
21	15.9	0.03	2.5	0.01	0.02	0.01	0.001	0.012	0.021	0.001	3.92	0.07	115.2	2.1
22AK-023-1-1														
1	3.3	0.03	0.9	0.01	0.01	0.01	-0.005	0.013	0.001	0.000	3.39	0.18	100.0	5.1
2	12.4	0.03	2.7	0.01	0.04	0.01	-0.027	0.013	0.012	0.001	3.27	0.06	96.5	1.7
3	18.1	0.03	4.2	0.01	0.05	0.01	-0.023	0.014	0.016	0.001	3.22	0.04	95.0	1.2
4	16.2	0.03	4.8	0.01	0.08	0.01	0.047	0.013	0.002	0.000	3.22	0.03	95.1	0.9
5	11.9	0.03	3.5	0.01	0.05	0.01	-0.011	0.014	0.001	0.000	3.26	0.04	96.2	1.2
6	7.7	0.03	2.3	0.01	0.03	0.02	-0.007	0.013	0.002	0.000	2.99	0.06	88.4	1.6
7	18.7	0.03	5.6	0.01	0.05	0.01	-0.004	0.012	0.003	0.000	3.14	0.02	92.7	0.7
8	14.0	0.03	3.8	0.01	0.04	0.01	0.028	0.012	0.009	0.001	3.01	0.04	89.0	1.2
9	19.0	0.03	5.7	0.01	0.06	0.01	0.006	0.013	0.002	0.000	3.24	0.03	95.6	0.7
10	22.2	0.03	6.8	0.01	0.10	0.02	0.014	0.013	0.002	0.000	3.17	0.02	93.6	0.6
22AK-037-1-1														
1	6.8	0.03	1.8	0.01	0.01	0.01	-0.025	0.014	0.004	0.000	3.07	0.08	90.7	2.4
2	11.9	0.03	3.0	0.01	0.03	0.01	-0.015	0.012	0.010	0.000	3.00	0.05	88.7	1.5
3	16.6	0.03	2.7	0.01	0.05	0.01	0.010	0.013	0.028	0.001	3.06	0.07	90.3	2.0
4	9.6	0.03	2.5	0.01	0.03	0.01	0.019	0.012	0.006	0.001	3.12	0.06	92.1	1.9
5	22.5	0.03	6.6	0.01	0.07	0.02	-0.005	0.013	0.009	0.001	2.98	0.02	88.1	0.7
6	15.8	0.03	4.7	0.01	0.05	0.02	0.015	0.012	0.002	0.000	3.21	0.03	94.7	0.9
7	7.8	0.03	1.9	0.01	0.03	0.02	0.011	0.013	0.007	0.001	3.05	0.08	90.1	2.4
8	19.5	0.03	5.1	0.01	0.08	0.01	-0.005	0.012	0.011	0.001	3.20	0.03	94.6	1.0
9	19.4	0.03	4.6	0.01	0.06	0.02	0.007	0.012	0.016	0.001	3.19	0.04	94.2	1.1
10	19.0	0.03	5.4	0.01	0.08	0.01	-0.004	0.012	0.005	0.001	3.28	0.03	96.8	0.8
11	27.4	0.03	6.3	0.01	0.07	0.02	-0.024	0.012	0.025	0.001	3.15	0.03	93.1	0.8

4.4 THERMOMETRY

Carbonaceous material within the samples collected was analysed using Raman spectroscopy. Examples of the carbonaceous material targeted, as well as the raw and background-corrected processed spectra, for specimens 22AK-055-2-1 and 22AK-052-1-1 are shown in Figure 4.27. Spectra for the D1 (1350 cm^{-1}) and G (1580 cm^{-1}) bands (see methods section) were collected for each specimen, with some also showing a D2 band (1620 cm^{-1}). The average D1, G, and D2 peak positions for each specimen are reported in Table 4.4 with one standard deviation and associated number of spots (the amount of targetable material within each sample limited the total number of spot analyses that could be collected).

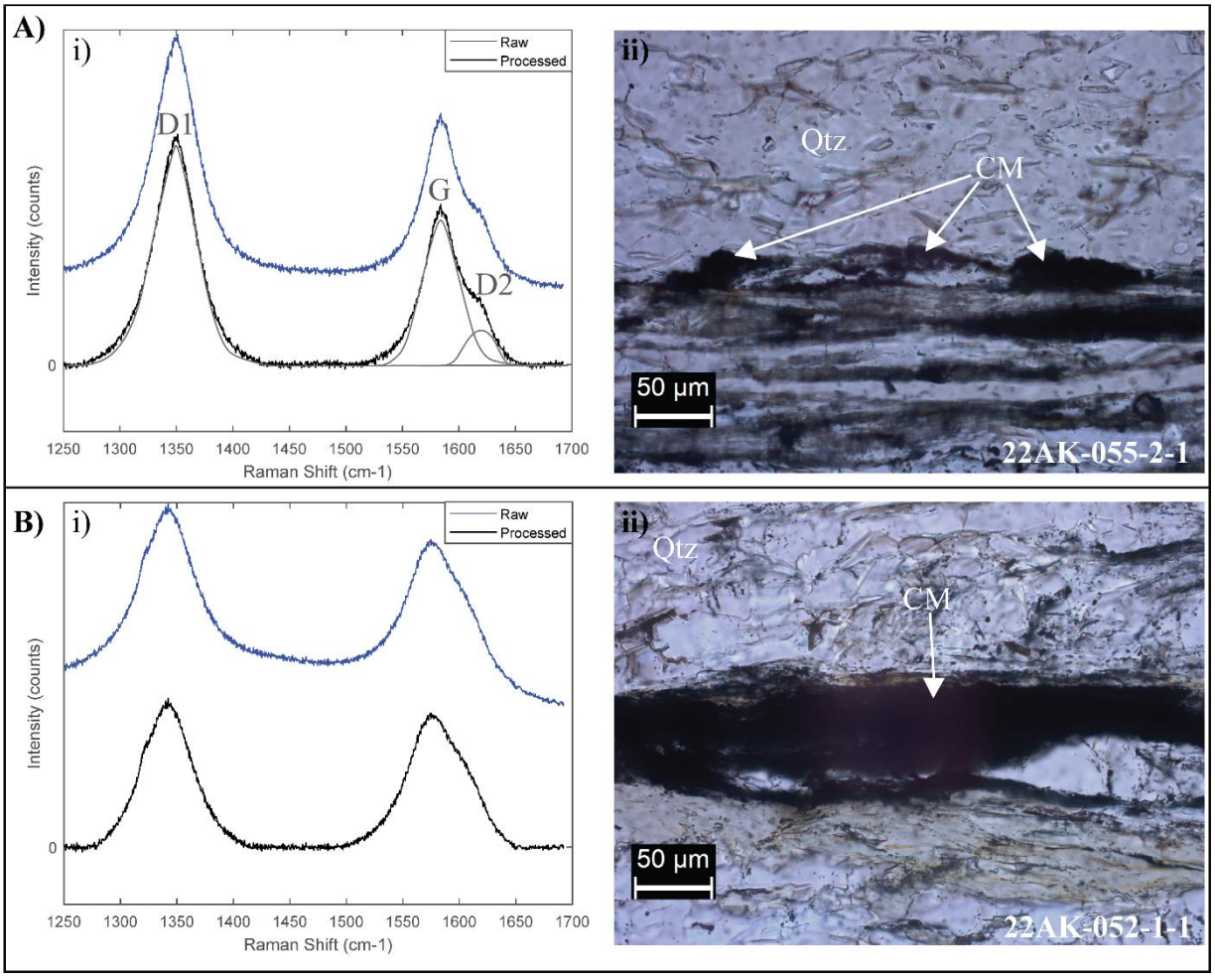


Figure 4.26: Carbonaceous material spectra in i) of both and A) and B), with an example of carbonaceous material from the respective thin section (PPL) in ii) for both A and B.

Apart from sample 22AK-079-1-1, samples in which there was no detectable D2 band had a G position that was higher than 1580cm^{-1}. The peak intensity ratio (R1) and the peak area ratio (R2) were calculated for each specimen and reported with one standard deviation in Table 4.2, following the method of Beyssac et al. (2002). Peak temperatures were also calculated following (Beyssac et al., 2002) as:

$$T\ (°C) = -445(R2) + 641 \quad (5)$$

The resulting temperatures are presented alongside the R1 and R2 ratios in Table 4.3.

Samples collected from the hanging wall of the RST (22AK-061-1-1, 22AK-006-1-2, and 22AK-079-1-1) (Fig. 4.1) are characterized by lower R1 and R2 ratios and higher temperatures (456 to 588 °C) than the other investigated samples. Moving northeast from these samples, the first samples in the footwall (22AK-060-1-1, and 22AK-001-1-1, and 22AK-080-1-1; Fig. 4.1) are characterized by slightly higher R1 and R2 ratios and lower temperatures (400 to 507 °C) than the other investigated samples. Apart from sample 22AK-082-1-1 on Sourdough Hill, the general trend of increasing R1 and R2 ratios and decreasing temperatures towards the northeast holds across the field area, even with some overlapping uncertainties. The samples with the lowest calculated temperatures and highest R1 and R2 ratios are from Bunker Hill (Fig. 4.1). However, moving northward from Bunker Hill, the carbonaceous material in the samples decrease in R1 and R2 ratios and increase in temperature. The higher temperatures and lower R1 and R2 ratios farther north are apparent in the samples on Keno Hill (22AK-029-1-1, 22AK-037-1-1, and 22AK-073-1-1 (Table 4.3; Fig. 4.1)). Overall, without uncertainties, the peak metamorphic temperature ranges from 398-545 °C (average ~ 475 °C) and shows a general decrease away from the RST, except for the structurally lowest sample (Fig. 4.27).

Table 4.2: Average G, D1, and D2 position reported with one standard deviation and the corresponding number of spots targeted per thin section as well as the number of D2 peaks observed. Samples are listed in order of relative structural position.

Sample	n	G	1σ	D1	1σ	D2	1σ	n (D2)
22AK-079-1-1	12	1577	3.75	1345	3.68	1614	4.40	6
22AK-061-1-1	11	1586	4.41	1343	7.72	1623	8.89	6
22AK-006-1-2	10	1584	4.95	1345	3.92	1611	2.57	2
22AK-001-1-1	11	1583	3.59	1351	3.18	1621	2.96	11
22AK-080-1-2	11	1581	5.59	1346	4.87	1617	3.91	10
22AK-072-1-2	12	1584	1.29	1351	1.44	1620	1.59	12
22AK-082-1-1	12	1585	2.03	1349	4.08	1622	5.85	7
22AK-045-2-1	11	1581	5.13	1348	3.95	1617	4.18	11
22AK-060-1-1	12	1581	3.99	1348	2.90	1616	3.34	12
22AK-049-1-1	11	1580	4.19	1345	3.81	1616	3.65	11
22AK-052-1-1	12	1580	3.33	1344	2.59	1616	2.88	12
22AK-055-2-1	12	1582	3.63	1348	2.94	1618	3.15	12
22AK-029-1-1	8	1585	4.25	1344	4.66	1616	1.22	2
22AK-037-1-1	9	1587	4.24	1338	4.85	1606	-	1
22AK-073-1-1	9	1585	1.97	1352	1.64	1620	2.07	9
22AK-081-1-2	12	1580	1.22	1351	3.26	1617	4.22	10

Table 4.3: Peak intensity ratio (R1), peak area ratio (R2) and temperature (°C) reported with one standard deviation for each sample. Samples are listed in order of relative structural position.

Sample	R1	1σ	R2	1σ	T (°C)	1σ
22AK-079-1-1	0.59	0.12	0.35	0.07	486	30
22AK-061-1-1	0.53	0.13	0.28	0.06	518	25
22AK-006-1-2	0.36	0.18	0.27	0.10	545	43
22AK-001-1-1	0.76	0.19	0.40	0.10	464	43
22AK-080-1-2	0.75	0.17	0.40	0.09	463	39
22AK-072-1-2	0.99	0.20	0.49	0.05	422	22
22AK-082-1-1	0.50	0.26	0.25	0.13	532	57
22AK-045-2-1	0.93	0.16	0.47	0.06	434	27
22AK-060-1-1	0.68	0.13	0.39	0.05	467	23
22AK-049-1-1	0.78	0.17	0.41	0.06	456	28
22AK-052-1-1	1.22	0.18	0.50	0.04	417	19
22AK-055-2-1	1.24	0.19	0.55	0.04	398	20
22AK-029-1-1	0.67	0.28	0.36	0.12	482	54
22AK-037-1-1	0.40	0.18	0.24	0.08	532	34
22AK-073-1-1	0.65	0.09	0.36	0.04	483	17
22AK-081-1-2	0.24	0.11	0.26	0.08	527	34

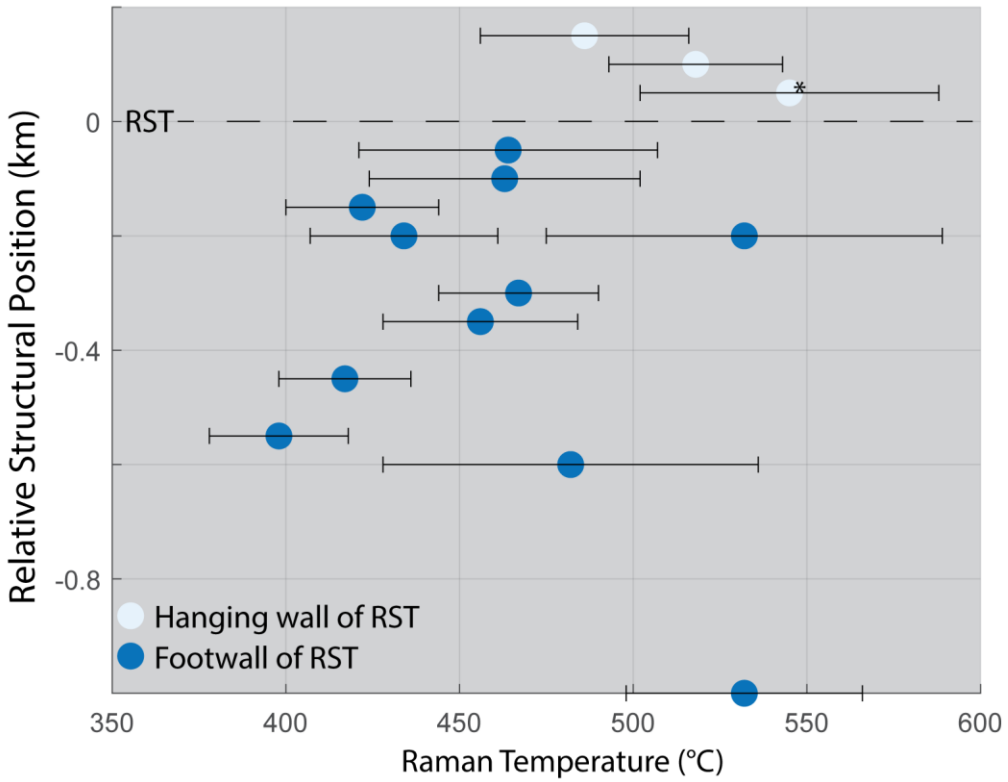


Figure 4.6: Raman spectroscopy of carbonaceous material (RSCM) temperature plotted alongside relative structural position of the samples.

5 INTERPRETATIONS

5.1 STRUCTURAL FRAMEWORK

The new field observations and data from the present work, along with the 1:5000 scale mapping of Read et al. (2020), inform a schematic geologic cross-section (Fig. 5.1). In cross-section, isoclinal folds (F_1) are depicted as having initiated prior to thrusting. This interpretation is informed by observations of outcrop-scale isoclinal folds that are truncated by curvy-planar thrust faults (Fig. 4.4A). Moreover, some of the thrust faults have drag folds in the hanging wall with the same orientation as the isoclinal folds; the similar geometry may indicate that thrusting transposed isoclinal folding. Furthermore, the geochronology data highlights a break in dates across the approximate Robert Service Thrust (RST) which could indicate that thrusting occurred after the isoclinal folding event, as the rocks in the hanging wall and footwall are both isoclinally folded. If the thrusting were to predate the isoclinal folding event, the geochronology data would not necessarily show a break in dates across the RST. Finally, field evidence (Fig. 4.3) indicates that the open folding (F_2) event and associated crenulation lineation overprint the isoclinal folding event at the metre-scale (schematically depicted in Fig. 5.1).

Klippe on Sourdough Hill

The schematic cross-section in Fig. 5.1 and geologic map in Fig. 4.1 depicts a klippe of the RST on Sourdough Hill. This depiction is based on previous mapping (Murphy and Roots, 1996; Read et al., 2020), but, as previously stated, the quartz grit schist units from both the hanging wall and the footwall of the RST on Sourdough Hill are nearly indistinguishable in the field and in thin section. As such, the data presented in Fig. 5.2 are projected with the samples' relative structural position both if a klippe does occur at Sourdough Hill and if there is no klippe on Sourdough Hill (see Figure caption).

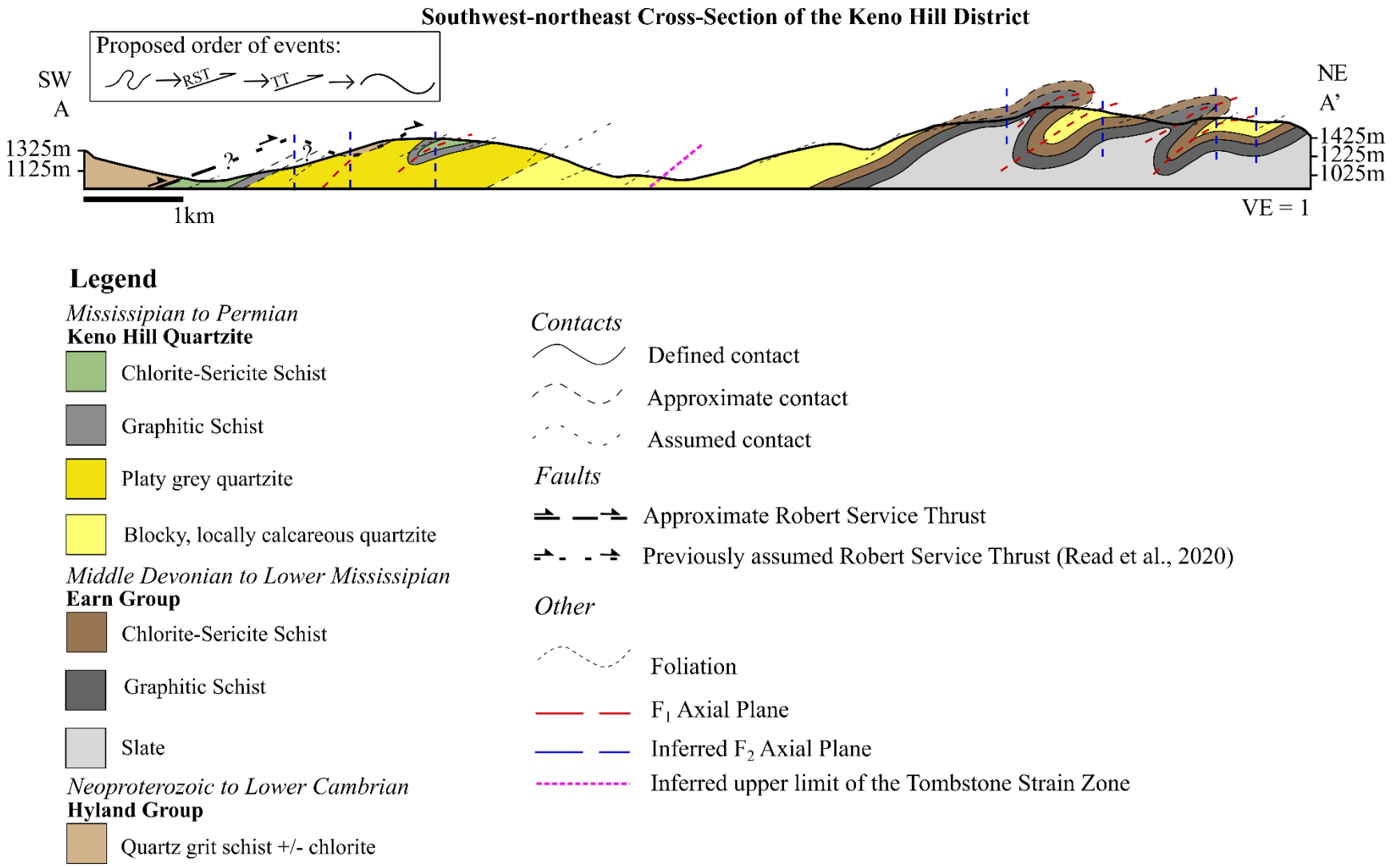


Figure 5.1: Schematic geologic cross-section of the Keno Hill area along the A-A' transect presented in the geologic map in Figure 4.1.

5.2 MICROTECTONICS

5.2.1 Microstructures

The dominant quartz microstructures observed across the field area appear to record subgrain rotation recrystallization (Passchier & Trouw, 2005) (i.e., small equant grains moating larger, more elongate grains). Subgrain rotation recrystallization is the dominant recrystallization mechanism in quartz under moderate temperatures of ~400-500 °C (Stipp et al., 2002).

The size and shape of the quartz grains varies across the field area. In rocks close to the trace of the Robert Service Thrust (RST), quartz occurs as large grains (~20 µm – 2 mm), often exhibiting polygonal shapes and triple junctions. The shapes of the grains are consistent with grain boundary area reduction (GBAR), indicating the samples underwent static recrystallization after deformation (Passchier & Trouw, 2005). In contrast, samples collected closer to the approximate trace of the Tombstone Thrust (TT) (such as those from Keno Hill), consistently have smaller (~10 – 500 µm), more interlobate quartz grains (Fig. 4.10). The decrease in apparent GBAR in proximity to the TT (Fig. 5.2) is interpreted to indicate that the structurally shallower TT was active/reactivated more recently than the RST under lower temperatures. This interpretation is based on GBAR often outlasting deformation and is further supported by the younger $^{87}Rb/^{87}Sr$ and $^{40}Ar/^{39}Ar$ dates farther north. As the TT underlies the RST and resides closer to the foreland basin, more recent movement along the TT would indicate in-sequence thrusting (Fossen, 2016). Post-RST (re)activation of the TT could also be consistent with local overprinting related to the Tombstone strain zone (TSZ), as suggested by previous work in the study area (Murphy, 1997; Roots, 1997).

5.2.2 Quartz CPOs

Distribution Type

Quartz crystallographic preferred orientations (CPOs) across the field area are primarily single girdles, consistent with non-coaxial strain (Heilbronner & Tullis, 2006; Hunter et al., 2018). Some samples from the area yield Type I (e.g. Lister & Hobbs, 1980) or Type II (e.g. Schmid & Casey, 1986) crossed girdle distributions, which have been interpreted to reflect plane strain and a component of constrictional strain, respectively (e.g. Lister & Hobbs, 1980; Xypolias et al., 2013).

There does not, however, appear to be a pattern in the spatial variation of the strain geometry interpreted from the CPO pattern (Fig. 4.12).

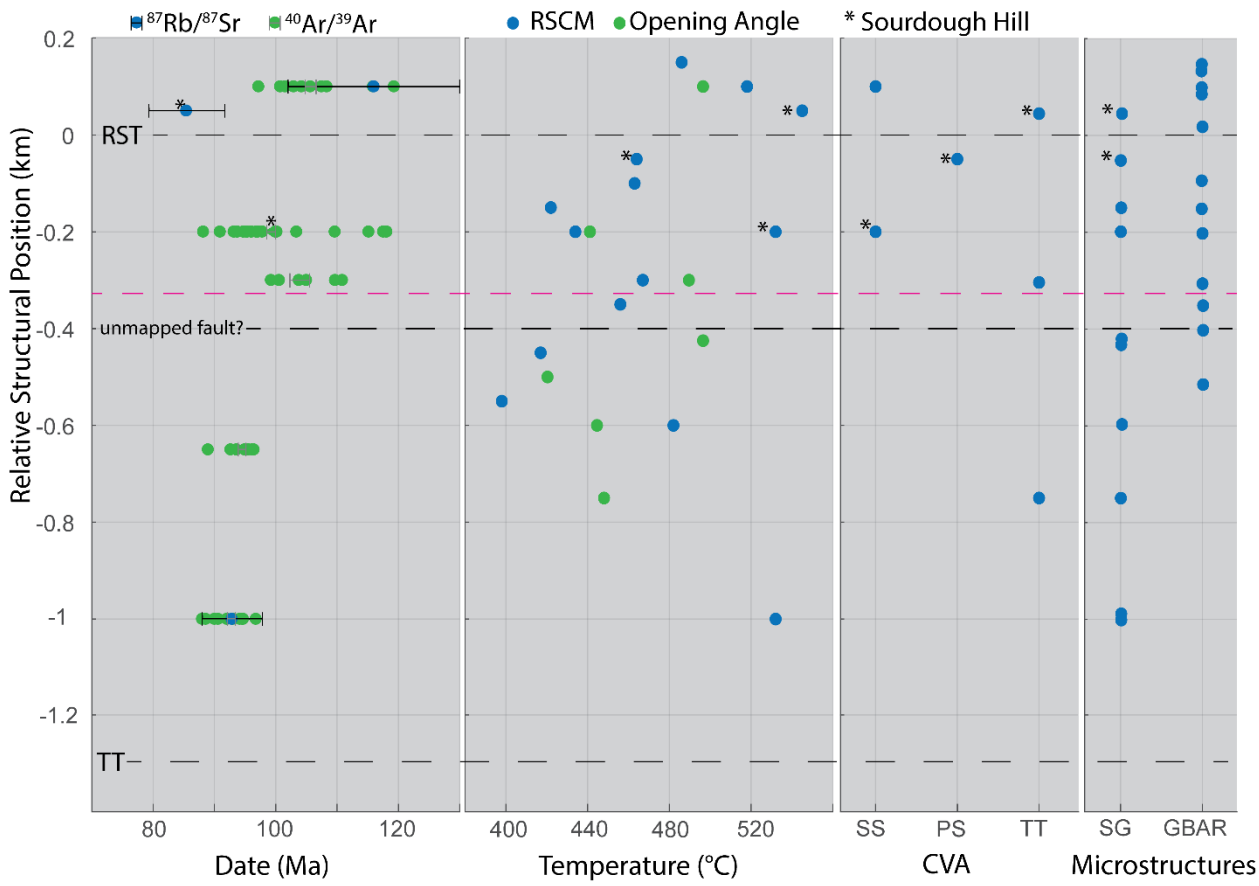


*Figure 5.2: Spatial variations of in situ geochronology dates ($^{40}Ar/^{39}Ar$ laser spot dates and $^{87}Rb/^{87}Sr$ sample dates), temperatures (Raman spectroscopy of carbonaceous material = RSCM), CVAs (Simple Shear = SS; Pure Shear = PS; and Transtension = TT), and microstructures (subgrain rotation dominant = SG; grain boundary area reduction = GBAR). The error bars on the geochronology data represent two standard error (absolute) of the statistical mean of the sample (for both $^{87}Rb/^{87}Sr$ and $^{40}Ar/^{39}Ar$). The * refers to samples collected on Sourdough Hill, with the pink dashed line representing the relative structural position the samples would lie below if the klippe is not there. The location of the Robert Service Thrust (RST), Tombstone Thrust (TT), and a potential unmapped fault are depicted with a dashed line.*

Slip Systems

Quartz slip systems can be used to estimate the approximate temperature of deformation, assuming the samples were exposed to similar other factors, such as strain rate, strain magnitude, and fluids (Passchier & Trouw, 2005). Quartz has four dominant slip systems as illustrated in Figure 5.3A. Slip systems can be interpreted following the keys presented in Figure 4.12 for quartz *c*-axis equal area pole figures, and Figure 5.3B for low angle misorientation inverse pole figures. Interpreting slip systems from misorientation axes requires that each slip system has a unique rotational axis within the crystal lattice (Neumann, 2000; Piette-Lauzière et al., 2020). In this

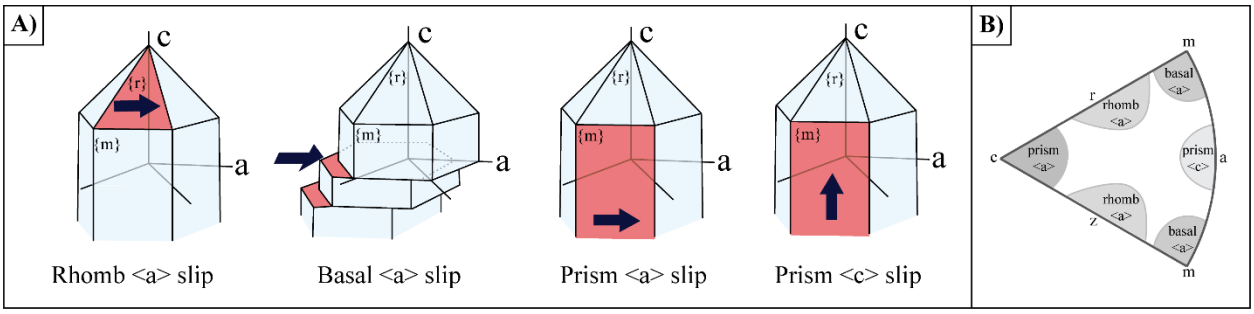


Figure 5.3: A) Quartz slip systems (modified from Fossen (2016)). B) Misorientation axes inverse pole figure slip system key (modified and simplified from Piette-Lauzière et al. (2020)).

study, the Fabric Analyser, electron backscatter diffraction (EBSD) quartz *c*-axis CPO plots, and the low angle misorientation inverse pole figures (Fig. 4.12, 4.16-4.22) demonstrate a combination of prism <a>, rhomb <a>, minor basal <a>, and in some cases prism <c> slip systems. While previous studies have noted a relationship between the activation of prism <c> slip and temperatures exceeding 650 °C (e.g., Mainprice et al., 1986), there are numerous factors (such as water weakening, grain size reduction, low strain rate, or mechanical rotation of lineation-parallel elongate quartz grains (e.g., Larson et al., 2014)) that can favour activation of the prism <c> slip system (Zuo et al., 2021). The predominant activation of the prism <a> slip system in the recrystallized grains is consistent with deformation temperatures of 400-500 °C (Passchier & Trouw, 2005).

Opening Angles

Kruhl (1998) noted the approximately linear relationship of the opening angle in crossed girdle *c*-axis patterns and temperature across approximately greenschist to amphibolite facies (~300 to 700 °C). This relationship is thought to reflect the shift in dominant slip systems near the primitive of the plots from mainly basal <a> toward prism <c> slip. The relationship between temperature and opening angle is not precise, and as such has an absolute uncertainty of +/- 50 °C to account for natural variability in strain rate, hydrolytic weakening, and other compounding variables (Kruhl, 1998). For this study, opening angle temperature estimates were calculated using the equation:

$$\mathrm{T}\ (°\mathrm{C}) = 6.9\ OA(\mathrm{degrees}) + 48, \qquad (6)$$

for 250°C ≤ T ≤ 650°C and OA ≤87° proposed by Faleiros et al. (2016), wherein temperatures have a linear relationship with opening angles, independent of pressure. The temperatures derived from this equation range from ~420-500 °C using opening angles measured (Fig. 4.12) in the

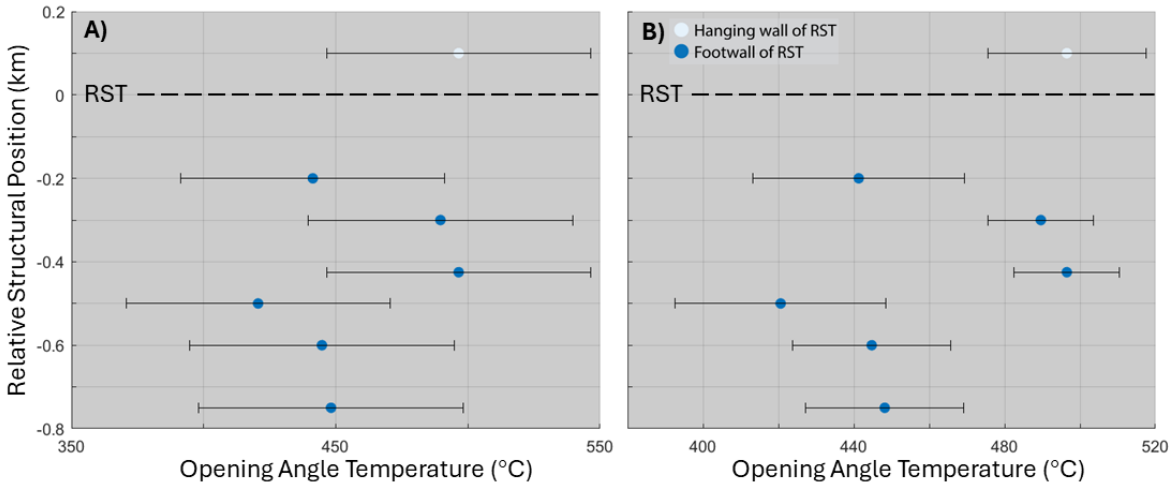


Figure 5.4: CPO opening angle temperature estimates plotted alongside relative structural position in relation to the RST showing A) absolute, and B) relative uncertainties.

samples. With the proposed uncertainty, there is no resolvable difference across the field area when considering full absolute uncertainties (Fig. 5.4A). However, assuming deformation conditions were similar across the field area, the relative uncertainty between the samples would be significantly smaller (i.e., 14 to 28 °C; e.g., Fraser et al., 2000; Fig. 5.4B). The uncertainties presented in Figure 5.4B are based on the difference in temperature as calculated from the largest and smallest measured opening angle (of the two defined by the distribution) and/or the estimated uncertainty in the measurement of the opening angles (when the two opening angles are approximately equal). In Figure 5.4 the upward decreasing temperature gradient beginning at a structural height of -0.4 km, resembles the pattern observed in Figure 4.27 (i.e., increase in RSCM temperature at around -0.4 km; Fig. 5.2). The similar trends could indicate an unmapped structure within the field area, possibly within the blocky quartzite unit.

5.2.3 Quartz Crystallographic Vorticity Axes

CVAs with point maxima at the centres of stereographic projections (22AK-061-1-1 and 22AK-082-1-1) are consistent with simple shear-dominant, monoclinic strain. In contrast, CVAs with maxima at the E-W poles of the stereographic projections (22AK-001-1-1) indicate pure shear-dominant, monoclinic strain (Michels et al., 2015). Finally, CVAs with maxima located at the N-S poles of the plot (22AK-060-1-1, 22AK-060-1-1 and 22AK-032-1-2) indicate transtensional strain (Brown, 2022). While there is apparent heterogeneity in flow as recorded by the CVAs across the field area, the lack of spatial relationships of the CVA orientations (Fig. 5.2) in the region may reflect partial overprinting by later deformation (e.g. Piette-Lauzière et al.,

2020), or that the vorticity axis did not maintain a constant orientation throughout deformation, which could reflect triclinic flow (e.g., Jiang & Williams, 1998).

5.3 GEOCHRONOLOGY

The *in situ* $^{87}Rb/^{87}Sr$ dates from samples 22AK-082-1-1, 22AK-011-1-1, and 22AK-023-1-1 have large uncertainties that overlap with all the other investigated samples, and as such their dates cannot be used to provide unique interpretations about the field area. Sample 22AK-061-1-1, from the hanging wall of the RST, yielded an *in situ* $^{87}Rb/^{87}Sr$ date of 116 +/- 14 Ma and an *in situ* $^{40}Ar/^{39}Ar$ date of 105.97 +/- 0.86 Ma. These dates are consistent with an *in situ* $^{87}Rb/^{87}Sr$ date from farther north from the same structural position and lithology (115 +/- 15 Ma on foliation defining white mica and calcite, McQuesten Lake area; D. Skipton, personal communication, April 24, 2024) as well as step-heating and *in situ* $^{40}Ar/^{39}Ar$ dates (ca. 100-104 Ma) from the hanging wall of the RST (Mair et al., 2006). The two date populations in the $^{40}Ar/^{39}Ar$ spot dates could represent two geologic events. The older (~ 117 Ma, in line with the $^{87}Rb/^{87}Sr$ date) could represent mica formation, while the younger date (~ 103 Ma) could represent Ar loss as a result of continuing deformation and/or the introduction of fluids in an open system.

The remaining *in situ* $^{40}Ar/^{39}Ar$ dates from 4 samples show a general decrease in age from southwest (103.9 +/- 1.5 Ma) to northeast (92.75 +/- 0.64 Ma). The maximum and minimum spot date populations range from 115 Ma to 95 Ma in the southwest and from 96 to 88 Ma in the northeast (Fig. 5.2). That trend differs from the *in situ* $^{87}Rb/^{87}Sr$ data, where the youngest date is from a previously inferred RST klippe on Sourdough Hill (85.5 +/- 6.2 Ma; Fig. 4.1), which overlaps in uncertainty with the farthest north sample (22AK-037-1-1; 92.9 +/- 4.9 Ma; Fig. 4.1). Moreover, if the klippe exists, there could be a break in $^{40}Ar/^{39}Ar$ dates (no overlap in the spot dates between adjacent samples along the transect) at around 400m below the approximate trace of the RST (Fig. 5.2). Previous studies have interpreted white mica $^{40}Ar/^{39}Ar$ dates between ca. 98-65 Ma in the area to reflect the timing of regional plutonism and/or the onset of mineralization (Craggs, 2022; McOnie, 2016). Although, in this study, samples were collected farther away from mineralized veins than previous studies (e.g., Craggs, 2022), the chlorite that forms irregular shapes at an angle to foliation could reflect late alteration. Therefore, the dates ranging between ca. 94 to 79 Ma may have been variably affected by fluid alteration associated with mineralization and/or plutonism.

The spatial trends in dates are similar to those of quartz textures, with distinct features (e.g., GBAR dominance) in proximity to the RST compared to the samples farther north and structurally closer to the TT (Fig. 5.2). Given the similarities between the spatial trends defined by geochronology and strain, the older $^{87}Rb/^{87}Sr$ and $^{40}Ar/^{39}Ar$ dates (ca. 117-113 Ma) from samples 22AK-061-1-1, 22AK-060-1-1 and 22AK-082-1-1 could reflect mica growth, possibly around the onset of movement along the RST, whereas the younger population (ca. 105-100 Ma) is interpreted to record dynamic recrystallization and/or cooling associated with the movement along the RST. Additionally, the decrease in evidence for GBAR farther north, apparent heterogeneous strain, and systematically decreasing *in situ* $^{40}Ar/^{39}Ar$ dates from samples 22AK-082-1-1, 22AK-023-1-1, and 22AK-037-1-1 may indicate spatially local, yet progressively increasing structural overprinting toward the TT. If related to the TT, the overprinting could indicate that movement or reactivation along the TT continued until ca. 88 Ma, having caused partial resetting of the white mica in structurally higher samples, with no apparent break in the geochronology data.

5.4 THERMOMETRY

RSCM thermometry shows that samples in the hanging wall of the RST generally have higher average peak temperatures than those collected from the footwall (Fig. 4.27). The systematic decrease in temperature moving down from the approximate trace of RST is interrupted only by a slight apparent increase in temperature at around 0.4 km below the RST before decreasing at structurally lower levels (Fig. 5.2).

RSCM temperatures can increase in proximity to the core of shear zones for a variety of reasons (e.g., focused hydrothermal fluids, strain-induced reorganization, or shear heating). It is unlikely that the approximate linear increase in temperature up structural section observed in footwall samples approaching the trace of the RST can be attributed to hydrothermal fluids as the fluid-rock interactions would most likely not result in a systematic increase in temperatures (Petroccia et al., 2022 and references therein). Nor can the linear progression be attributed to strain-induced reorganization of graphite due to temperatures exceeding 350 °C (Petroccia et al., 2022; Wang et al., 2019). Previous studies have shown that shear heating can increase temperatures by more than 100 °C, dependent on strain rate, convergence rate, and width of shear zone (e.g., Mako & Caddick, 2018). However, in natural shear zones the temperature increase due to shear heating

is likely to be in the range of ~10-60 °C (Petroccia et al., 2022 and references therein), which is consistent with the RSCM temperature gradient of the current study.

While the general decrease in temperature down structurally from the RST observed in this study could reflect a decrease in shear heating away from the RST, additional data from farther south/southwest into the hanging wall of the RST are needed to verify whether there is a mirrored systematic decrease at structurally higher levels. If the hanging wall of the RST showed higher peak temperatures, with no decrease away from the approximate trace of the RST, this could indicate overthrusting of hot hanging wall material (e.g., Célérier et al., 2009).

6 DISCUSSION

6.1 STRAIN

The field area contains top-to-the northwest shear sense indicators although the dominant structures (i.e., foliation, isoclinal folds, open folds, and thrust faults) strike northwest to southeast. Previous geologic work has noted that the Robert Service Thrust (RST) records progressive deformation (Craggs, 2022; Mair et al., 2006) and that various shear sense indicators may have formed as a result of changes in vergence overtime (Mair et al., 2006), yet no unique deformation signature has been associated with movement along it (Roots, 1997). Mair et al. (2006) did note, however, that the lower structural levels of the hanging wall of the RST record an evolution from pure shear to simple shear; a trend also observed in the hanging wall of the Tombstone Thrust (TT).

This study presents quartz *c*-axis distributions, and crystallographic vorticity axis (CVA) data that indicate primarily non-coaxial strain with a variable constrictional component. While most samples show evidence of pure shear (e.g. 22AK-001-1-1), there are samples/localities in which simple shear is dominant (i.e. 22AK-061-1-1 and 22AK-082-1-1). An increase in apparent shear strain in proximity to the inferred location of the RST, noted during structural field mapping, and increased grain boundary area reduction (GBAR) of quartz in proximity to the approximate RST, may indicate that deformation related to the TT does not overprint into the hanging wall of the RST, at least within the Keno Hill area. In the footwall of the RST, however, heterogenous strain (lack of spatial relationships with quartz *c*-axis distributions, distribution strengths, and orientation of CVAs) across the field area, with decreasing GBAR towards the TT, may indicate partial overprinting/recrystallization related to movement along the TT.

6.2 STRUCTURAL FRAMEWORK

Murphy (1997) proposed a high strain zone that extends from the TT into the hanging wall of the RST, which was termed the Tombstone Strain Zone (TSZ). Mair et al. (2006) collected samples from the hanging wall of the RST, south of the Keno Hill area, and suggested they were within the TSZ. However, the geochronology and strain data from this study indicate that the RST is not overprinted by the TSZ, and instead it appears the upper limit of the TSZ may lie somewhere within the middle of the field area, possibly north of Sourdough Hill (Fig. 5.1). This interpretation

is based on the transition of the dominant quartz microstructure from GBAR to subgrain rotation, younging of $^{40}Ar/^{39}Ar$ dates, and the increased variability in shear sense at outcrop-scale toward lower structural levels. These trends in data are consistent with increasing overprinting by a later deformation event toward the location of the TT.

In addition, while some of the results presented in this study are variable (e.g. RSCM thermometry, quartz CPO and CVA), other datasets (i.e., geochronology, microstructures) seem to be consistent with a lack of a klippe occurring at Sourdough Hill. The $^{87}Rb/^{87}Sr$ and $^{40}Ar/^{39}Ar$ dates decrease down structural section when Sourdough Hill is not considered to host a klippe. This trend is inconsistent with the oldest dates occurring in the RST hanging wall. Moreover, quartz microstructures at Sourdough Hill (both within and outside the previously mapped klippe) are subgrain rotation-dominant, which contrasts the GBAR-dominant microstructures in proximity to the main RST.

6.3 THERMAL HISTORY

Previous geologic work concluded that the Keno Hill area underwent greenschist facies metamorphism, based on mineral assemblages (e.g. Murphy, 1997). Raman spectroscopy presented in the current study confirms that the Keno Hill area records peak temperatures of ~400-550 °C. Moreover, quartz textures, quartz CPO opening angle temperature estimates, and temperature estimates from slip systems are all consistent with deformation temperatures in the 400-500 °C range.

An increase in peak metamorphic temperature in proximity to the approximate trace of the RST may reflect shear heating (e.g., Petroccia et al., 2022) or conduction into the footwall as a result of overthrusting of a hot hanging wall (e.g., Célérier et al., 2009). More data are required from higher structural levels within the hanging wall of the RST to determine whether there is a systematic increase in temperature in proximity to the thrust fault or if the hanging wall has consistently higher temperatures than the footwall. There is potential, given that the isoclinal folds are locally truncated by thrust faults (Fig. 4.4), that the apparent break in temperature at ~400 m below the RST (Fig. 4.27 and Fig. 5.2) represents a previously unrecognized structure, possibly duplicating the blocky quartzite unit. This break in temperature mimics the apparent break in temperature across the RST, whereas the $^{40}Ar/^{39}Ar$ dates highlight a systematic decrease in age

towards the TT, which may indicate in-sequence thrust deformation. Studies in the Himalaya have identified similar previously unrecognized structures (termed tectonometamorphic discontinuities) at a larger scale within that orogen (e.g., Larson et al., 2015) that are variably in- and out-of-sequence.

6.4 TIMING

Field evidence presented herein indicates that isoclinal folding in the area occurred prior to local thrusting. This interpretation is consistent with isoclinal folds occurring at all structural levels and breaks in data occurring across the position of the RST (Fig. 6.1). The *in situ* $^{87}Rb/^{87}Sr$ and $^{40}Ar/^{39}Ar$ data record a decrease in dates from southwest to northeast, with the $^{87}Rb/^{87}Sr$ data showing an apparent break across the RST. Combined with the heterogeneity in quartz textures (increased GBAR towards the RST), and the RSCM temperature break across the RST, it appears that the RST in the study area is not overprinted by deformation related to the TT. Therefore, the *in situ* $^{87}Rb/^{87}Sr$ date of 116 +/- 14 Ma and the coinciding $^{40}Ar/^{39}Ar$ date of 105.97 +/- 0.88 Ma of sample 22AK-061-1-1 (Fig. 4.1) are thought to reflect movement along the RST. Both dates overlap with $^{87}Rb/^{87}Sr$ data collected from the same structural level farther north (115 +/- 15 Ma; Skipton, personal communication, April 24, 2024) and *in situ* and step-heating $^{40}Ar/^{39}Ar$ data collected farther south in the hanging wall of the RST (100-104 Ma; Mair et al., 2006). Combined, this could indicate that movement along the RST occured from ca. 116 to 100 Ma (Fig. 6.1B).

Evidence for the timing of the open folding event in relation to the Mayo and Tombstone Suite intrusions is not presented in this study, though previous geologic work has variably argued that the open folding either predates (Green, 1971) or postdates the 98-90 Ma (Colpron et al., 2016) intrusions and is contemporaneous with mineralization (Craggs, 2022). This study argues the open folding event occurred after regional scale thrusting (Fig. 6.1D) as crenulation lineations that parallel the fold axis of the open folds maintain a constant orientation across the field area. The timing of Ag-Pb-Zn mineralization in NE-trending, normal, oblique faults followed the cessation of intrusions (either ca. 89 Ma (McOnie, 2016) or ca. 82-77 Ma (Craggs, 2022); Fig. 6.1D). Step-heat $^{40}Ar/^{39}Ar$ white mica dates from mineralized veins and altered country rock from the Keno Hill area (Craggs, 2022; Skipton, personal communication, October 24, 2023) returned dates ranging from ca. 86 to 64 Ma. In this study, the $^{87}Rb/^{87}Sr$ and $^{40}Ar/^{39}Ar$ dates with overlapping

uncertainty in the ca. 94 to 79 Ma timeframe could reflect the local plutonism (Fig. 2.4) and/or mineralization. Alternatively, the geochronology data could indicate that the TT is younger than previously interpreted, possibly still active at ca. 88 Ma, as the $^{40}Ar/^{39}Ar$ data records a systematic decrease toward the TT. Furthermore, the temperature break observed in the middle of the field area was not apparent in the *in situ* geochronology dataset, possibly indicating that the inferred

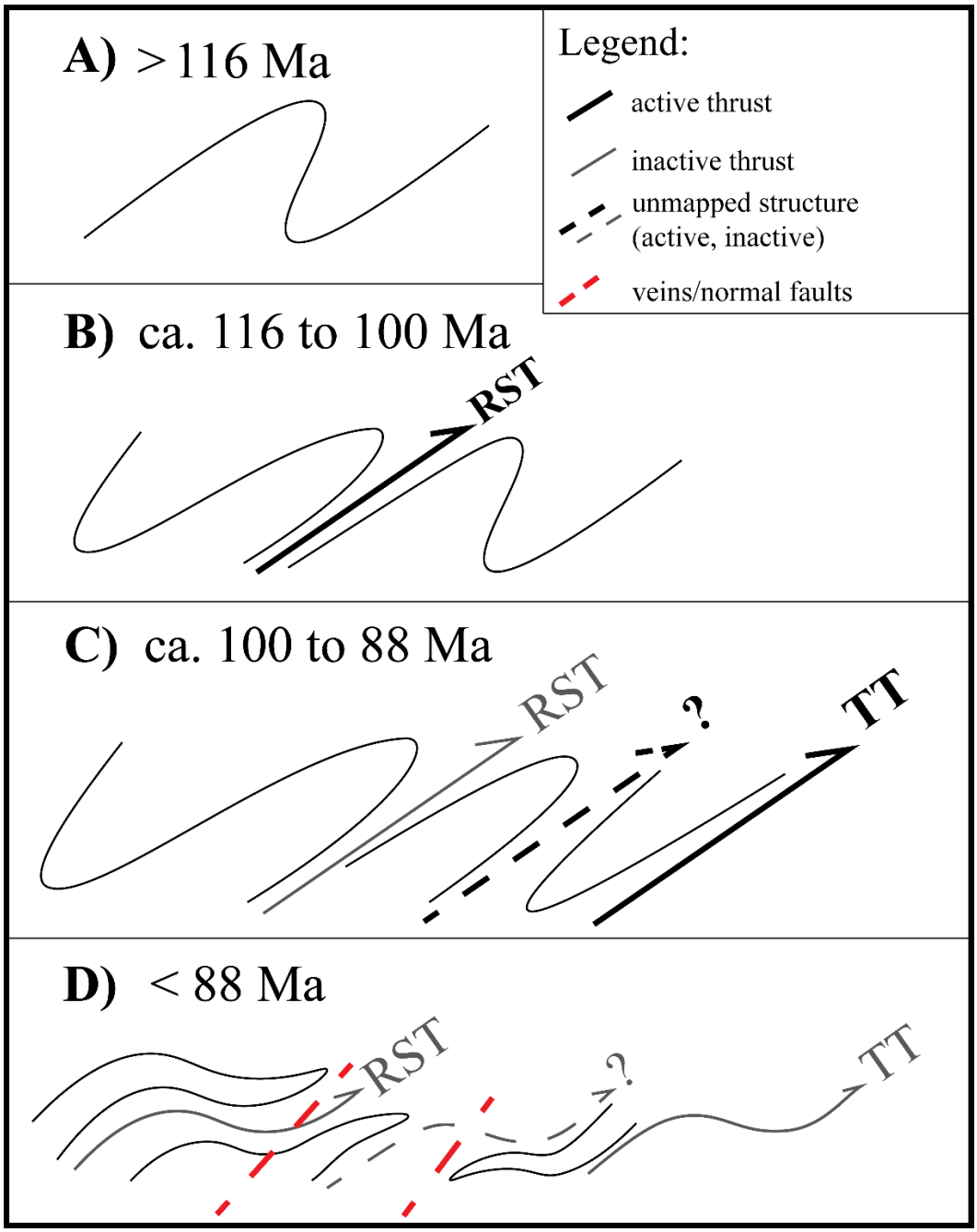


Figure 6.1: Schematic diagram of the structural evolution of the Keno Hill area (with the black thin line indicating bedding. Depicting: A) isoclinal folding event; B) movement along the Robert Service Thrust (RST); C) in-sequence (re)activation of the Tombstone Thrust (TT) and an unmapped structure; D) open folding event and the late veins/normal-oblique faults.

structure formed as a result of in-sequence deformation, between the activation of the RST and (re)activation of the TT without a resolvable time-gap. This interpretation could then indicate that movement along the TT, and the unmapped structure, possibly spanned ca. 100 to 88 Ma (Fig. 6.1 C).

6.5 REGIONAL KINEMATIC FRAMEWORK

Northeast-directed compression across the northern Cordillera during the Jurassic-Cretaceous timeframe resulted in the development of thrust and fold structures that extend across the Selwyn Basin (Gordey & Anderson, 1993; Nelson et al., 2013). These structures include isoclinal folds, the RST, TT, open folds, and brittle normal-oblique faults in the study area. Over the years there have been many interpretations regarding the order in which these structures evolved (see previous chapters). This study presents temporal, temperature, and strain data from samples within the Keno Hill area which indicate the following structural evolution (Fig. 6.1):

1) initiation of isoclinal folding (F_1),
2) activation of RST and possible continuation of F_1,
3) activation of TT,
4) open folding.

Murphy (1997) proposed the RST predates isoclinal folding whereas Read et al. (2021) proposed isoclinal folding predates the RST (Fig. 1.2). This study proposes that the isoclinal F_1 folds predate (and are possibly syn-kinematic with) the RST as the folds are both truncated by and occur as drag folds on the hanging wall side of local curviplanar thrust faults. Later formation (or re-activation) of the TT is supported by the younging of *in situ* geochronology of foliation-defining white mica towards the north/northeast paired with a decrease in GBAR. From the data presented in this study, the absolute timing of the open folding event remains unknown but postdates the isoclinal folds and probably the regional-scale thrusting given the consistent orientation of the crenulation lineation across the field area.

Because the results of strain and deformation geometry investigations in this study are variable, it remains unclear what event(s) the top-to-the northwest shear sense is related to. Shear sense indicators do appear to become more variable towards the northeast, away from the RST, which may indicate that northwest-shear is related to movement along the structure.

The geochronological data presented in this study indicate both a break across the RST ($^{87}Rb/^{87}Sr$), and a systematic decrease from southwest to northeast, toward the TT ($^{40}Ar/^{39}Ar$). As thermometry data show higher temperatures in the hanging wall of the RST and decreasing temperatures in the footwall, the decrease in age towards the northeast could reflect that movement along the thrust faults spanned a longer period of time than previous interpretations have suggested. This interpretation supports progressive deformation at structurally shallower levels, which is consistent with in-sequence thrusting. While the timing of mineralization is not agreed upon, studies have suggested that mineralization either occurred at 87 +/- 3 Ma (McOnie, 2016) or between ca. 82 and 77 Ma (Craggs, 2022). While it is possible that the *in situ* $^{87}Rb/^{87}Sr$ and $^{40}Ar/^{39}Ar$ dates ranging from 98 to 88 Ma in the footwall of the RST reflect some overprinting by fluid alteration associated with mineralization and/or plutonism, the samples in this study were not collected within, or close to, mineralized veins. The dates could, alternatively, indicate that movement along the TT continued until ca. 88 Ma (or some combination thereof). This interpretation can be further supported with the mapped locations of plutons exceeding 10 km of the collected samples (e.g., Fig. 2.4) making it unlikely that the dates herein reflect fluid alteration associated with plutonism. The strain geometry and flow regime across the field area is heterogeneous, with the results consistent with partial overprinting related to movement along the TT.

The RST, TT, and Dawson Thrust (structurally highest to lowest, respectively) extend northwest across central Yukon and accommodated displacement from northeast-directed Jurassic-Cretaceous convergence (e.g., Mair et al., 2006). Previous interpretations of these regional-scale structures have suggested in-sequence thrusting, with the end of ductile deformation related to movement along the TT at ca. 100-104 Ma (Mair et al., 2006). The Selwyn Basin (Gordey & Anderson, 1993) was intruded by various undeformed plutonic suites that are interpreted to post-date ductile deformation (Anderson, 1987) and stitch early structures (e.g. Murphy, 1997). However, a study of the Deadman pluton in the hanging wall of the Dawson Thrust, north-northeast of Dawson City (Symons et al., 2006), reports geophysical evidence supporting post-mid-Cretaceous (i.e., <91 Ma) deformation possibly attributed to displacement along the Dawson Thrust.

Although from a different structural level, the results presented in this study are similar to that of Symons et al. (2006), in that the geochronology data herein supports later (re)activation of the TT. By integrating similar microstructural and *in situ* geochronological investigations to other localities within the Selwyn basin, the interpretations presented herein could change the model for the structural evolution of the Selwyn thrust and fold belt by potentially re-bracketing the timeframe in which the TT and Dawson Thrust were active (or the possibility of out-of-sequence reactivation) if similar results are obtained along other structural transects. Furthermore, similar to the work on the Deadman pluton, recent studies have shown that the Roop Lakes pluton may not stitch the RST as previously mapped (Read et al., 2021). Future studies would benefit from a revisit of key locations along the RST, TT, and Dawson Thrust, and the corresponding relationships with non-foliated plutons that have been inferred to crosscut these structures regionally.

7 CONCLUSIONS

Previous studies of the Keno Hill area have largely focussed on the late, brittle structures that host the Ag-Pb-Zn mineralization. The few studies that have focussed on the early, ductile structures proposed variable interpretations for their structural evolution (e.g. Murphy, 1997; Read et al., 2021). Most notably, Murphy (1997) proposed that regional scale thrusting predates isoclinal folding whereas Read et al. (2021) proposed the opposite.

This study presents temporal, thermometric, and strain data from samples collected throughout the Keno Hill area, orthogonal to the strike of the dominant structures. The data presented throughout this thesis indicate that isoclinal folding initiated prior to the regional scale thrusting and that movement along the Robert Service Thrust (RST) likely predates movement along the Tombstone Thrust (TT). *In situ* geochronology on foliation-defining white mica indicates that slip along the RST occurred ca. 115 Ma and slip along the TT may have continued until ca. 88 Ma, with deformation occurring at near-peak temperatures of 400-550 °C. The structural complexity of the region, including a possible cryptic structural break in metamorphic temperature, may indicate partial overprinting by subsequent or progressive deformation events. The results presented herein suggests the framework for the evolution of the Selwyn thrust and fold belt be revised, since latest movement along the faults may not be bracketed by the emplacement of the Mayo and Tombstone Plutonic Suites as previously assumed.

7.1 RECOMMENDATIONS FOR FUTURE WORK

Fieldwork

The fieldwork in this study focussed primarily on samples in the footwall of the RST. It is recommended that additional fieldwork be extended into the hanging wall of the RST and into the footwall of the TT. This approach would be ideal to determine if there are any changes in deformation style at different structural levels of this fold and thrust belt, and to collect samples for temperature, strain, and *in situ* geochronology. It is also recommended that more fieldwork and sample collection be conducted in the Sourdough Hill area (e.g., Read et al., 2020) to confirm geochronological differences between similar lithologies in direct proximity to and from the known hanging wall of the RST. Farther east lies the Roop Lakes Pluton (Yukon Geological Survey, 2024), however recent studies have noted that the pluton may not plug the RST (Read et

al., 2021). As such, revisiting the relationship between the regional scale thrust faults and the Mayo and Tombstone Suite plutons, could allow the timing of movement along the faults to be better understood.

Geochronology

In situ geochronology on foliation-defining white mica should be extended farther into the hanging wall of the RST and into the footwall of the TT. The results could then possibly bracket the timeframe in which the regional scale faults were active. It is also recommended that detrital zircon geochronology on quartz grit schists collected from within and outside of the previously mapped klippe on Sourdough Hill be investigated in conjunction with known samples of the Hyland Group from the hanging wall of the RST. The investigation of the klippe could then possibly determine why the geochronology data from the klippe in this study does not align with the results from the other hanging wall sample farther south.

Temperature and Strain

Raman spectroscopy-based thermometry of carbonaceous materials from samples collected farther into the hanging wall of the RST would help investigate the cause for the systematically decreasing temperatures below the trace of the RST. If the results mirror a systematic decrease away from the approximate fault trace, this could indicate shear heating (e.g. Petroccia et al., 2022), whereas overall higher temperatures, could indicate conduction into the footwall of the RST as a result of overthrusting of hot hanging wall material (e.g. Célérier et al., 2009). Quartz *c*-axis crystallographic preferred orientations (CPOs) and crystallographic vorticity axis investigations farther southwest and northeast could show spatial or structural variations with strain geometry and flow regime, respectively.

REFERENCES

Anderson, R. G. (1987). Plutonic Rocks in the Dawson map area, Yukon Territory. *Geological Survey of Canada, Paper, 87-1A*, 689–697.

Barnes, C. J., Schneider, D. A., Majka, J., Camacho, A., Bukała, M., & Włodek, A. (2023). 40Ar/39Ar dates controlled by white mica deformation and strain localization: Insights from comparing in situ laser ablation and single-grain fusion techniques. *Journal of Metamorphic Geology*, *41*(9), 1143–1166. https://doi.org/10.1111/jmg.12739

Beyssac, O., Goffé, B., Chopin, C., & Rouzaud, J. N. (2002). Raman spectra of carbonaceous material in metasediments: a new geothermometer. *Journal of Metamorphic Geology*, *20*, 859–871.

Bouchez, J.-L., & Pecher, A. (1981). The Himalayan Main Central Thrust pile and its quartz-rich tectonites in central Nepal. *Tectonophysics*, *78*, 23–50.

Brown, V. (2022). *Integrating Microkinematic Crystallographic Vorticity Axis (CVA) Analysis and Petrochronology to Investigate the Temporal Development of Fabric Within a Transpressional Shear Zone, New Zealand*. California State University, Northridge.

Camacho, A., Lee, J. K. W., Zhao, J., Abdu, Y. A., Fayek, M., & Creaser, R. A. (2020). A test of the interlayer ionic porosity model as a measure of argon diffusivity in trioctahedral micas. *Geochimica et Cosmochimica Acta*, *288*, 341–368. https://doi.org/10.1016/j.gca.2020.07.041

Célérier, J., Harrison, T. M., Beyssac, O., Herman, F., Dunlap, W. J., & Webb, A. G. (2009). The Kumaun and Garwhal Lesser Himalaya, India: Part 2: Thermal and deformation histories. *Bulletin of the Geological Society of America*, *121*(9–10), 1281–1297. https://doi.org/10.1130/B26343.1

Colpron, M., Israel, S., & Friend, M. (2016). Yukon Plutonic Suite. Yukon Geological Survey, Open File 2016-37, Scale 1:750000.

Craggs, S. D. (2022). *Structural Geological Controls And Timing Of Ag-Pb-Zn Mineralisation At The Keno Hill Deposit, Yukon*.

Cross, A. J., Prior, D. J., Stipp, M., & Kidder, S. (2017). The recrystallized grain size piezometer for quartz: An EBSD-based calibration. *Geophysical Research Letters*, *44*(13), 6667–6674. https://doi.org/10.1002/2017GL073836

Faleiros, F. M., Moraes, R., Pavan, M., & Campanha, G. A. C. (2016). A new empirical calibration of the quartz c-axis fabric opening-angle deformation thermometer. *Tectonophysics*, *671*, 173–182. https://doi.org/10.1016/j.tecto.2016.01.014

Fossen, H. (2016). *Structural Geology* (Second). Cambridge University Press.

Fraser, G., Worley, B., & Sandiford, M. (2000). High-precision geothermobarometry across the high Himalayan metamorphic sequence, Langtang Valley, Nepal. *Journal of Metamorphic Geology*, *18*(6), 665–681. https://doi.org/10.1046/j.1525-1314.2000.00283.x

Gordey, S. (1990). Geology Map of the Tiny Island Lake Map Area (105M/16). *Yukon Geological Survey, Open File 1990-2*.

Gordey, S. P., & Anderson, R. G. (1993). *Evolution of the northern Cordilleran miogeocline, Nahanni map area (105I), Yukon and Northwest Territories*. Natural Resources Canada, Geological Survey of Canada, Energy, Mines and Resources Canada.

Graziani, R. (2022). random_pair_analysis _relict_rex. Unpublished.

Green, L. H. (1971). Geology of Mayo Lake, Scougale Creek and McQuesten Lake map-areas. *Geological Survey of Canada, Memoir 357, 1971, 72 Pages (7 Sheets), Https://Doi.Org/10.4095/100655*.

Heilbronner, R., & Tullis, J. (2006). Evolution of c axis pole figures and grain size during dynamic recrystallization: Results from experimentally sheared quartzite. *Journal of Geophysical Research: Solid Earth*, *111*(10). https://doi.org/10.1029/2005JB004194

Hippertt, J. F. (1994). Microstructures and c-axis fabrics indicative of quartz dissolution in sheared quartzites and phyllonites. *Tectonophysics*, *229*(3–4), 141–163. https://doi.org/10.1016/0040-1951(94)90026-4

Hunter, N. J. R., Weinberg, R. F., Wilson, C. J. L., & Law, R. D. (2018). A new technique for quantifying symmetry and opening angles in quartz c-axis pole figures: Implications for interpreting the kinematic and thermal properties of rocks. *Journal of Structural Geology*, *112*, 1–6. https://doi.org/10.1016/j.jsg.2018.04.006

Jiang, D., & Williams, P. F. (1998). High-strain zones: a unified model. *Journal of Structural Geology*, *20*(8), 1105–1120.

Kruhl, J. H. (1998). Reply: Prism- and basal-plane parallel subgrain boundaries in quartz: a microstructural geothermobarometer. *Journal of Metamorphic Geology*, *16*(1), 142–146. https://doi.org/10.1111/j.1525-1314.1998.00063.x

Larson, K., Graziani, R., Kilian, R., & Piette-Lauzière, N. (2023a). Practical Assessment of Quartz Crystallographic Preferred Orientation Strength. *Tektonika*, *1*(1), 101–111. https://doi.org/10.55575/tektonika2023.1.1.23

Larson, K. P. (2018). Refining the structural framework of the Khimti Khola region, east-central Nepal Himalaya, using quartz textures and c-axis fabrics. *Journal of Structural Geology*, *107*, 142–152. https://doi.org/10.1016/j.jsg.2017.12.014

Larson, K. P., Ambrose, T. K., Webb, A. G., Cottle, J. M., & Shrestha, S. (2015). Reconciling Himalayan midcrustal discontinuities: The Main Central thrust system. *Earth and Planetary Science Letters*, *429*, 139–146. https://doi.org/10.1016/j.epsl.2015.07.070

Larson, K. P., Button, M., Shrestha, S., & Camacho, A. (2023b). A comparison of 87Rb/87Sr and 40Ar/39Ar dates: Evaluating the problem of excess 40Ar in Himalayan mica. *Earth and Planetary Science Letters*, *609*. https://doi.org/10.1016/j.epsl.2023.118058

Larson, K. P., Lamming, J. L., & Faisal, S. (2014). Microscale strain partitioning? Differential quartz crystallographic fabric development in Phyllite, Hindu Kush, Northwestern Pakistan. *Solid Earth*, *5*(2), 1319–1327. https://doi.org/10.5194/se-5-1319-2014

Larson, K. P. (2022). FabricPlotR (v.13). OSF. https://doi.org/10.17605/OSF.IO/MJTXV.

Larson, K.P. (2024). *Process Iolite Rb Sr Data v4.R.*

Li, Z., Deng, L., Kinloch, I. A., & Young, R. J. (2023). Raman spectroscopy of carbon materials and their composites: Graphene, nanotubes and fibres. In *Progress in Materials Science* (Vol. 135). Elsevier Ltd. https://doi.org/10.1016/j.pmatsci.2023.101089

Lister, G. S. (1977). Discussion: Crossed-girdle c-axis fabrics in quartzites plastically deformed by plane strain and progressive simple shear. *Tectonophysics*, *39*, 51–54.

Lister, G. S., & Hobbs, B. E. (1980). The simulation of fabric development during plastic deformation and its application to quartzite: the influence of deformation history. *Journal of Structural Geology*, *2*(3), 355–370.

Mainprice, D., Bachmann, F., Hielscher, R., & Schaeben, H. (2015). Descriptive tools for the analysis of texture projects with large datasets using MTEX: strength, symmetry and components. *Geological Society, London, Special Publications*, *409*, 251–271.

Mainprice, D., Bouchez, J.-L., Blumenfeld, P., & Tubià, J. (1986). Dominant c slip in naturally deformed quartz: Implications for dramatic plastic softening at high temperature. *Geology*, *14*(10), 819–822.

Mair, J. L., Hart, C. J. R., Goldfarb, R.J., O'Dea, M., & Harris, S. (2000). Geology and metallogenic signature of gold occurrences at Scheelite Done, Tombstone gold belt, Yukon. *Yukon Exploration and Geology 1999, Exploration and Geological Division, Yukon, Indian and Northern Affairs Canada*, 165-176.

Mair, J. L., Hart, C. J. R., & Stephens, J. R. (2006). Deformation history of the northwestern Selwyn Basin, Yukon, Canada: Implications for orogen evolution and mid-Cretaceous magmatism. *Bulletin of the Geological Society of America*, *118*(3–4), 304–323. https://doi.org/10.1130/B25763.1

Mako, C. A., & Caddick, M. J. (2018). Quantifying magnitudes of shear heating in metamorphic systems. *Tectonophysics*, *744*, 499–517. https://doi.org/10.1016/j.tecto.2018.07.003

McDougall, I., & Harrison, T. M. (1999). *Geochronology and Thermochronology by the 40Ar/39Ar Method* (Second). Oxford University Press.

McKenzie, W. F., Dyck, B., Gibson, H. D., & Larson, K. (2024). A record of Late Cretaceous to early Paleogene Insular terrane accretion within the northern Cordillera: Insights from monazite petrochronology across the Kluane Schist, southwest Yukon, Canada. *Geological Society of America Bulletin*. https://doi.org/10.1130/B37198.1

McOnie, A. (2016). *The Keno Hill Silver Mining District*.

McTaggart, K. C. (1960). The geology of Keno and Galena Hills, Yukon Territory. *Geological Survey of Canda*.

Michels, Z. D., Tikoff, B., Kruckenberg, S. C., & Davis, J. R. (2015). Determining vorticity axes from grain-scale dispersion of crystallographic orientations. *Geology*, *43*(9), 803–806. https://doi.org/10.1130/G36868.1

Monger, J., & Price, R. (1979). Geodynamic evolution of the Canadian Cordillera-progress and problems. *Canadian Journal of Earth Sciences*, *16*(3), 770–791.

Monger, J., & Price, R. (2002). The Canadian Cordillera: Geology and Tectonic Evolution. *CSEG Recorder*, *February 2002*, 17–36.

Monger, J. W. H. (2008). Evolution of Canada's western mountains. In *Geological Survey of Canada, Open File 5804, 1 Poster*. Geological Survey of Canada.

Morgan, S. S., & Law, R. D. (2004). Unusual transition in quartzite dislocation creep regimes and crystal slip systems in the aureole of the Eureka Valley-Joshua Flat-Beer Creek pluton, California: A case for anhydrous conditions created by decarbonation reactions. Tectonophysics, 384(1–4), 209–231. https://doi.org/10.1016/j.tecto.2004.03.016

Murphy, D. C. (1997). Geology of the McQuesten River Region, Northern McQuesten and Mayo Map Areas, Yukon Territory (115P/14, 15, 16; 105M/13, 14). *Exploration and Geological Services Division, Yukon, Indian and Northern Affairs Canada, Bulletin 6*.

Murphy, D. C., & Heon, D. (1996). Geological map of Sprague Creek map area, western Selwyn Basin, Yukon, NTS 115P/15. *Exploration and Geological Services Division, Yukon, Indian and Northern Affairs Canada, Geoscience Map 1996-2, Scale 1:50 000*.

Murphy, D. C., Heon, D., & Hunt, J. A. (1996). Geological map of Clear Creek area, western Selwyn Basin, Yukon. *Exploration and Geological Services Division, Yukon, Indian and Northern Affairs Canada, Geoscience Map 1996-1, 1:50 000 Scale*.

Murphy, D. C., & Roots, C. F. (1996). Geological map of Keno Hill Area, Central Yukon (105 M/14). *Exploration and Geological Services Division, Indian and Northern Affairs Canada, Map 1996-1, Scale-1:50 000*.

Nelson, J., & Colpron, M. (2007). Tectonics and Metallogeny of the British Columbia, Yukon, and Alaskan Cordillera, 1.8 Ga to the Present. *Mineral Deposits of Canada: A Synthesis OfMajor Deposit-Types, District Metallogeny, the Evolution of Geological Provinces, and Exploration Methods: Geological Association of Canada, Mineral Deposits Division, Special Publication*, *5*, 755–791.

Nelson, J. L., Colpron, M., & Israel, S. (2013). The Cordillera of British Columbia, Yukon, and Alaska: Tectonics and Metallogeny. *Society of Economic Geologists, Special Publication*, *17*, 53–109. http://pubs.geoscienceworld.org/books/book/chapter-pdf/3811598/9781629491639_ch03.pdf

Neumann, B. (2000). Texture development of recrystallised quartz polycrystals unravelled by orientation and misorientation characteristics. *Journal of Structural Geology*, *22*, 1695–1711. www.elsevier.nl/locate/jstrugeo

Passchier, C. W., & Trouw, R. A. J. (2005). *Microtectonics* (Second). Springer.

Paton, C., Hellstrom, J., Paul, B.,Woodhead, J. & Hergt, J. (2011). Iolite: Freeware for the visualisation and processing of mass spectrometric data. Journal of Analytical Atomic Spectrometry. doi:10.1039/c1ja10172b.

Petroccia, A., Carosi, R., Montomoli, C., Iaccarino, S., & Vitale Brovarone, A. (2022). Deformation and temperature variation along thrust-sense shear zones in the hinterland-foreland transition zone of collisional settings: A case study from the Barbagia Thrust (Sardinia, Italy). *Journal of Structural Geology*, *161*. https://doi.org/10.1016/J.JSG.2022.104640

Piette-Lauzière, N., Larson, K. P., Kellett, D. A., & Graziani, R. (2020). Intracrystalline vorticity record of flow kinematics during shear zone reactivation. *Journal of Structural Geology, 140*. https://doi.org/10.1016/j.jsg.2020.104134

Poulton, T. P., & Templeman-Kluit, D. J. (1982). Recent discoveries of Jurassic fossils in the lower schist division of central Yukon. *Current Research, Part C, Geological Survey of Canada, Paper 82-1C*, 91–94.

Read, P. B., McOnie, A., & Iles, S. (2020). Geology of the Keno Hill District, Yukon. *Yukon Geological Survey, Open File 2020-42, 2 Sheets, 1:25 000 Scale and 1:2 500 Scale*.

Read, P. B., Mconie, A., & Iles, S. (2021). *Keno Hill Mining Camp*. https://data.geology.gov.yk.ca/Reference/95881#InfoTab.

Redaa, A., Farkaš, J., Gilbert, S., Collins, A. S., Wade, B., Löhr, S., Zack, T., & Garbe-Schönberg, D. (2021). Assessment of elemental fractionation and matrix effects during: In situ Rb-Sr dating of phlogopite by LA-ICP-MS/MS: Implications for the accuracy and precision of mineral ages. *Journal of Analytical Atomic Spectrometry*, *36*(2), 322–344. https://doi.org/10.1039/d0ja00299b

Roots, C. F. (1997). Geology of the Mayo Map Area, Yukon Territory (105M). *Exploration and Geological Services Division, Yukon, Indian and Northern Affairs Canada*, *Bulletin 7*.

Schaen, A. J., Jicha, B. R., Hodges, K. V., Vermeesch, P., Stelten, M. E., Mercer, C. M., Phillips, D., Rivera, T. A., Jourdan, F., Matchan, E. L., Hemming, S. R., Morgan, L. E., Kelley, S. P., Cassata, W. S., Heizler, M. T., Vasconcelos, P. M., Benowitz, J. A., Koppers, A. A. P., Mark, D. F., … Singer, B. S. (2021). Interpreting and reporting 40Ar/39Ar geochronologic data. *Bulletin of the Geological Society of America*, *133*(3–4), 461–487. https://doi.org/10.1130/B35560.1

Schmid, S. M., & Casey, M. (1986). Complete fabric analysis of some commonly observed quartz c-axis patterns. *Mineral and Rock Deformation Laboratory Studies*. Geophysical Monograph Series, American Geophysical Union, 263–286.

Sinclair A.J., Tessari, O.J. and Harakal, J.E. (1980). Age of Ag-Pb-Zn Mineralization, Keno Hill – Galena Hill Area, Yukon Territory. Canadian Journal of Earth Sciences, vol. 17, p. 100-1103.

Stipp, M., Stunitz, H., Heilbronner, R., & Schmid, S. (2002). The eastern Tonale fault zone: a `natural laboratory' for crystal plastic deformation of quartz over a temperature range from 250 to 700 8C. *Journal of Structural Geology*, *24*, p. 1861–1884. www.elsevier.com/locate/jstrugeo

Symons, D. T., Harris, M. J., Hart, C. J. R., & McCausland, P. J. A. (2006). Paleomagnetism of the ~91 Ma Deadman pluton: post-mid-Cretaceous tectonic motion in central Yukon. *Yukon Exploration and Geology 2005,* Edmond, D. S., Bradshaw, G. D., Lewis, L. L., & Weston, L. H. (Eds.), Yukon Geological Survey, p. 299-313.

Tupper, D., & Bennett, V. (2010). Observations of polymetallic Ag-Pb-Zn (± Au ± In) mineralization at the Eagle and Fisher vein-faults, airborne total field magnetics and identification of Tombstone age-equivalent aplite dykes in the Galena Hill area, Keno City, Yukon. *Yukon Exploration and Geology 2009,* MacFarlane, K.E., Weston, L.H. and Blackburn, L.R. (Eds.), Yukon Geological Survey, p. 305-330.

Vermeesch, P., 2018, IsoplotR: a free and open toolbox for geochronology. Geoscience Frontiers, v.9, p.1479-1493, doi:10.1016/j.gsf.2018.04.001.2023. mtex-5.9.0. MTEX. https://mtex-toolbox.github.io/download [6 February 2024]

Vice, L., Gibson, H. D., & Israel, S. (2020). Late Cretaceous to Paleocene Tectonometamorphic Evolution of the Blanchard River Assemblage, Southwest Yukon: New Insight into the Terminal Accretion of Insular Terranes in the Northern Cordillera. *Lithosphere*, *2020*(1), 1–22. https://doi.org/10.2113/2020/2298288

Wang, L., Cao, D., Peng, Y., Ding, Z., & Li, Y. (2019). Strain-induced graphitization mechanism of coal-based graphite from lutang, hunan province, china. *Minerals*, *9*(10). https://doi.org/10.3390/min9100617

Woodhead, J. D., & Hergt, J. M. (2001). Strontium, neodymium and lead isotope analyses of NIST glass certified reference materials: SRM 610, 612, 614. *Geostandards Newsletter*, *25*(2–3), 261–266. https://doi.org/10.1111/j.1751-908x.2001.tb00601.x

Xypolias, P. (2010). Vorticity analysis in shear zones: A review of methods and applications. In *Journal of Structural Geology* (Vol. 32, Issue 12, pp. 2072–2092). https://doi.org/10.1016/j.jsg.2010.08.009

Xypolias, P., Chatzaras, V., Beane, R., & Papadopoulou, S. (2013). Heterogeneous constrictional deformation in a ductile shear zone resulting from the transposition of a lineation-parallel fold. *Journal of Structural Geology*, *52*(1), 44–59. https://doi.org/10.1016/j.jsg.2013.05.001

Yukon Geological Survey. (2020). A digital atlas of terranes for the northern Cordillera. *Yukon Geological Survey*. https://data.geology.gov.yk.ca/Compilation/2

Yukon Geological Survey. (2024). Bedrock geology map. *Government of Yukon*. https://www.arcgis.com/home/webmap/viewer.html?webmap=b950bd1b5afa4eab9885d505a3ed98b4

Zack, T., & Hogmalm, K. J. (2016). Laser ablation Rb/Sr dating by online chemical separation of Rb and Sr in an oxygen-filled reaction cell. *Chemical Geology*, *437*, 120–133. https://doi.org/10.1016/j.chemgeo.2016.05.027

Zuo, J., Webb, A. A. G., Piazolo, S., Wang, Q., Müller, T., Ramírez-Salazar, A., & Haproff, P. J. (2021). Tectonics of the Isua Supracrustal Belt 2: Microstructures Reveal Distributed Strain in the Absence of Major Fault Structures. *Tectonics*, *40*. https://doi.org/10.1029/2020TC006514

APPENDICES

APPENDIX A: FIELDWORK STATION DESCRIPTIONS

Station #	Latitude (N)	Longitude (W)	Observations	Structures and Samples
22AK-001	63.89320	135.27867	• Metamorphosed fine to medium grain, thinly bedded, quartz rich sandstone. • Minerals: quartz, chlorite, calcite • Asymmetric folds and isoclinal folds • Isoclinal anticline: top to north, amplitude 15cm, wavelength 10cm • Foliation defined by chlorite +/- white mica. • Recessive layers interbedded with quartz dominant layers • Photos 1-2: Asymmetric and isoclinal folds	Foliation: 122/24 Foliation: 130/25 Asymmetric fold axis: 27→146 Asymmetric fold axial plane: 352/74 Isoclinal fold axis: 02→060 Isoclinal fold limb: 038/53 Sample 22AK-001-1-1: Foliation 110/30 Bottom
22AK-002	63.89607	135.27610	• Fine grained meta-sandstone • Minerals: quartz, white mica • Phyllitic foliation defined by white mica. Quartz vein parallel to foliation. • Partially slumped, altered, and weathered. • Photos 3-6: Fabric	Foliation: 088/14 Sample 22AK-002-1-1
22AK-003	63.89542	135.27745	• Weakly foliated limestone • Calcite veins parallel to foliation • Undulating fabric • Photo 7: Fabric	Foliation: 250/02 No Sample
22AK-004	63.89783	135.27450	• Chlorite +/- Graphitic schist • Minerals: White mica, quartz, chlorite, +/- graphite • Undulating fabric. Phyllitic texture. Shale and fine to medium grain sandstone interbedded. Quartz veining parallel to foliation. Foliation deformed by open folding. Mineral lineations are roughly parallel to fold axis. Parasitic folds and crenulations. • Shear sense: Top to the northwest • Photos 8-12: Shear sense, isoclinal folds, open fold, crenulations.	Open Fold [1] Fold Axis: 22→146 Open Fold [1] Axial Plane: 155/82 Open Fold [2] Fold Axis: 18→170 Open Fold [2] Axial Plane: 350/79 Foliation: 147/11 Foliation: 134/54 Foliation: 130/25 Foliation: 088/14 Lineation – Crenulation: 30→141 Lineation – Crenulation: 36→139

Station #	Latitude (N)	Longitude (W)	Observations	Structures and Samples
				Samples 22AK-004-1-1, 22AK-004-1-2, and 22AK-004-1-3
22AK-005	63.89933	135.27393	• Shale to phyllitic fine grained siltstone. • Minerals: chlorite, white mica, quartz, +/- graphite, +/- calcite • Well defined wavy foliation deformed by open and isoclinal folds. Isoclinal folding of quartz veins. Structurally higher than graphitic and chloritic shists. ~1cm thick limestone lens. • Shear sense: Top to the northwest • Photos 15-17, 223-228: fabric, and fold.	Isoclinal fold - Axial Plane: 104/10 Foliation: 112/19 Fold Axis: 32→158 Axial Plane: 319/84 Open Fold Axis: 24→148 Open Axial Plane: 328/63 Samples 22AK-005-1-1, 22AK-005-1-2
22AK-006	63.89097	135.27932	• Quartz grit sandstone • Minerals: Quartz, white mica • Foliation well defined by mica. • Photos 20-21: fabric and outcrop	Foliation: 070/24 Foliation: 084/24 Sample 22AK-006-1-1, and 22AK-006-1-2: Foliation 070/25 Top
22AK-007	63.89073	135.27568	• Quartz grit sandstone • Minerals: Quartz, white mica, +/- chlorite • Foliation well defined by mica and quartz veining. • Photo 22: fabric	Foliation: 087/25 Sample: 22AK-007-1-1
22AK-008	63.90002	135.25253	• Lithology 1: thinly interbedded chert, quartz rich siltstone, and phyllitic shale. Lithology 2: locally calcareous quartzite. Lithology 3: graphitic schist +/- chlorite. • Minerals: 1) chert, quartz, white mica; 2) quartz, white mica, +/- calcite; 3) graphite, quartz, white mica, chlorite. • All three lithologies exhibit well defined foliations. Elongated quartz boudins. Folded quartz veins. Subtle mineral lineations in lithology 1 that run parallel to fold hinges. • Shear sense: Top to the northwest • Photos 23-33: Fabric, folding, and outcrop.	*Lithology 1:* Foliation: 092/29 Foliation: 090/20 Foliation: 087/18 Foliation: 114/30 Isoclinal fold axis [1]: 05→270 Isoclinal fold axial plane [1]: 090/16 Isoclinal fold axis [2]: 02→270 Isoclinal axial plane [2]: 090/17 *Lithology 2:* Foliation: 106/14 Foliation: 125/21 *Lithology 3:* Foliation: 070/10 Foliation: 110/22 Foliation: 119/29 Foliation: 105/26

Station #	Latitude (N)	Longitude (W)	Observations	Structures and Samples
				Samples: 22AK-008-1-1: Foliation 105/19 Top, 22AK-008-1-2: non foliation surface 127/85 Top, 22AK-008-2-1: Foliation 125/38 Bottom, 22AK-008-3-1, 22AK-008-3-2: Foliation 120/30 Top
22AK-009	63.90453	135.330917	• Lithology 1: graphitic schist. Lithology 2: limestone. Lithology 3: shale to siltstone. • Minerals: 1) graphite, quartz, white mica, +/- chlorite; 2) calcite; 3) clay, quartz, +/- white mica, +/- chlorite. • Lithology 1 and 2 are thinly interbedded. Lithology 1 and 3 exhibits well developed foliation. Mineral lineations in lithologies 1 and 3. Minor fold with southeast axial trace. • Shear sense: Top to the northwest • Photos 34-37: Fabric.	*Lithology 1:* Foliation: 110/39 Foliation: 109/40 Lineation – Crenulation: 20→128 *Lithology 2:* Foliation: 108/33 Foliation: 110/22 *Lithology 3:* Lineation – Crenulation: 30→130 Samples: 22AK-009-1-1: Foliation 109/30 Top, 22AK-009-3-1
22AK-010	63.90388	135.27095	• Graphitic schist thinly interbedded with quartzite. • Minerals: graphite, quartz, white mica, +/- chlorite. • Well defined foliation. Quartz veins run parallel to foliation. Crenulated fabric. Undulating foliation across outcrop. Isoclinal and open folds. • Photos 38-39: Fabric, folding, and outcrop.	Foliation: 110/44 Foliation: 112/25 Open fold axis: 33→170 Open fold axial plane: 170/84 Isoclinal fold axial plane: 098/18 Lineation – crenulation: 14→171 Samples: 22AK-010-1-1: Foliation 070/24 Bottom
22AK-011			• Lithology 1: graphite-muscovite schist, thinly interbedded with lithology 2: blocky quartzite. • Minerals: quartz, graphite, white mica, +/- chlorite. • Foliation planes with 0.5cm scale deformed by open, sub horizontal folds, isoclinal folds and locally crenulated fabric. Foliation undulates with open fold. Isoclinal folds are folded by open fold. Quartzite layers are 10-30cm thick, sometimes exhibiting boundinage morphology. • Shear sense: Ambiguous to Top to the north/northwest. • Photos 40-48: Fabric, folding, and outcrop.	Foliation: 105/53 Foliation: 105/44 Minor fold axis: 16→140 Minor fold axial plane: 140/51 Isoclinal fold axis: 22→159 Isoclinal fold axial plane: 159/35 Large parasitic fold axis: 17→278 Large parasitic fold axial plane: 278/64 Small parasitic fold axis: 15→275 Small parasitic fold axial plane: 275/42

Station #	Latitude (N)	Longitude (W)	Observations	Structures and Samples
				Samples: 22AK-011-1-1: Foliation 095/29 Top, 22AK-011-1-2: Foliation 126/43 Top, 22AK-011-2-1: Foliation 095/29 Bottom
22AK-012	63.94131	135.21893	• Lithology 1: Greenstone. Lithology 2: quartz rich chloritic schist. • Minerals: 1) chlorite +/- calcite, and 2) quartz, chlorite, +/-white mica, +/- graphite • Greenstone is blocky, locally calcareous, and 10-15m thick. Schist unit has well developed foliation defined by micaceous layers. Isoclinal folds and quartz veins observed in this unit. Lithology 2 is structurally lower than Lithology 1. • Photos 49-52: Fabric and outcrop.	Foliation: 121/31 Foliation: 112/20 Samples: 22AK-012-2-1: Foliation 125/37 Bottom
22AK-013	63.94251	135.21310	• Lithology 1: chloritic-muscovite schist. Lithology 2: Greenstone. • Minerals: 1) chlorite, white mica, quartz, +/- graphite and 2) chlorite +/- calcite, +/- sulfides, +/- biotite. • Foliation of lithology 1 is locally wavy and has planes that 1-5mm apart and dip moderately to the south. Undulating fabric attributed to open fold. Quartz veins common. • Photos 53-57: Fabric.	Foliation: 105/42 Foliation: 107/36 Lineation – crenulation: 15→289 Lineation – crenulation: 18→285 Samples: 22AK-013-1-1: Foliation 155/38 Top
22AK-014	63.95654	135.23777	• Lithology 1: chloritic schist. Lithology 2: interbedded shale and limestone. Lithology 3: greenstone. • Minerals: 1) chlorite, white mica, quartz, +/- calcite, +/- graphite. 2) clay, calcite, +/- graphite, and 3) chlorite, actinolite. • Foliation planes of schist are 1-3mm apart and orient parallel to bedding. Crenulation fabric present in schist layer. Limestone beds are 10-30cm thick, shale beds are 3-5cm thick. Cleavage observed in shale, oblique to bedding. Massive, blocky greenstone is crosscut by 30cm wide quartz vein. Possible folding. • Photos 58-62: Fabric and outcrop.	Foliation: 105/30 Cleavage: 050/42 Cleavage: 040/37 Bedding: 115/50 Bedding: 113/30 Lineation – intersection: 27→180 Samples: 22AK-014-1-1, 22AK-014-2-1: Cleavage 055/35 Top
22AK-015	63.93412	135.22952	• Chlorite-muscovite schist • Minerals: chlorite, white mica, quartz, +/- graphite • Localized C-S Fabric and deformed quartz veins show top the southeast shear sense. Isoclinal S-folds in quartz veins with top to the north-northwest. • Photos 65-71: Fabric, fold, and outcrop.	Foliation: 115/16 Foliation: 110/14 Samples: 22AK-015-1-1: Foliation 105/32 Top
22AK-016	63.95200	135.19264	• Chlorite-muscovite schist. • Minerals: chlorite, white mica, quartz, +/- graphite	Foliation: 114/15 Foliation: 105/32

Station #	Latitude (N)	Longitude (W)	Observations	Structures and Samples
			• Wavy to folded foliation planes. Undulating fabric attributed to open fold. Deformed quartz veins common. Local crenulated fabric. • Photos 86-93: Fabric, fold, and outcrop.	Foliation: 110/23 Open fold axis: 33→145 Open fold axial plane: 325/74 Asymmetric fold axis: 08→225 Asymmetric fold axial plane: 045/10 Lineation – crenulation: 10→141 Lineation – crenulation: 29→126 Samples: 22AK-016-1-1: non foliation surface 221/32 Top
22AK-017	63.95077	135.18220	• Chlorite-muscovite schist. • Minerals: chlorite, white mica, quartz, +/- graphite, +/- calcite • Wavy to folded foliation planes. Undulating fabric attributed to open fold. Deformed quartz veins running parallel to foliation common. Local crenulated fabric. • Shear sense: Top to northwest. • Photos 94-100: Fabric, fold, and outcrop.	Foliation: 103/44 Foliation: 113/42 Lineation – crenulation: 31→125 Fold Axis: 30→165 Axial Plane: 105/22 Samples: 22AK-017-1-1: non-foliation surface 075/36 Top
22AK-018	63.94938	135.18358	• Lithology 1: Chloritic schist. Lithology 2: graphitic schist. • Minerals: 1) chlorite, white mica, quartz, +/- graphite, and 2) graphite, white mica, quartz, +/- chlorite. • Chlorite schist is ~10m thick overlying ~1m thick graphitic schist. Both lithologies have well-developed foliation (Lithology 1 – wavy, Lithology 2 – planar) and local crenulated fabric. Abundant deformed quartz veining in chloritic schist. Less quartz veining in graphitic schist. • This outcrop is stratigraphically higher than station 22AK-017, suggesting alternating schistose layers. • Shear sense: Top to northwest • Photos 101-112: Fabric and folds.	Foliation: 126/34 Foliation: 117/31 Foliation: 107/32 Lineation – Crenulation: 12→129 Lineation – Crenulation: 22→126 Samples: 22AK-018-1-1: Foliation 120/25 Top, 22AK-018-2-1: Foliation 115/10 Top
22AK-019	63.94656	135.18383	• Lithology 1: greenstone. Lithology 2: graphitic schist. • Minerals: 1) chlorite, actinolite, and 2) graphite, white mica, quartz, +/- chlorite. • Massive, blocky greenstone sill is ~20m thick overlying ~5-10m thick platy graphitic schist containing abundant quartz veins. Well developed foliation and local crenulated fabric in graphitic schist. Open folding visible in lithology 2.	Foliation: 106/41 Open Fold Axis: 17→146 Open Fold Axial Plane: 326/70 Lineation – Crenulation: 21→130 Samples: 22AK-019-1-1: Foliation 092/40 Bottom

Station #	Latitude (N)	Longitude (W)	Observations	Structures and Samples
			• Photos 113-114: Outcrop and fold.	
22AK-020	63.94853	135.19578	• Interbedded chlorite, graphite, and quartz rich schists. • Minerals: graphite, white mica, quartz, chlorite. • Well developed foliation and local crenulations present in all layers. • Photos 115-117: Fabric and folds.	Foliation: 095/06 Foliation: 105/17 Lineation – Crenulation: 26→135 Samples: 22AK-020-1-1: non-foliation surface 020/22 Top, 22AK-020-1-2: Foliation 09026 Top
22AK-021	63.93346	135.23773	• Lithology 1: Chloritic schist. Lithology 2: graphitic quartzite. • Minerals: 1) chlorite, white mica, quartz, +/- graphite, and 2) quartz, graphite. • Lithology 1 has a wavy foliation, local crenulated fabric, and abundant deformed quartz veins. Lithology 2 has alternating quartz rich and graphite rich layers at the mm scale. Open fold. Poorly developed shear sense indicators. • Photos 118-123: Fabric and folds.	Foliation: 110/13 Foliation: 112/22 Foliation: 116/37 Lineation – Crenulation: 1→134 Open Fold Axis: 26→140 Open Axial Plane: 320/72 Samples: 22AK-021-1-1: non-foliation surface 065/05 Top, 22AK-021-2-1: non-foliation surface 057/33 Bottom
22AK-022	63.93358	135.34085	• Quartz rich graphitic schist • Minerals: graphite, quartz, white mica, +/- calcite, +/- pyrite • Abundant deformed quartz veins both concordant and discordant. Isoclinal folds and crenulated fabric. Undulating foliation. • Photos 124-129: Fabric and folds.	Foliation: 124/55 Foliation: 116/44 Lineation – Crenulation: 14→130 Lineation – Crenulation: 23→125 Samples: 22AK-022-1-1: Foliation 125/37 Top
22AK-023	63.93978	135.42398	• Chlorite-muscovite schist • Minerals: chlorite, white mica, quartz, +/- graphite • Isoclinal folds and crenulated fabric. Wavy and folded foliation. Deformed quartz veins. • Photos 130-137: Fabric and folds.	Foliation: 120/22 Fold Axis: 39→158 Axial Plane: 158/82 Isoclinal Fold Axis: 05→095 Isoclinal Fold Axial Plane: 095/15 Samples: 22AK-023-1-1: Foliation 110/20 Top
22AK-024	63.94164	135.24175	• Quartzite • Minerals: quartz, +/-white mica, +/- graphite • Massive, blocky appearance. Quartz veins with isoclinal folds. • Photos 138-141: Fabric and folds.	Samples: 22AK-024-1-1: non-foliation surface 185/73 Top
22AK-025	63.93955	135.23751	• Chlorite-muscovite schist	Foliation: 95/22

Station #	Latitude (N)	Longitude (W)	Observations	Structures and Samples
			• Minerals: chlorite, white mica, quartz, +/- graphite • Crenulated fabric. Wavy foliation. Deformed quartz veins. Fabric undulates with open fold. • Photos 142-148: Fabric, folds, and outcrop.	Foliation: 102/43 Fold Axis: 17→125 Axial Plane: 305/86 Lineation – Crenulation: 32→149 Lineation – Crenulation: 27→144 Samples: 22AK-025-1-1: non-foliation surface 050/25 Top
22AK-026	63.94089	135.19604	• Same as previous station. Z-fold. • Shear sense: Top to the northwest • Photos 149-159, 412-418: Fabric and folds.	Foliation: 089/27 Foliation: 098/37 Lineation – Crenulation: 41→150 Fold Axis [1]: 20→228 Fold Axial Plane [1]: 105/32 Fold Axis [2]: 14→217 Fold Axial Plane [2]: 137/60 Samples: 22AK-026-1-1: Foliation 110/34 Bottom
22AK-027	63.92876	135.18367	• Lithology 1: quartz rich graphitic schist. Lithology 2: greenstone. • Minerals: 1) graphite, quartz, white mica, +/- calcite, and 2) chlorite +/- actinolite. • Lithology 1 has a wavy foliation, is blocky to platy in appearance and contains deformed quartz veins. Open fold present. Lithology 2 overlies lithology 1 and is massive, blocky. • Photos 174-175: Folds, and outcrop.	Foliation: 092/16 Foliation: 119/47 Foliation: 112/46 Open Fold Axis: 20→175 Open Fold Axial Plane: 355/83 No sample.
22AK-028	63.92950	135.17458	• Same as previous station. • Photos 176-178: Outcrop, and fabric.	Foliation: 089/28 Foliation: 093/25 Foliation: 099/29 Lineation – Crenulation: 14→130 Lineation – Crenulation: 32→140 Samples: 22AK-028-1-1: Foliation 105/35 Top
22AK-029	63.93060	135.17534	• Same as previous station. Lithology 1 interbedded with locally calcareous quartzite and has isoclinal folds. • Photos 179-182: Outcrop, folds, and fabric.	Foliation: 105/23 Foliation: 113/25 Lineation – Crenulation: 10→139 Fold Axis [SE Face]: 09→310 Axial Plane [SE]: 130/32 Fold Axis [NE Face]: 05→125

Station #	Latitude (N)	Longitude (W)	Observations	Structures and Samples
				Axial Plane [NE]: 305/10 Samples: 22AK-029-1-1: Foliation 100/20 Top, 22AK-029-2-1: Foliation 125/17
22AK-030	36.93742	135.16066	• Graphite bearing Chlorite-muscovite schist. • Minerals: chlorite, white mica, quartz, graphite • Crenulated fabric. Wavy foliation. Deformed quartz veins. Open fold. Photos 183-185: Fabric, and outcrop.	Foliation: 124/24 Foliation: 111/32 Lineation – Crenulation: 14→134 Open Fold Axis: 07→135 Open Fold Axial Plane: 315/60 Samples: 22AK-030-1-1: Foliation 147/30 Top
22AK-031	63.93374	135.13406	• Lithology 1: quartzite. Lithology 2: quartz rich chlorite-muscovite schist. Lithology 3: graphitic schist. • Minerals: 1) quartz, graphite, white mica, 2) chlorite, white mica, quartz, +/- graphite, and 3) graphite, quartz, white mica. • Lithology 1 overlies the other two lithologies and has poorly developed foliation defined by mica and/or graphite. Lithology 2 and lithology 3 are interbedded and both have abundant deformed quartz veins. Lithology 2 has a wavy foliation and lithology 3 has a platy appearance. Open fold and local crenulations. C-S fabric. • Shear sense: top to the northwest. • Photos 186-194: Folds, fabric, and outcrop.	Foliation & Bedding: 114/31 Foliation: 119/46 Foliation: 111/31 Fold Axis: 34→200 Axial Plane: 200/76 Lineation – Crenulation: 10→139 Samples: 22AK-031-1-1: Foliation 121/22 Top, 22AK-031-2-1: Foliation 132/28 Top, 22AK-031-3-1: Foliation 120/47 Top
22AK-032	63.94257	135.16894	• Lithology 1: graphitic schist. Lithology 2: quartzite. Lithology 3: greenstone. • Minerals: 1) graphite, quartz, white mica, 2) quartz, graphite, white mica, and 3) chlorite. • Lithology 1 has well developed, platy foliation, local crenulations, and abundant deformed quartz veins. Lithology 2 is blocky but has a poorly developed foliation defined by micas and/or graphite and quartz veins. Open fold. • Shear sense: top to the northwest. • Photos 195-200: Folds, fabric, and outcrop.	Foliation: 096/30 Foliation & Bedding: 145/21 Lineation – Crenulation: 143/24 Fold Axis: 09→223 Fold Axial Plane: 043/81 Samples: 22AK-032-1-1: non-foliation surface 067/27 Bottom, 22AK-032-2-1: foliation 155/14 Top
22AK-033	63.94339	135.16193	• Chlorite-muscovite schist • Minerals: chlorite, white mica, quartz, +/- graphite, +/- pyrite	Foliation: 123/22 Foliation: 114/40 Fold Axis [1]: 36→209

Station #	Latitude (N)	Longitude (W)	Observations	Structures and Samples
			• Wavy foliation, locally folded, abundant deformed quartz veins, and platy appearance. Locally crenulated. • Photos 201-204: Outcrop and folds.	Axial Plane [1]: 029/72 Fold Axis [2]: 34→235 Axial Plane [2]: 055/72 Lineation – Crenulation: 16→138 Samples: 22AK-033-1-1: Foliation 110/23 Top
22AK-034	63.94512	135.15238	• quartzite • Minerals: quartz, graphite, white mica, +/- calcite, +/- pyrite • Planar foliation, concordant and discordant quartz veins.	Foliation: 122/30 Foliation & Bedding: 116/24 Fold Axis: 29→235 Axial Plane: 055/ 76 Lineation – Crenulation: 04→305 Lineation – Crenulation: 22→315 Samples: 22AK-034-1-1: Foliation 165/30 Top
22AK-035	63.94805	135.14259	• Same as previous station. No discordant quartz veins at this location. Z-fold quartz veins. • Shear sense: Top to the northwest • Photos 205-209: Fabric, and fold.	Foliation & Bedding: 096/12 Foliation & Bedding: 104/14 Fold Axis: 18→202 Axial Plane: 022/77 Samples: 22AK-035-1-1: Foliation 155/21 Top
22AK-036	63.94142	135.18786	• Chlorite-muscovite schist • Minerals: chlorite, white mica, quartz, +/- graphite • Wavy foliation, abundant deformed quartz veins, and platy appearance. Locally crenulated. C-S Fabric. • Shear sense: Top to the northwest • Photos 210-212: Outcrop and fabric.	Foliation: 113/19 Foliation: 104/25 Lineation – Crenulation: 8→144 Lineation – Crenulation: 16→146 No sample.
22AK-037	63.95747	135.18584	• Quartz rich Chlorite-muscovite schist • Minerals: chlorite, white mica, quartz, +/- graphite, +/- pyrite • Wavy foliation, abundant deformed quartz veins, and platy appearance. Locally crenulated. Undulating fabric attributed to open folding. • Photos 213-216: Outcrop, fold, and fabric.	Foliation: 093/29 Foliation: 102/26 Fold Axis: 16→221 Axial Plane: 041/85 Lineation – Crenulation: 06→136 Samples: 22AK-037-1-1: Foliation 098/22 Top

Station #	Latitude (N)	Longitude (W)	Observations	Structures and Samples
22AK-038	63.95800	135.19384	• Lithology 1: Quartz rich Chlorite-muscovite schist. Lithology 2: quartzite. • Minerals: 1) chlorite, white mica, quartz, +/- graphite, +/- pyrite, and 2) quartz, graphite, +/- white mica • Lithology 1 has wavy foliation, abundant deformed quartz veins, and platy appearance. Locally crenulated. Lithology 2 has planar foliation defined by graphite layers. Z-fold quartz vein. C-S fabric. • Shear sense: Ambiguous to top to the northwest. • Photos 217-222: Fold, and fabric.	Foliation: 125/25 Foliation: 117/31 Foliation & Bedding: 115/20 Lineation – Crenulation: 06→138 Samples: 22AK-038-1-1: Foliation 095/21 Top, 22AK-038-2-1: Foliation 090/25 Bottom
22AK-039	63.90127	135.27467	• Lithology 1: Chlorite-muscovite schist. Lithology 2: graphitic schist. • Minerals: 1) chlorite, white mica, quartz, +/- graphite, +/- pyrite, and 2) graphite, quartz +/- white mica • Lithology 1 has wavy foliation, deformed by open and isoclinal folds and contains deformed quartz veins. Locally crenulated. Lithology 2 has wavy foliation and contains deformed quartz veins and folds. S-fold. • Shear sense: Ambiguous to top to the northwest. • Photos 229-233: Fold, and fabric.	Foliation: 106/37 Fold Axis [1]: 17→160 Axial Plane [1]: 160/86 Fold Axis [2]: 32→140 Axial Plane [2]: 320/78 Fold Axis [3]: 36→176 Axial Plane [3]: 356/75 Samples: 22AK-039-1-1: Foliation 115/34 Bottom, 22AK-039-2-1: non-foliation surface 080/32 Bottom
22AK-040	63.85677	135.18436	• Quartz rich graphitic schist. • Minerals: quartz, +/- white mica, +/- graphite • Wavy foliation, abundant deformed quartz veins, platy appearance. Locally crenulated and undulating foliation attributed to an open fold. • Shear sense: Ambiguous to top to the northwest. • Photos 250-256: outcrop, fold, and fabric.	Foliation: 132/31 Foliation: 139/41 Fold Axis: 17→215 Axial Plane: 042/65 Quartz vein Fold Axis: 06→295 Quartz vein Axial Plane: 295/58 Samples: 22AK-040-1-1: Foliation 115/15 Top
22AK-041	63.85734	135.18274	• Same as previous station. Z-fold isoclinal quartz veins. High shear strain. • Shear sense: Ambiguous to top to the northwest. • Photos 257-261: Fabric, and fold.	Foliation: 142/31 Fold Axis: 03→357 Fold Axial Plane: 357/31 Samples: 22AK-041-1-1: Foliation 145/32 Bottom
22AK-042	63.85997	135.18085	• Same as previous station. • Shear sense: Ambiguous to top to the northwest.	Foliation: 129/39 Fold Axis: 20→232 Axial Plane: 052/6

Station #	Latitude (N)	Longitude (W)	Observations	Structures and Samples
			• Photos 262-270: Fabric, and fold.	Samples: 22AK-042-1-1: Foliation 130/29 Top
22AK-043	63.86115	135.18326	• Chlorite-muscovite schist • Minerals: chlorite, white mica, quartz • Wavy foliation, abundant deformed quartz veins, and platy appearance. Locally crenulated. Undulating foliation. • Photos 271-272: fold, and fabric.	Foliation: 098/25 Open Fold Axis: 02→160 Open Fold Axial Plane: 340/71 Samples: 22AK-043-1-1: non-foliation surface 210/29 Top
22AK-044	63.86344	135.18544	• Low grade slate. • Minerals: clay, quartz, +/- white mica, +/- graphite • Planar foliation, deformed quartz veins, platy appearance. • Shear sense: Ambiguous to top to the northwest. • Photos 273-275: outcrop, fold, and fabric.	Foliation: 134/25 Fold Axis: 08→315 Axial Plane: 315/65 Samples: 22AK-044-1-1: Foliation 117/11 Bottom
22AK-045	63.86598	135.18981	• Lithology 1: low grade slate. Lithology 2: graphite-muscovite schist. Lithology 3: coal boudins within lithology 2. • Minerals: 1) clay, quartz, +/- white mica, +/- graphite, 2) graphite, white mica, quartz, +/- chlorite, and 3) coal +/- calcite. • Lithology 1 and 2 have planar foliation. Local small folds. C-S Fabric. • Shear sense: top to the northwest • Photos 276-284: fabric, and fold.	Foliation: 128/29 Fold Axis: 27→008 Axial Plane: 188/88 Samples: 22AK-045-1-1: Foliation 128/23 Top, 22AK-045-2-1: Foliation 105/38 Top, 22AK-045-3-1
22AK-046	63.87111	135.14889	• Low grade slate • Minerals: clay, quartz, +/- white mica, +/- graphite. • Planar foliation, local tight folds and crenulations, abundant deformed quartz veins. • Photos 285-286: fabric and fold.	Foliation: 159/27 Foliation: 141/70 Open Fold Axis [1]: 34→145 Open Fold Axial Plane [1]: 147/55 Open Fold Axis [2]: 27→329 Open Fold Axial Plane [2]: 329/80 Fold Axis: 30→148 Axial Plane: 328/16 Samples: 22AK-046-1-1: Foliation 173/37 Top
22AK-047	63.87307	135.15565	• Same as previous station. • Shear sense: top to the northwest. • Photos 287-296: Fabric and fold.	Foliation: 135/24 Foliation: 172/21 Fold Axis: 28→224 Axial Plane: 224/89 Isoclinal Fold Axis: 31→259

Station #	Latitude (N)	Longitude (W)	Observations	Structures and Samples
				Isoclinal Fold Axial Plane: 079/06 Quartz Vein Fold Axis: 21→177 Quartz Vein Fold Axial Plane: 357/08 Samples: 22AK-047-1-1: Foliation 167/17 Top
22AK-048	63.87241	135.16109	• Graphite-muscovite schist • Minerals: graphite, white mica, quartz, +/- calcite, +/- pyrite • Wavy foliation, deformed quartz veins, and local limestone lenses. Multiple isoclinal to open folds. • Shear sense: Ambiguous to top to the northwest. • Photos 297-303: fold, and fabric.	Foliation: 145/22 Fold Axis [1]: 17→245 Axial Plane [1]: 065/76 Isoclinal Fold Axis: 11→276 Isoclinal Fold Axial Plane: 096/15 Fold Axis [2]: 07→157 Axial Plane [2]: 337/66 Fold Axis [3]: 05→152 Axial Plane [3]: 332/76 Samples: 22AK-048-1-1: Foliation 160/30 Top
22AK-049	63.87218	135.16843	• Lithology 1: quartzite. Lithology 2: graphite-muscovite schist. • Minerals: 1) quartz, graphite, white mica, and 2) graphite, quartz, white mica. • Lithology 1 has poorly developed foliation defined by graphitic layers and is isoclinally folded. Lithology 2 is structurally below Lithology 1 and has wavy foliation. C-S Fabric. • Photos 304-311: Folds and fabric.	Foliation: 124/24 Foliation: 141/23 Fold Axis: 04→214 Isoclinal Fold Axial Plane: 214/05 Samples: 22AK-049-1-1: Foliation 154/27 Top
22AK-050	63.87200	135.17434	• Same as previous station. Lithology 1 and 2 are interbedded. • Shear sense: top to the northwest. • Photos 312-320: Fabric and fold.	Foliation: 168/34 Fold Axis: 23→242 Axial Plane: 125/30 Fold Axis: 16→203 Axial Plane: 023/52 Quartz Fold Axis: 22→270 Quartz Fold Axial Plane: 090/55 No Sample.
22AK-051	63.87178	135.17856	• Same as previous station. • Photos 321-324: Fabric and outcrop.	Foliation: 145/39 No sample.

Station #	Latitude (N)	Longitude (W)	Observations	Structures and Samples
22AK-052	63.88160	135.14077	• Quartzite • Minerals: quartz, graphite, +/-white mica • Beds are openly folded. Deformed quartz veins. • Shear sense: Ambiguous to top to the northwest. • Photos 325-331: Fabric and folds.	Foliation: 130/32 Foliation: 100/24 Fold Axis [1]: 24→235 Axial Plane [1]: 055/79 Fold Axis [2]: 05→277 Axial Plane [2]: 097/65 Samples: 22AK-052-1-1: Foliation 135/32 Top
22AK-053	63.88797	135.14197	• Greenstone • Minerals: chlorite, plagioclase • Poorly developed foliations. Greenstone is overlying the quartzite of the previous station. • Photos 332: Fabric.	Foliation: 097/37 Samples: 22AK-053-1-1: Foliation 110/38 Top
22AK-054	63.89084	135.14712	• Quartzite • Minerals: quartz, +/- graphite, +/- white mica • Blocky, possibly folded. • Photos 333-334: Fabric.	Foliation & Bedding: 105/25 Lineation - Mineral Growth: 06→118 Cleavage: 043/89 Cleavage: 000/73 Samples: 22AK-054-1-1: Bedding/Foliation 110/36 Top
22AK-055	63.89501	135.15447	• Same as previous station with thin ~5cm limestone layers. • Just north the quartzite is interbedded with graphitic schist (lithology 2) which has well developed foliation, locally folded, and contains deformed quartz veins. • Photos 335-340: Fabric and outcrop.	Foliation: 104/23 Foliation & Bedding: 096/09 Isoclinal Fold Axis: 05→271 Isoclinal Fold Axial Plane: 091/23 Open Fold Axis: 03→181 Open Axial Plane: 181/72 Samples: 22AK-055-2-1: Foliation 120/22 Top
22AK-056	63.90048	135.17041	• Quartzite interbedded with limestone layers • Minerals: quartz, +/- graphite, +/- white mica • Blocky, deformed quartz veins, z-folds, open fold. • Photos 341-346: Fabric and folds.	Foliation & Bedding: 100/09 Z-Fold Axis: 09→269 Z-Fold Axial Plane: 089/02 Open Fold Axis: 05→141 Open Fold Axial Plane: 141/86

Station #	Latitude (N)	Longitude (W)	Observations	Structures and Samples
				Samples: 22AK-056-1-1: Foliation/bedding 095/11 Top
22AK-057	63.90309	135.17872	• Quartzite interbedded with limestone and graphitic schist layers • Same as previous. Isoclinal Fold. • Photos 347: Fold.	Foliation: 127/20 Isoclinal Fold Axis: 10→267 Isoclinal Fold Axial Plane: 087/10 No Sample.
22AK-058	63.91366	135.29166	• Lithology 1: quartzite. Lithology 2: graphitic schist. • Minerals: 1) quartz, graphite, white mica, and 2) graphite, quartz, white mica. • Lithology 1 is blocky, intruded by greenstone sill, has bedding ~30-60cm thick. Large syncline. Lithology 2 is interbedded with Lithology 1, forms layers ~20-30cm thick, has wavy foliation, and contains deformed quartz veins. • Photos 348-350: Folds, fault, and outcrop.	Foliation: 100/32 Fold Axis: 25→202 Axial Plane: 022/70 Isoclinal Fold Axis: 13→094 Isoclinal Axial Plane: 094/41 Vein Fault Plane: 030/72 No sample.
22AK-059	63.89385	135.57150	• Same as previous station. Isoclinal folds. Graphitic schist (Lithology 1) beds are ~5-10cm thick and Quartzite (Lithology 2) beds are ~20cm thick. • Photos 351-353: Fabric and folds.	Foliation: 073/42 Fold Axis: 41→187 Axial Plane: 007/36 Fold Axis: 36→231 Axial Plane: 051/20 Samples: 22AK-059-1-1: Foliation 073/44 Top
22AK-060	63.87922	135.37786	• Graphitic schist with quartz rich layers. • Minerals: graphite, quartz, white mica, +/- calcite • Wavy foliation that undulates across outcrop. • No photos.	Foliation: 152/17 Foliation: 149/34 Foliation: 098/20 Samples: 22AK-060-1-1: Foliation 107/11 Top
22AK-061	63.86395	135.41108	• Quartz grit schist. • Minerals: quartz, white mica, +/- graphite • Wavy foliation, some deformed quartz veins • Photos 354: Fabric.	Foliation: 119/15 Samples: 22AK-061-1-1: Foliation 090/07 Bottom
22AK-062	63.90579	135.32979	• Lithology 1: Muscovite schist interbedded with Lithology 2: Graphitic schist.	Foliation: 119/62 Foliation: 086/20 Open Fold Axis: 27→114

Station #	Latitude (N)	Longitude (W)	Observations	Structures and Samples
			• Minerals: 1) white mica, quartz, +/- graphite, and 2) graphite, quartz, white mica • Wavy foliation that undulates across outcrop. Deformed quartz veins. Isoclinal folds, s-fold, open folds. • Shear sense: Top to the northwest. • Photos 370-374	Open Fold Axial Plane: 114/77 Fold Axis: 11→204 Axial Plane: 024/30 S-Fold (open) Axis: 15→137 S-fold (open) Axial Plane: 317/71 Samples: 22AK-062-1-1: non-foliation surface 025/27
22AK-063	63.90848	135.42953	• Muscovite schist • Minerals: white mica, quartz, graphite, chlorite • Wavy and folded foliation, and deformed quartz veins. • Photos 375-376: folds.	Foliation: 189/51 Foliation: 087/44 Open Fold Axis: 54→147 Open Fold Axial Plane: 147/74 Samples: 22AK-063-1-1: non-foliation surface 045/43 Top, 22AK-063-1-2, 22AK-063-1-3: non-foliation surface 043/52 Top
22AK-064	63.90398	135.45239	• Muscovite schist overlying graphitic schist. • Minerals: white mica, quartz, +/- graphite, +/- chlorite • Wavy and folded foliation, and abundant deformed quartz veins. Undulating foliation. Isoclinal fold folded by later fold. Local crenulated fabric. • Shear sense: Ambiguous to top to the northeast. • Photos 377-381: folds and fabric.	Foliation: 093/25 Fold Axis: 46→152 Axial Plane: 152/74 Lineation – Crenulation: 24→155 Samples: 22AK-064-1-1: Foliation 110/20 Top
22AK-065	63.90862	135.35548	• Lithology 1: greenstone. Lithology 2: graphitic schist. Lithology 3: muscovite schist. • Minerals: 1) chlorite, 2) graphite, chlorite, quartz, +/- white mica, and 3) white mica, chlorite, quartz. • Lithology 2 has a planar foliation and abundant deformed quartz veins. Lithology 3 has a wavy foliation and deformed quartz veins. • No photos.	Foliation: 110/20 Foliation: 128/14 Foliation: 187/16 Samples: 22AK-065-3-1: non-foliation surface 220/23 Top
22AK-066	63.90891	135.35904	• Muscovite schist • Minerals: white mica, quartz, graphite, chlorite • Wavy and folded foliation, and deformed quartz veins. Partially slumped in spots – low confidence measurements.	Foliation: 108/40 Open Fold Axis: 48→135 Open Fold Axial Plane: 306/52 Open Fold Axis: 64→121

Station #	Latitude (N)	Longitude (W)	Observations	Structures and Samples
			• Photos 382: outcrop and fold.	Lineation – Crenulation: 29→134 Samples: 22AK-066-1-1
22AK-067	63.91701	135.39244	• Quartzite • Minerals: quartz, +/- graphite, +/- white mica, • Weakly foliated/planar fabric. Blocky. Possibly slumped. • No photos.	Foliation: 085/19 Samples: 22AK-067-1-1: Foliation 115/13 Top
22AK-068	63.8769	135.18468	• Graphitic schist interbedded with low grade slate. • Minerals: graphite, white mica, quartz. • Wavy to planar foliation. Deformed quartz veins. Isoclinal and open folds. Partially slumped in spots – lower confidence measurements. • Shear sense: Ambiguous to top to the northeast. • Photos 387-395, 409-410: folds, outcrop, and fabric.	Foliation: 182/31 Foliation: 152/30 Fold Axis [1]: 17→157 Axial Plane [1]: 157/25 Open Fold Axis: 16→176 Open Fold Axial Plane: 356/78 Fold Axis [2]: 08→159 Axial Plane [2]: 159/05 Samples: 22AK-068-1-1: Foliation 170/15 Top, 22AK-068-1-2: Foliation 170/30 Bottom.
22AK-069	63.88044	135.17646	• Lithology 1: Muscovite schist interbedded with Lithology 2: Quartzite. • Minerals: 1) white mica, quartz, +/- graphite, and 2) quartz, white mica, +/- pyrite. • Planar foliation. Local deformed quartz veins. S-fold. C-S Fabric. • Shear sense: Top to the northwest. • Photos 396-399: folds, outcrop, and fabric.	Foliation & Bedding: 140/41 Samples: 22AK-069-1-1: Foliation 130/47 Bottom, 22AK-069-2-1: Foliation 132/46 Bottom, 22AK-069-2-2
22AK-070	63.88182	135.16237	• quartzite. • Minerals: Quartz, graphite. • Talus field. Float shows isoclinal fold folded by open fold. • Photo 400: fold.	Samples: 22AK-070-1-1
22AK-071	63.87925	135.20652	• Graphitic schist. • Minerals: graphite, white mica, quartz.	Foliation: 090/24 Isoclinal Fold Axis: 01→283 Isoclinal Axial Plane: 103/29

Station #	Latitude (N)	Longitude (W)	Observations	Structures and Samples
			• Wavy, folded foliation. C-S Fabric. Abundant deformed quartz veins. S-fold. Isoclinal folds. • Photos 401-406: fold and fabric.	Fold Axis [1]: 26→160 Axial Plane [1]: 160/71 Fold Axis [2]: 21→024 Axial Plane [2]: 153/17 Fold Axis [3]: 04→269 Axial Plane [3]: 089/64 Samples: 22AK-071-1-1: Foliation 075/28
22AK-072	63.87748	135.21520	• Muscovite schist. • Minerals: white mica, chlorite, quartz, +/- graphite. • Planar foliation. Deformed quartz veins. C-S Fabric. Undulating fabric. • Photo 407-408, 411: fabric and fold	Foliation: 137/31 Foliation: 082/21 Foliation: 275/42 Fold Axis: 16→319 Axial Plane: 319/15 Samples: 22AK-072-1-1: Foliation 130/32 Top, 22AK-072-1-2: non-foliation surface 275/22 Top.
22AK-073	63.95473	135.14009	• Muscovite schist. • Minerals: white mica, chlorite, quartz, graphite, +/- staurolite? • Planar foliation. Possible aplite in proximity. Undulating fabric. • Photo 419-423: fabric and outcrop.	Foliation: 054/25 Samples: 22AK-073-1-1: Foliation 065/16 Bottom.
22AK-074	63.95884	135.11516	• Lithology 1: Graphitic schist. Lithology 2: greenstone. • Minerals: 1) graphite, quartz, and 2) chlorite, +/- calcite, +/- plagioclase. • Lithology 1 has a wavy to planar foliation. Lithology 2 is block in appearance. • No photos.	Foliation: 125/60 Samples: 22AK-074-1-1
22AK-075	63.95353	135.1394	• Chlorite-Muscovite schist. • Minerals: white mica, chlorite, quartz, graphite. • Planar foliation. Undulating fabric due to open fold. Deformed quartz veins. • Photo 424: fabric.	Foliation: 125/56 Open Fold Axis: 34→149 Open Fold Axial Plane: 329/73 Samples: 22AK-075-1-1: Foliation 098/73 Bottom.
22AK-076	63.86200	135.20229	• Low grade slate. • Minerals: clay, graphite, quartz, +/- pyrite.	Foliation: 131/33 Foliation: 128/44

Station #	Latitude (N)	Longitude (W)	Observations	Structures and Samples
			• Planar foliation. Deformed quartz veins. • No photos.	Samples: 22AK-076-1-1: Foliation 122/21 Bottom
22AK-077	63.86070	135.20045	• Same as previous station. High shear strain. Isoclinal folds. • Photos 425-430: Fabric and folds.	Foliation: 140/37 Foliation: 131/35 Samples: 22AK-077-1-1: Foliation 115/35 Bottom
22AK-078	63.85819	135.20217	• Quartz grit schist. • Minerals: quartz, white mica, graphite, +/- chlorite. • Planar foliation. Deformed quartz veins. High shear strain. • Photos 431-432: fabric	Foliation: 129/20 Foliation: 152/16 Samples: 22AK-078-1-1: Foliation 150/16 Bottom.
22AK-079	63.85639	135.20003	• Quartz rich graphitic schist • Minerals: quartz, graphite, +/- pyrite. • Planar foliation. Deformed quartz veins. Z-fold. • Photo 433: fold.	Foliation: 140/19 Foliation: 139/24 Z-Fold Axis: 30→171 Z-fold Axial Plane: 351/70 Samples: 22AK-079-1-1: Foliation 129/11 Top.
22AK-080	63.86382	135.20749	• Lithology 1: quartz rich graphitic schist interbedded with Lithology 2: low grade slate. • Minerals: 1) graphite, quartz, white mica, and 2) clay, graphite, quartz. • Lithology 2 has planar foliation, lithology 1 has planar to wavy foliation. Deformed quartz veins. Isoclinal folds. Z-folds. • Shear sense: ambiguous to top to the northwest. • Photo 434-440: folds and fabric.	Foliation: 116/16 Z-Fold Axis: 18→228 Z-fold Axial Plane: 048/73 Samples: 22AK-080-1-1: Foliation 119/14 Bottom.
22AK-081	63.98900	134.94673	• Graphitic schist • Minerals: graphite, biotite, quartz, +/- garnet, +/- staurolite. • Cobalt Hill. Wavy to planar foliation. Deformed quartz veins. Isoclinal folds. Subvertical foliation in spots. Multiple folds. • Photo 441-446: folds and fabric.	Foliation: 106/34 Open Fold Axis [2]: 06→303 Open Fold Axial Plane [2]: 303/77 Isoclinal Fold Axis: 26→235 Isoclinal Fold Axial Plane: 061/16 Open Fold Axis [1]: 21→120 Open Fold Axial Plane [1]:115/30

Station #	Latitude (N)	Longitude (W)	Observations	Structures and Samples
				Samples: 22AK-081-1-1: Foliation 105/44 Bottom, 22AK-081-1-2: Foliation 103/75 Bottom, 22AK-081-1-1: Foliation 100/76 Bottom.
22AK-082	63.89502	135.26427	• Quartz grit schist. • Minerals: quartz, white mica, +/- graphite. • Planar foliation. Deformed quartz veins. • Photos 447-448: fabric	Foliation: 121/42 Samples: 22AK-082-1-1: Foliation 098/17 Top, 22AK-082-1-2.

APPENDIX B: THIN SECTION DESCRIPTIONS

Sample ID	Lithology, Composition, and Quartz : Phyllosilicate Abundance Ratio	Textures	Fabric
22AK-001-1-1	• Quartzite • Quartz, White mica, opaques • 70-85 : 15-30	• Medium to very fine grained. Possibly two different compositional layers - white mica occurs in thicker layers and has higher birefringence where quartz grains are smaller and white mica occurs in thinner layers and has lower birefringence where quartz grains are coarser. • Quartz: Undulose extinction. Bimodal grainsize. Inequigranular to seriate. Polygonal to Interlobate. Subhedral. Sub-grain rotation (SGR). • Limited Grain Boundary Area Reduction (GBAR), Low recovery.	• Well developed foliations defined by white mica mats. Layers are discontinuous and wavy near the cut corner and continuous and wavy on the other long end of the thin section. Aggregate preferred orientation. • Low-Medium Shear Strain. • Shear sense: Inconclusive.
22AK-006-1-1	• Quartz grit schist • Quartz, white mica, plagioclase, opaques • 65-80 : 20-35	• Sericitization of feldspar. Coarse grained to fine grained. • Quartz: Some quartz boudins. Undulose extinction. Bimodal grainsize seriate to inequigranular. Polygonal to interlobate. Subhedral. SGR. • Some GBAR, low recovery	• Well developed fabric with foliations that are poorly defined by discontinuous (straight to partially wavy) thin white mica layers and quartz grains. Aggregate preferred orientation. • Low-Medium Shear Strain
22AK-006-1-2	• Quartz grit schist • Quartz, white mica, plagioclase, potassium feldspar, opaques, chlorite • 65-80 : 20-35	• Sericitization of feldspar. Medium grained to fine grained. • Quartz: Undulose extinction. Bimodal grainsize seriate to inequigranular. Polygonal to interlobate. Subhedral. Subgrain rotation. SGR. Partial Grain boundary migration (GBM): dragging. • Some GBAR, low recovery	• Well developed fabric with foliations that are poorly defined by discontinuous (straight to partially wavy) thin white mica layers and quartz grains parallel to foliation. Aggregate preferred orientation. • Low-Medium Shear Strain • Shear sense: Inconclusive
22AK-011-1-1	• Sericite schist • Quartz, white mica, opaques • 75-90 : 10-25	• Fine to very fine grained. Possible chloritization. • Quartz: equigranular to inequigranular. Polygonal. Subhedral. Undulose extinction. Partial SGR. GBM: dragging, pinning. • Some GBAR, recovery evident	• Well developed fabric with foliations defined by thin, straight continuous white mica layers. Possible proto–CS Fabric. • Low-Medium Shear Strain • Shear sense: Top to the NW

Sample ID	Lithology, Composition, and Quartz : Phyllosilicate Abundance Ratio	Textures	Fabric
22AK-023-1-1	• Chlorite-sericite schist • Quartz, chlorite, white mica, opaques • 75-90 : 10-25	• Fine to very fine grained. • Quartz: Inequigranular. Interlobate. Subhedral. Undulose extinction. SGR. • Some GBAR, Recovery evident	• Well developed fabric. Foliations defined by thin continuous to discontinuous wavy to straight layers of white mica. Asymmetric fold with Top to the West. Some quartz grain alignment with fabric, particularly along the fold. CS Fabric shows top to the west shear as well. • Low Shear Strain • Shear sense: Top to the W
22AK-029-1-1	• Graphite-muscovite schist • Quartz, white mica, graphite, pyrite, calcite • 75-90 : 10-25	• Fine to very fine grained. Discontinuous Calcite grains. • Quartz: Equigranular to inequigranular. Interlobate to Polygonal. Subhedral. Undulose extinction. SGR. • Limited GBAR, Low recovery	• Well developed fabric with foliations defined by continuous to discontinuous thin to thick white mica layers. • Low Shear Strain • Shear sense: Inconclusive
22AK-032-2-1	• Quartzite • Quartz, white mica, opaque, chlorite • >95 : <5	• Fine to very fined grained with some medium grained by a possibly cross cutting quartz vein. • Quartz: Inequigranular. Interlobate. Subhedral-anhedral. SGR. Undulose extinction. • Minimal GBAR, Lowest Recovery	• Poorly developed fabric defined by partially elongated/oriented quartz grains. quartz vein cross cutting thin section shows asymmetric folding with top to the SE. Some thin, straight, discontinuous white mica • Low-Medium Shear Strain • Shear sense: Inconclusive
22AK-037-1-1	• Chlorite-muscovite schist • Quartz, chlorite, white mica, plagioclase • 55-70 : 30-45	• Medium to very fine grained. Crenulated white mica. • Quartz: Interlobate to polygonal. Inequigranular to seriate. Subhedral to anhedral. SGR. Undulose extinction. GBM: window structure, dragging. • Minimal GBAR, Lowest Recovery	• Well developed fabric with foliation defined by thin to thick discontinuous white mica layers that are folded and sheared. Some quartz grains are elongated and folded parallel to the white mica. Chlorite not oriented parallel to fabric. Minor folds in the limbs of the larger fold. • Low Shear Strain • Shear sense: Inconclusive

Sample ID	Lithology, Composition, and Quartz : Phyllosilicate Abundance Ratio	Textures	Fabric
22AK-041-1-1	• Quartz rich Graphite-muscovite schist • Quartz, white mica, opaques • 80-95 : 5-20	• Medium to very fined grained. Crenulated white mica • Quartz: Polygonal to interlobate. Inequigranular to seriate. Subhedral. Undulose extinction. SGR. GBM: dragging, pinning, window structure. Elongated grains. • GBAR evident, More recovery	• Well developed fabric defined by elongated quartz grains and discontinuous to continuous thin straight white mica layers. Possible CS fabric that is developing with top to the SE • Low Shear Strain • Shear sense: Top to the SE.
22AK-043-1-1	• Chlorite-muscovite schist • Quartz, chlorite, white mica, plagioclase, opaques • 70-85 : 15-30	• Medium to very fine grained. Crenulated white mica. • Quartz: Polygonal to interlobate. Seriate. Subhedral. Undulose extinction. SGR. Partial GBM: dragging, pinning, window structure. • Some GBAR, recovery evident	• Well developed fabric with foliation defined by thin to thick discontinuous wavy white mica layers that are folded. • Low Shear Strain • Shear sense: Inconclusive.
22AK-045-2-1	• Graphite-muscovite schist • Quartz, white mica, opaques, chlorite • 70-85 : 15-30	• Medium to very fine grained. • Quartz: Polygonal to interlobate. Seriate to inequigranular. Subhedral. Undulose extinction. SGR. • Minimal GBAR, Lowest Recovery	• Well developed fabric defined by thin discontinuous straight white mica layers and some oriented/elongated quartz grains. Possibly a proto-CS fabric/shear sense indicator? • Low-Medium Shear Strain • Shear sense: Ambiguous – predominantly top the SE.
22AK-045-3-1	• Coal. • Coal, quartz • 100 : 0	• Coarse to fine grained. • Quartz: Polygonal. Euhedral to Subhedral. Seriate. Undulose extinction. Very minor subgrain rotation.	• Vesicular texture infilled by quartz grains and other detrital material. quartz grains do not exhibit strongly deformed textures. • Low Shear Strain
22AK-049-1-1	• Quartzite • Quartz, white mica, opaques • 90->95 : <5-10	• Medium to very fined grained. • Quartz: Seriate to inequigranular. Subhedral. Polygonal to interlobate. SGR. Possible deformation lamellae. • Some GBAR, recovery evident	• Developed fabric defined by elongated quartz grains that are oriented parallel to very thin wavy discontinuous to continuous white mica layers and bands of coarser grained quartz (quartz veins). • Low-Medium Shear Strain

Sample ID	Lithology, Composition, and Quartz : Phyllosilicate Abundance Ratio	Textures	Fabric
22AK-052-1-1	• Quartzite • Quartz, white mica, opaques, chlorite, calcite • 65-80 : 20-35	• Fine to very fine grained. Highly deformed. • Quartz: Interlobate to polygonal. Inequigranular. Subhedral. Undulose extinction. SGR. Partial bulging. • Limited GBAR, Low recovery	• Well developed fabric defined by white mica layers and elongated quartz grains. • Low Shear Strain • Shear sense: Inconclusive
22AK-053-1-1	• Greenstone • Clinopyroxene, Chlorite, actinolite, orthopyroxene, opaques, quartz, calcite, plagioclase • 15-30 : 70-85	• Coarse to very fine grained. Heavily altered and chloritized. Some grains have a recrystallized and altered halo. • Quartz: Anhedral. Undulose extinction. Inequigranular. Interlobate.	• Well developed fabric defined by thick mats of actinolite, chlorite, and orthopyroxene. Possibly 2-3 phases of deformation recorded based on varying (but consistent) angles of actinolite and chlorite habit. • Medium Shear Strain • Shear sense: Inconclusive
22AK-054-1-1	• Quartzite • Quartz, white mica • >95 : <5	• Fine to very fine grained. • Quartz: Polygonal to interlobate. Subhedral. Equigranular to inequigranular. SGR. Partial bulging. • Some GBAR, recovery evident	• Fabric defined by elongated quartz grains, and very thin wavy discontinuous white mica layers. • Low-Medium Shear Strain
22AK-055-2-1	• Quartz rich graphite-muscovite schist • Quartz, opaques, white mica • 65-80 : 20-35	• Very fine grained with some fine-grained layers (possibly veins). Some crenulated white mica. • Quartz: Interlobate to polygonal. Subhedral. Inequigranular. SGR. Partial bulging. • Some GBAR, recovery evident.	• Well developed fabric defined by thin straight continuous white mica layers and some elongated quartz grains. • Low Shear Strain • Shear sense: Inconclusive
22AK-060-1-1	• Quartz rich graphite-muscovite schist • Quartz, white mica, opaques, calcite • 80-95 : 5-20	• Calcite located on the side of a quartz grain. Variable grain size. • Quartz: Seriate. Polygonal. Subhedral. SGR. Possible deformation lamellae. Undulose extinction. • Some GBAR, recovery evident	• Well developed fabric defined by thin straight discontinuous white mica layers and elongated quartz grains. Crosscut by a discordant quartz vein. • Low-Medium Shear Strain • Shear sense: Top to the SE.

Sample ID	Lithology, Composition, and Quartz : Phyllosilicate Abundance Ratio	Textures	Fabric
22AK-061-1-1	• Quartz grit schist • Quartz, white mica • 70-85 : 15-30	• Coarse to very fine grained (bimodal). • Quartz: Inequigranular. Polygonal, Subhedral. Undulose extinction. Possible deformation lamellae. SGR. GBM: left over grains, window, pinning. Triple Junctions. • GBAR evident, More recovery	• Well developed fabric defined by thin discontinuous to continuous straight white mica layers and elongated / oriented quartz grains. quartz grains are not organized by grain size. Aggregate preferred orientation. • Low-High Shear Strain • Shear sense: Top to the E.
22AK-067-1-1	• Quartzite • Quartz, white mica • >95 : <5	• Very fine grained. • Quartz: subgrain rotation. Undulose extinction. Equigranular to inequigranular. Interlobate to polygonal. Subhedral. SGR. • Minimal GBAR, Lowest Recovery	• Developed fabric defined by elongated quartz grains and very thin discontinuous white mica layers. • Medium Shear Strain • Shear sense: Inconclusive.
22AK-069-2-1	• Quartzite • Quartz, white mica, calcite, opaques • 80-90 : 10-20	• Medium to very fine grained. Crenulated white mica. • Quartz: Inequigranular. Polygonal. Subhedral. Undulose extinction. Possible deformation lamellae. SGR. • Some GBAR, recovery evident	• Well developed fabric defined by thin discontinuous wavy white mica layers and elongated quartz grains. Possible boudinage calcite vein. • Low-Medium Shear Strain • Shear sense: Top to the NE.
22AK-072-1-1	• Quartz grit schist • Quartz, white mica, opaques • 40-50 : 50-60	• Coarse to very fine grained (bimodal). Quartz boudins. • Quartz: inequigranular. Polygonal to interlobate. Subhedral to euhedral. SGR. Undulose extinction. Partial GBM: left over grains, window microstructure. • Some GBAR, recovery evident	• Well developed fabric defined by thin-thick continuous straight mats of white mica and some elongated quartz grains. Aggregate preferred orientation. • Medium-High Shear Strain • Shear sense: Inconclusive
22AK-072-1-2	• Quartzite • Quartz, white mica, calcite • 70-80 : 20-30	• Medium to very fine grained. • Quartz: Inequigranular to seriate. Polygonal to interlobate. Subhedral. SGR. Undulose extinction. Elongated Quartz grains • Minimal GBAR, Lowest Recovery	• Well developed fabric defined by thin straight continuous to discontinuous white mica layers and elongated/oriented quartz grains. Pockets of calcite appear to be randomly dispersed. • Low-Medium Shear Strain • Shear sense: Inconclusive.

Sample ID	Lithology, Composition, and Quartz : Phyllosilicate Abundance Ratio	Textures	Fabric
22AK-073-1-1	• Sericite schist • Quartz, white mica, calcite, re-crystallized staurolite? • 70-85 : 15-30	• Very fine grained with the exception of the altered staurolite which is coarse to medium grained. • Quartz: Polygonal. Euhedral to subhedral. Inequigranular. Undulose extinction. Some acicular/elongated quartz grains.	• Well developed fabric defined by very thin elongated quartz grains and some white mica grains. Altered staurolite crosscuts foliation indicating that it formed post deformation in the area. • High Shear • Shear sense: Inconclusive.
22AK-078-1-1	• Quartzite • Quartz, white mica, opaques • 85-95 : 5-15	• Medium to very fine grained. • Quartz: Polygonal. Seriate. Subhedral to euhedral. SGR. Undulose extinction. • GBAR evident, More recovery	• Well developed fabric defined by thin discontinuous to continuous straight to wavy white mica layers and some elongated quartz grains. • Low-Medium Shear Strain • Shear sense: Top to the E
22AK-079-1-1	• Quartz rich Graphite-muscovite schist • Quartz, white mica, opaques • 70-85 : 15-30	• Mica appears to be growing perpendicular to foliation in some localities. Medium to fine grained. • Quartz: Polygonal to interlobate. Seriate. Subhedral. Undulose extinction. SGR. Partial GBM: Window structure, possible pinning. • Some GBAR, recovery evident	• Well developed fabric defined by thin, straight to wavy, continuous white mica layers and some elongated quartz grains. • Low-Medium Shear Strain • Shear sense: Inconclusive.
22AK-080-1-1	• Quartz rich Graphitic schist • Quartz, white mica, opaques • 75-90 : 10-25	• Fine to very fine grained. • Quartz: Interlobate to polygonal. Seriate to inequigranular. Undulose extinction. SGR. Subhedral. Partial GBM: dragging, pinning. • Some GBAR, recovery evident.	• Well developed fabric defined by some thin, straight, continuous to discontinuous white mica layers and some elongated quartz grains. Some possible CS fabric indicating shear sense. • Low-Medium Shear Strain • Shear sense: Top to the ESE
22AK-081-1-2	• Graphitic schist • Quartz, Biotite, Opaques, chlorite, white mica • 75-90 : 10-25	• Very different metamorphic grade than other samples. Coarse to very fine grained. Biotite is replacing another mineral. • Quartz: Inequigranular. Subhedral to anhedral. Interlobate to polygonal. SGR. Undulose extinction. Partial GBM: dragging. • Some GBAR, recovery evident.	• Well developed fabric defined by some thin, wavy, continuous to discontinuous white mica layers and some elongated quartz grains. Some shear sense indication by asymmetric folding in the foliation. • Low Shear Strain • Shear sense: Top to the W

Sample ID	Lithology, Composition, and Quartz : Phyllosilicate Abundance Ratio	Textures	Fabric
22AK-082-1-1	• Quartz grit schist • Quartz, white mica, opaques • 65-80 : 20-35	• Fine to very fine grained, a few medium grains. • Quartz: Inequigranular Subhedral. Polygonal to Interlobate. SGR. Undulose extinction. Partial GBM: left over grains, pinning microstructure, dragging microstructure, window microstructure. Triple Junctions. • GBAR evident, More recovery	• Well developed fabric defined by thin to thick, wavy to straight, continuous white mica layers and some elongated quartz grains. • Low-Medium Shear Strain • Shear sense: Inconclusive
18-709	• Muscovite schist • White mica, quartz, chlorite, calcite, opaques • 40-50 : 50-60	• Coarse to very fine grained, inequigranular. • Quartz: mostly very fine grained. SGR. Inequigranular to equigranular. Subhedral. Interlobate to polygonal. Undulose extinction. Partial GBM: dragging microstructure, left over grains, window microstructure. • Limited GBAR, Low recovery	• Well developed fabric defined by thick, straight, continuous white mica layers and some elongated (dragged) quartz grains. Possible CS Fabric. • Low-Medium Shear Strain

APPENDIX C: SAMPLE QUARTZ *C*-AXIS CPO DESCRIPTIONS

Sample	Lithology	Thin Section Orientation (Left-Right)	Interpretation
22AK-001-1-1	Quartzite	S-N	• Slip Systems: rhomb <a>, prism <a> • Relative Fabric Strength: Strong. • Fabric Type: Single Girdle. • Relative Temperature: Low-Medium. • Shear Sense: Top to the north. • Other: Weaker fabric shows a possible cross girdle.
22AK-006-1-2	Quartz grit schist	NNE-SSW	• Slip Systems: rhomb <a>, prism <a> • Relative Fabric Strength: Weak. • Fabric Type: Irregular. • Relative Temperature: Low-Medium. • Shear Sense: Inconclusive.
22AK-011-1-1	Muscovite Schist	SE-NW	• Slip Systems: rhomb <a>, basal <a>, prism <a> • Relative Fabric Strength: Weak. • Fabric Type: Single girdle to Type I crossed girdle. • Relative Temperature: Low • Shear Sense: Inconclusive.
22AK-023-1-1	Chlorite-muscovite schist	W-E	• Slip Systems: basal <a>, prism <a> • Relative Fabric Strength: Weak. • Fabric Type: Irregular to single girdle. • Relative Temperature: Low. • Shear Sense: Ambiguous to top to the east.
22AK-029-1-1	Graphite-muscovite schist	WNW-ESE	• Slip Systems: rhomb <a>, prism <a>, basal <a> • Relative Fabric Strength: Weak. • Fabric Type: Irregular. • Relative Temperature: Low. • Shear Sense: Ambiguous to west-northwest.
22AK-032-2-1	Quartzite	SE-NW	• Slip Systems: rhomb <a>, prism <a>, basal <a> • Relative Fabric Strength: Strong. • Fabric Type: Single girdle. • Relative Temperature: Low • Shear Sense: Top to the northwest.
22AK-037-1-1	Chlorite-muscovite schist	S-N	• Slip Systems: rhomb <a>, prism <a>, basal <a> • Relative Fabric Strength: Weak

Sample	Lithology	Thin Section Orientation (Left-Right)	Interpretation
			• Fabric Type: irregular. Possible transition of cleft girdle to type II crossed girdle. • Relative Temperature: Low • Shear Sense: Inconclusive
22AK-041-1-1	Quartz rich graphite-muscovite schist	SE-NW	• Slip Systems: prism <a>, rhomb <a> • Fabric Strength: Strong. • Fabric Type: Irregular • Relative Temperature: Low-Medium • Shear Sense: Top to the northwest.
22AK-043-1-1	Chlorite-muscovite schist	NE-SW	• Slip Systems: prism <a>, rhomb <a> • Relative Fabric Strength: Strong. • Fabric Type: Single point to single girdle. • Relative Temperature: Low-Medium • Shear Sense: Top to the northeast. • Other: Weaker fabric shows a possible cross girdle.
22AK-045-2-1	Graphite-muscovite schist	SE-NW	• Slip Systems: rhomb <a>, prism <a>, basal <a> • Relative Fabric Strength: Strong. • Fabric Type: Single girdle. • Relative Temperature: Low • Shear Sense: Top to the northwest.
22AK-049-1-1	Quartzite	W-E	• Slip Systems: prism <a>, rhomb <a> • Relative Fabric Strength: Very Strong. • Fabric Type: Single Girdle. • Relative Temperature: Low-Medium. • Shear Sense: Top to the west.
22AK-052-1-1	Quartzite	NNW-SSE	• Slip Systems: basal <a>, prism <a>, rhomb <a> • Relative Fabric Strength: Very weak. • Fabric Type: Irregular. • Relative Temperature: Low. • Shear Sense: Inconclusive.
22AK-054-1-1	Quartzite	SE-NW	• Slip Systems: rhomb <a>, basal <a>, prism <a> • Relative Fabric Strength: Strong. • Fabric Type: Single girdle. • Relative Temperature: Low. • Shear Sense: Top to the northwest.

Sample	Lithology	Thin Section Orientation (Left-Right)	Interpretation
			• Other: Weaker fabric shows a possible cross girdle.
22AK-055-2-1	Quartz rich graphite-muscovite schist	S-N	• Slip Systems: prism <a>, rhomb <a>, basal <a> • Relative Fabric Strength: Very strong. • Fabric Type: Single point. • Relative Temperature: Low. • Shear Sense: Inconclusive.
22AK-060-1-1	Quartz rich graphite-muscovite schist	NW-SE	• Slip Systems: rhomb <a>, prism <a>, basal <a> • Relative Fabric Strength: Weak. • Fabric Type: Single girdle. • Relative Temperature: Low. • Shear Sense: Top to the northwest. • Other: Weaker fabric shows a possible cross girdle.
22AK-061-1-1	Quartz grit schist	W-E	• Slip Systems: rhomb <a>, prism <a>, basal <a> • Relative Fabric Strength: Strong. • Fabric Type: Type I Crossed girdle. • Relative Temperature: Low • Shear Sense: Top to the west.
22AK-067-1-1	Quartzite	SW-NE	• Slip Systems: rhomb <a>, prism <a> • Relative Fabric Strength: Very strong. • Fabric Type: Type II crossed girdle. • Relative Temperature: Low-Medium. • Shear Sense: Ambiguous to top to the southwest.
22AK-069-2-1	Quartzite	NE-SW	• Slip Systems: rhomb <a>, prism <a> • Relative Fabric Strength: Weak. • Fabric Type: Single point to Type II crossed girdle. • Relative Temperature: Low-Medium. • Shear Sense: Ambiguous to top to the northeast.
22AK-072-1-1	Quartz grit schist	NE-SW	• Slip Systems: prism <a>, rhomb <a>, basal <a> • Relative Fabric Strength: Very weak. • Fabric Type: Irregular to single point. • Relative Temperature: Low. • Shear Sense: Inconclusive.
22AK-072-1-2	Quartzite	S-N	• Slip Systems: prism <a>, rhomb <a>, basal <a> • Relative Fabric Strength: Strong • Fabric Type: Single point.

Sample	Lithology	Thin Section Orientation (Left-Right)	Interpretation
			• Relative Temperature: Low. • Shear Sense: Inconclusive.
22AK-078-1-1	Quartzite	W-E	• Slip Systems: basal <a>, prism <a>, rhomb <a> • Relative Fabric Strength: Weak. • Fabric Type: Single girdle. • Relative Temperature: Low. • Shear Sense: Top to the west. • Other: Weaker fabric shows a possible cross girdle.
22AK-079-1-1	Quartz rich Graphite-muscovite schist	W-E	• Slip Systems: rhomb <a>, prism <a>, basal <a> • Relative Fabric Strength: Weak. • Fabric Type: Type 1 crossed girdle. • Relative Temperature: Low. • Shear Sense: Inconclusive.
22AK-080-1-1	Quartz rich Graphitic schist	WNW-ESE	• Slip Systems: rhomb <a>, prism <a>, basal <a> • Relative Fabric Strength: Weak. • Fabric Type: Irregular to Type II crossed girdle. • Relative Temperature: Low. • Shear Sense: Ambiguous to top to the west-northwest.
22AK-081-1-2	Graphitic schist	W-E	• Slip Systems: prism <a>, rhomb <a>, basal <a> • Relative Fabric Strength: Very weak. • Fabric Type: Single girdle to Type I crossed girdle. • Relative Temperature: Low. • Shear Sense: Inconclusive.
22AK-082-1-1	Quartz grit schist	ESE-WNW	• Slip Systems: prism <a>, basal <a>, rhomb <a> • Relative Fabric Strength: Weak. • Fabric Type: Type II crossed girdle. • Relative Temperature: Low. • Shear Sense: Top to the west-northwest.

APPENDIX D: GEOCHRONOLOGY

Appendix D.1: $^{87}Rb/^{87}Sr$

Appendix D.1.1: Sample isochron dates with and without outliers

Sample	All Data	All Data – Outliers Removed	Run 1	Run 1 – Outliers Removed
22AK-061-1-1	133 +/- 11 Ma (MSWD = 6.4, n = 70/70)	116 +/- 14 Ma (MSWD = 1, n= 60/70)	103 +/- 18 Ma (MSWD = 4.8, n = 57/57)	89 +/- 19 Ma (MSWD = 1.4, n = 56/57)
22AK-006-1-2	84.8 +/- 6.1 Ma (MSWD = 1.2, n = 68/68)	85.5 +/- 6.2 Ma (MSWD = 0.7, n = 64/68)	N/A	N/A
22AK-082-1-1	158 +/- 120 Ma (MSWD = 1.4, n = 60/60)	137 +/- 121 Ma (MSWD = 0.97, n = 57/60)	N/A	N/A
22AK-011-1-1	N/A	N/A	84 +/- 27 Ma (MSWD = 1.4, n = 60/60)	128 +/- 33 Ma (MSWD = 0.83, n = 51/60)
22AK-023-1-1	81 +/- 31 Ma (MSWD = 1, n = 60/60)	75 +/- 33 Ma (MSWD = 0.72, n = 56/60)	N/A	N/A
22AK-037-1-1	83.6 +/- 4.7 Ma (MSWD = 3.9, n = 146/146)	92.9 +/- 4.9 Ma (MSWD = 0.86, n = 138/146)	91.0 +/- 7.5 Ma (MSWD = 1.1, n = 127/127)	90.8 +/- 7.5 Ma (MSWD = 0.89, n = 124/127
22AK-037-1-1A	81.7 +/- 4.9 Ma (MSWD = 6.2, n = 80/80)	92.9 +/- 5.3 Ma (MSWD = 0.65, n = 74/80)	91 +/- 16 Ma (MSWD = 1.1, n = 61/61)	93 +/- 16 Ma (MSWD = 0.68, n= 60/61)
22AK-037-1-1B	81.6 +/- 7.2 Ma (MSWD = 6, n = 85/85)	97.6 +/- 7.7 Ma (MSWD = 0.98, n = 78/85)	100 +/- 16 Ma (MSWD = 1.1, n = 66/66)	101 +/- 16 Ma (MSWD = 1.1, n = 64/66)

Appendix D.1.2: Spot Locations

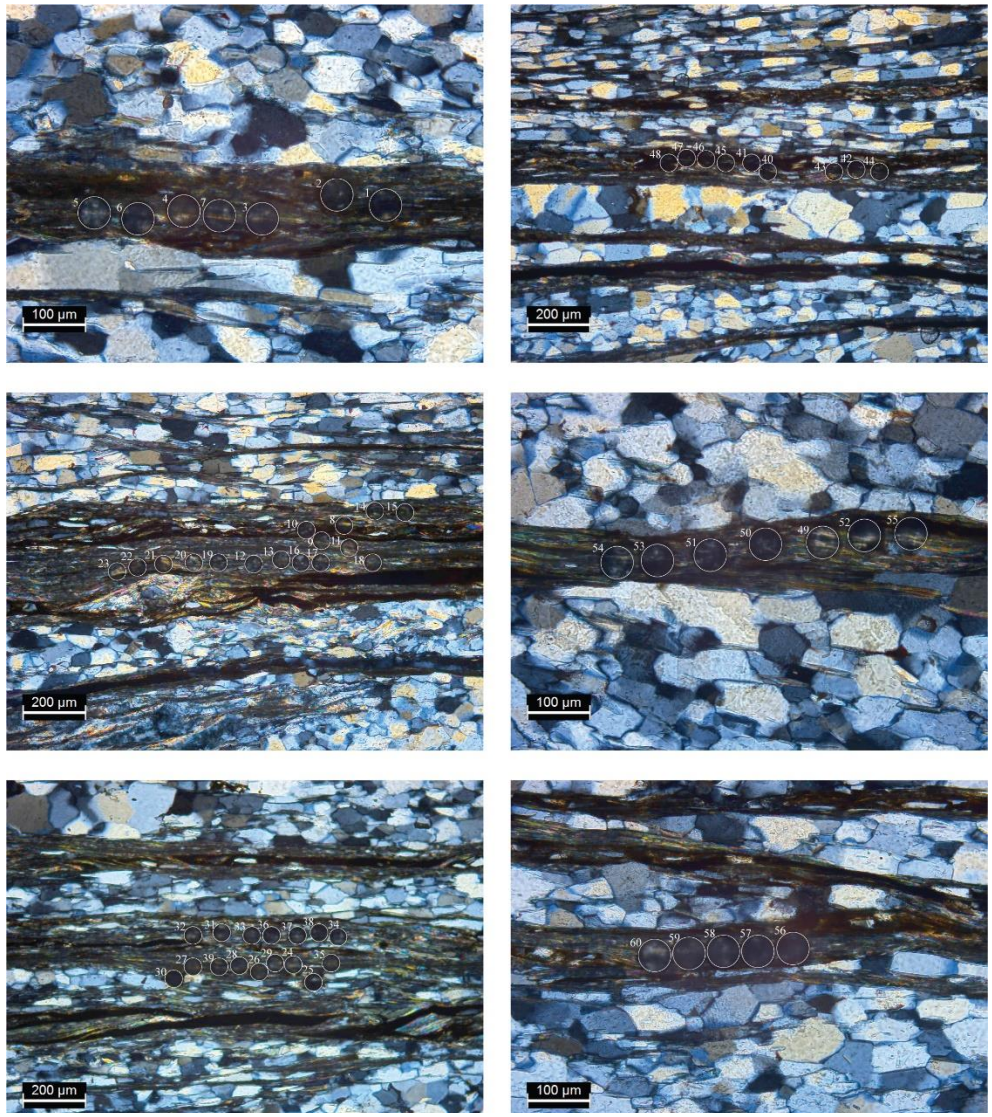


Figure D.1: Sample 22AK-011-1-1. November 22nd, 2022.

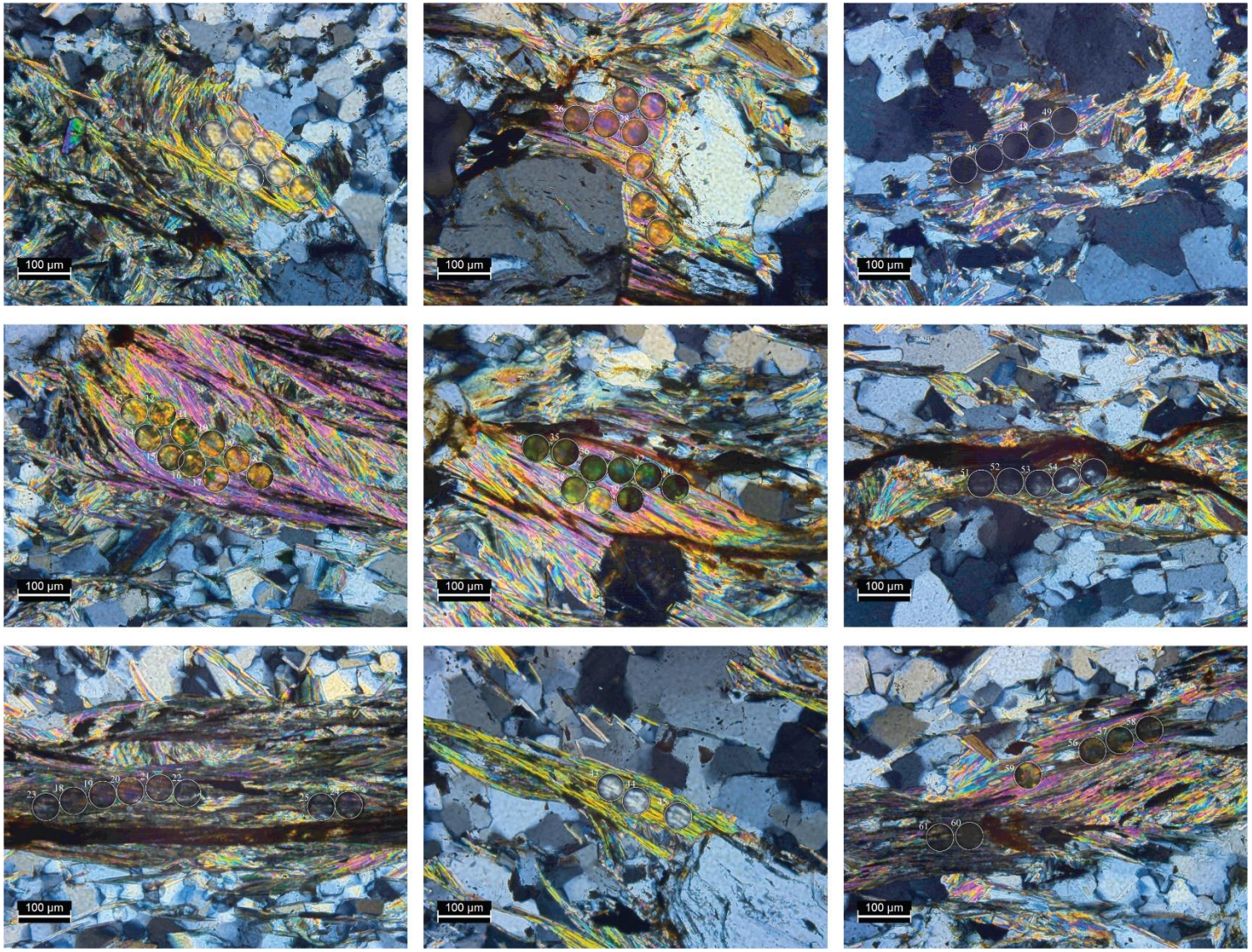


Figure D.2: Sample 22AK-037-1-1. Group 1. November 22nd, 2022.

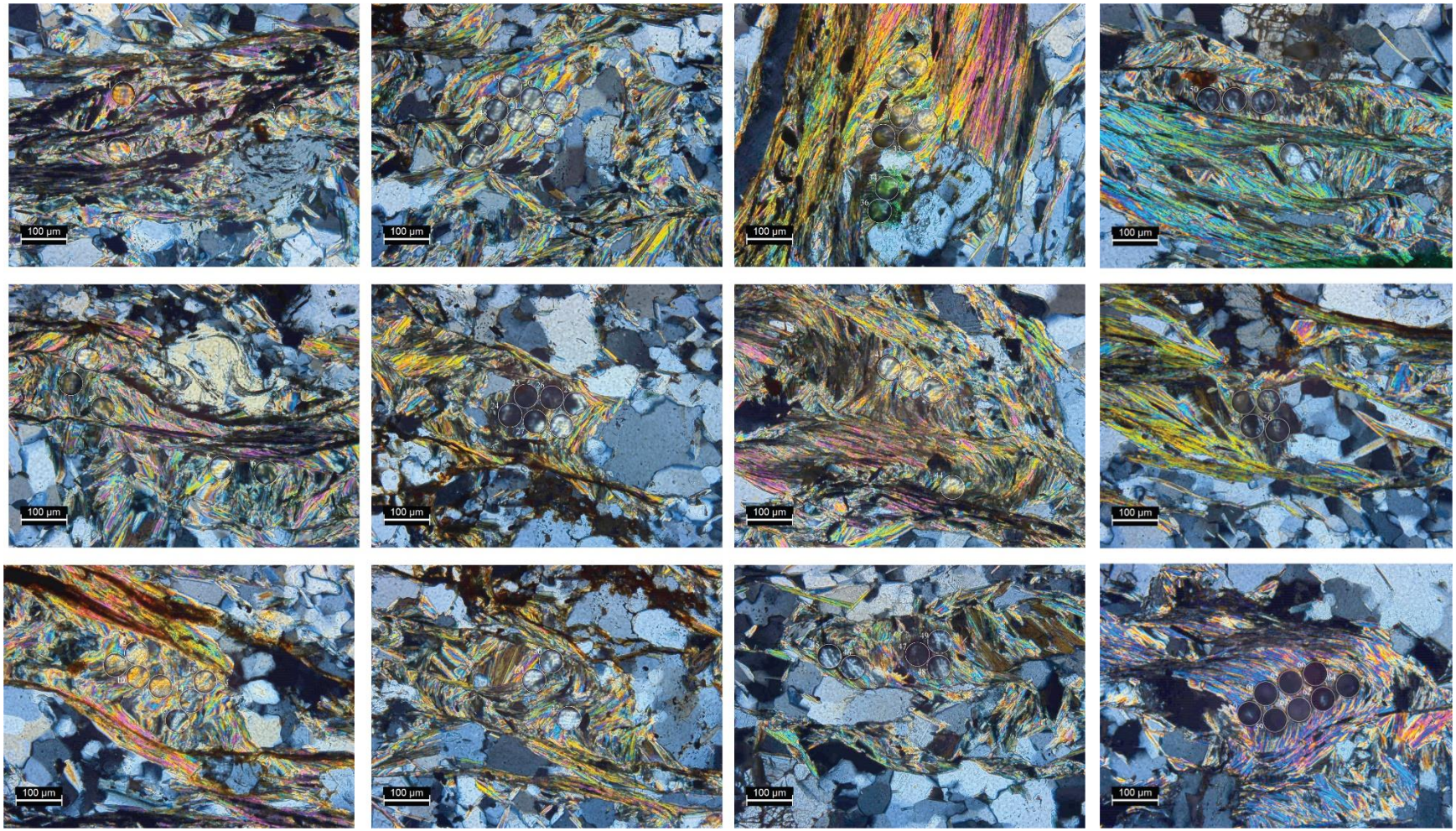


Figure D.3: Sample 22AK-037-1-1. Group 2. November 22nd, 2022.

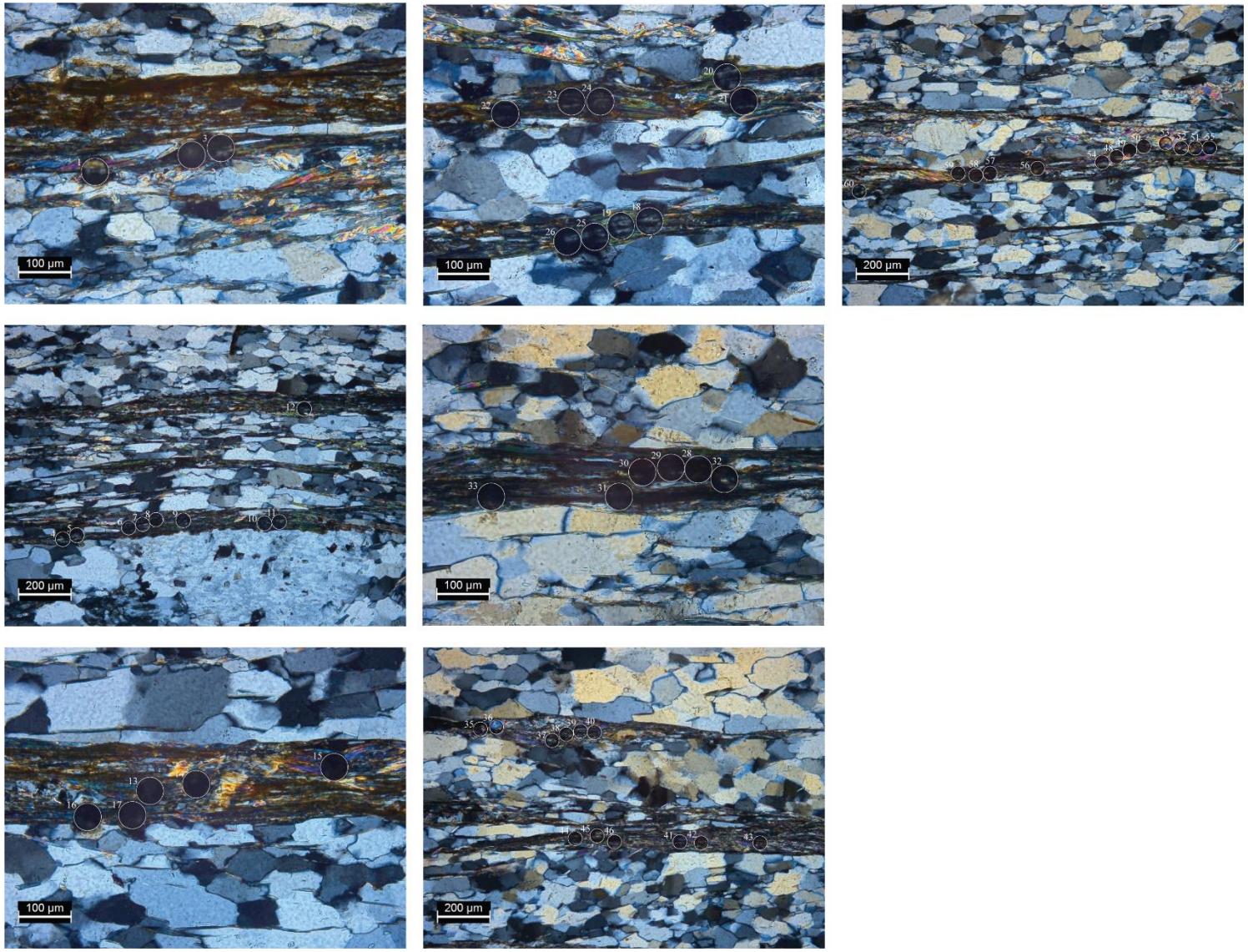


Figure D.4: Sample 22AK-061-1-1. November 22nd, 2022.



Figure D.5: Sample 22AK-037-1-1. January 16th, 2023.

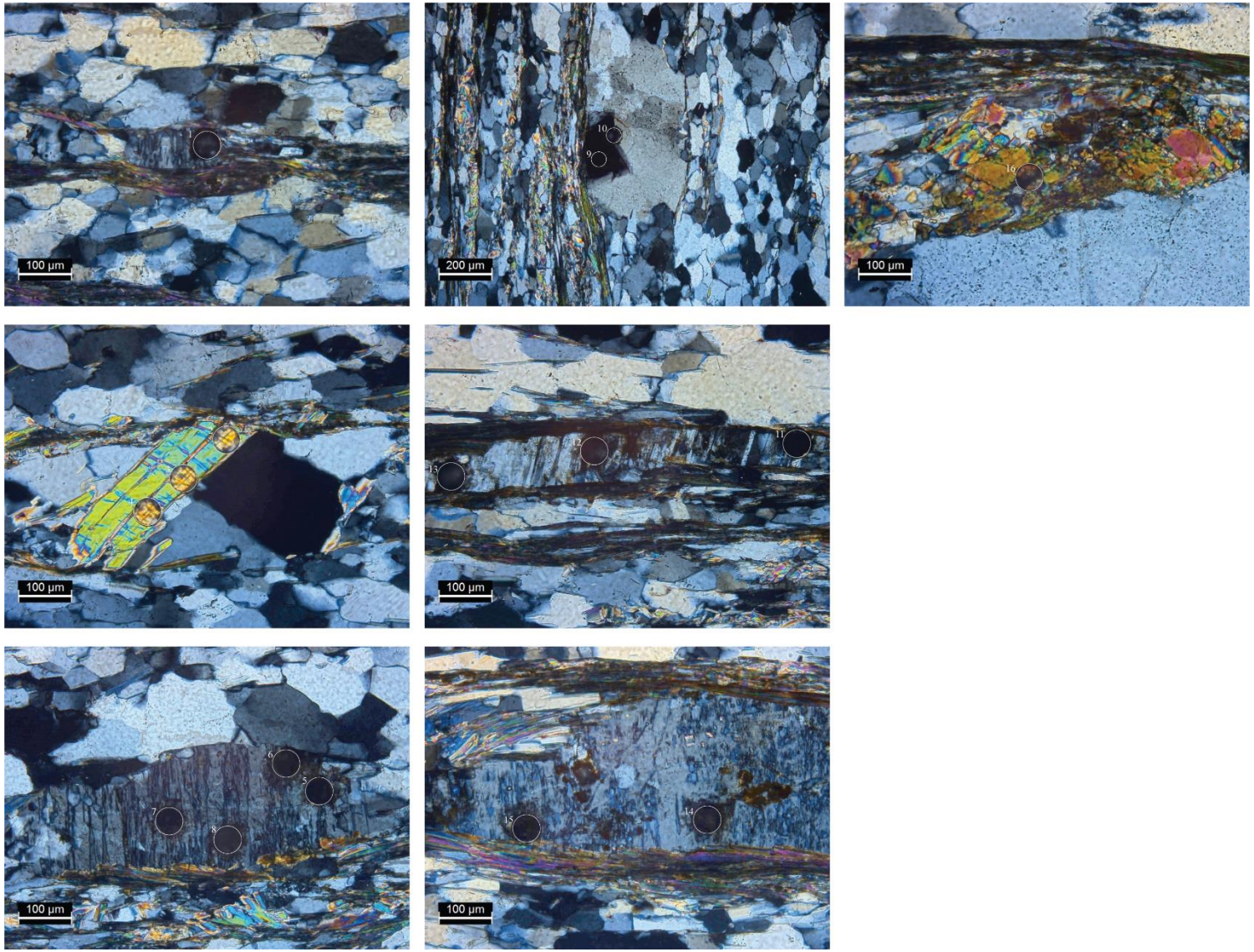


Figure D.6: Sample 22AK-061-1-1. January 16th, 2023.

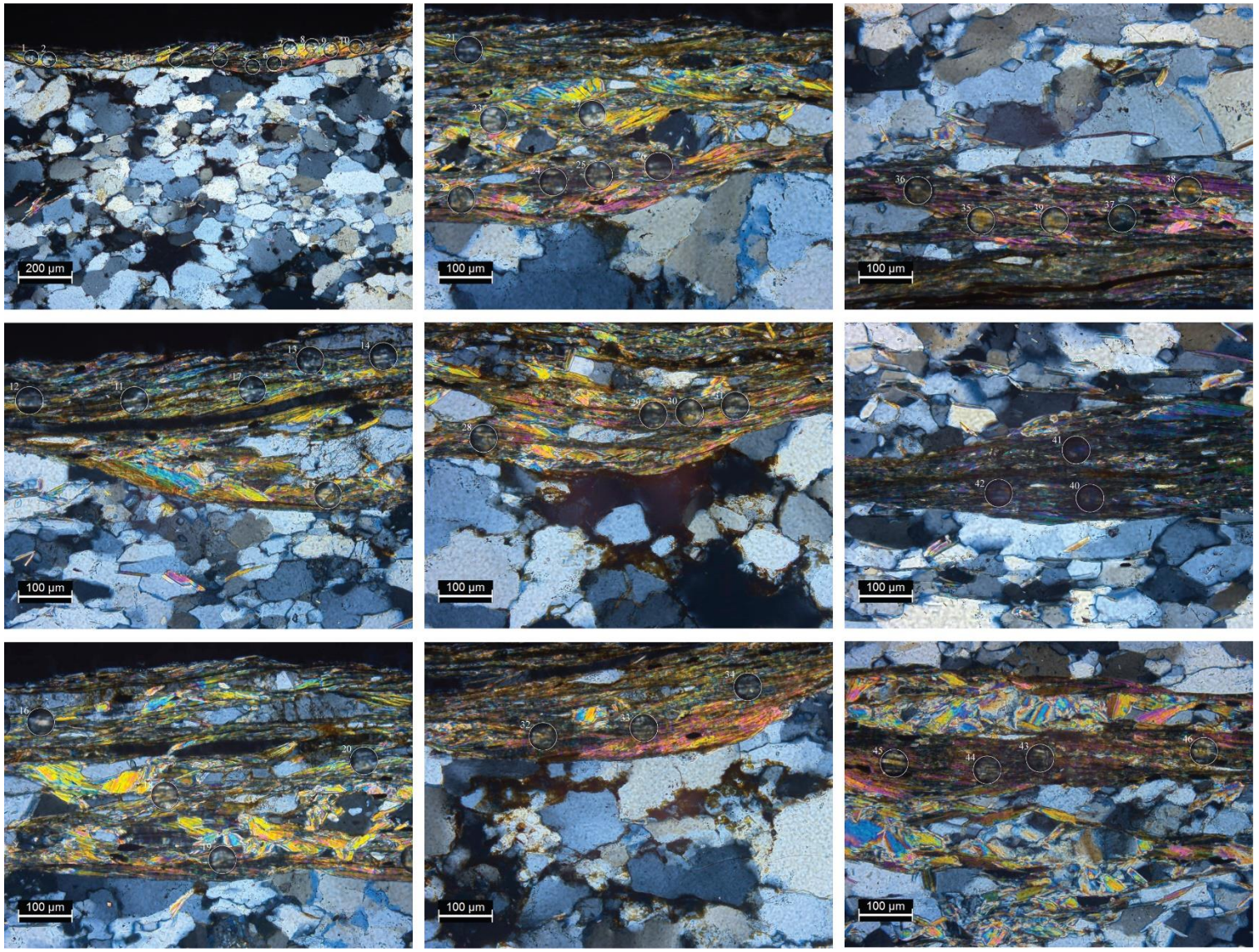


Figure D.7: Sample 22AK-006-1-2. Part 1. March 3rd, 2023.

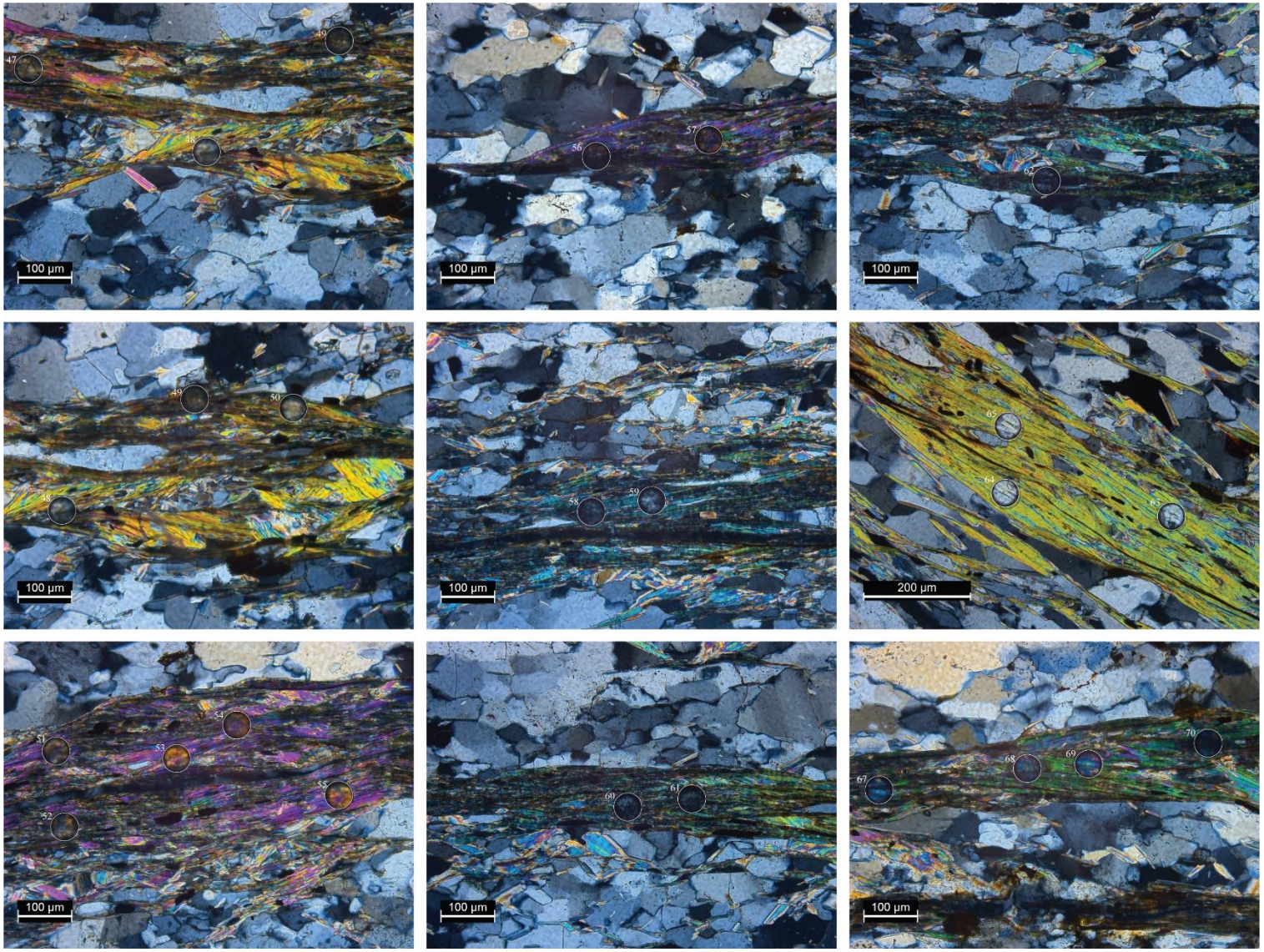


Figure D.8: Sample 22AK-006-1-2. Part 2. March 3rd, 2023.

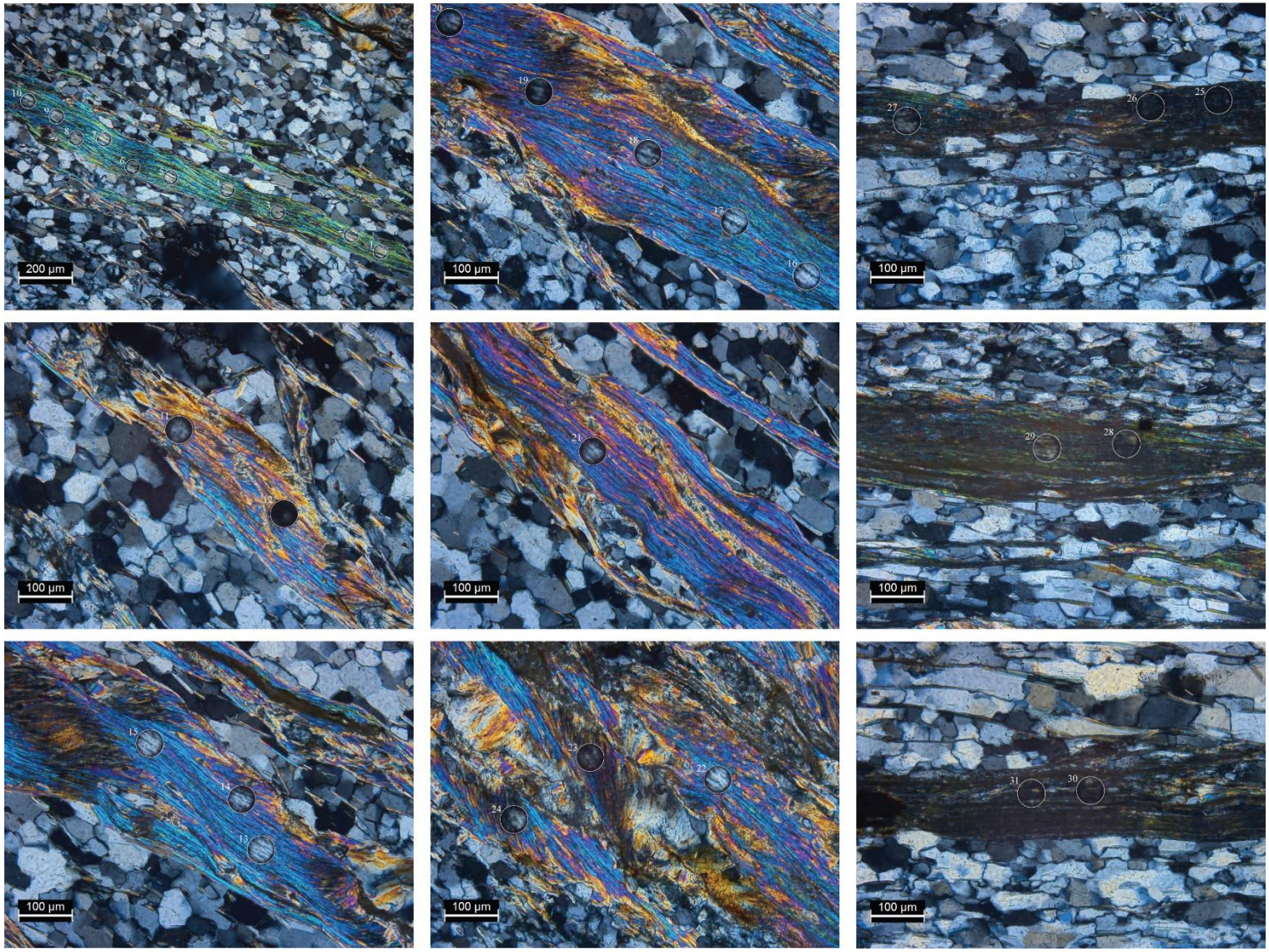


Figure D.9: Sample 22AK-023-1-1. Part 1. March 3rd, 2023.

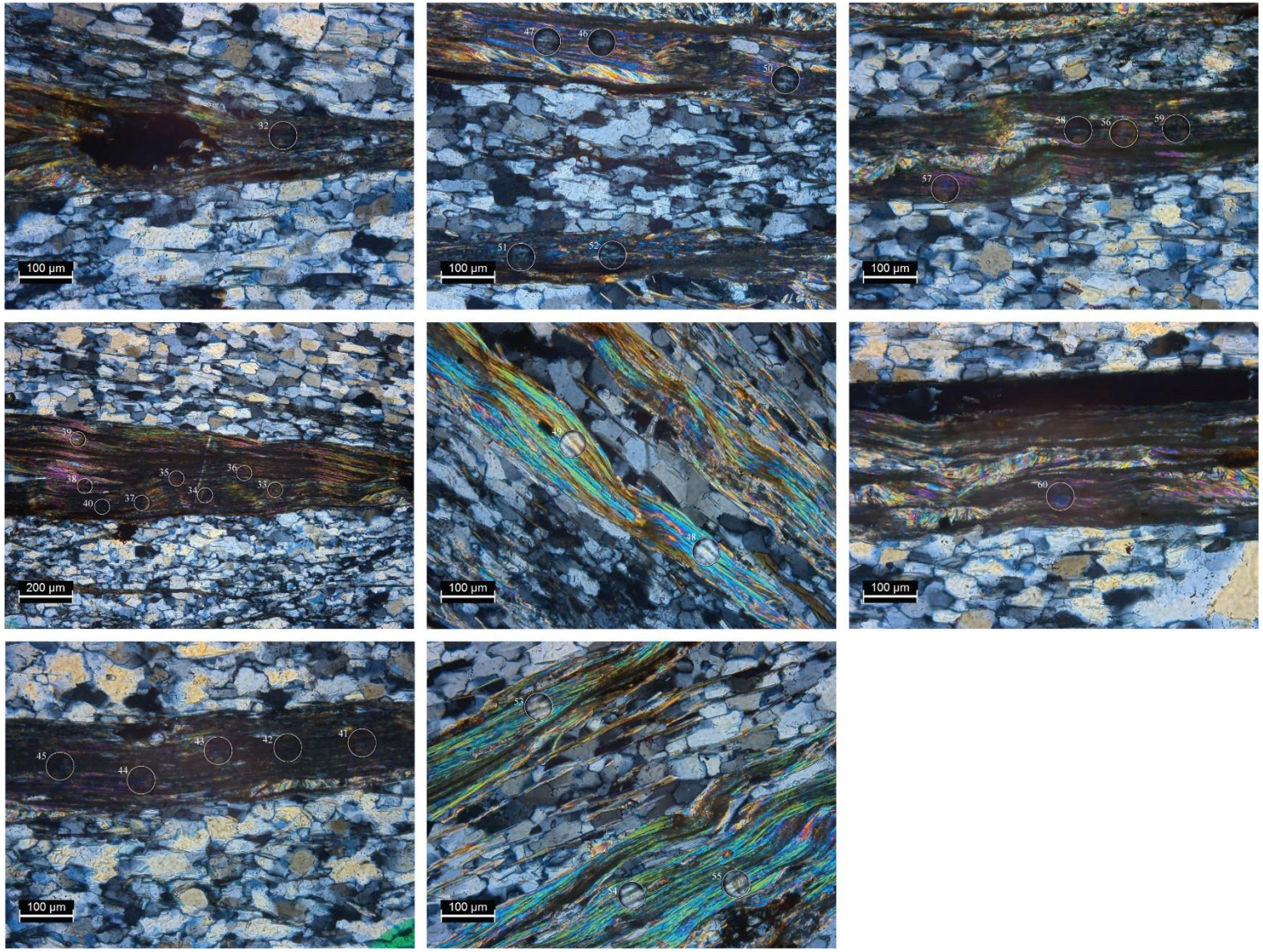


Figure D.10: Sample 22AK-023-1-1. Part 2. March 3rd, 2023.

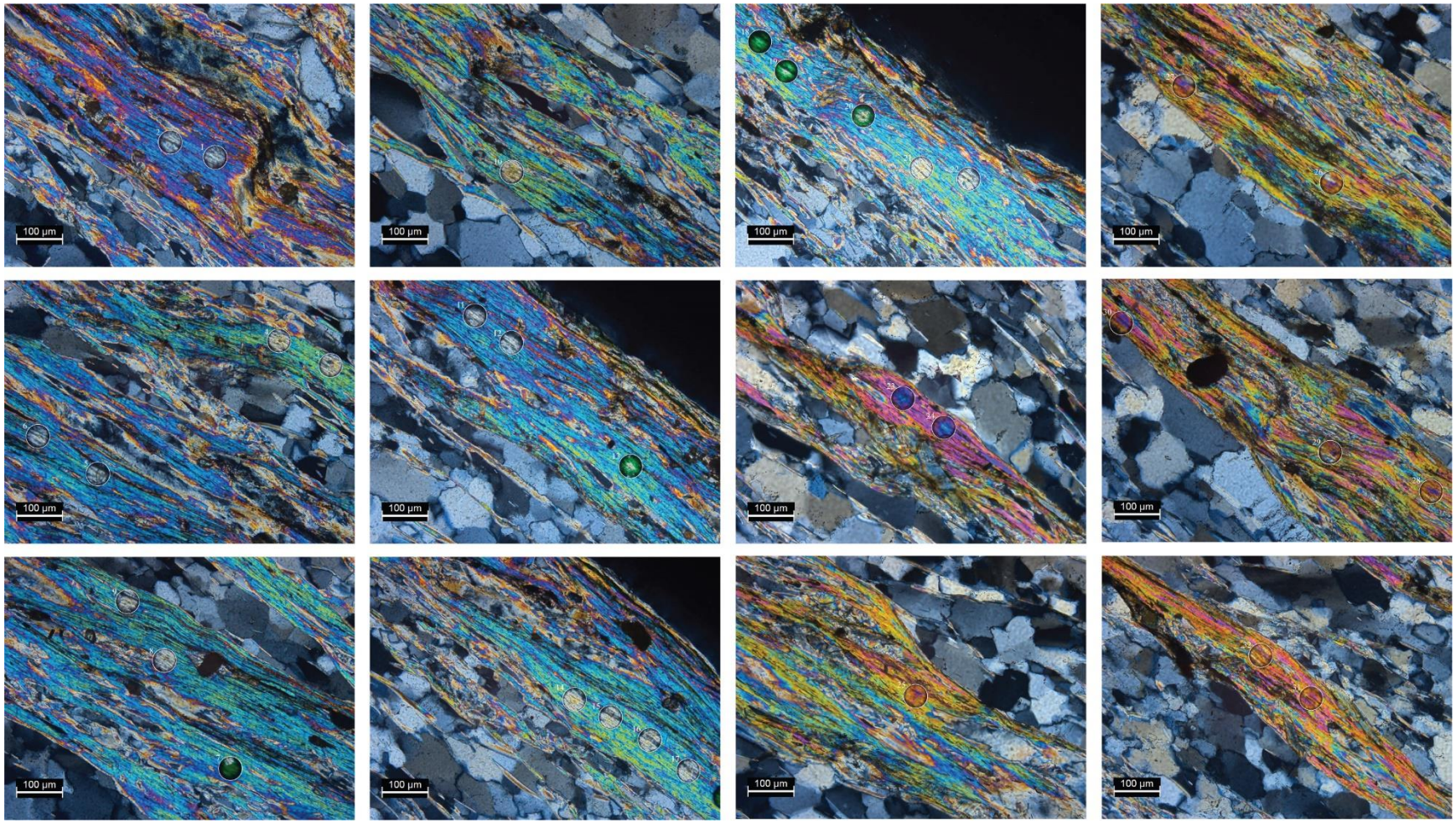


Figure D.11: Sample 22AK-082-1-1. Part 1. March 3rd, 2023.

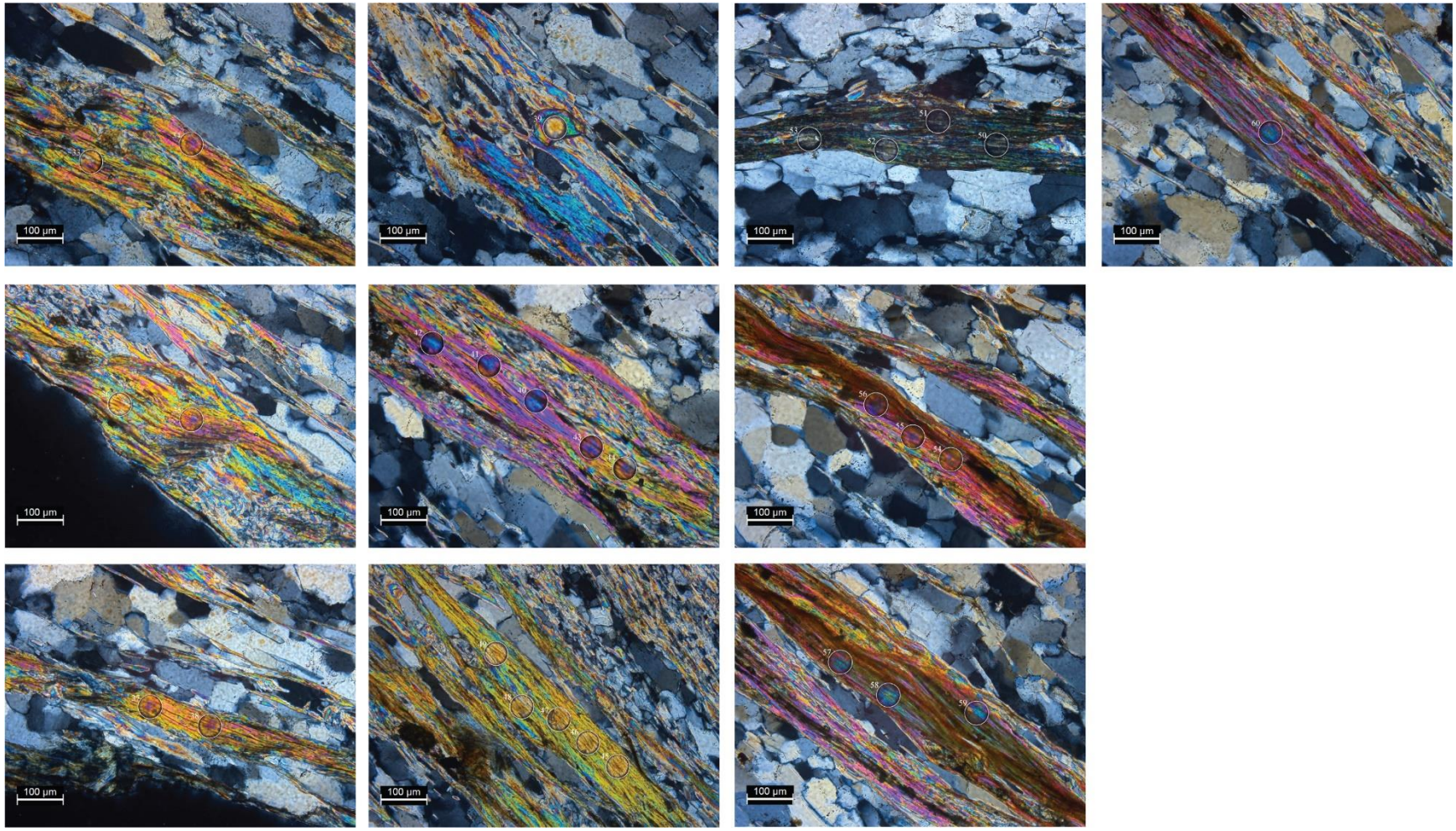


Figure D.12: 22AK-081-1-2. Part 2. March 3rd, 2023.

Appendix D.2: $^{40}Ar/^{39}Ar$

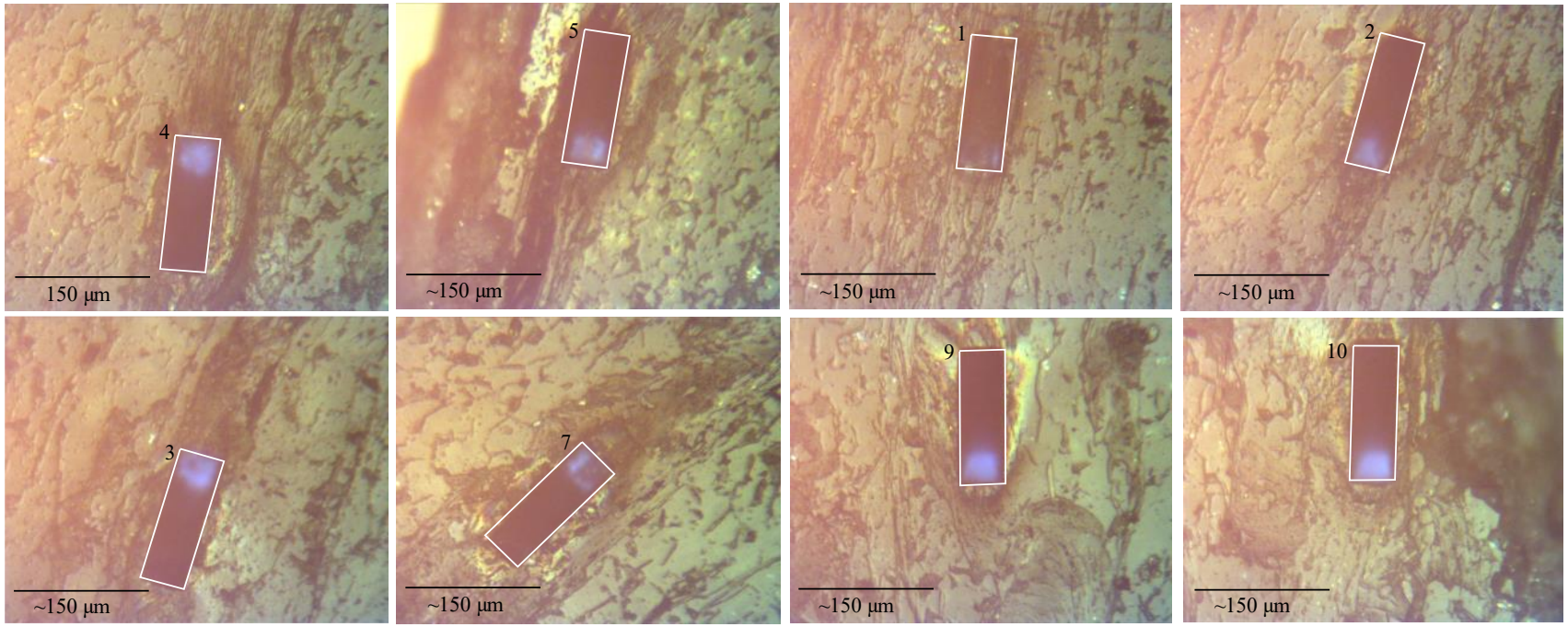


Figure D.13: Sample 22AK-023-1-1 in situ *$^{39}Ar/^{40}Ar$ spots.*

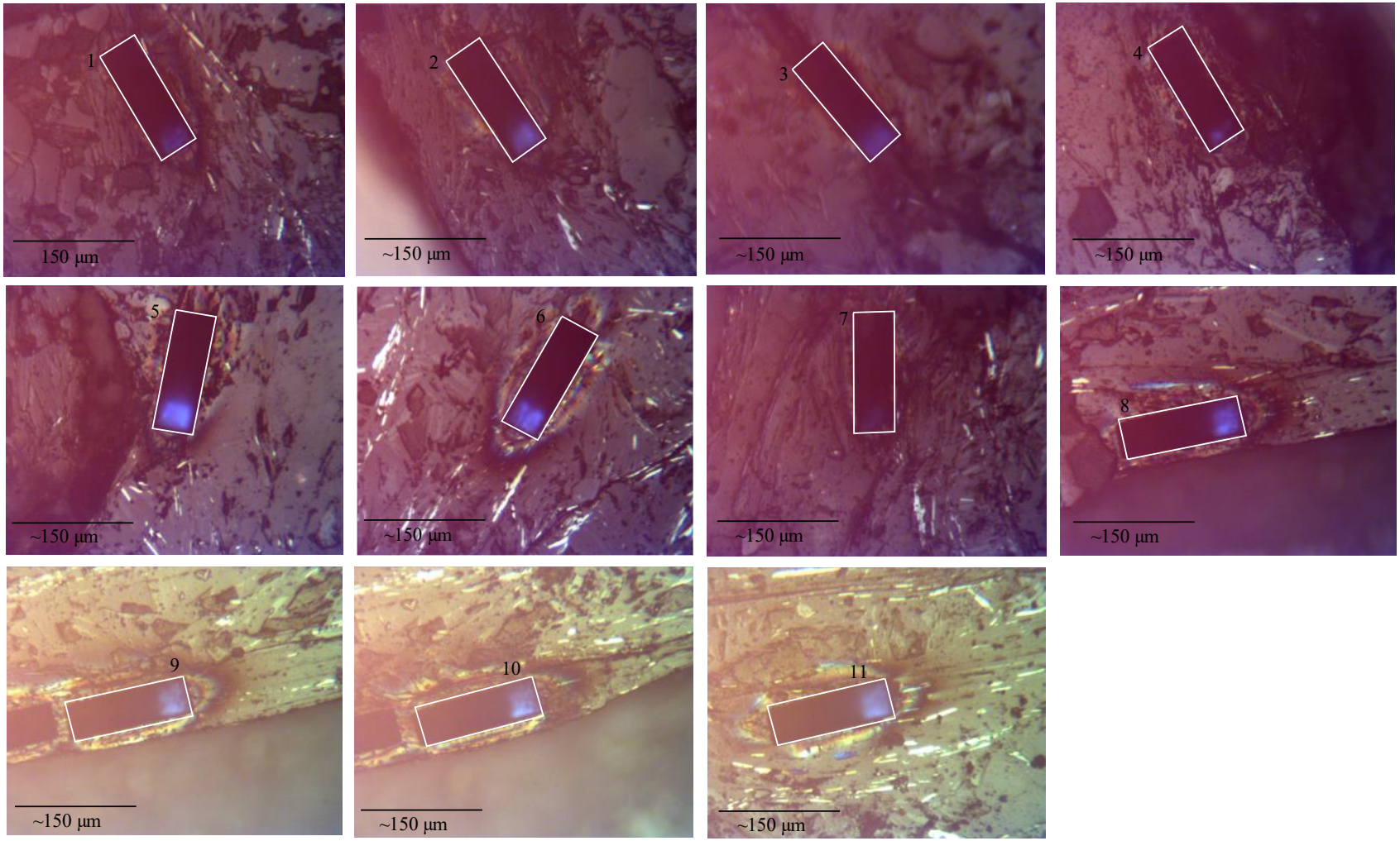


Figure D.14: Sample 22AK-037-1-1 in situ $^{40}Ar/^{39}Ar$ *spots.*

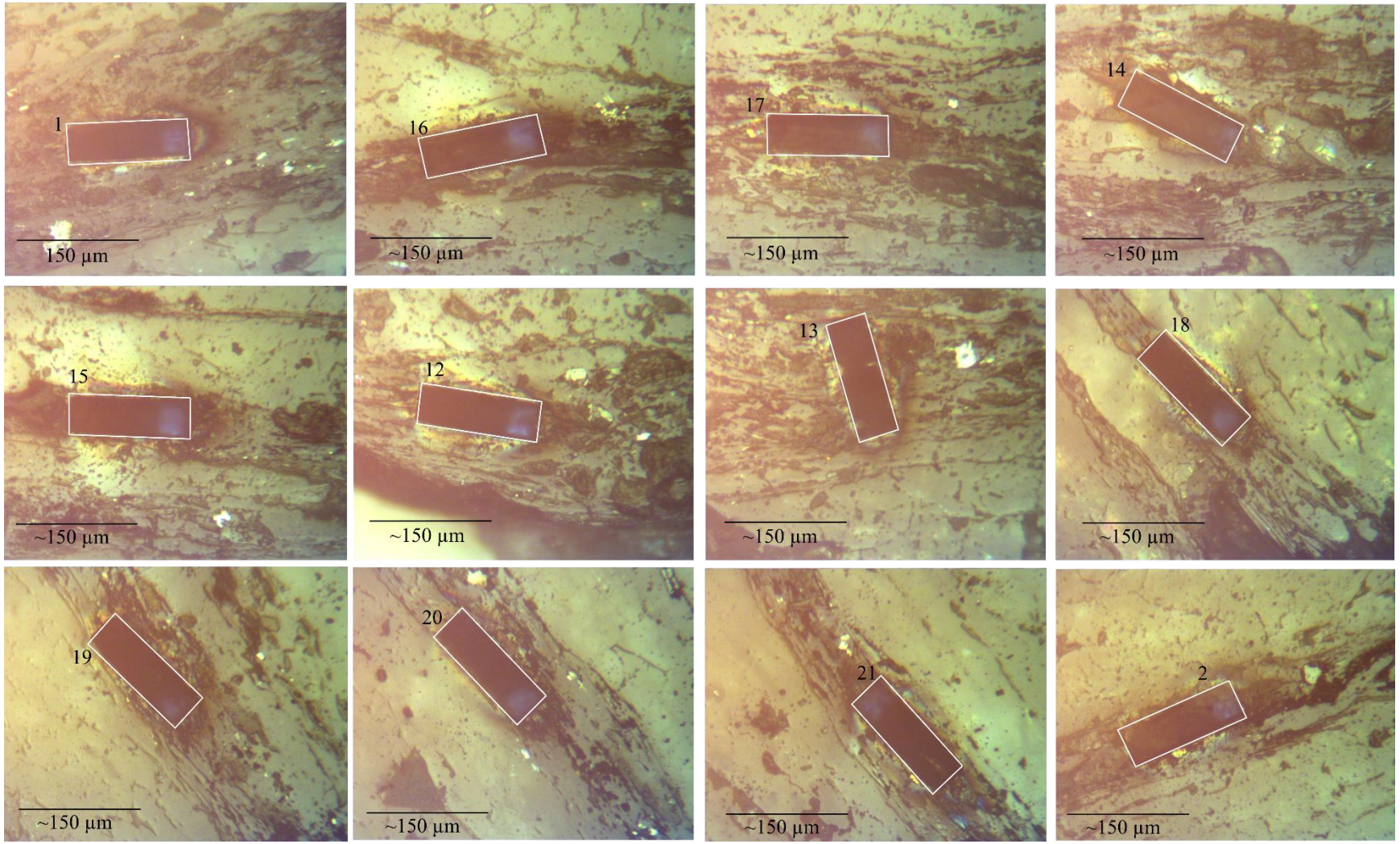


Figure D.15: Sample 22AK-082-1-1 in situ $^{40}Ar/^{39}Ar$ *spots.*

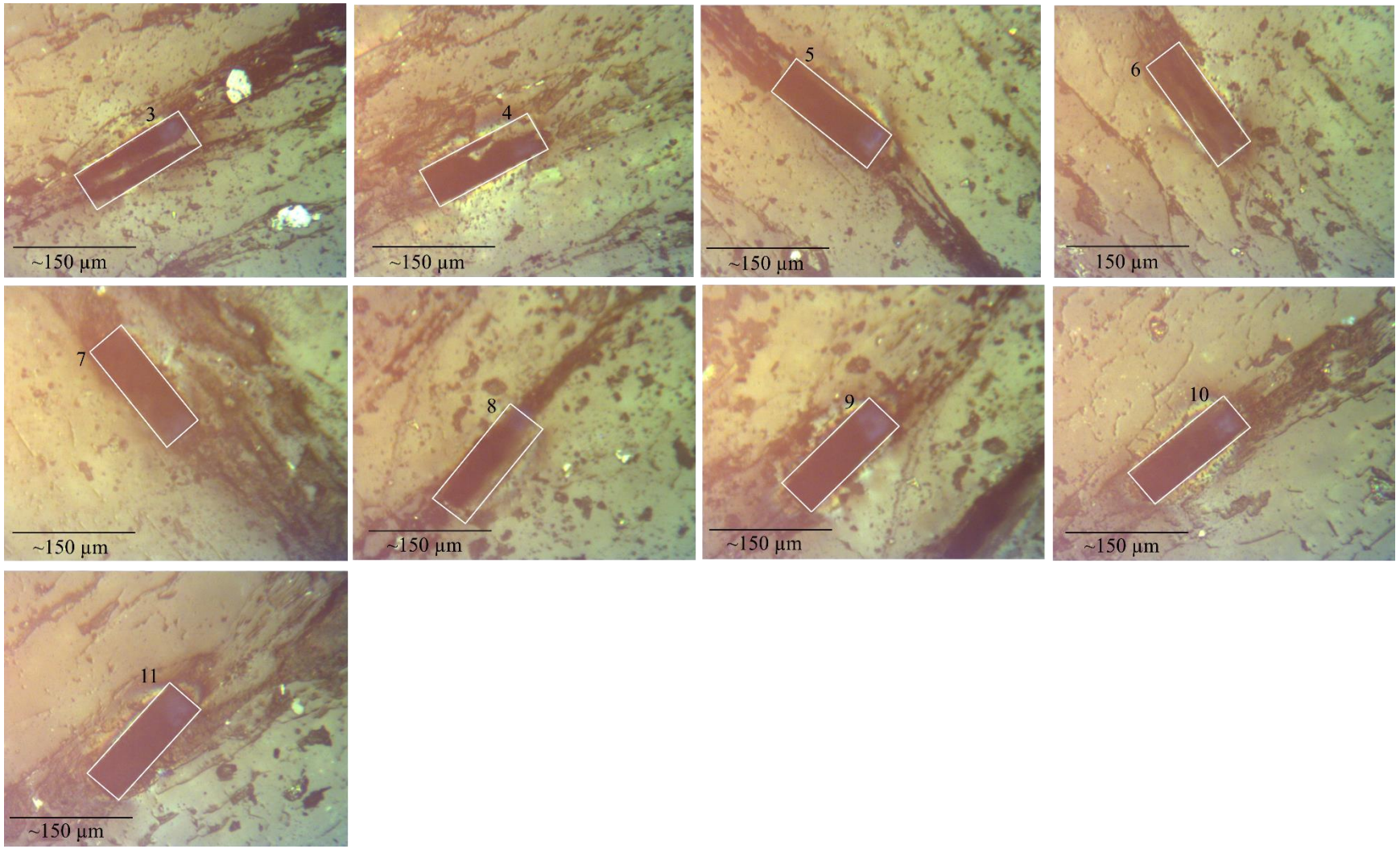


Figure D.16: Sample 22AK-082-1-1 in situ $^{40}Ar/^{39}Ar$ *spots.*

APPENDIX E: THERMOMETRY DATA

Sample	*Site*	*D1 – position*	*D1 - amplitude*	*D1 - area*	*G - position*	*G - amplitude*	*G - area*	*D2 - position*	*D2 - amplitude*	*D2 - area*
22AK-001-1-1	1	1351.974	319.218	14958.18	1584.804	359.382	14634.18	1620.749	64.1865	1493.395
	2	1351.288	743.8413	32372.13	1583.166	694.2135	25001.07	1619.335	147.7265	3883.072
	3	1352.158	270.4312	11054.84	1584.043	446.5129	16271.4	1619.942	79.2872	2109.92
	4	1351.996	92.2032	2632.472	1586.251	108.8696	2645.833	1615.451	32.0239	1111.787
	5	1343.022	349.154	14807.03	1583.741	581.6754	34711.52	1620.957	122.0484	3000.525
	7	1350.94	727.1127	32240.88	1583.503	778.4582	30640.4	1620.015	151.5522	3735.075
	8	1350.783	692.0888	29711.04	1582.998	777.746	30752.95	1619.441	150.7025	3913.99
	9	1351.75	164.9338	6823.65	1584.03	219.9631	8227.217	1620.567	35.20549	973.1917
	10	1353.579	81.3696	3088.104	1585.103	188.1362	10072.79	1622.621	30.8145	776.267
	11	1346.052	127.4189	6223.937	1572.874	217.9035	14190.58	1627.866	29.7165	1223.963
	12	1352.983	129.1046	5318.839	1585.44	177.3733	7040.821	1621.281	29.7812	793.7827
22AK-006-1-2	1	1352.013	1471.529	110898.9	1589.128	4143.502	303338.7			
	2	1342.804	84.6701	4487.784	1585.889	257.5494	18837.81			
	3	1338.972	294.3106	15478.29	1586.644	1002.98	71445.07			
	4	1341.287	79.75983	4514.787	1588.483	273.946	19549.77			
	5	1346.491	298.9038	13317.46	1577.082	347.5082	13432.76	1613.233	59.3251	1476.662
	6	1347.958	87.561	4705.328	1582.455	323.918	25965.49			
	7	1342.82	53.131	2566.484	1583.603	138.498	11175.87			
	9	1348.18	43.02	3023.309	1588.241	149.87	10666.75			
	10	1347.706	30.362	1979.122	1583.977	116.084	8607.892			
	14	1343.704	176.4999	9808.137	1574.254	670.745	47750.01	1609.596	435.701	23329.67
22AK-029-1-1	1	1346.673	102.686	6704.709	1589.008	287.6046	22148.87			
	2	1340.067	71.6905	4069.067	1589.531	191.21	14247.76			
	3	1345.939	258.639	12127.87	1580.57	330.64	16063.68			
	6	1350.249	218.41	8729.675	1581.234	255.198	9902.92	1616.762	57.55	1178.39
	7	1348.535	681.259	32835.23	1579.39	767.07	28970.54	1615.03	178.77	3861.425
	9	1339.57	653.94	38319.7	1589.635	1981.958	153606.5			
	10	1337.775	243.21	12754.77	1585.745	328.701	22205.84			
	14	1341.127	117.35	6336.282	1586.78	113.92	7259.021			
22AK-037-1-1	2	1336.78	234.334	12401.75	1591.23	369.495	24834.63			

Sample	*Site*	*D1 – position*	*D1 - amplitude*	*D1 - area*	*G - position*	*G - amplitude*	*G - area*	*D2 - position*	*D2 - amplitude*	*D2 - area*
	4	1334.685	52.327	7996.99	1589.745	268.54	28001.48			
	5	1339.778	139.742	8208.856	1588.848	530.614	41412.09			
	10	1347.805	955.53	59458.92	1590.01	2986.86	206763.6			
	11	1340.363	656.898	43814.81	1585.606	2182.54	165068.2			
	19	1333.74	295.35	14307.92	1584.49	468.883	34147.6			
	23	1333.55	1067.21	64222.41	1589.182	2089.33	136251.2			
	25	1334.24	463.89	28819.09	1579.24	901.456	61961.38			
	27	1342.385	39.25	2016.08	1581.17	192.28	10985.03	1606.498	74.93	4087.15
22AK-045-2-1	1	1351.13	568.5	26278.05	1585.08	508.64	16086.6	1619.04	148.91	4088.26
	2	1352.2	277.5	11567.8	1585.4	253.7	8887.72	1620.6	78.92	2236.68
	3	1351.3	915.02	43936.3	1584.97	739.2	27410.3	1620.47	220.77	6070.37
	4	1345.97	1743.55	84984.49	1577.38	1848.76	77632.66	1613.51	411.57	11611.69
	5	1342.97	870.28	43424.64	1574.62	1135.37	47799.03	1611.07	271.45	7381.64
	6	1341.8	668.4	32945.98	1574.01	845.78	37426.2	1611.35	175.2	4881.39
	7	1347.3	346.5	15665.3	1584.88	354.01	16503.08	1620.13	105.32	2530.48
	8	1343.14	1208.17	59530.07	1574.37	1498.35	70702.54	1611.45	340.7	9609.48
	9	1349.88	201.6	8747.64	1585.51	260.71	10060.3	1618.46	100.9	3252.25
	10	1352.46	137.6	5286.24	1585.93	157.6	5378.76	1620.66	69.48	2527.09
	11	1349.64	687.8	32373.2	1583.63	801.65	36767.99	1620.21	161.48	3963.36
22AK-049-1-1	1	1344.9	859	39303.46	1577.28	869.96	34071.89	1613.58	186.83	4787.88
	2	1350.1	564.7	24365.47	1583.86	809.48	37632.82	1621.15	121.71	2632.45
	3	1350.1	160.5	7199.8	1584.6	160.02	5110.7	1616.09	48.48	1807.2
	4	1340.5	1085.23	54951.6	1583.05	1472.7	81741.27	1616.29	212.73	4478.16
	5	1345.14	782.54	35729.65	1578.96	940.69	47285.4	1615.27	299.76	9972.7
	6	1344.5	646.7	29150	1576.45	915.08	42225.3	1612.998	206.77	6540.54
	7	1349.05	442.6	22027.55	1584.82	452.65	21007.3	1620.7	118.15	2843.18
	8	1342.5	1017.6	51846.6	1571.5	1269.13	57727.45	1609.4	246.03	7320.18
	9	1346.15	803.3	42040.6	1577.42	1138.6	50800.9	1615.7	211.8	5904.5
	11	1338.3	106.03	6539.8	1579.3	219.1	12393.8	1617.75	54.65	1726.04
	12	1347.25	410.3	22199.4	1582.5	679.7	36338.6	1620.9	124.5	3492.9
22AK-052-1-1	1	1341.466	1208.408	70114.12	1577.083	1141.787	71001.14	1614.536	193.5539	5949.494

Sample	*Site*	*D1 – position*	*D1 - amplitude*	*D1 - area*	*G - position*	*G - amplitude*	*G - area*	*D2 - position*	*D2 - amplitude*	*D2 - area*
	2	1344.343	1460.436	76282.47	1580.874	1041.601	55434.66	1617.058	269.9762	7489.645
	3	1341.703	1538.343	84926.91	1577.141	999.1372	55228.37	1615.134	208.8545	6488.63
	4	1345.283	1323.244	71370.39	1583.767	1353.727	83790.15	1619.858	202.5479	5212.148
	5	1343.925	926.0686	45324.99	1577.73	740.0622	39612.16	1616.398	237.701	9511.938
	6	1344.129	1061.97	57732.85	1580.795	782.049	40522.63	1616.326	250.2656	8534.092
	7	1342.491	959.0649	49831.3	1576.613	717.3285	36272.6	1612.236	210.7326	7174.883
	8	1345.049	824.0175	41607.87	1584.139	811.5015	48559.61	1620.379	132.3257	3418.678
	9	1341.773	903.8395	50305.88	1578.502	721.2358	35738	1613.439	264.7035	8761.091
	10	1343.327	879.4362	46753.24	1578.692	776.7631	41674.5	1614.243	144.5631	3463.946
	11	1342.591	616.6246	31256.2	1576.05	610.025	31615.05	1613.811	145.6492	4372.066
	12	1351.033	107.882	4657.037	1586.094	80.3571	3052.133	1620.97	42.8157	2037.008
22AK-055-2-1	1	1343.341	776.0929	41243.54	1575.84	665.7038	32552.76	1611.913	159.853	4554.977
	2	1348.921	650.6308	35615.61	1584.024	455.0293	21099.96	1619.559	116.3018	3060.197
	3	1350.984	338.356	15710.25	1583.526	369.1624	15945.94	1620.05	77.8998	2201.625
	4	1351.141	283.1255	13309.26	1585.807	191.9957	8060.649	1621.499	48.4389	1195.343
	5	1349.164	698.8531	36677.83	1583.944	594.6159	29536.57	1620.005	134.965	3255.536
	6	1350.944	248.7856	11780.31	1585.767	193.2584	8125.78	1621.152	37.4497	858.2103
	7	1345.029	783.7011	39168.22	1577.123	803.8189	38002.52	1614.575	149.1485	4165.656
	8	1347.641	878.0891	41104.76	1581.333	812.4116	33857.55	1617.735	193.062	4746.298
	9	1351.121	391.0558	18896.93	1585.326	275.4845	11880.11	1620.89	64.9458	1592.34
	10	1343.872	1457.3	77888.83	1577.857	1091.54	53633.07	1614.967	287.1379	8305.471
	11	1350.988	400.5839	20115.89	1586.215	278.5636	11332.41	1621.215	78.6093	1861.64
	12	1347.341	833.1567	43473.11	1582.207	699.2434	31412.4	1616.879	172.5724	4105.002
22AK-060-1-1	1	1349.77	902.58	41386.48	1584.59	1336.27	58061.5	1617.606	317.95	7595.99
	2	1345.51	1410.99	64441.7	1574.58	2496.16	98454.4	1610.63	493.122	13546.99
	3	1345.42	1209.52	61767.4	1575.87	1230.7	56851.2	1611.98	326.76	9226.5
	4	1348.2	1083.95	50111.11	1581.2	1345.95	63120.03	1617.55	306.62	8652.82
	5	1346.86	1035.09	42218.54	1578.32	1519.95	65166.2	1614.3	412.692	12423.95
	6	1345.98	1385.35	64591.71	1576.29	1919.2	80055.03	1612.75	486.17	13701.53
	7	1351.72	555.82	23887.56	1583.86	1087.94	39766.51	1619.87	138.08	3116.59
	8	1349.45	1274.3	57699.14	1582.43	1951.57	79693.74	1617.55	281.66	6967.03

Sample	*Site*	*D1 – position*	*D1 - amplitude*	*D1 - area*	*G - position*	*G - amplitude*	*G - area*	*D2 - position*	*D2 - amplitude*	*D2 - area*
	9	1353.63	335.6	11944.72	1585.95	461.72	14021.86	1618.87	81.99	1894.88
	10	1352.3	319.95	14342.27	1585.01	452.7	15541.16	1620.4	88.88	2326.34
	11	1345.29	1441.83	67065.06	1580.07	2548.35	102034.2	1613.68	537.08	12898.72
	12	1347.38	980.3	39810.03	1584.71	1935.7	94892.4	1619.09	246.5	5239.97
22AK-061-1-1	3	1344.588	85.51	4978.45	1585.596	194.745	14881.24			
	4	1341.687	460.879	26827.18	1589.08	686.51	45469.57			
	5	1344.41	77.97	3790.06	1586.276	95.988	5538.87	1621.54	25.42	797.61
	9	1335.38	607.02	32572.94	1575.15	1059.857	61639.3	1605.867	566	23705.02
	10	1335.08	1851.99	116307.8	1584.75	4603.54	327996.2			
	11	1334.89	158.27	8898.31	1582.52	422.92	33280.99			
	12	1333.466	159.63	8719.91	1584.78	296.74	22248.56			
	13	1351.26	19.8	949.44	1586.94	45.195	2995.35	1626.105	8.43	191.1
	14	1352.32	32.56	1431.27	1592.52	77.52	4781.5	1630.45	22.63	657.13
	15	1353.73	50.78	2263.6	1588.97	85.62	5420.07	1628.24	14.9	381.404
	16	1349.6	57.3	2798.36	1586.52	95.82	5983.3	1625.62	17.88	444.99
22AK-072-1-1	1	1352.4	228.9	9456.6	1585.98	243.5	9288.6	1621.9	61.6	1616.3
	2	1350.4	1206.3	55661.9	1583.7	1155.15	44258	1619.4	271.8	6445.09
	3	1352.3	474.9	19637.8	1585.35	486.5	16944.99	1620.36	109.64	2595.43
	4	1350.84	806.68	35899.1	1583.6	885.7	37540.66	1619.8	203.2	4694
	5	1347.6	451.85	21615.5	1584.3	290.1	12702.02	1618.8	75.53	1505.4
	6	1351.4	939.3	43664.6	1584.4	975.04	35856.9	1619.9	204.2	4691.65
	7	1351.4	1009.16	43851.65	1583.8	1284.22	45574.8	1618.75	224.77	5323.6
	8	1352.1	690.54	30534.1	1584.96	721.2	26122.78	1619.62	147.02	3357.76
	9	1349.3	2064.5	98132.4	1581.06	2627.7	104385	1615.9	583.2	15681.84
	10	1352.26	662.6	28188.09	1585.03	726.1	27381.6	1620.66	168.4	4230.98
	11	1352	360.7	14554.3	1585.5	409.7	16831.8	1622.02	121	3370.14
	12	1350.4	631	29414.05	1583.6	568.07	22640.4	1619.6	145.94	3512.5
22AK-073-1-1	1	1352.7	151.2	6598.6	1587.2	264.56	12386.26	1619.5	74.79	1994.4
	2	1353.6	60.5	2458.7	1585.2	84.2	3018.8	1617.8	24.8	869.99
	3	1353.5	164.8	6518.35	1585.7	280.17	9703.56	1620.7	50.88	1187.23
	10	1352.4	156.8	6509	1584.56	297.85	13421.55	1619.9	71.2	1802.7

Sample	*Site*	*D1 – position*	*D1 - amplitude*	*D1 - area*	*G - position*	*G - amplitude*	*G - area*	*D2 - position*	*D2 - amplitude*	*D2 - area*
	11	1350.4	448.8	18988.9	1581.53	643.2	25365.2	1617.65	128.4	3317.25
	13	1350.4	331.28	13730.76	1582.5	454.3	17538.3	1619.2	113.99	2985.09
	19	1350.06	146.8	6288.5	1586.7	193.9	11377.3	1623.38	44.56	1089.4
	22	1353.8	49.6	1996.9	1586.9	72.25	3009.97	1622.4	15.04	395.08
	23	1354.25	35.96	1430.82	1585.9	63.26	2667.5	1622.5	15.8	435.8
22AK-079-1-1	1	1339.891	317.0258	14825.09	1573.802	682.0687	37727.16	1613.757	203.5798	7636.865
	2	1342.602	310.7663	14322.15	1571.777	727.0933	39882.08	1610.398	153.3656	5571.552
	3	1344.628	405.165	21659.11	1581.795	819.6713	52853.87	1621.185	75.16976	1414.53
	4	1342.612	873.211	40980.27	1572.579	1513.915	65447.02			
	5	1339.058	442.2756	22677.39	1574.959	847.0988	49557.36			
	6	1344.097	605.1168	27381.59	1575.896	1065.26	52941.61			
	7	1344.358	1276.517	61309.82	1574.021	2067.67	87195.03	1609.735	441.589	11937.94
	8	1351.02	494.0878	22591.62	1581.546	921.5485	37342.78			
	9	1347.539	696.7735	31402.04	1579.873	1157.649	48620.3			
	11	1344.069	1125.605	49814.78	1574.954	1493.048	72594.66			
	12	1350.67	1220.375	52639.98	1582.355	1420.344	54879.33	1617.826	197.7269	3963.11
	13	1345.489	1148.821	52913.66	1576.446	1759.886	89981.89	1613.541	398.8154	10854.09
22AK-080-1-1	1	1350.716	460.7335	18850.84	1583.014	623.1273	24612.7	1619.536	107.2	2613.003
	2	1349.918	206.6187	8662.271	1585.198	265.7076	11899.84	1620.43	51.1323	1152.016
	3	1346.943	53.6206	2601.314	1587.339	75.5362	3637.05	1621.69	19.7817	598.0281
	4	1342.511	785.8412	49091.11	1585.89	1281.692	74633.54	1613.421	261.0646	7697.751
	5	1351.106	544.6732	23737.86	1583.896	525.0092	17159.95	1618.643	123.4838	3299.224
	6	1350.944	700.2402	31434.81	1583.67	754.6702	26352.91	1619.147	139.5079	3347.852
	7	1351.065	860.7844	36253.46	1583.017	1060.708	38320.64	1618.288	168.2329	3682.684
	8	1338.247	457.8512	28538.23	1575.947	1032.554	76010.56	1610.946	496.5647	25407.93
	9	1342.493	826.0434	36692.75	1573.605	1367.447	57106.29	1610.86	557.2527	21243.04
	11	1344.769	1019.544	48623.07	1578.479	1164.914	61545.3	1615.99	299.0464	8468.904
	12	1339.913	890.8314	42011.71	1570.011	1334.535	66979.98			
22AK-081-1-2	1	1581.095	1502.244	38944.27	1620.347	76.1098	1251.705	1353.426	207.7624	8878.386
	2	1578.75	1074.271	27701.4	1619.609	51.7984	551.3769	1352.131	205.5017	8175.092
	3	1580.85	480.3807	12695.11	1354.12	101.0325	4168.919	1621.421	27.3729	379.5178

Sample	*Site*	*D1 – position*	*D1 - amplitude*	*D1 - area*	*G - position*	*G - amplitude*	*G - area*	*D2 - position*	*D2 - amplitude*	*D2 - area*
	4	1345.725	162.7446	7023.672	1580.455	382.7851	12212.37	1613.161	37.1116	1180.919
	5	1349.051	120.0121	4769.976	1581.868	290.4849	7867.772	1615.042	27.949	895.9503
	6	1345.488	154.1104	8517.318	1580.598	971.1921	33404.21	1611.209	166.4055	5132.939
	7	1581.056	285.4904	7058.477	1355.842	31.4158	1162.562			
	8	1349.741	233.9146	10316.21	1578.348	1092.831	28788.54	1610.379	62.425	2280.496
	9	1353.905	61.5476	3132.595	1582.358	171.3387	4878.992			
	10	1348.933	722.2662	31769.53	1580.222	2560	71979.6	1615.719	140.7927	3672.986
	11	1578.896	1342.737	32259.72	1350.002	257.3487	10732.75	1620.551	68.6246	1233.189
	12	1580.469	1028.556	25436.57	1351.191	170.4284	7728.874	1620.551	51.4101	1086.357
22AK-082-1-1	1	1352.871	95.9072	3799.646	1585.423	184.186	12244.4	1625.005	33.45	1087.027
	2	1352.557	24.334	738.8606	1581.8	97.0977	8190.09	1613.222	5.9757	198.3556
	3	1351.525	112.9813	4419.089	1584.878	146.3175	6804.585	1623.346	51.9042	1738.847
	4	1351.559	99.7657	3978.734	1585.78	138.9988	6533.907	1622.844	32.5442	885.3991
	7	1343.346	98.0034	5613.883	1586.764	439.1875	33650.83			
	8	1342.181	74.5939	3883.117	1585.479	185.278	14095.91			
	9	1353.376	23.1197	643.9557	1589.929	98.7747	6277.035	1631.319	40.9705	1452.128
	10	1345.117	102.8529	5633.81	1585.081	275.799	20036.9			
	11	1349.586	63.3183	2777.818	1585.042	74.2553	3288.648	1619.81	21.6777	655.5334
	12	1351.443	190.3177	7507.505	1584.457	202.4681	6779.037	1616.961	42.2045	1093.119
	13	1344.825	78.6564	4046.868	1582.57	181.4924	13205.63			
	14	1346.269	100.3837	4997.986	1584.178	329.4831	24949.07			